Università degli Studi di Genova

Dottorato di Ricerca in Fisica – XIV Ciclo

Study of $B \rightarrow \psi(2S)K$ decays with $\psi(2S) \rightarrow J/\psi\, \pi^0\pi^0$ in the BABAR experiment

Candidato:
Dott. Francesca Pastore

Relatori:
Prof. Alberto Santroni
Dott. Stefano Passaggio

Relatore esterno:
Dott. Giancarlo Piredda
Università di Roma

A mamma e papá,
per aver sopportato tutto
senza avere chiaro il perchè..

The mathematical sciences particularly
exhibit order, symmetry, and limitation;
and these are the greatest forms
of the beautiful.

Aristotle, *Metaphysica 3-1078b*

Contents

Introduction

Symmetries and violations of symmetries have been fundamental tools to build up many new theories in modern physics. In particle physics the violation of the CP symmetry has been a central argument since its discovery in 1964 in the neutral kaon system and its study is far from being concluded. Besides its implications for the study of fundamental interaction, *CP* violation is also related to the matter/antimatter asymmetry of the observable universe and thus to cosmological problems.

CP violation arises naturally in the Standard Model with three quark generations, however it still remains one of the least experimentally constrained sectors of the model. The consistency of the Standard Model itself can be probed by testing the unitarity of the Cabibbo-Kobayashi-Maskawa (CKM) matrix, which describes the weak interactions of the quarks. Any deviation from unitarity can address to new physics beyond the Standard Model.

The study of the neutral B mesons decays is a fertile ground for *CP* violation studies. The $B^0\overline{B}^0$ system offers the possibility to measure many parameters of the Standard Model, since in this system *CP* violation manifests itself through not highly suppressed elements of the CKM matrix. The most promising processes are the decays of the neutral B mesons to final CP eigenstates with a charmonium resonance and a kaon. In these processes the time-dependent asymmetry between the rates of the B^0 and the $\overline{B}^0$ decays to the same CP eigenstate is simply correlated, without theoretical uncertainties, to $\sin 2\beta$, one of the parameters of the CKM matrix.

A measurement of the time-dependent *CP* asymmetry in the $\overline{B}^0$ system has being performed at B Factory experiments as *BABAR* at SLAC and BELLE at KEK. These asymmetric B Factories operate at the $\Upsilon(4S)$ resonance, producing a $B\overline{B}$ pair in e^+e^- high luminosity collisions. The coherence of the two mesons state allows to know the flavor (flavor tagging) of both the B mesons when one of them decays, and thus makes it possible to measure the *CP* asymmetry as a function of time.

In this thesis, I'm describing the search for $B^0 \to \psi(2S) K^0_S$ ($K^0_S \to \pi^+\pi^-$) and $B^\pm \to \psi(2S) K^\pm$ processes, using the decay $\psi(2S) \to J/\psi\,\pi^0\pi^0$, in the data collected by the *BABAR* experiment, corresponding to an integrated luminosity of $44.7\,\mathrm{fb}^{-1}$. The $B^0 \to \psi(2S) K^0_S$ decay events allow the measurement of $\sin 2\beta$. Up to now, this decay process has provided the second largest sample of CP eigenstates for the measurement of $\sin 2\beta$. In this sample the $\psi(2S)$ mesons are identified through the $J/\psi\,\pi^+\pi^-$ and $\ell^+\ell^-$ final states, which are respectively the most abundant and the most easly detectable exclusive modes. The $\psi(2S) \to J/\psi \pi^0\pi^0$ channel, main topic of this work, is the second largest decay process of the $\psi(2S)$ meson. Hence this analysis is aimed at identifying an additional and independent sample of events for the CP asymmetry study. The requirements of a high purity in the CP sample is the main constraint, with the drawback of a low selection efficiency.

The selection described in this thesis makes widely use of results provided by experiments which were dedicated to the study of charmonium decays. In particular the precision measurements of the $\pi^0\pi^0$ invariant mass spectrum of the $J/\psi \pi^0\pi^0$ final state and the careful study of its angular distributions are very powerful tools to reject of combinatorial background, related to the low energy neutral pions, and therefore to enhance the purity of the sample.

The results from measurements of the Branching Ratios for the charged channel $B^\pm \to \psi(2S) K^\pm$, studied as a control sample with high statistics, and the neutral channel $B^0 \to \psi(2S) K^0_S$, using the decay $\psi(2S) \to J/\psi \pi^0\pi^0$ are also presented. These measurements, besides their intrinsic value, can be considered as a consistency check of the selection, which, as already stated, has anyhow been tuned toward the collection of a sample intended for the *CP* asymmetry measurement.

This thesis is organized as follows.

The first Chapter describes the main motivation leading to this analysis, briefly discussing how *CP*-violating phenomena can be used to test the Standard Model consistency or alternatively to indicate the existence of new physics. In the framework of the Standard Model, the $B^0 \to \psi(2S) K^0_S$ decay is one of the processes that can give a direct measurement of the time-dependent asymmetry providing a measure of the $\sin 2\beta$ parameter.

In the second Chapter a description of the *BABAR* detector installed at the PEP-II B Factory is given. Special attention is devoted to the subdetectors and the experimental tools relevant to this analysis: mainly the electromagnetic Calorimeter performances are emphasized, as well as the related neutral clusters reconstruction procedures.

Each particle involved in the $B \to \psi(2S)(\to J/\psi \pi^0\pi^0)$ K ($K^\pm$ or $K^0_S \to \pi^+\pi^-$) decays needs a dedicated reconstruction procedure which exploits all information on stable particles made available from within the individual *BABAR* sub-detectors. This is described in the third Chapter along with the presentation of some analysis tools.

The fourth Chapter mainly describes the kinematical properties of the $\psi(2S) \to J/\psi \pi^0\pi^0$ decay process. It first introduces the theoretical and experimental results obtained up to now on this decay. Among them, we concentrate on the observed shape of the dipion invariant mass spectrum, since it proves to be one of the most efficient variables to reject the aboundant combinatorial background, characteristic of this decay. Other variables are also exploited to enhance the purity of the selection, like the event topology and the helicity angle of the $\psi(2S)$ meson, whereas the experimentally clear J/ψ decay into leptons allows to easly identify the $\psi(2S)$ decay vertex.

The main topic of the fifth Chapter is the Branching Ratio analysis. This has been tuned on Monte Carlo samples following two simultaneous requirements: first, minimizing the statistical error on the Branching Ratio results and the sensitivity to $\sin 2\beta$ measurement, second reaching the highest signal purity, while keeping an acceptable efficiency in the selection. Due to the presence of two soft neutral pions in the decay process, a low efficiency is however expected and, consequentely, a small statistical significance on the Branching Ratio measurements.

With the aim of measuring the $\sin 2\beta$ parameter with this sample, the background composition is accurately estimated. Each background source brings a different asymmetry and that must be accounted for when performing the $\sin 2\beta$ measurement. In the sixth Chapter an overview is presented of the whole procedure of the measurement, which have brought to the first observation of CP violation asymmetry in the B meson system.

Chapter 1

CP Violation in the B Meson System

1.1 Introduction

The violation of the *CP* symmetry is still one of the central open problems in particle physics, though its discovery in the K^0 system dates back to more than thirty years ago. Standard Model with three quark generations predicts a small CP violation and accurate experimental tests are therefore needed to arrange this phenomenon within the model and ensure the validity of the model itself.

In this Chapter an introduction to CP violation in the $\overline{B}^0$ system is presented, since it's expected to show up sizeble CP violating asymmetries within the framework of the Standard Model. The common formalism to describe the neutral B mesons system is introduced, emphasizing the mixing and the time evolution of a coherent $\overline{B}^0$ state, such as that produced at the Υ(4S) resonance in the B-Factories. Above all, I point out the group of B meson decays with a charmonium resonance in the final state, since their decay mechanism can explicitely provide information on the broken CP symmetry *in the interference between decays with and without mixing*: this asymmetry is an observable quantity accessible at a high luminosity e^+e^- B Factory.

In Section 1.4 the CKM picture of CP violation is given, in which the unitarity of the CKM matrix, which describes the interactions between different generations of quarks, translates into the closing conditions of the unitarity triangles and introduces the now usual formalism of the angles α, β and γ. A non-zero value of one of this angles proves that the CP violation may also accour in the $\overline{B}^0$ system, whereas the size of the violating term may suggest whether the Standard Model is a complete theory or must be extended toward new physics.

1.2 *CP* violation

A complete set of discrete trasformations on the Hilbert space preserving the Minkowski distance are the three independent operators: charge conjugation (C), parity (P) and time reversal (T). Any other discrete interval-preserving transformation can be formed by C, P, T and the group of the continuos Lorentz and gauge rotations. They are potential simmetries of a field theory Lagrangian: P reverses the handedness of space, $(t, \vec{x}) \rightarrow (t, --\vec{x})$, T interchanges the forward and the backward ligh-cones, $(t, \vec{x}) \rightarrow (--t, \vec{x})$, and C interchanges particles and antiparticles. The combination CP replaces a particle by its antiparticle and reverses its momentum and helicity. CP violation arises in any field theory described by complex coupling constants in the Lagrangian, when they cannot be removed by any choice of the phase convention of the theory.

The invariance of any local Lorentz-invariant quantum field theory under CPT trasformations is ensured theoretically by the Pauli-Lüders' theorem [2] and confirmed experimentally up to now. For example, a recent estimate of the relative $K^0\overline{K}^0$ mass difference [3], found $\left|M_{K^0} - M_{\overline{K}^0}\right| / M_{K^0} \leq 10^{-18}$, strongly disfavouring CPT violation, at least in the K^0 system.

The electromagnetic interaction, in both its classical and quantum-relativistic description, shows a complete invariance under C, P and T trasformations, so that all nuclear interactions were initially assumed to obey the same symmetry. This was proved to be true for strong interactions, while for weak interactions the behaviour was quite different. The first description of weak interactions, introduced by Fermi in 1933-34 [4], was modelled on QED to describe the β decays, assuming a complete *CP* symmetry. Later on, the observation of a maximal parity violation in weak interactions, experimentally discovered by Madame Wu [5], and of the following charge-conjugation violation [6] forced to introduce new violating terms in the Lagrangian, leading to the V-A theory of weak interactions. Landau suggested [7] that the two violations should show themselves in such a way so that their combined product *CP* be conserved. Thus the discovery by Cronin and Fitch in 1964 [8] of a small, but measurable, contribution to the $K^0 \rightarrow \pi^+\pi^-$ (*CP*-even state) branching ratio by the long lived and *CP*-odd component of the K^0 mixture was really remarkable.

Although *CP* violation had not been anticipated, the experimental findings as well as their interpretation were soon accepted. Since then an enourmous amount of theoretical work has been done to try to understand the phenomenon. In 1973 Kobayashi and Maskawa [9], in order to accomodate *CP* violation into the framework of the Standard Model, proposed to extend to 6 the number of basic matter component, i.e. the quark flavors. Subsequent discoveries of c, b and t quarks proved this hypothesis and led to the CKM description of the Standard Model.

In 1980, Sanda and Carter pointed out that this CKM model contained the possibility of a sizeble *CP* violating asymmety in some B meson decay modes [10]. An observation of *CP* violation in the B meson system would be a solid confirmation of the Standard Model. The consistency of the model can be definitely probed by the validity of the unitarity of the CKM 3x3 matrix. Any violation of the unitarity, that can be evaluated by independent measurements of the angles of the 'unitarity triangles', could be a symptom of the existence of new physics, and the need to extend the theory to new particles and decays. Therefore major theory issues in b-phyisics are (1) whether the CKM description of CP violation is correct or there are other sources and (2) whether the Standard Model is the correct effective theory up to scales of order $\sim$ 1 TeV. The second assumption could be probed for example by the observation of flavor-changing-neutral current (FNCN) decays such as $b \rightarrow s\gamma$, $b \rightarrow s\ell^+\ell^-$ and $b \rightarrow sq\overline{q}$. Both questions can be addressed in a unique way, which has stimulated many experimental and theoretical activities.

1.2.1 Present Searches of CP Violation

Until very recently, *CP* violation had been observed only in the neutral kaon system, but two new important collaborations, *BABAR* at SLAC, within which this thesis work was carried out, and BELLE [13] at KEK-B (Japan), announced the observation of *CP* violation in the $B^0\overline{B}^0$ system.

Other experiments are interested in this physics: HERA-B [11] at DESY is taking data with competitive schedule, while Tevatron [12] collider and LHC [14] project have planned experiments addressing the same B physics study. It is believed that, with the CP violation predicted by the Standard Model, it is not possible to generate the observed size of matter-antimatter asymmetry of the Universe [15, 16]. Currently experimental efforts are concentrated on neutral systems such as K^0-$\overline{K}^0$, B^0-$\overline{B}^0$ and D^0-$\overline{D}^0$ complex. Other searches divide into two classes. First class involves weak interactions or parity violation; the most sensitive are the searches for an electric dipole moment of the elementary particles such as neutron and electron. Second class involves processes otherwise allowed by the strong or electromagnetic interactions. This includes the search for C violation in η decay and searches for T violation in a number of nuclear and electromagnetic reactions.

1.3 The $B^0\overline{B}^0$ system

In this Section the most rilevant characteristics of the $B\overline{B}$ system are introduced, in a way that is completely model-independent, since are mainly based on the quantum mechanics properties of the two states system. Later on, all the physical quantities that can be extracted will be correlated to the fundamental parameters of the Standard Model, that is the only context we work in. The presence of an irreducible phase in the Cabibbo–Kobayashi–Maskawa matrix suggests the possibility of *CP*-violating phenomena in the processes, similar to the ones already observed in $K^0\overline{K}^0$ decays; the study of these asymmetries can probe the role of *CP* asymmetry in and beyond the Standard Model.

The system of interest is a pair of self-conjugate mesons B_d, involving b and d type quarks, which must be distinguished from the B_s mesons, made of b and s type quarks.

The neutral B meson system exhibits, like the neutral K, the phenomenon of particle–antiparticle mixing. The mesons are produced in a defined flavor state, which then evolves into a time-dependent quantum superposition of them until they finally decay; in absence of *CP* violation, the mass and lifetime eigenstates are also *CP* eigenstates.

Although the $B^0\overline{B}^0$ system is quite alike the $K^0\overline{K}^0$, from a phenomenological point of view there are many differences, due to the fact that *CP* violation in the $K^0\overline{K}^0$system has to go through higher generations. It is therefore strongly suppressed by off-diagonal elements in the CKM matrix, while it is expected to be more important in the B system. Furthermore, while the K mass eigenstates K^0_L and K^0_S are nearly degenerate in mass but have very different lifetimes (by nearly a factor of 600), the B^0–$\overline{B}^0$mass difference is expected to be about some 10^{-3} eV, and the difference in lifetimes very small as well. This may be true only for the B_d and not for the B_s; in the following discussion, however, only the former mesons will be taken into account.

1.3.1 The $B^0\overline{B}^0$ mixing

B^0 mesons are produced as well-defined flavor eigenstates, either B^0 ($=\overline{b}d$) or $\overline{B}^0$ ($=\overline{d}b$) [1]. Since B^0 and $\overline{B}^0$ can mix, the mass eigenstates are a superposition of $a|B^0\rangle + b|\overline{B}^0\rangle$ which obeys the Schrodinger equation

$$i\frac{d}{dt}\begin{pmatrix} a \\ b \end{pmatrix} = \mathcal{H}\begin{pmatrix} a \\ b \end{pmatrix} = \left(\mathbf{M} - \frac{i}{2}\mathbf{\Gamma}\right)\begin{pmatrix} a \\ b \end{pmatrix}. \tag{1.1}$$

where $\mathbf{M}$ and $\mathbf{\Gamma}$ are 2×2 Hermitian matrices ($M_{12} = M_{21}^*$ and $\Gamma_{12} = \Gamma_{21}^*$). CPT invariance ensures that $H_{11} = H_{22}$; we thus define $\Gamma \equiv \Gamma_{11} = \Gamma_{22}$ and $M \equiv M_{11} = M_{22}$. If CP is not conserved then the eigenvectors, the mass eigenstates $|B_L\rangle$ and $|B_H\rangle$, are not the CP eigenstates but are

$$|B_L\rangle = p|B^0\rangle + q|\overline{B}^0\rangle, \quad |B_H\rangle = p|B^0\rangle - q|\overline{B}^0\rangle, \tag{1.2}$$

where the ratio q/p is

$$\frac{q}{p} = +\sqrt{\frac{M_{12}^* - \frac{1}{2}\Gamma_{12}^*}{M_{12} - \frac{1}{2}\Gamma_{12}}}. \tag{1.3}$$

CP is violated if the conditions $|p/q|^2 \neq 1$ or $\mathcal{I}m\,(M_{12}\Gamma_{12}^*) \neq 0$ are satisfied. The time dependence of the mass eigenstates is

$$\begin{aligned} |B_L(t)\rangle &= e^{-\Gamma_L t/2} e^{i m_L t/2} |B_L(0)\rangle \\ |B_H(t)\rangle &= e^{-\Gamma_H t/2} e^{i m_H t/2} |B_H(0)\rangle \end{aligned} \tag{1.4}$$

leading to the time evolution of the flavor eigenstates as

$$\begin{aligned} |B^0(t)\rangle &= e^{-\left(iM_B + \frac{\Gamma}{2}\right)t}\left(\cos\frac{\Delta M_B t}{2}|B^0(0)\rangle + i\frac{q}{p}\sin\frac{\Delta M_B t}{2}|\overline{B}^0(0)\rangle\right) \\ |\overline{B}^0(t)\rangle &= e^{-\left(iM_B + \frac{\Gamma}{2}\right)t}\left(i\frac{p}{q}\sin\frac{\Delta M_B t}{2}|B^0(0)\rangle + \cos\frac{\Delta M_B t}{2}|\overline{B}^0(0)\rangle\right) \end{aligned} \tag{1.5}$$

where $M_B = (m_L + m_H)/2$, $\Delta M_B = m_H - m_L \equiv \Delta m_d$ and $\Gamma = \Gamma_L \approx \Gamma_H$, and t is the decay time in the B^0 rest frame. It's straightforward to compute the time-dependent probability $|\mathcal{F}(t)_\pm|^2$ of finding a B^0 (+) or a $\overline{B}^0$ (-) from a B meson produced at $t = 0$ as a B^0

$$|\mathcal{F}(t)_\pm|^2 = \frac{1}{2}e^{-\Gamma t}\left(\cosh\frac{1}{2}\Delta\Gamma t \pm \cos\Delta m_d t\right) \tag{1.6}$$

[1] The convenction is that, similarly to the K mesons, B^0 is the isospin partner of B^+, therefore it contains the $\overline{b}$ quark.

The appareance of a $\overline{B}^0(B^0)$ from a $B^0(\overline{B}^0)$ is commonly defined as $B^0\overline{B}^0$ mixing or beauty oscillation, since the *beauty* content of the initial B meson changes in time. Δm_{d} is therefore the mixing frequency of the $B^0\overline{B}^0$ system. In the absence of CP violation, the mass and width differences become simply:

$$\Delta m_{\mathrm{d}} = 2\,|M_{12}|\,, \quad \Delta\Gamma = 2\,|\Gamma_{12}|\,.$$

Whereas Δm_{d} has been measured to be $(0.33 \pm 0.28)\,\mathrm{MeV}$ [3], the difference in lifetime can be safely assumed to be much smaller than the lifetime itself, since the many channels that produce that width contribute, with different signs, with branching ratios of the order of 10^{-3}. Therefore, it is possible to assume, model-independently, that

$$\left.\begin{array}{l} x_d \equiv \Delta m_{\mathrm{d}}/M_B = 0.73 \pm 0.05 \\ y_d \equiv \Delta\Gamma_B/2\Gamma_B = \mathcal{O}\left(10^{-2}\right) \end{array}\right\} \Longrightarrow \Delta\Gamma_B \ll \Delta m_{\mathrm{d}}. \tag{1.7}$$

By using Eq. 1.7 in 1.3, the expression for q/p becomes simply

$$\frac{q}{p} \simeq -\frac{M_{12}}{|M_{12}|} \tag{1.8}$$

1.3.2 *CP* violation in *B* decays

The operations of Charge Conjugation C and Parity P operate on B and $\overline{B}$ meson states as follow:

$$\begin{array}{ll} C|B(\overrightarrow{p})\rangle = |\overline{B}(\overrightarrow{p})\rangle, & C|\overline{B}(\overrightarrow{p})\rangle = |B(\overrightarrow{p})\rangle \\ P|B(\overrightarrow{p})\rangle = -|B(-\overrightarrow{p})\rangle, & P|\overline{B}(\overrightarrow{p})\rangle = -|\overline{B}(-\overrightarrow{p})\rangle \\ CP|B(\overrightarrow{p})\rangle = -|\overline{B}(-\overrightarrow{p})\rangle, & CP|\overline{B}(\overrightarrow{p})\rangle = -|B(-\overrightarrow{p})\rangle \quad . \end{array} \tag{1.9}$$

CP violation can be measured whenever a process $B \to f$ goes via two amplitudes $\mathcal{A}$ and $\mathcal{B}$, from the interference of the decay rate with that of its CP conjugate process $\overline{B} \to \overline{f}$. This is due to the presence of two types of non-trivial phases, usually referred in literature as strong, $\delta_{\mathcal{A}}$, and weak, $\phi_{\mathcal{A}}$. Then the amplitude (A_f) of the decay and that of its CP conjugate process $(\overline{A}_{\overline{f}})$ are:

$$\begin{array}{rcl} A_f &=& \left(|\mathcal{A}|\,e^{i(\delta_{\mathcal{A}}+\phi_{\mathcal{A}})} + |\mathcal{B}|\,e^{i(\delta_{\mathcal{B}}+\phi_{\mathcal{B}})}\right)^2 \\ \overline{A}_{\overline{f}} &=& \left(|\mathcal{A}|\,e^{i(\delta_{\mathcal{A}}-\phi_{\mathcal{A}})} + |\mathcal{B}|\,e^{i(\delta_{\mathcal{B}}-\phi_{\mathcal{B}})}\right)^2 \end{array} \tag{1.10}$$

Complex parameters in any Lagrangian term that contributes to the amplitude appear in complex conjugate form in the CP conjugate amplitude.

Thus their phases appear with opposite signs in A_f and $\overline{A}_{\overline{f}}$. In the Standard Model these phases only accour in the CKM matrix which describes the electroweak sector, hence these phases are often called "weak". "Strong" phases can appear in the Lagrangian, even when it is real, because of the final states rescattering in the decay process, which is mainly due to strong interactions. Such phases do not violate CP and thus appear in A_f and $\overline{A}_{\overline{f}}$ with the same sign.

CP violation, correlated to the weak phases, can then be extracted from the interference of the two decay rates:

$$A_f - \overline{A}_{\overline{f}} = 2\,|\mathcal{AB}|\,\sin(\delta_{\mathcal{A}} - \delta_{\mathcal{B}})\,\sin(\phi_{\mathcal{A}} - \phi_{\mathcal{B}}) \tag{1.11}$$

Any two amplitudes can contribute, though the effect is more evident when they are of approximately equal size. Thus charged B decays can exhibit CP violation as well as neutral B decays. In some cases, we will see that it is possible to guarantee that $|\sin(\delta_{\mathcal{A}} - \delta_{\mathcal{B}})|$ is unity, so we can get clean information on the weak phases. In the case of neutral B decays, mixing can be the second amplitude.

Thus *CP* violation can manifest itself in three distinct ways in the B meson system:

1. *CP* **violation in mixing**, from a nonvanishing relative phase between the mass and the width parts of the mixing matrix, thus not allowing to choose the mass eigenstates as *CP* eigenstates;

2. *CP* **violation in decay**, arising in B decays when the amplitude for a decay and its *CP* conjugate have different magnitudes;

3. *CP* **violation in interference** between decays with and without mixing, which can occur for modes in which the final state is accessible to both B^0 and $\overline{B}^0$.

The three types can be present independently or together. Each has different implications and can be studied in different processes; however, it is not always simple to isolate contributions from each to an observed asymmetry. This leads to the search for particular "clean" modes in which the contribution of a single one is dominant.

In the Standard Model context, each of these types has a tight connection with different terms in the Lagrangian, although some of them are intrinsically coupled to strong interactions, thus not leading clear information.

CP Violation in Mixing

Indirect CP violation, or CP violation in mixing, arises when the quantity q/p defined in Eq. 1.3 is not a pure phase; its magnitude is independent of phase conventions, therefore

$$\left|\frac{q}{p}\right|^2 \neq 1 \Longrightarrow CP \text{ Violation.}$$

In the neutral B system, this effect can be observed through asymmetries in semileptonic decays; the time-dependent asymmetry is given by:

$$a_{\mathrm{SL}} = \frac{\Gamma\left(\overline{B}^0(t) \to \ell^+\nu X\right) - \Gamma\left(B^0(t) \to \ell^+\nu X\right)}{\Gamma\left(\overline{B}^0(t) \to \ell^+\nu X\right) + \Gamma\left(B^0(t) \to \ell^+\nu X\right)} = \frac{1-|q/p|^4}{1+|q/p|^4}. \tag{1.12}$$

CP violation in mixing has been observed in the neutral kaon system ($\mathcal{R}e\,\epsilon_K \neq 0$). From the assumption in Eq. 1.7, one expects effects from indirect CP violation to be $\mathcal{O}(10^{-2})$; in the context of the Standard Model, it is possible (by explicit calculation of the diagrams) to further reduce the expected magnitude violation to $\mathcal{O}(10^{-3})$. Furthermore, large hadronic uncertainities would make the extraction of their relation to fundamental Standard Model parameters very problematic. However, the very smallness of the effect make this a possibly fruitful area to search for new physics.

CP Violation in Decay

This kind of asymmetry, sometimes called *direct CP* violation, arises from complex coupling constants in the Lagrangian that introduce irremovable phases in the decay amplitudes. As will be discussed in section 1.4, this is the case of the Kobayashi–Maskawa phase in the three-generations Standard Model mixing matrix. If F is a a final state accessible by both B^0 and $\overline{B}^0$, one defines the amplitudes

$$\begin{aligned} A_f &= \langle f|\mathbf{H}|B^0\rangle, \\ \overline{A}_f &= \langle f|\mathbf{H}|\overline{B}^0\rangle. \end{aligned} \tag{1.13}$$

If several amplitudes contribute to $B^0 \to$f, by separating the contributions of the "weak" and "strong" phases into $e^{i\varphi_i}$ and $e^{i\delta_i}$, A_f can be written as

$$A_f = \sum_i A_i e^{i(\delta_i+\varphi_i)}, \tag{1.14}$$

It should be noted that a process, to exhibit this type of CP asymmetry, need two contributions in the cross section to differ in both their strong and weak phases, thus are unlikely to appear in purely leptonic and semileptonic decays dominated by a single diagram.

As there is freedom in the choice of the phase in the CP operator, the CP-conjugated amplitude is

$$\overline{A}_{\overline{f}} = e^{i\xi} \sum_i A_i e^{i(\delta_i - \varphi_i)}, \tag{1.15}$$

with ξ arbitrary. The ratio of the two quantities is independent from phase conventions, and equals to one when CP is conserved (since the weak phases φ_i are all equal). Therefore,

$$\left| \frac{\overline{A}_{\overline{f}}}{A_f} \right| = \left| \frac{\sum_i A_i e^{i(\delta_i - \varphi_i)}}{\sum_i A_i e^{i(\delta_i + \varphi_i)}} \right| \neq 1 \Longrightarrow CP \text{ Violation.}$$

Any CP asymmetry in $B^{\pm}$ decays is from this kind of CP violation, whereas in neutral B's it competes with the other two. There are difficulties in relating this kind of asymmetries to Standard Model parameters, since the ones involving strong phases rely on QCD calculations, giving strongly model-dependent results.

Recent results from CLEO [17] ($a_{CP}\,(B^{\pm} \to J/\psi\, K^{\pm}) = (1.8 \pm 4.3 \pm 0.4)\,\%$) give a strong limit on direct CP violation in charged B decays.

CP Violation in Interference between decays with and without mixing

This kind of effect is apparent in decays to CP eigenstates to which both the B^0 and the $\overline{B}^0$ have access; the second amplitude necessary for interference is provided by mixing. An asymmetry of this kind has been observed unambiguously in the neutral kaon system.

Figure 1.1 shows the B decay into f either directly or indirectly via mixing.

If f_{CP} is a final CP eigenstate with eigenvalue $\eta_{f_{CP}}$, we define the quantity

$$\lambda_{f_{CP}} \equiv \frac{q}{p} \frac{\overline{A}_{f_{CP}}}{A_{f_{CP}}} = \eta_{f_{CP}} \frac{q}{p} \frac{\overline{A}_{\overline{f}_{CP}}}{A_{f_{CP}}} \tag{1.16}$$

that is independent of any phase convention. When CP is conserved, for the reasons exposed in the two preceding sections, $|q/p| = 1$ and $\left| \overline{A}_{\overline{f}_{CP}} / A_{f_{CP}} \right| = 1$; the condition for CP violation now is $\lambda \neq \pm 1$. However, a more interesting

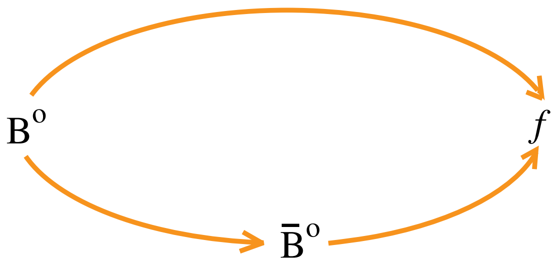

Figure 1.1: Two interfering ways for a B^0 to decay into a final state f.

case is that in which both *CP* violation in decay and in mixing are, to a good approximation, not present, yet there is *CP* violation, which requires only that λ acquires a non-zero phase. The condition becomes

$$|\lambda| = 1, \;\; \mathcal{I}m\,\lambda \neq 0 \Longrightarrow CP \text{ Violation.}$$

This is, from the experimental point of view, the most promising type of asymmetry, for two orders of reasons. First, the large range of possible final *CP* eigenstates comprises a good laboratory to search for asymmetries; second, no nontrivial strong phases are necessary. When it occurs without direct *CP* violation, the asymmetry is easily related to fundamental electroweak Lagrangian parameters, and can either yield a precise measurement or an unambiguous hint for new physics. This is true for the channels dominated by a single phase, for which the expression of the asymmetry greatly simplifies. We describe these cases in the next sections.

1.4 *CP* Violation in the Standard Model

The Standard Model is the most successful gauge theory describing the present knowledge of elementary particles and interactions. Although many problems are still open, over the years a large quantity of data (for example, the electroweak measurements at LEP) have tested it to a very high precision. The effects of radiative corrections on cross sections have been compared at LEP with experimental data, testing the Standard Model at the one-loop level; such good agreement poses tight limits to new physics observable at current energies.

In this framework, *CP* violation is a good opportunity to test the Cabibbo–Kobayashi–Maskawa picture; some of the quantities describing the asymmetries can be unambiguously correlated to fundamental parameters of the mixing matrix. Some tests have been passed, since for example recent results from the study of the $K^0\overline{K}^0$ system at CERN (NA48) and at Fermilab (KTeV) strongly disfavour the possibility that CP asymmetries arise from a new CP-violating superweak interaction superimposed over a perfectly CP-conserving electroweak interaction. Others have not: the Standard Model cannot provide large enough asymmetries to explain the cosmological baryonic asymmetry [18].

The Standard Model unifies the strong and electroweak forces in the gauge symmetry group

$$SU(3)_{\mathrm{C}} \otimes SU(2)_{\mathrm{L}} \otimes U(1)_{\mathrm{Y}}$$

Although the gauge theory describing strong interactions, Quantum Chromodynamics (QCD), is arguably part of the Standard Model [19], in the following the focus will be on the electroweak sector, the Glashow–Weinberg–Salam unified theory [20, 21, 22]. The $SU(3)_{\mathrm{C}}$ colour gauge group pertains to strong interactions only, and will not be discussed further since electroweak interactions are "colour-blind".

Invariance under the action of a gauge group is assumed to insure the renormalizability of the theory, extending it to Yang–Mills theories, that are invariant under non-Abelian local gauge transformations. However, masses explicitly assigned to the bosons would spoil the renormalizability, so they must be introduced by the Higgs mechanism, that accounts also for fermion masses. In particular the complex nature of the interaction matrices between quarks and the single Higgs scalar dublet is the source of CP violation in the Standard Model. The fact that only one phase appears in the three generations Standard Model makes sure that all possible CP-violating effects in this theory are very closely related.

1.4.1 Weak Interactions and the CKM Matrix

The physical states of the Standard Model are comprised of left-handed doublets containing leptons and quarks and right handed singlets

$$\begin{bmatrix} u \\ d \end{bmatrix}_L \begin{bmatrix} c \\ s \end{bmatrix}_L \begin{bmatrix} t \\ b \end{bmatrix}_L, \qquad u_R,\ d_R,\ c_R,\ s_R,\ t_R,\ b_R \tag{1.17}$$

$$\begin{bmatrix} e^- \\ \nu_e \end{bmatrix}_L \begin{bmatrix} \mu^- \\ \nu_\mu \end{bmatrix}_L \begin{bmatrix} \tau^- \\ \nu_\tau \end{bmatrix}_L, \qquad e^-_R,\ \mu^-_R,\ \tau^-_R,\ \nu_{eR},\ \nu_{\mu R},\ \nu_{\tau R}. \tag{1.18}$$

The gauge bosons $W^{\pm}$, γ and Z^o couple to mixtures of the physical d, s and b states through the Cabibbo-Kobayashi-Maskawa (CKM) matrix.

The Lagrangian describing charged current weak decays is

$$\mathcal{L}_{cc} = -\frac{g}{\sqrt{2}} J^{\mu}_{cc} W^{\dagger}_{\mu} + h.c., \tag{1.19}$$

where

$$J^{\mu}_{cc} = \left[\overline{\nu}_e,\ \overline{\nu}_\mu,\ \overline{\nu}_\tau\right] \gamma^\mu V_{MNS} \begin{bmatrix} e_L \\ \mu_L \\ \tau_L \end{bmatrix} + \left[\overline{u}_L,\ \overline{c}_L,\ \overline{t}_L\right] \gamma^\mu V_{CKM} \begin{bmatrix} d_L \\ s_L \\ b_L \end{bmatrix} \tag{1.20}$$

and

$$V_{CKM} = \begin{bmatrix} V_{ud} & V_{us} & V_{ub} \\ V_{cd} & V_{cs} & V_{cb} \\ V_{td} & V_{ts} & V_{tb} \end{bmatrix} \tag{1.21}$$

is the 3×3 Cabibbo-Kobayashi-Maskawa matrix [23, 9]. Multiplying the mass eigenstates (d_L, s_L, b_L) by the CKM matrix leads to the weak eigenstates. V_{MNS} is the analogous matrix required for massive neutrinos.

There are nine (3×3) complex CKM elements. These 18 numbers can be reduced to 4 independent quantities because of unitarity constraints and the fact that the phases of the quark wave functions are arbitrary. Among them, three are real numbers (the Euler mixing angles) and one is an irreducible phase δ_{KM}. These four remaining numbers are **fundamental constants** of nature that need to be determined from experiment, like any other fundamental constant such as α or G.

The irremovable phase in the CKM matrix allows *CP* violation. This comes from the *CP* transformation properties of scalar, pseudoscalar and vector fields, and of their derivatives, and from the properties of Lorentz invariance and hermiticity of the Lagrangian. Each combination of fields and derivatives of fields appearing in the Lagrangian trasforms under *CP* into its hermitian conjugate, whereas their coefficients, which can be either coupling constants or particle masses, do not traform. If any of these quantities is complex, then the corresponding CP-related terms are the complex conjugates of each other, and *CP* is not necessarily a good symmetry of the Lagrangian. Not all lagrangian phases are physically meaningful and part of them can be removed by simply redefining the fields: *CP* violation then arises if a non-zero phase remains for couplings after all possible redefinitions of fields.

In particular, *CP* operation interchanges the coupling terms of the W^+ and the W^- bosons to quarks, apart from the V_{ij} and V^*_{ij} coupling constants.

Thus the single δ_{KM} phase is responsible for any *CP* violating effect in the Standard Model.

The CKM matrix can of course be parametrized in infinite ways; a practical one, adopted by the Particle Data Group (PDG) [3] is the Maiani parameterization, where the four parameters have a clear physical meaning, being the mixing angles between the quark families (θ_{12}, θ_{23} and θ_{13}). If we put $c_{ij} \equiv \cos\theta_{ij}$ and $s_{ij} \equiv \sin\theta_{ij}$ the CKM matrix can be written as:

$$V = \begin{bmatrix} c_{12}c_{13} & s_{12}c_{13} & s_{13}e^{-i\delta} \\ -s_{12}c_{23} - c_{12}s_{23}s_{13}e^{-i\delta} & c_{12}c_{23} - s_{12}s_{23}s_{13}e^{-i\delta} & s_{23}c_{13} \\ s_{12}s_{23} - c_{12}c_{23}s_{13}e^{-i\delta} & -c_{12}c_{23} - s_{12}s_{23}s_{13}e^{-i\delta} & c_{23}c_{13} \end{bmatrix}$$

A practical parameterization is the Wolfenstein 's approximation [24] for small angles, in which the matrix tends to the unitary matrix. It's written in terms of $\lambda = |V_{us}| = \sin\theta_C \simeq 0.22$ acting as the expansion parameter[2]. Including the order λ^3 the matrix appears as:

$$V = \begin{bmatrix} 1-\frac{1}{2}\lambda^2 & \lambda & A\lambda^3\left(\rho - i\eta\right) \\ -\lambda & 1-\frac{1}{2}\lambda^2 & A\lambda^2 \\ A\lambda^3\left(1-\rho-i\eta\right) & -A\lambda^2 & 1 \end{bmatrix} + \mathcal{O}\left(\lambda^4\right) \qquad (1.22)$$

In this approximate parametrization the hierarchy of the angles is emphasized. A way to include the $\mathcal{O}\left(\lambda^4\right)$ terms, which explain CP violation in the K^o system, is the Buras parameterization [25] that uses the $\overline{\rho} = \rho(1-\frac{\lambda^2}{2})$ and $\overline{\eta} = \eta(1-\frac{\lambda^2}{2})$ parameters instead of ρ and η. This latter method is largely used to study the CKM matrix characterizations. The constants λ and A are determined from charged-current weak decays. The measured values are $\lambda = 0.2205 \pm 0.0018$ and A=0.784 ± 0.043, while ρ and η are constrainted from other measurements, as will be described later in Chapter 6. *CP* violation can occur because of the imaginary term in the CKM matrix, proportional to η in this representation [26].

The most recent review by the PDG [3], analyzing a large wealth of data on tree-level processes and using unitarity constraints in the three-generation hypothesis, gives the following 90% confidence limits on the magnitude of the CKM elements (dropping the three-generation constraint the ranges are, especially in the third row, significantly larger):

$$V \sim \begin{pmatrix} 0.9742 \div 0.9757 & 0.219 \div 0.226 & 0.002 \div 0.005 \\ 0.219 \div 0.225 & 0.9734 \div 0.9749 & 0.037 \div 0.043 \\ 0.004 \div 0.014 & 0.035 \div 0.043 & 0.9990 \div 0.9993 \end{pmatrix}. \qquad (1.23)$$

[2] θ_C is the Cabibbo angle [23].

1.4.2 Unitarity Conditions and the Unitarity Triangles

As a result of the unitarity of the matrix, the scalar products of any two rows is zero. Thus, in particular for the B_d meson, the complex quantities

$$
\begin{aligned}
V_{ud}V_{ub}^{*} &= A\lambda^{3}\left(\rho + i\eta\right), \\
V_{td}V_{tb}^{*} &= A\lambda^{3}\left(1-\rho + i\eta\right), \\
V_{cd}V_{cb}^{*} &= -A\lambda^{3}
\end{aligned}
\tag{1.24}
$$

form a triangle of area $|J|/2$, with $J = \Im m\,(V_{ik}V_{jk}^{*}V_{il}V_{jl}^{*}) \sim A^2\lambda^6\eta$, in the (ρ, η) plane (as in Fig. 1.2); the triangle is often rescaled by dividing all the sides by $A\lambda^3$, so that the coordinates of A are simply (ρ, η).

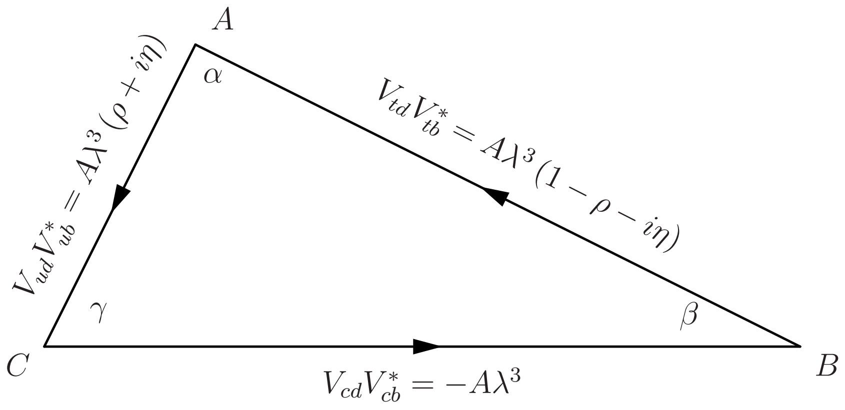

Figure 1.2: The unitarity triangle in the (ρ, η) plane.

The three angles of the Unitarity Triangle,

$$
\begin{aligned}
\alpha &\equiv \arg\left(-\frac{V_{td}V_{tb}^{*}}{V_{ud}V_{ub}^{*}}\right) = \arg\left(-\frac{1-\rho-i\eta}{\rho+i\eta}\right) \\
\beta &\equiv \arg\left(-\frac{V_{cd}V_{cb}^{*}}{V_{td}V_{tb}^{*}}\right) = \arg\left(\frac{1}{1-\rho-i\eta}\right) \\
\gamma &\equiv \arg\left(-\frac{V_{ud}V_{ub}^{*}}{V_{cd}V_{cb}^{*}}\right) = \arg\left(\rho+i\eta\right)
\end{aligned}
\tag{1.25}
$$

are all measurable physical quantities. In particular $B_d \to \pi^+\pi^-$, $B_d \to J/\psi\, K_S^0$ and $B_s \to \rho^0 K_S^0$ are those B decays most commonly proposed in order to measure angle α, β and γ respectively.

CP violation in the Standard Model arises if $J \neq 0$, that is if the triangle has a non-zero area. These conditions must be also true for the other two unitarity triangles, defined as $V_{id}V_{is}^*$, concerning the kaon decays, and $V_{is}V_{ib}^*$, concerning the B_s decays. Knowing the experimental values of the corresponding CKM elements, in these triangles one side is much shorter than the other two, and so they almost collapse to a line. This gives a clear understanding of the difficulty in measuring *CP* violation in leading K and B_s decays, whereas in the B_d triangle the lenghts of the sides are comparable, leading to large angles and potentially large CP-violating asymmetries.

It is crucial to check if measurements of the sides, of order λ^3, and the angles are consistent, i.e. whether or not they actually form a triangle. Deviations from unitarity would imply inconsistence in the theory and hence the presence of new physics in the processes. The Standard Model indeed is incomplete, since too many parameters must be fixed in the theory: besides the four CKM quantities, there are the six quarks masses, the gauge bosons masses and all the coupling constants. Measurements of the angles and the sides of the unitarity triangles could show us how these parameters are related, or what is missing, potentially bringing us beyond the Standard Model.

1.5 *B* Decay Mechanisms

There exists a myriad of decay channels available to B mesons, many of which carry contributions from several different diagrams. Figure 1.3 shows the quark diagram for tree, QCD and electroweak penguin contributions. While quark diagrams can be easly classified in this way, the B decays are not, since long distance physics effects must be taken into account. The decay amplitudes for $b \to q\bar{q}q'$ can always be written as a sum of tree and penguin terms with definite CKM coefficients. Because of the large mass of the b quark, the decays of B mesons are dominated by spectator type decays (both hadronic and semi-leptonic) with the quark-level process $b \to cW^+$.

As mentioned above, *direct CP* violations require two contributions to the decay process which differ in both their strong phases and their weak phases so that $|\overline{A}/A| \neq 1$. Purely leptonic and semileptonic decays are dominated by a single diagram and thus are unlikely to exhibit any measurable direct *CP* violation. Nonleptonic decays often have two terms that are comparable in magnitude and hence could have significant direct *CP* violations. The theoretical calculation requires knowledge of strong phase shifts and of absolute values of various amplitudes, the estimates therefore necessarily have hadronic uncertainties. In contrast, a clean relationship between measured asymmetries and CKM phases is obtained when studying *CP* violation in

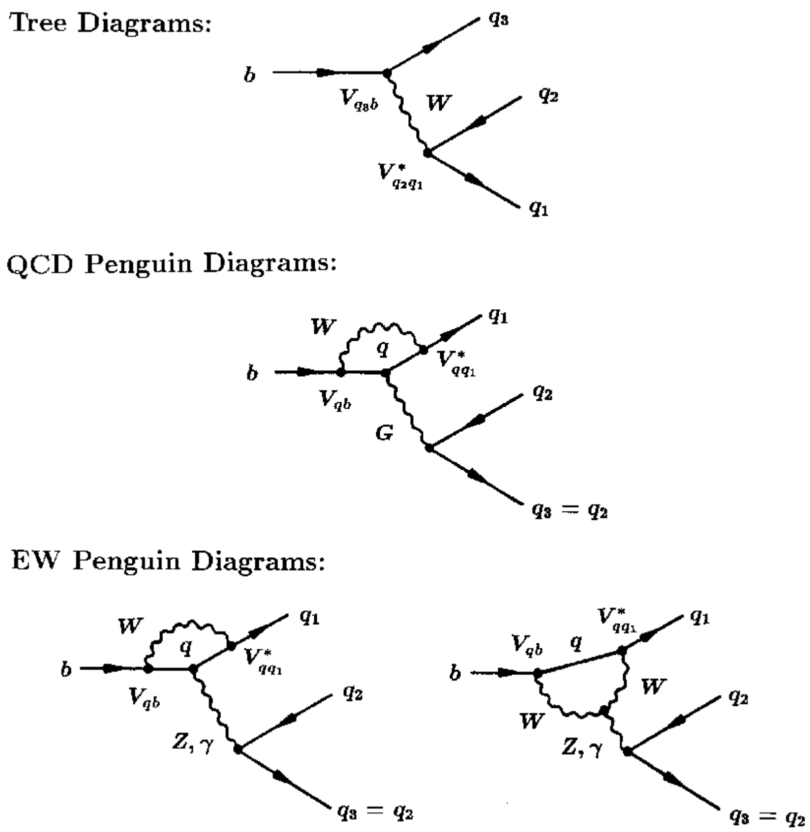

Figure 1.3: Quark diagrams contributing to b decays.

the interference between decays with and without mixing for *CP* eigenstate modes dominated by a single term in the decay amplitude.

As such, the overall picture of *CP* violation in the B meson system is very complicated. To broach this subject, we can classify the various types of B decays to *CP* eigenstates according to how they might manifest *CP* violation:

1. Decays dominated by a single term, such as $b \rightarrow s\bar{s}s$ or $b \rightarrow c\bar{c}s$. Since the Standard Model predicts a very small direct *CP* violation for such decays, these provide the cleanest method for directly measure CKM phases via *CP* violation in interference.

2. Decays with a large tree level term, and suppressed penguin contributions, such as $b \rightarrow c\bar{c}d$ or $b \rightarrow u\bar{u}d$. To the extent that direct *CP* contribution from the penguin terms can be estimated the asymmetries for

these decays can be related to CKM phases.

3. Decays with highly suppressed or null tree contributions, such as $b \to u\overline{u}s$, $b \to s\overline{s}d$ or $b \to s\gamma$. The possibility for relatively large cross terms between various penguins loops and tree diagrams allow several competing *CP* violating terms and significantly complicate analyses.

It's evident that, to extract clear indication on CKM matrix elements, processes of class 1 must be studied. The $B^0 \to J/\psi\, K^0_S$ and $B^0 \to \psi(2\mathrm{S})K^0_S$ processes fall into this category, and they will be described in the next section.

1.5.1 Two-body Decays into Charmonium Hadrons

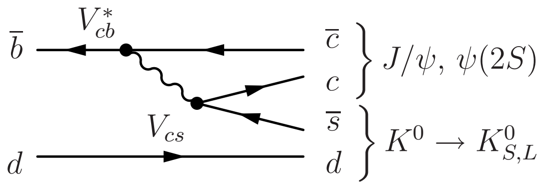

Figure 1.4: Quark diagrams for $B^0 \to J/\psi\, K^0$ and $B^0 \to \psi(2\mathrm{S})K^0$.

Two-body B^0 decays into charmonium hadrons can only be reached by the color suppressed spectator diagram in Figure 1.4 driving the W-mediated process $b \to c\overline{c}s$. The final state can comprise J/ψ as well as $\psi(2\mathrm{S})$ mesons together with the neutral kaon. It contributes an amplitude ratio:

$$\frac{\overline{A}_{c\overline{c}K^0}}{A_{c\overline{c}K^0}} = \eta_{CP}\left(\frac{V_{cb}V^*_{cs}}{V^*_{cb}V_{cs}}\right)e^{-2i\xi_B}. \tag{1.26}$$

In the amplitude for the process $b \to c\overline{c}s$, the penguins contributions are very small, and share the same weak phase with the tree level part. Thus, no direct *CP* violation in decay is expected in these channels, clearing the field from hadronic uncertainities. Furthermore, for all neutral B decays indirect *CP* violation in mixing is expected to be $\mathcal{O}\,(10^{-2})$. Then, since to a good approximation $|\lambda| = 1$, any nonzero immaginary part of λ would be a sign of *CP* violation in interference between decays with and without mixing.

A critical element in such decays is the subsequent $K^0\overline{K}^0$ mixing: it is only because of it that there are common final states for both the B's. Since $B^0 \to K^0$ and $B^0 \to \overline{K}^0$, we must also consider the contribution from the kaon appearing as a K^0_S rather than a K^0_L:

$$\left(\frac{q}{p}\right)_K = \frac{V_{cs}V^*_{cd}}{V^*_{cs}V_{cd}}e^{-2i\xi_K}. \tag{1.27}$$

From the theoretical point of view, the two processes are identical; the only difference is that, since K_L^0 and K_S^0 have opposite CP eigenvalues, the asymmetries are expected to have the same magnitude but opposite sign. From an experimentally point of view, the two processes are very different, since the K_L^0 must be detected as a neutral hadron because of its long lifetime. That is the reason of a bigger background contribution to this decay process detection.

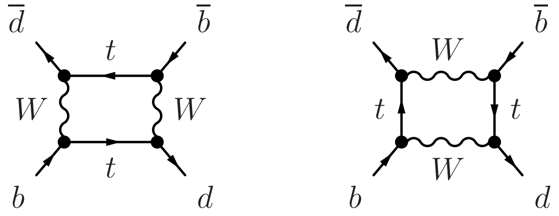

Figure 1.5: The box diagrams of $B^0\overline{B}^0$ mixing, for the $\overline{d}b \to d\overline{b}$.

Since in the B^0-system we have $\Delta\Gamma_B \ll \Delta m_{\mathrm{d}}$, the CP phase from mixing (Eqn. 1.8) is due to the M_{12} term only. This is dominated by the box diagrams of Fig. 1.5 with a top quark in the intermediate state , which have a common factor $(V_{tb}^* V_{td})^2$. The diagrams for $\overline{b}d \to b\overline{d}$ similarly share a factor $(V_{tb}V_{td}^*)^2$; thus, to a very good approximation,

$$\left(\frac{q}{p}\right)_B = \frac{V_{tb}^* V_{td}}{V_{tb} V_{td}^*} e^{2i\xi_B}. \tag{1.28}$$

At present the sensitivity to V_{td} is not limited by the experimental precision on Δm_{d}, but by other incertainties in the calculation of the strong interactions matrix elements.

The CP-violation parameter λ is thus written, putting together Eqs. 1.16, 1.26, 1.27 and 1.28, as

$$\begin{aligned}
\lambda_{B\to c\overline{c}K} &= \frac{q}{p}\frac{\overline{A}_{c\overline{c}K}}{A_{c\overline{c}K}} = \\
&= \left(\frac{V_{tb}^* V_{td}}{V_{tb} V_{td}^*} e^{2i\xi_B}\right)\left(\eta_{CP}\frac{V_{cb} V_{cs}^*}{V_{cb}^* V_{cs}} e^{-2i\xi_B}\right)\left(\frac{V_{cs} V_{cd}^*}{V_{cs}^* V_{cd}} e^{-2i\xi_K}\right) \\
&= \eta_{CP}\left(\frac{V_{tb}^* V_{td}}{V_{tb} V_{td}^*}\right)\left(\frac{V_{cb} V_{cs}^*}{V_{cb}^* V_{cs}}\right)\left(\frac{V_{cs} V_{cd}^*}{V_{cs}^* V_{cd}}\right)
\end{aligned} \tag{1.29}$$

where η_{CP} is the CP eigenvalue for the final state (-1 for $c\overline{c}K_S^0$, $+1$ for $c\overline{c}K_L^0$). The first two terms come from $B^0\overline{B}^0$ and $K^0\overline{K}^0$ mixing, the third term from the amplitude ratio.

By simplifying and substituting the definition of the angle β from Eq. 1.25, one obtains that

$$\lambda_{B\to c\bar{c}K} = \eta_{CP}\, e^{-2i\beta} \tag{1.30}$$

thus $\mathcal{I}m\,\lambda = \pm\sin 2\beta$, the imaginary part of λ only contains information of the CKM angle β. This happens because such $b{\to}c\bar{c}s$ decays have a zero weak phase in the standard (Wolfenstein) representation, which requires non-zero weak phases only for transitions between the first and the third generation. The phase, and then the angle β is introduced in the process by the B^0-$\overline{B}^0$ mixing.

The first to point out $B^0 \to J/\psi\, K^0_S$ as an optimal channel for detecting CP asymmetry were Bigi and Sanda in 1981 [27]. Together with the already mentioned peculiarity of the single dominating weak phase, this decay provides other advantages from the experimental point of view, namely a small but not minimal branching ratio, $\mathcal{B}\,(J/\psi\, K^0) = (8.9 \pm 1.2) \times 10^{-4}$ [3], and a clean signature due to the $J/\psi\ \to \ell^+\ell^-$ decay. The $\psi(2\mathrm{S})K^0_S$ final state has a slightly smaller decay rate, as reported by the latest *BABAR* measurements, $\mathcal{B}\,(\psi(2\mathrm{S})K^0) = (6.8 \pm 1.0 \pm 1.1) \times 10^{-4}$ [84].

It is possible to reproduce the above argument with decays involving an intermediate K^{*0}, provided that the K^{*0} decays to a CP eigenstate such as $K^0_S\pi^0$, rather than a flavor eigenstate such as $K^+\pi^-$. However, since the K^{*0} is a vector particle, this decay chain has the disadvantage of having contributions from different angular momentum states, which must either separated out or averaged over.

1.6 CP Asymmetries in a B-factory

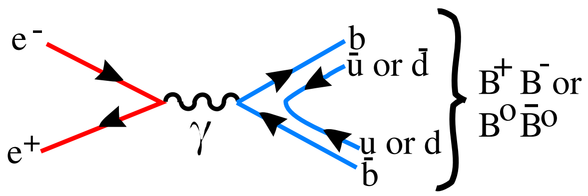

Figure 1.6: B production at the $\Upsilon(4S)$.

Since the mass eigenstates of the $B^0\overline{B}^0$ system have almost identical lifetimes, it is not possible to selectively produce, as in the $K^0\overline{K}^0$, a beam of particles of one type or the other. It is however possible, exploiting an Einstein–Podolski–Rosen-like mechanism, to extract the time-dependent asymmetries from the decays.

To do so, it is necessary to exploit the associate production of a B^0 and a $\overline{B}^0$ in a defined state: this happens at the e^+e^- B-Factories, which are e^+e^- colliders operating at the $\Upsilon(4S)$ resonance, where the two mesons are produced in a coherent $L = 1$ state from the decay of the Υ. They therefore evolve obeying the equations of Section 1.3.1, but they do so *in phase*, i.e. there is only one B^0 and one $\overline{B}^0$ at any given moment. When one of the mesons eventually decays, the other continues to oscillate until it decays, either as a B^0 or a $\overline{B}^0$. There will then be events with two B^0 or two $\overline{B}^0$ whose probability is governed by the time interval between the two decays through Eq. 1.6.

To study these processes, one should search for B decays that identify the flavor of the original B meson. The charges of identified leptons and kaons are the primary indicators of the flavor of the tagging B, but other particles also carry flavor information that can be exploited with a neural network algorithm. Once identified the sign of the tagging B by its decay products, the coherence of the states ensures that the other one begins to oscillate (at the time of the decay of the first one) from the opposite state. Thus, by measuring the proper time of the two decays it is possible to study the mixing time development of the system; for example, if the second B is a CP eigenstate, CP violation in the interference between decays with and without mixing can be looked for. Note that this is true even if the tagging decay occurs *after* the CP one. The coherence of the state is ensured if the center-of-mass energy is below the threshold of the pion hadronization, which otherwise would add a phase shift between the two states. Other experimental requirements for a e^+e^- B Factory are described in the next Chapter 2.

Here we want to stress the basic steps involved in measuring the time-dependent CP asymmetry:

- For each CP eigenvalue (± 1), a sample of B mesons decaying into CP eigenstates B_{CP} must be collected.
- Each meson of these samples must be tagged by its counterpart, B_{tag}.
- The time difference Δt between any two mesons can be measured through the Δz distance between the two vertices and the decay time distribution is fitted to extract physical quantities.

Several additional information come from a dedicated study of the flavor oscillation of the $B^0\overline{B}^0$ system, that can be performed on a wider sample of B meson decays, those into flavor eigenstates $B_{\rm flav}$. The techniques to extract the mixing frequency $\Delta m_{\rm d}$ from the $B_{\rm flav}$ sample and the time-dependent CP asymmetry from the $B_{\rm CP}$ sample, as well as most of the experimental uncertainties on these measurements, are indeed the same.

1.6.1 The Time-Dependent Asymmetry

If we consider two coherent mesons which decay to states f_1 and f_2 at proper times t_1 and t_2, we can write the coherent state as

$$\begin{aligned} S\left(t_1,t_2\right) = \frac{1}{\sqrt{2}} e^{\left(-\frac{\Gamma}{2}+iM\right)(t_1+t_2)} \Bigg[& \cos\frac{\Delta m_{\rm d}}{2}\left(t_1-t_2\right)\left(B_1^0\overline{B}_2^0 - \overline{B}_1^0 B_2^0\right) \\ & - i\sin\frac{\Delta m_{\rm d}}{2}\left(t_1-t_2\right)\left(\frac{p}{q}B_1^0 B_2^0 - \frac{q}{p}\overline{B}_1^0\overline{B}_2^0\right)\Bigg] \sin\theta \end{aligned} \tag{1.31}$$

The two particles are identified by the angle θ and $\pi-\theta$ (with θ running over $0-\pi$) that they make with the e^- beam direction in the center-of-mass frame, in which they are back-to-back. Furthermore we have $t_1 = t_2$ untill one of the two particles decays since the momentum magnitudes are equal in this frame. Eqn. 1.31 can in turn be used to calculate the decay amplitude

$$\begin{aligned} A\left(t_1+t_2,\Delta t\right) = \frac{1}{\sqrt{2}} e^{\left(-\frac{\Gamma}{2}+iM\right)(t_1+t_2)} \Bigg[& \cos\frac{\Delta m_{\rm d}}{2}\Delta t\left(A_1\overline{A}_2 - \overline{A}_1 A_2\right) \\ & - i\sin\frac{\Delta m_{\rm d}}{2}\Delta t\left(\frac{p}{q}A_1 A_2 - \frac{q}{p}\overline{A}_1\overline{A}_2\right)\Bigg] \sin\theta \end{aligned} \tag{1.32}$$

where A_i is the amplitude for a B^0 to decay to the state f_i, $\overline{A}_i$ is the amplitude for a $\overline{B}^0$ to decay to the *same* state f_i and $\Delta t \equiv t_1 - t_2$. The overall sign that depends on the ordering of (t_1, t_2) and that vanishes when calculating the rates, has been dropped.

Any state that identifies the flavor of the parent B, *i.e.* the tagging B, has either $\overline{A}_f$ or $A_f = 0$. Now suppose to choose a tagging mode accessible only to $\overline{B}^0$, *i.e.* $A_2 = 0$ and $\overline{A}_2 = A_{\rm tag}$. If at the time $t_1 = t_{CP}$ the other B decays to a CP eigenstate f_{CP}, having been positively identified as a B^0 at the time $t_2 = t_{\rm tag}$, the calculation for the time-dependent rate for producing the combined final state $(f_{CP},\ f_{\rm tag})$ gives

$$\begin{aligned} \mathfrak{F}_{B^0}\left(t_{CP},t_{\rm tag}\right) = C e^{-\Gamma(t_{CP}+t_{\rm tag})} & \left|\overline{A}_{\rm tag}\right|^2 \left|A_{CP}\right|^2 \big\{1 + \left|\lambda_{CP}\right|^2 \\ & + \cos[\Delta m_{\rm d}\left(t_{CP}-t_{\rm tag}\right)]\left(1-\left|\lambda_{CP}\right|^2\right) \\ & -2\sin[\Delta m_{\rm d}\left(t_{CP}-t_{\rm tag}\right)]\, \mathfrak{Im}\,\lambda_{CP}\big\} \end{aligned} \tag{1.33}$$

having introduced the quantity λ_{CP} of Eq. 1.16. Here an integral over the polar angle has been performed and an overall normalization factor C has appeared. The absence of *CP* violation in the mixing ia also imposed, $|q/p| = 1$, which means that the amplitudes for the two opposite tags are the same. If the *CP*-side B is identified as a $\overline{B}^0$ by the tagging mechanism, Eq. 1.33 for $\mathcal{F}_{\overline{B}^0}(t_{CP}, t_{\rm tag})$ has the signs of the sine and cosine term flipped, remaining otherwise unchanged. Then it's possible to calculate the time-dependent *CP* asymmetry as

$$\begin{aligned} a_{CP} &\equiv \frac{\mathcal{F}_{B^0}(\Delta t) - \mathcal{F}_{\overline{B}^0}(\Delta t)}{\mathcal{F}_{B^0}(\Delta t) + \mathcal{F}_{\overline{B}^0}(\Delta t)} \\ &= \frac{\left(1 - |\lambda_{CP}|^2\right)\cos(\Delta m_{\rm d}\Delta t) - 2\,\Im m\,\lambda_{CP}\sin(\Delta m_{\rm d}\Delta t)}{1 + |\lambda_{CP}|^2} \end{aligned} \tag{1.34}$$

where $\Delta t \equiv t_{CP} - t_{\rm tag}$.

It's important to note that this expression can be integrated over the variable $(t_1 + t_2)$, and the dependence on $(t_1 - t_2)$ can be measured without having to know the $\Upsilon(4S)$ decay time. The fact that the variable $(t_1 - t_2)$ can be related to the distance between the locations of the two decays is of course the prime reason for building an energy-asymmetric collider for the B Factory. Infact if we integrate over this variable as well, all the information on the sine coefficient would be lost, since it's a coherent state, and the experiment would be sensitive only to those *CP*-violating effects that give $|\lambda| \neq 1$.

For the cases where there is only one decay amplitude A, such as the $b{\rightarrow}c\bar{c}s$ decays described in Sec. 1.5.1, then $|\lambda|$ equals 1 and the time-dependent rate of decay of the B_{CP} final state is then given by

$$\mathcal{F}^{CP}_{\pm}(\Delta t; \Gamma, \Delta m_{\rm d}, \sin 2\beta) = \frac{\Gamma}{4} e^{-\Gamma|\Delta t|} \times [1 \mp \eta_{CP} \sin 2\beta \sin \Delta m_{\rm d}\Delta t] \tag{1.35}$$

Thus the asymmetry is:

$$a_{CP} = -\,\Im m\,\lambda_{CP}\sin(\Delta m_{\rm d}\Delta t) = -\eta_{CP}\,\sin 2\beta\,\sin(\Delta m_{\rm d}\Delta t) \tag{1.36}$$

Only the amplitude of this asymmetry, $\Im m\,\lambda_{CP}$, contains information about the level of *CP* violation, while the sine term is determined by the B_d mixing.

1.6.2 Measurement of B^0 oscillations

The phenomenon of particle–antiparticle mixing in the neutral B meson system has been described in Section 1.3.1. The oscillation frequency $\Delta m_{\rm d}$ in the B^0-$\overline{B}^0$ mixing has been extensively studied with both time-integrated and time-dependent techniques [3]. Since the measurement of $\Delta m_{\rm d}$ incorporates all elements of the analysis for time-dependent *CP* asymmetries, including B reconstruction, tagging, Δt determination and resolution, it is a fundamental test of the understanding of these aspects in the measurement of the asymmetries. The measurement of $\Delta m_{\rm d}$ requires one neutral B to be fully reconstructed in a flavor eigenstate as for example $D^{(*)-}\pi^+(\rho^+, a_1^+)$ or $J/\psi\, K^{*0}$ ($K^{*0} \to K^+\pi^-$), while the second is tagged by its decay products. The probability for B^0-$\overline{B}^0$ mixing is a function of $\Delta m_{\rm d}$ and of the time difference between the two B decays Δt, since from Eqn. 1.6 the decay time distribution is:

$$\mathcal{F}_{\pm}^{\rm mix} = \frac{1}{4}\Gamma e^{-\Gamma|\Delta t|}\left[1 \pm \cos \Delta m_{\rm d}\Delta t\right] \tag{1.37}$$

where $(+)$ is for unmixed ($B^0\overline{B}^0$ and $\overline{B}^0 B^0$) and $(-)$ is for mixed ($B^0 B^0$ and $\overline{B}^0\overline{B}^0$) events. Thus the asymmetry is given by the difference between the unmixed and the mixed events:

$$a_{\rm mix}(\Delta t) \equiv \frac{\mathcal{F}_+(\Delta t) - \mathcal{F}_-(\Delta t)}{\mathcal{F}_+(\Delta t) + \mathcal{F}_-(\Delta t)} = \cos \Delta m_{\rm d}\Delta t \tag{1.38}$$

and is a cosine function of Δt with unit amplitude. The clear pattern of the oscillation is shown by the *BABAR* data, displayed in Fig. 1.7.

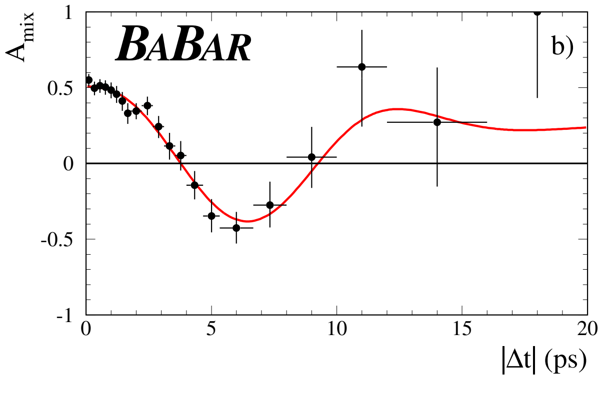

Figure 1.7: Time-dependent asymmetry $a(\Delta t)$ between unmixed and mixed events as a function of $|\Delta t|$.

1.6.3 Dilution Factor and Resolution Function

All previous results are obtained in case of a perfect tagging. However since the tagging algorithm can incorrectly identify the tag, the mistag probability

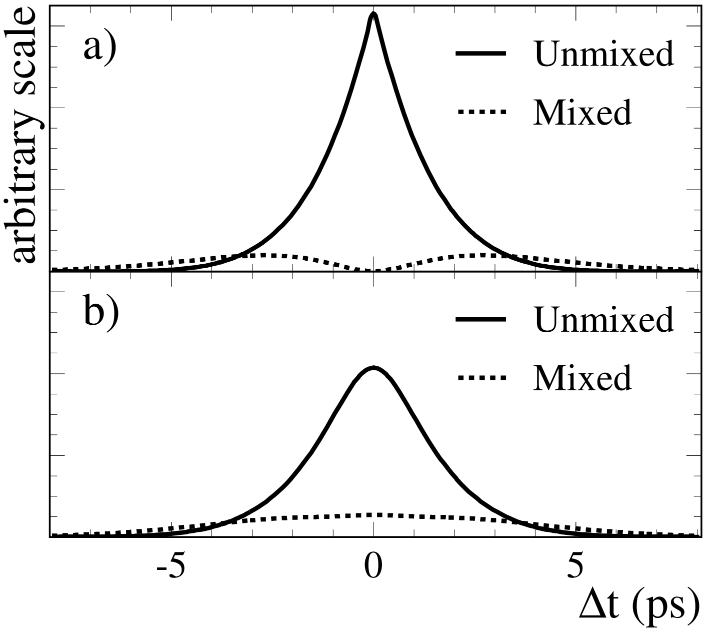

Figure 1.8: Expected Δt distribution for mixed and unmixed events a) with perfect tagging and Δt resolution, and b) with typical mistag rates and Δt resolution.

w is introduced to account for this effect. The amplitude of the oscillation is reduced by a dilution factor $\mathcal{D} = (1 - 2w)$. When more than one type of flavor tag is used, each has its own mistag rate, w_i. Furthermore both the mixing and the CP asymmetries have to include the finite resolution of the detector, thus the decay time distributions must be convoluted with a time resolution function $\mathcal{R}(\delta_{\mathrm{t}} = \Delta t - \Delta t_{\mathrm{true}}; \hat{a})$:

$$\mathcal{H}_{\pm}(\Delta t; \Gamma, \Delta m_{\mathrm{d}}, w, \hat{a}) = \mathcal{F}_{\pm}(\Delta t_{\mathrm{true}}; \Gamma, \Delta m_{\mathrm{d}}, w) \otimes \mathcal{R}(\delta_{\mathrm{t}}; \hat{a}), \tag{1.39}$$

where $\mathcal{F}_{\pm}$ is given either by $\mathcal{F}_{\pm}^{\mathrm{mix}}$ in Eqn. 1.37 or $\mathcal{F}_{\pm}^{CP}$ in Eqn. 1.35. $\hat{a}$ represent the set of parameters that describe the resolution function. Figure 1.9 and 1.8 illustrates the impact of typical mistag and Δt resolution effects on the Δt distributions for B^0- and $\overline{B}^0$-tagged CP events and mixed and unmixed event, respectively.

It's assumed a perfect determination of the flavor of the fully-reconstructed neutral B_{flav}, so that the dilution in the mixed and unmixed amplitudes arises solely from the B_{tag} side, allowing the values of the mistag fractions w_i to be the same on both B_{flav} and B_{CP} samples.

Therefore a simultaneus maximum likelihood study on the decay time distributions $\mathcal{H}_{\pm}^{\mathrm{mix}}$ of B^0-$\overline{B}^0$ mixing and $\mathcal{H}_{\pm}^{CP}$ of CP asymmetries allows the

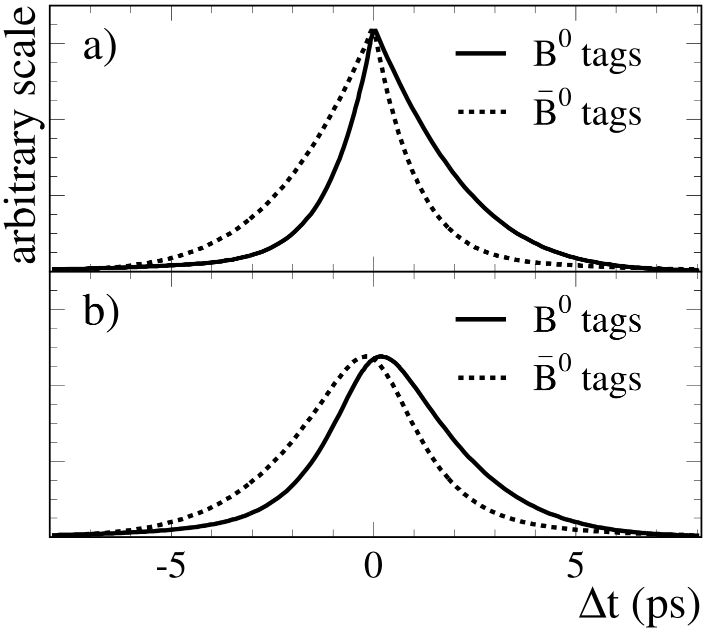

Figure 1.9: Expected Δt distribution for B^0- and $\overline{B}^0$-tagged CP events a) with perfect tagging and Δt resolution, and b) with typical mistag rates and Δt resolution.

determination of both Δm_{d}, the mistag rates w_i, the resolution parameters $\hat{a}$ and the free parameter sin2β. The likelihood functions are constructed summing all the different tag types and the $\mathcal{H}_{\pm}^{\mathrm{mix}}$ for mixed/unmixed events and $\mathcal{H}_{\pm}^{CP}$ for $B^0/\overline{B}^0$ events :

$$\ln \mathcal{L}_{\mathrm{mix}} = \sum_{i}^{\mathrm{tagging}} \left[\sum_{\mathrm{unmixed}} \ln \mathcal{H}_{+}^{\mathrm{mix}}(\Delta t; \Gamma, \Delta m_{\mathrm{d}}, w_i, \hat{a}_i) + \sum_{\mathrm{mixed}} \ln \mathcal{H}_{-}^{\mathrm{mix}}(\Delta t; \Gamma, \Delta m_{\mathrm{d}}, w_i, \hat{a}_i) \right] \tag{1.40}$$

and

$$\begin{aligned} \ln \mathcal{L}_{CP} = \sum_{i}^{\mathrm{tagging}} \Bigg[& \sum_{B^0 \ \mathrm{tag}} \ln \mathcal{H}_{+}^{CP}(\Delta t; \Gamma, \Delta m_{\mathrm{d}}, \hat{a}, w_i, \sin 2\beta) \\ & + \sum_{\overline{B}^0 \ \mathrm{tag}} \ln \mathcal{H}_{-}^{CP}(\Delta t; \Gamma, \Delta m_{\mathrm{d}}, \hat{a}, w_i, \sin 2\beta) \Bigg] \end{aligned} \tag{1.41}$$

The correlation between w_i and Δm_{d} is small, because the rate of mixed events near $\Delta t = 0$, where the B^0-$\overline{B}^0$ mixing probability is small, is principally governed by the mistag rate. Conversely, the sensitivity to Δm_{d} increases at larger values of Δt; when Δt is approximately twice the B lifetime, half of the neutral B mesons will have oscillated.

Chapter 2

The BABAR Experiment

As outlined in the previous section, the main physics program for *BABAR* is to probe *CP* violation in the B system. While *CP* asymmetries are expected to be relatively large, all the processes involved share a low branching ratio (tipically 10^{-4}), so the number of $B^0\overline{B}^0$ pairs needed is quite large; about $10\,\mathrm{fb}^{-1}$ were needed for a first measurement.

The extraction of the asymmetries from these decays requires to fully reconstruct the exclusive final states of an $\Upsilon(4S) \to B\overline{B}$ decay in which one of the Bs decays in a *CP* eigenstate. One of the sides is used to tag the B meson flavour, while the final state of the *CP* side is used to measure the asymmetric process. All of these put some general, but stringent requirements [31] for a B-Factory to provide a good tool to explore *CP* violation, both for the machine and the detector:

Machine requirements

- Use of an e^+e^- collider, to obtain a high enough signal-to-background ratio with reasonably low multiplicity and rates;
- Operation at the $\Upsilon(4S)$ resonance peak, exploiting coherent production of the B mesons to tag one side of the final state, while reducing backgrounds;
- An asymmetric B Factory, i.e. a collider with beams of unequal energy, provides a boost that enables the decay lengths (and hence proper times) of the B mesons to be resolved and measured;
- Last, a very high luminosity machine is required to overcome the low branching ratios to reconstuctable interesting final states.

Detector requirements [29, 30]:

- A detector with the highest possible acceptance, especially in the forward region where the boost pushes a large fraction of the tracks;
- A high performance tracking system, with excellent vertex resolution, particularly in the z-direction, to ease the discrimination of flavour vertices and the resolution of decay lengths;
- A good Particle Identification system, to discriminate between e, μ, π, K and p, and the capability to identify neutral hadrons (namely, K^0_L);
- Wide energy and momentum ranges: $60\,\mathrm{MeV/c} \lesssim p_\mathrm{t} \lesssim 4\,\mathrm{GeV/c}$ for tracking, and $20\,\mathrm{MeV} \lesssim \mathrm{E} \lesssim 5\,\mathrm{GeV}$ for photon and π^0 detection.

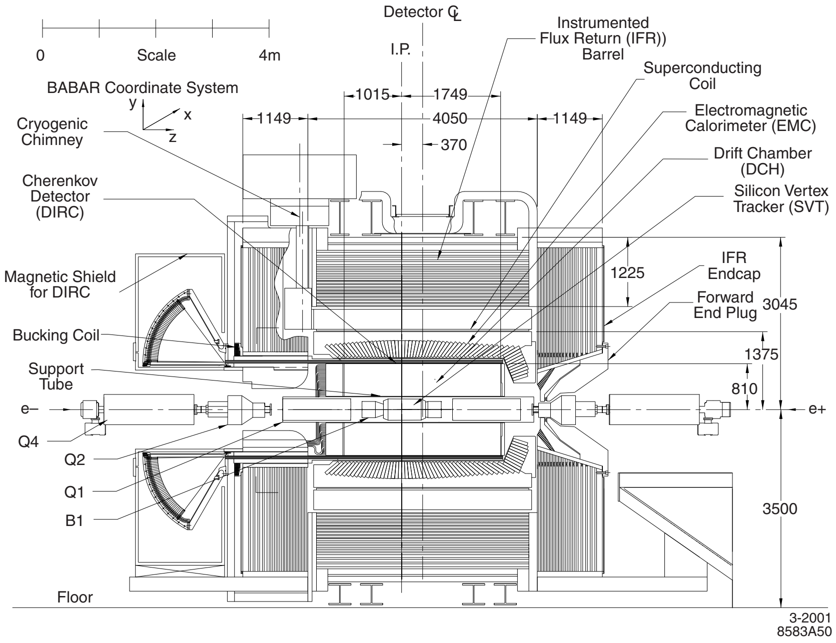

Figure 2.1: *BABAR* Detector longitudinal section.

The PEP-II linear collider at the Stanford Linear Accelerator Center and the *BABAR* detector were designed and built to these specifications, and began taking data on May 26$^{\mathrm{th}}$, 1999. The first physics results were presented at the ICHEP 2000 conference in Osaka, Japan, on July 29, 2000.

2.1 The PEP-II Collider

The PEP-II B Factory is an e^+e^-storage ring system designed to operate at a luminosity of $3 \times 10^{33}\ \mathrm{cm}^{-2}\mathrm{s}^{-1}$ and above, at a center of mass (CMS) energy of $\sqrt{s} = 10.58\,\mathrm{GeV}$, the mass of the $\Upsilon(4S)$ resonance. The first collisions (without the *BABAR* detector) were recorded in July 1998.

Most of the data are recorded at the peak of the $\Upsilon(4S)$ resonance: they are referred to as *on-resonance data*. In Tab.2.1 the main processes active at the $\Upsilon(4S)$ resonance are summarized with their cross sections: the production of light quark pairs (u, d, s) and *charm* quark pairs is usually referred to as *continuum* production. In order to allow for studies of this non-resonant continuum about 12% of data are taken at a CMS energy 40 MeV below the $\Upsilon(4S)$. They are commonly referred to as *off-resonance data*.

Table 2.1: Production cross-sections at $\sqrt{s} = M_{\Upsilon(4S)}$. The *Bhabha* cross-section into e^+e^- is the effective cross-section, expected within the experimental acceptance.

$e^+e^- \to$	Cross-section (nb)
$b\overline{b}$	1.05
$c\overline{c}$	1.30
$s\overline{s}$	0.35
$u\overline{u}$	1.39
$d\overline{d}$	0.35
$\tau^+\tau^-$	0.94
$\mu^+\mu^-$	1.16
e^+e^-	~ 40

The final design brought the use of the existing Linear Accelerator as injector and features two independent storage rings, stacked in the existing PEP (2.2 Km long) tunnel: the HER (High Energy Ring, built reusing the existing PEP magnets) for the production of 9.0 GeV electrons and the LER (Low Energy Ring) for 3.1 GeV positrons . The asymmetric beams system corresponds to a moving center of mass of $\beta\gamma$=0.56, thus providing the needed feature of asymmetric collisions to measure the time dependent *CP* violating asymmetries. This is equivalent to an average separation of $\beta\gamma c\tau$=250 μm between the two B vertices, which is crucial for studying the cleanest and most promising *CP* violating modes.

To achieve the designed high luminosity, the beams are colliding head-on, separated in the horizontal plane by a pair of dipole permanent magnets (B1 in Fig. 2.1), placed within 20 cm of the interaction point (IP). The presence of these magnets caused a peculiar geometry of the vertex tracker, and more important, the reduction of acceptance and the increment of background. High corrent beams are also required: 1A current for the HER and 2A for the LER beam. The interaction region is included in 2.5 cm beryllium beam-pipe, corresponding to a total 0.006 interaction lenght. With the designed luminosity the $B\overline{B}$ pair production frequency of $\mathcal{L}\times\ \sigma(e^+e^-\rightarrow \Upsilon(4S)) \sim 3$ Hz is achieved.

The collider design and the achieved performance characteristics are summarized in Tab. 2.2 at the end of this Chapter, while a more detailed performance report can be found in [33]. PEP-II has surpassed its design goals, both in terms of the instantaneous and the integrated daily luminosity, with significantly fewer bunches than anticipated. More recently PEP-II has reached the record peak luminosity of $4.1 \times 10^{33}\,\mathrm{cm^{-2}s^{-1}}$with a record daily integrated luminosity of 270 $\mathrm{pb^{-1}}$.

2.1.1 Machine Backgrounds

The peculiar geometry of the interaction region, with magnets right inside the *BABAR* detector, while needed to achieve the required high luminosity has the drawback of generating high backgrounds.

In average working conditions, backgrounds amount to about 35% of the Level-1 trigger rate. While the overall L1 rate is well within operational limits, Drift Chamber currents and radiation damage in the Vertex and the Calorimeter limit the acceptable level of backgrounds. The primary causes of backgrounds in PEP-II are, in order of increasing importance:

- Synchrotron radiation generated in the bending magnets and final focusing quadrupoles in the incoming HER and LER beam lines.

- Two-beam backgrounds from three sources: enhanced beam-gas interactions in the HER, due to low-energy interaction point synchrotron radiation impinging onto the incoming HER beam pipe; photons and low-energy $e^{\pm}$ from radiative-Bhabha scattering hitting nearby vacuum components; and tails generated by the beam-beam interaction and/or by the electron-cloud-induced blowup of the low-energy beam.

- The interaction of beam particles with residual gas around the rings (beam-gas), mainly from the HER.

Careful layout of the interaction-region area and a massive synchrotron radiation shielding have proven very effective for reducing backgrounds from the first mechanism, while the last still constitutes the primary source of radiation damage, occasionally limiting operational efficiency.

2.1.2 Monitoring of PEP-II parameters

The beam parameters that are most critical for the *BABAR* performance are the luminosity, the energies of the two beams, and the position, angles and size of the luminous region (*beamspot*). While PEP-II measures radiative Bhabha scattering to provide a fast monitor of the relative luminosity for operations, *BABAR* derives the absolute luminosity offline from other QED processes, primarily e^+e^- and $\mu^+\mu^-$ production. During operation, the mean energies of the two beams are calculated from the total magnetic bending strength and the average deviations of the accelerating frequencies from their central values. While the systematic uncertainty in the PEP-II calculation of the absolute beam energies is estimated to be 5–10 MeV, the relative energy setting for each beam is accurate and stable to about 1 MeV. The r.m.s. energy spreads of the LER and HER beams are 2.3 MeV and 5.5 MeV, respectively.

The direction of the beams relative to *BABAR* (about 20 mrad in the horizontal plane by construction) is measured run-by-run using $e^+e^- \to e^+e^-$ and $e^+e^- \to \mu^+\mu^-$ events.

The size and position of the luminous region are critical parameters for the decay-time-dependent analyses and their values are monitored continuously online and offline. The design values for the size of the luminous region are presented in Tab. 2.2. The vertical size, typically by 6-7 μm, is too small to be measured directly and is inferred from the measured luminosity, the horizontal size and the beam currents.

The transverse position, size and angles of the luminous region relative to the *BABAR* coordinate system are determined by analyzing the distribution of the distance of closest approach to the z-axis of the tracks in well measured two-track events as a function of the azimuth ϕ. The longitudinal parameters are derived from the longitudinal vertex distribution of the two tracks. The uncertainties in the average beam position are of the order of a few μm in the transverse plane and 100 μm along the collision axis. Run-by-run variations in the beam position are comparable to these measurement uncertainties, indicating that the beams are stable over the period of a typical run. These measurements are also checked offline by measuring the primary vertices in multi-hadron events[1]. The measured horizontal and longitudinal beam sizes, corrected for tracking resolution, are consistent with those measured by PEP-II.

First collisions from PEP-II were recorded by the detector on May 26, 1998. In Fig.2.2 the integrated luminosity delivered by PEP-II and recorded by *BABAR* is shown up to the beginning of January 2002. Data recorded during year 2000 are referred as Run 1 data, while Run 2 started at the beginning of 2001. In this analysis Run 2 data recorded and processed up to the end of October 2001 are considered.

2.2 The *BaBar* Detector

Figure 2.1 shows a longitudinal section through the detector center with the principal dimensions. The detector is configured around the PEP-II interaction region, including a 1.5 T superconducting solenoid. To maximize the geometric acceptance for the boosted $\Upsilon(4S)$ decays, the whole detector is offset relative to the IP by 0.37 m in the direction of the lower energy beam. The polar angle coverage extends to 350 mr in the forward direction and 400 mr in the backward direction, defined relative to the high energy beam.

The detector comprises five subdetectors, listed below and described in detail in the following sections:

SVT The Silicon Vertex Tracker, which provides resolution of the B vertexes together with tracking for low-momentum charged particles (Sec. 2.3.1);

DCH The Drift Chamber, the main tracker of the experiment, used also for charged particle momentum measurement and for Level 1 triggering (Sec. 2.3.2);

DRC The DIRC – Detector of Internally Reflected Čerenkov Light, a RICH of novel conception used for particle identification (Sec. 2.4.1);

EMC The Electromagnetic Calorimeter, a CsI crystal detector in two modules (Barrel and Forward Endcap), used also to discriminate between electrons and charged pions (Sec. 2.5);

[1]By vertexing all the reconstructed tracks in the event it is possible to have an estimate of the position of the *primary vertex*, that is of the $\Upsilon(4S)$ decay point. Because of the boost along z inducing a relative displacement of the two B mesons the resolution of this method is rather poor and it is worsened by the presence of long-lived particles in the transverse plane.

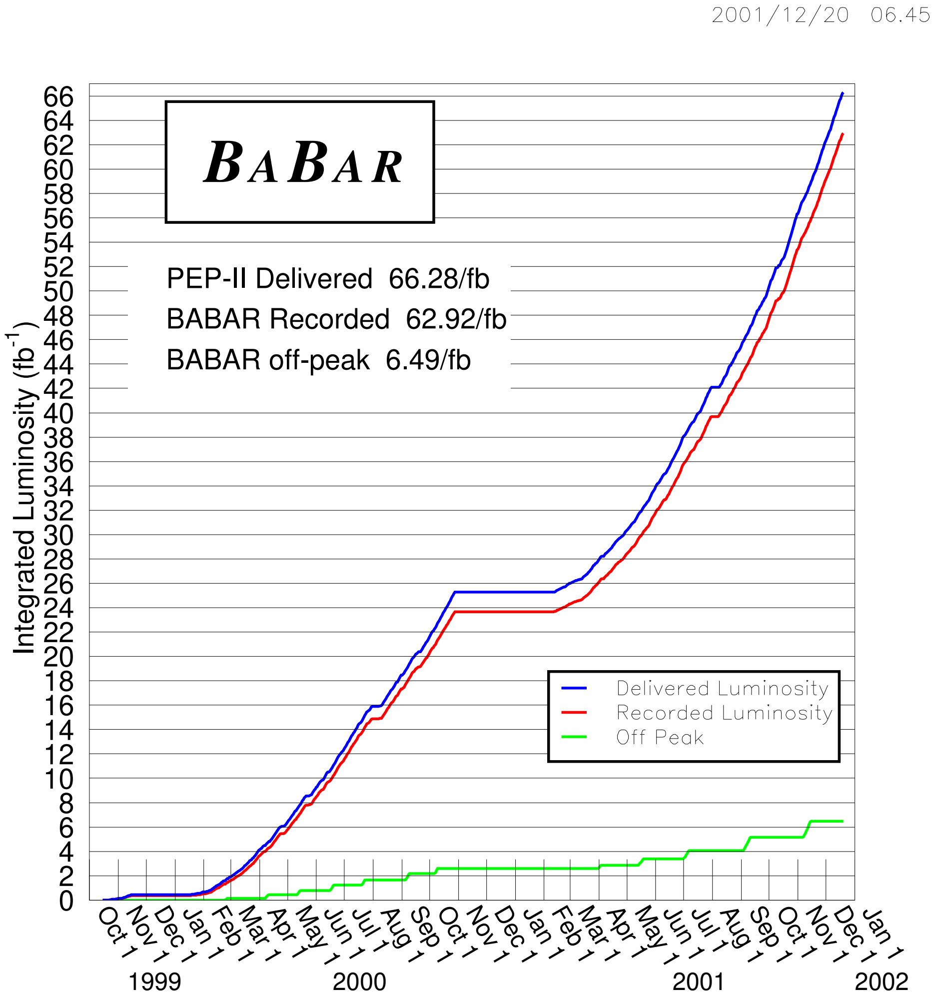

Figure 2.2: PEP-II delivered and recorded luminosity from the beginning of data taking

IFR The Instrumented Flux Return, a Resistive Plate Chambers system used for muon and neutral hadron detection. The muon system is completed by two layers of cylindrical RPCs located between the Calorimeter barrel and the magnet cryostat (Sec. 2.6).

The magnet is located between the calorimeter and the IFR, its physical dimensions are 140 cm of inner radius by 385 cm of length. The physical characteristics of the five subdetectors and their performance are summarized in tab. 2.3, while a complete description can be found in [34].

Strategy: Table 2.3 contains characteristics and performances of all the *BABAR* subdetectors. Among them, the description of the Electromagnetic

Calorimeter will be highlighted in the following, since its performances largely affect the results of the work presented in this thesis.

2.3 The BaBar Tracking System

The charged particle tracking system is made of two components, the vertex tracker (SVT) and the drift chamber (DCH).

2.3.1 The Silicon Vertex Tracker

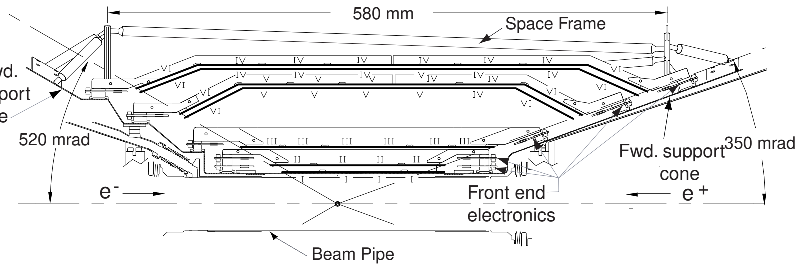

Figure 2.3: Schematic views of SVT: longitudinal section. The roman numerals label the six different types of sensors.

The required high vertex resolution is provided by the Silicon Vertex Tracker (SVT), which in addition helps in the charged particle tracking, in particular providing the stand-alone tracking for low transverse momentum particles ($p_t < 120\,\mathrm{MeV/c}$), which do not enter the drift chamber. As the innermost *BABAR* subdetector, a low mass design to minimize multiple scattering, and radiation hardness of its components were two important considerations. A detailed description of the SVT and its components can be found in [35].

The SVT contains 52 modules built out of double sided silicon strips detectors, organized in five radial layers and with a readout at each end, thus reducing the amount of inactive material in the acceptance volume (see Fig. 2.7 and 2.4. The three inner layers are crucial for vertex and tracking resolution, while the outer two layers are needed to provide additional measurements for stand alone low-momentum tracking. The first layers are mounted as close to

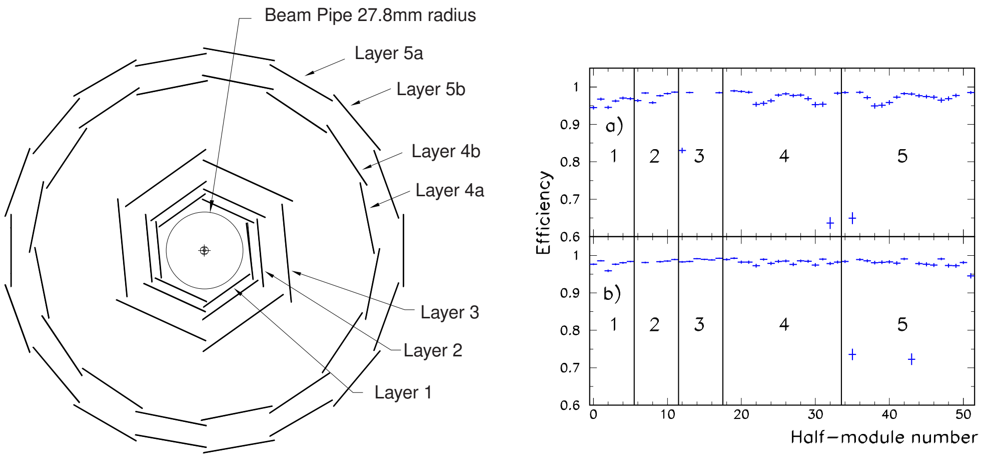

Figure 2.4: Left: Schematic views of SVT: transverse section. Right: SVT hit reconstruction efficiency, as measured on $\mu^+\mu^-$ events for a) forward half-modules and b) backward half-modules. The horizontal axis corresponds to the different modules, with the vertical lines separating the different layers as numbered. Missing values correspond to non-functioning half-modules.

the beryllium beam pipe as practical (at a radius $r = 3.2\,cm$), thus minimizing the impact of multiple scattering in the beam pipe on the extrapolation to the vertex.

A system consisting of 12 PIN photodiode sensors placed close to the first silicon layer is used to continuously monitor the radiation exposure of the SVT and manage its dose budget.

The SVT hit efficiency can be calculated for each half-module by comparing the number of associated hits to the number of tracks crossing the active area of the module. A combined hardware and software efficiencies of 97% is measured on $\mu^+\mu^-$ events (see Fig. 2.4.b). The spatial resolution of SVT hits is determined by measuring the distance (in the plane of the sensor) between the track trajectory and the hit, using high-momentum tracks in two prong events. Two-track vertices, such as $J/\psi \to \mu^+\mu^-$ are reconstructed with a typical resolution of $50\,\mu$m; the resolution on the z separation between the two B decay vertices is typically $110\,\mu$m, in good agreement with the design goals.

2.3.2 The Drift Chamber

Tracking for charged particles with $p_{\rm t} > 100\,$MeV/c is provided by the Drift Chamber, which also exploits the magnetic field to precisely measure trans-

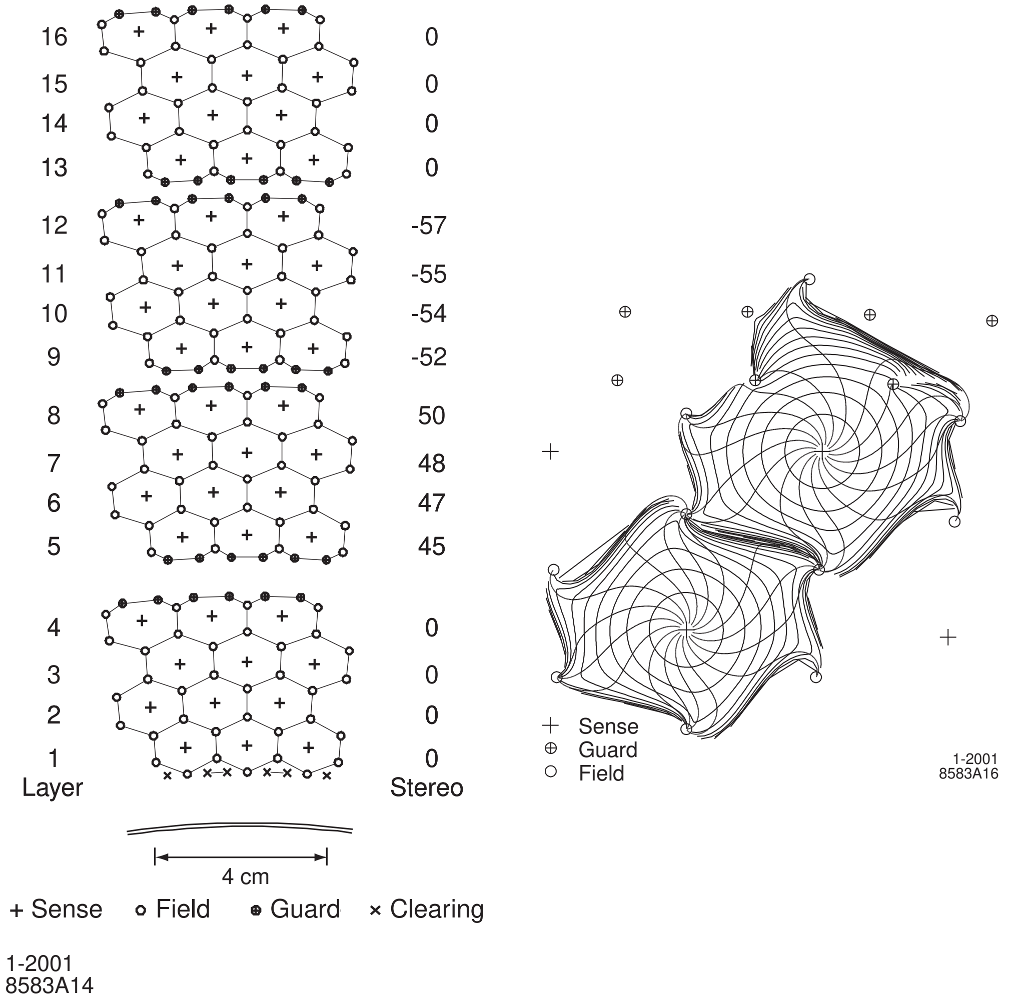

Figure 2.5: Left: Schematic layout of drift cells for the four innermost superlayers. Lines between field wires aid in visualization of the cell boundaries. The numbers on the right side give the stereo angles (mrad) of sense wires in each layer. The 1 mm-thick beryllium inner wall is shown inside of the first layer. Right: Drift cells isocrones, *i.e.* contours of equal drift times of iones, spaced by 100 ns.

verse momenta from the curvature of the trajectories. Prompt single-cell hit information from the chamber is also a basic component of the Level-1 trigger, with a maximum time jitter of 0.5 μs.

The drift system has a compact design made of 7104 hexagonal cells, consisting of one sense wire surrounded by six field wires, as shown in Fig.2.5. While the field wires are at ground potential, a positive high voltage is applied to the sense wires. An avalanche gain of approximately 5×10^4 is obtained at a typical operating voltage of 1960 Volt and with a 80:20 helium:isobutane gas mixture. During part of year 2000 the operating voltage was lowered to 1900 Volt to preserve some damaged sections of the DCH. The main effect was a reduced hit efficiency and, consequently, a reduced tracking efficiency and a worse momentum resolution with some impact on the final data analysis. During year 2001 data-taking the operating voltage was set to 1960 Volt.

Longitudinal information is derived from wires placed at small angles (*stereo layers*) to the principal axis. Wires in the *axial layers* are parallel to the principal axis and both axial and stereo layers provide curvature measurement of tracks. By choosing low-mass wires and supporting structure, and a helium-based gas mixture the multiple scattering inside the DCH is kept to a minimum. Also the readout electronics is mounted on the backward endplate of the chamber, minimizing the amount of material in front of the calorimeter endcap. The cells are arranged in 40 concentric layers, grouped into ten superlayers of four layers each, organized with alternate stereo/axial orientation.

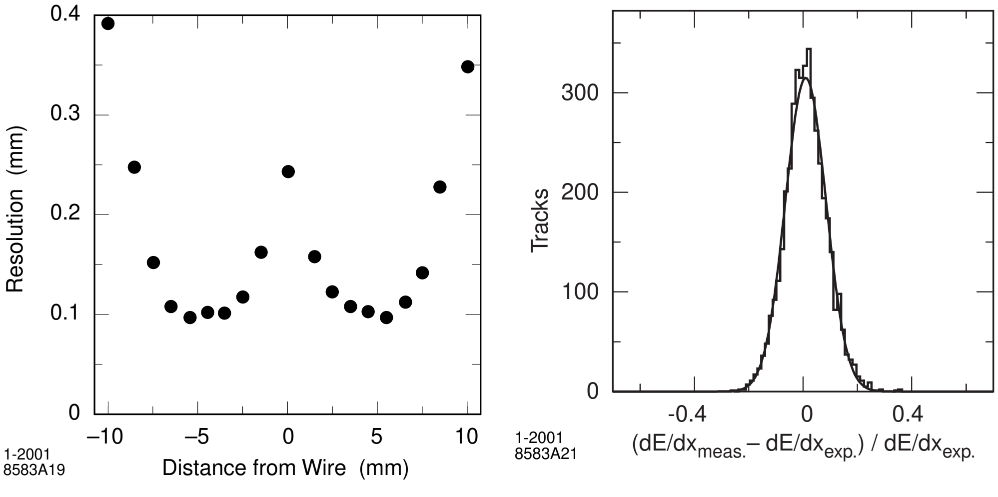

Figure 2.6: DCH Resolution

Left: DCH position resolution as a function of the drift distance in layer 18, for tracks on the left and right side of the sense wire. The data are averaged over all cells in the layer. Right: difference between the measured and expected energy loss $\mathrm{d}E/\mathrm{d}x$ for $e^{\pm}$ from Bhabha scattering, measured in the DCH at an operating voltage of 1900 Volt. The curve represents a Gaussian fit to the data with a resolution of 7.5%.

The nominal design for the chamber calls for an average $140\,\mu$m single point resolution. The single cell resolution function obtained from the ensemble of charged tracks in the normal event stream is shown in Figure 2.6 for operation at 1960 V, achieving a weighted average resolution of 125 μm.

Flash-ADCs are used both to record timing information for hits and to measure the time development of pulse height in the cell; digital signal processing converts this into a measurement of deposited energy. After the application of several corrections (individual gains, tilt angle etc.), the specific energy loss per track is computed as a truncated mean from the lowest 80% of the individual dE/dx measurements. The resulting distribution of the truncated mean dE/dx observed for Bhabha electrons is shown in Fig. 2.6. The observed resolution is found to be 7.5%.

2.3.3 Tracking System Alignements

The global coordinate system is defined by the DCH position: because of seismic activity the SVT moves with respect to the DCH and must be periodically aligned as a whole in the DCH system. Moreover, the SVT is not a perfect rigid body and the relative position of its 340 modules must be determined too. The alignement procedure is performed using tracks from $e^+e^- \to \mu^+\mu^-$ events and cosmic rays, and consists of a *global alignement* between SVT and DCH fitted tracks, and a *local alignement* performed only when needed, typically after magnet quenches or detector access. The SVT *local alignement* can represent a source of systematic bias or distortion in the measure of Δz and therefore it must be accounted for in the *CP* asymmetry analysis.

2.3.4 Charged Particles Reconstruction

Charged tracks are defined by five parameters $(d_0, \phi_0, \omega, z_0, \tan\lambda)$ and their associated error matrix. These parameters are measured at the point of closest approach to the z-axis; d_0 and z_0 are the distances of this point from the origin of the coordinate system in the x-y plane and along the z-axis, respectively. The angle ϕ_0 is the azimuth of the track, λ its dip angle relative to the transverse plane, and $\omega = 1/p_t$ is its curvature. d_0 and ω are signed variables; their sign depends on the charge of the track. The absolute event timing information (the event start time t_0) is determined iteratively by the track finding algorithms along with the five helix parameters.

Track reconstruction uses information from the SVT, the DCH and the L3 trigger. It starts with `pattern recognition` in the DCH, based on three different algorithms. In the first pass, L3 trigger performs fast track `pattern`

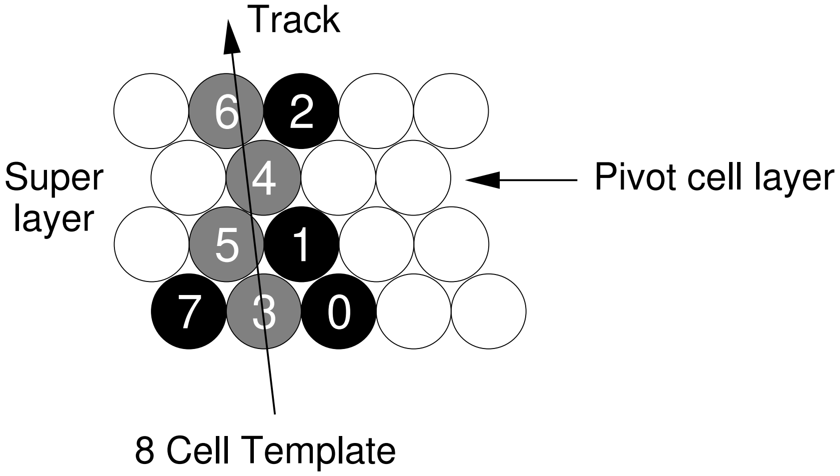

Figure 2.7: Track Segment Finder in L1, responsible of producing track segments in overlapping groups of continuous set of eigth cells in the four layers of a superlayer.

`recongnition` using `track segments`, which are structures of four contiguous `hits` identified in each DCH superlayers in L1. In the next two reconstruction procedures, tracks are selected by performing helix fits to the hits used by the L3 track finding algorithm; search for additional hits in the DCH that may belong on these tracks is performed, while t_0 is further improved by using only hits associated with tracks. Two more sophisticated tracking procedures are then applied, which are designed to find tracks that either do not pass through the entire DCH or do not originate from the IP. These algorithms primarily use track segments that have not already been assigned to other tracks, and thus benefit from the cleaner tracking information and the constantly improving t_0. At the end of this process, tracks are refit using a `Kalman filter` method [37] that takes into account the detailed distribution of material in the detector and the full map of the magnetic field. The resulting tracks are then extrapolated into the SVT and SVT track segments are added and selected performing Kalman fit to the full set of DCH and SVT hits.

Data analysis usually discards badly-fitted tracks, tracks not coming from the interaction point or pointing out of a fiducial volume. Different level of track *quality* can be set, for instance `good` tracks with `veryLoose`, `Loose` or `Tight` requirements. In this analysis tracks are used such that

N(DCH hits) $\geq$ 12 : **N(DCH hits)** is the number of DCH hits associated to the track fit: 12 hits is the minimum number of hits required to have a good track fit, since this is equivalent to having 4 hits per superlayer in 3 different superlayers,

$z_0 < 10$ cm and $d_0 < 1.5$ cm : d_0 and z_0 are the transverse and longitudinal distances of closest approach to the geometrical origin of *BABAR* and are used to reject tracks not pointing to IP;

$p_t > 100$ MeV/c : additional SVT hits originated from machine background generate fake tracks. In the DCH they have low transverse momentum, so a cut on p_t is used to suppress them;

$0.410 < \theta < 2.54$ rad : defines the fiducial volume where a reliable tracking efficiency is estimated.

These criteria are referred as `GoodTracksAccLoose` criteria. Whenever appropriate, tracks are required to pass this because the tracking efficiency is measured with the best precision. There are two classes of tracks for which the GoodTracksLoose selection is not applicable: those not originating near the beamspot, and those with momenta too low to penetrate far enough into the DCH. Pions from K_S^0 candidates fall into the first category, while the pions from $\psi(2S) \rightarrow J/\psi \pi^+\pi^-$ are an example of the second.

2.3.5 Tracking Efficiency and Resolution

The absolute DCH **tracking efficiency** [38] is determined as the ratio of the number of reconstructed DCH tracks to the number of tracks detected in the SVT, with the requirement that they fall within the acceptance of the DCH. Such studies have been performed using different samples of multi-hadron events. Fig. 2.8 shows the result of one of these studies for the two voltage settings in Run 1. At the design voltage of 1960 V, the per-track efficiency averages $(98 \pm 1)\%$ for $p_t > 200$ MeV/c and polar angles $\theta > 500$ mr. The data recorded at 1900 V show a reduction in efficiency by about 5% for tracks close to normal incidence, indicating that the cells are not fully efficient at this voltage.

The **resolution in the five track parameters** is monitored using e^+e^- and $\mu^+\mu^-$ events. It is further investigated offline for tracks in multi-hadron events and cosmic ray muons.

Cosmic rays that are recorded during normal data-taking offer a simple way of studying the track parameter resolution. The upper and lower halves of the cosmic ray tracks traversing the DCH and the SVT are fit as two separate tracks, and the resolution is derived from the difference of the measured

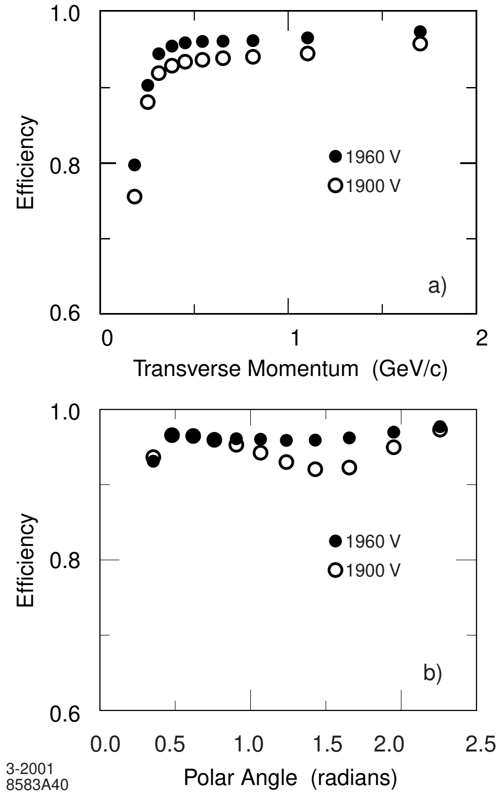

Figure 2.8: Tracking Efficiency

The track reconstruction efficiency in the DCH at operating voltages of 1900 V and 1960 V, as a function of a) transverse momentum, and b) polar angle. The efficiency is measured in multi-hadron events as the fraction of all tracks detected in the SVT for which the DCH portion is also reconstructed.

parameters for the two track halves. To assure that the tracks pass close to the IP, cuts are applied on the d_0, z_0 and $\tan\lambda$. The results of this comparison for the coordinates of the point of closest approach and the angles are shown in Fig. 2.9 for tracks with momenta above p_t of 3 GeV/c. As can be noticed the distributions are symmetric, with small non-Gaussian tails. The clear offset in the distributions for the differences in z_0 and $\tan\lambda$ are attributed to residual problems with the internal alignment of the SVT. Based on the full width at half maximum of these distributions the resolutions for single tracks can be stated as

$$\sigma_{d_0} = 23\mu m \qquad \sigma_{\phi_0} = 0.43\,\mathrm{mr}$$
$$\sigma_{z_0} = 29\mu m \qquad \sigma_{\tan\lambda} = 0.53\cdot 10^{-3}$$

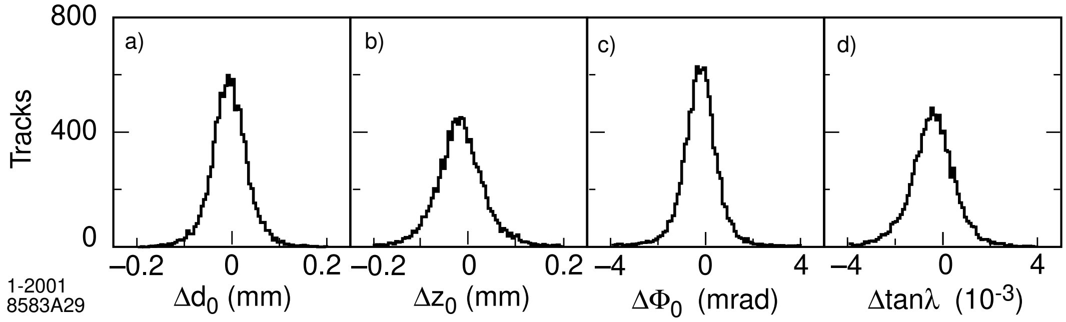

Figure 2.9: Measurements of the differences between the fitted track parameters of the two halves of cosmic ray muons, with transverse momenta above 3 GeV/c, a) Δd_0, b) Δz_0, c) $\Delta\phi_0$, and d) $\Delta\tan\lambda$.

The dependence of the resolution in d_0 and z_0 on the transverse momentum p_t is presented in Fig. 2.10 as obtained from tracks in multi-hadron events. The resolution is determined from the width of the distribution of the difference between the measured parameters, d_0 and z_0, and the coordinates of the vertex reconstructed from the remaining tracks in the event. These distributions peak at zero, but have a tail for positive values due to the effect of particle decays. Consequently, only the negative part of the distributions reflects the measurement error and is used to extract the resolution. Event shape cuts and a cut on the χ^2 of the vertex fit are applied to reduce the effect of weak decays on this measurement. The contribution from the vertex errors are subtracted in quadrature from the measured resolutions. The d_0 and z_0 resolutions so measured are about $25\,\mu$m and $40\,\mu$m respectively at $p_t = 3$ GeV/c. These values agree well with expectations, and are also in reasonable agreement with the results obtained from cosmic rays.

Fig. 2.10 also shows the estimated error in the measurement of the difference along the z-axis between the vertices of the two neutral B mesons. One of the B's is fully reconstructed, the other serves as a flavor tag (see Chapter 6). The r.m.s. of $190\,\mu$m is dominated by the reconstruction of the tagging B, the r.m.s. resolution for the fully reconstructed B meson is $70\,\mu$m.

While the position and angle measurements near the IP are dominated by the SVT, the DCH contributes primarily to the p_t measurement. The resolution in the transverse momentum derived from cosmic ray muons traversing both the DCH and the SVT is well represented by a linear function,

$$\sigma_{p_t}/p_t = (0.13 \pm 0.01)\% \cdot p_t + (0.45 \pm 0.03)\%, \tag{2.1}$$

where the transverse momentum p_t is measured in GeV/c. These values for

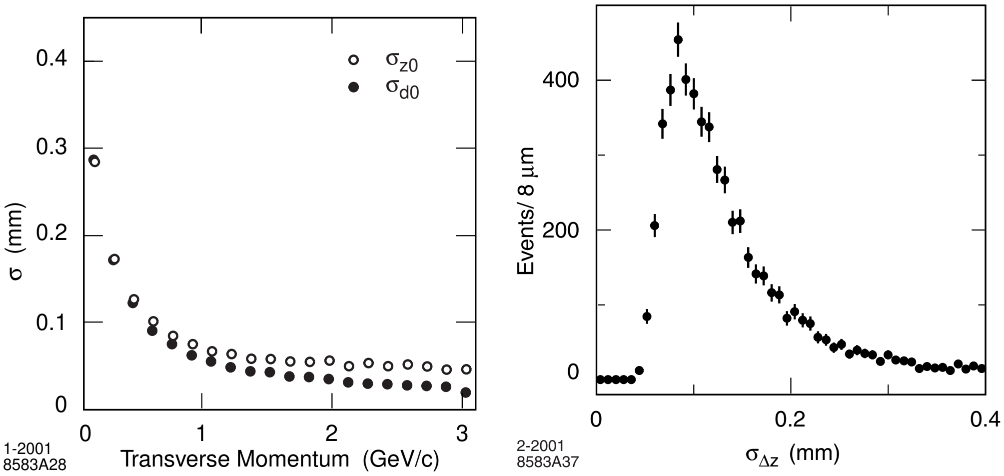

Figure 2.10: Left: Resolution in the parameters d_0 and z_0 for tracks in multi-hadron events as a function of the transverse momentum. The data are corrected for the effects of particle decays and vertexing errors. Right: Estimated error in the difference Δz between the B meson vertices for a sample of events in which one B^0 is fully reconstructed

the resolution parameters are very close to the initial estimates and can be well reproduced by Monte Carlo simulations.

2.4 Particle identification

The study of *CP*-violation using hadronic final states of the $B\overline{B}$ meson system requires the ability to identify the b-quark charge of one of the B mesons via the cascade decay $b \to c \to s$, while fully reconstructing the final state of the other over a large region of solid angle and momentum. The momenta of the kaons used for flavor tagging extend up to about 2 GeV/c, with most of them below 1 GeV/c, since they come from the secondary decays of *charm* mesons. *Particle Identification* (PID) below 700 MeV/c exploits primarily the dE/dx measurements in the DCH and SVT. In Fig.2.11 dE/dx in the DCH as a function of track momenta is shown for different control samples of particles. DCH dE/dx has a typical resolution of 7.5%, while in the SVT resolution is about 14%.

On the other hand, pions from the rare two-body decays $B^0 \to \pi^+\pi^-$and $B^0 \to K^+\pi^-$ must be well-separated from kaons. They have momenta between 1.7 and 4.2 GeV/c, a region where the mean DCH dE/dx for kaons and pions differ by only about 1σ. Moreover, given the momentum and therefore mass resolution at high momenta, from kinematics alone, one is not able to

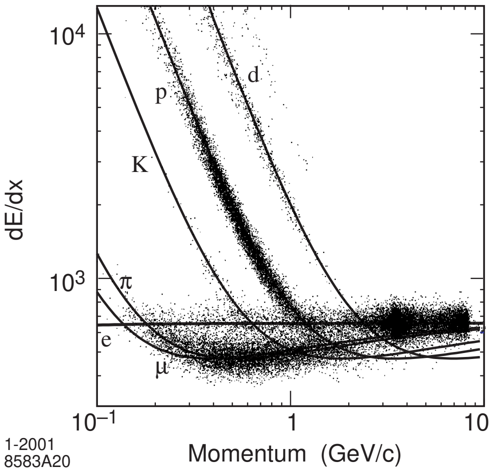

Figure 2.11: dE/dx in the DCH as a function of track momenta.
The data include large samples of beam background triggers, as evident from the high rate of protons. The curves show the Bethe-Bloch predictions derived from selected control samples of particles of different masses. It's clear that dE/dx in the DCH is able to separate pion from kaon at relatively low momenta.

adequately distinguish the two decays. *BABAR* has therefore a dedicated PID subdetector.

2.4.1 The DIRC

A novel type of Ring Imaging Čerenkov detector, based on the Detection of Internally Reflected Čerenkov light ("DIRC") was designed to be able to provide π/K separation of $\sim 4\sigma$ or greater, for all tracks from B-meson decays, with momentum ranging from the pion Čerenkov threshold up to 4.2 GeV/c.

The DIRC is placed before the calorimeter and therefore it should be thin and uniform in terms of radiation lengths and small in the radial dimension to reduce the volume, and hence, the cost of the calorimeter. Finally, for operation at high luminosity, it needs fast signal response, and should be able to tolerate high backgrounds. Fig. 2.12 shows a schematic of the DIRC geometry that illustrates the principles of light production, transport and imaging. The radiator material of the DIRC is synthetic, fused silica in the form of long, thin bars with rectangular cross section. These bars serve both as radiators and as light pipes for the portion of the light trapped in the radiator by total internal reflection.

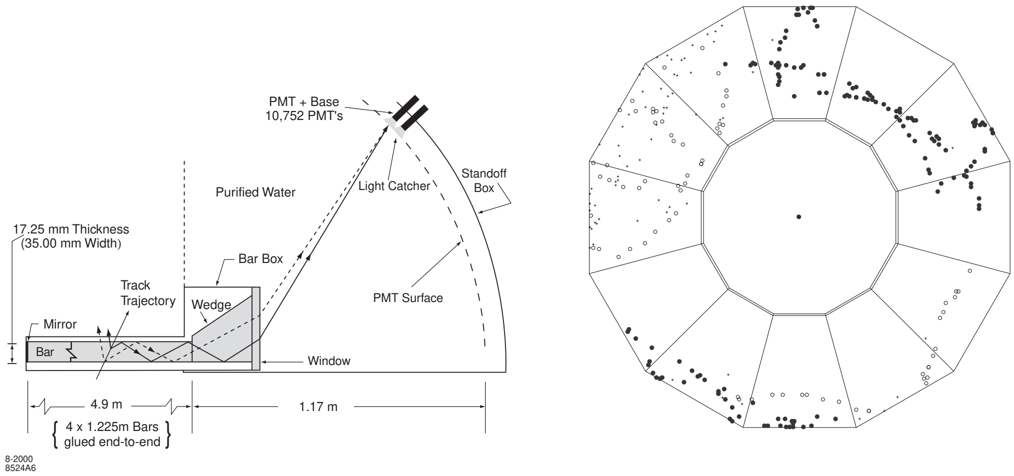

Figure 2.12: The DIRC principle

Left: Schematics of the DIRC fused silica radiator bar and imaging region. Not shown is a 6 mr angle on the bottom surface of the wedge. Right: PMT hits from a typical event projected onto the X-Y plane.

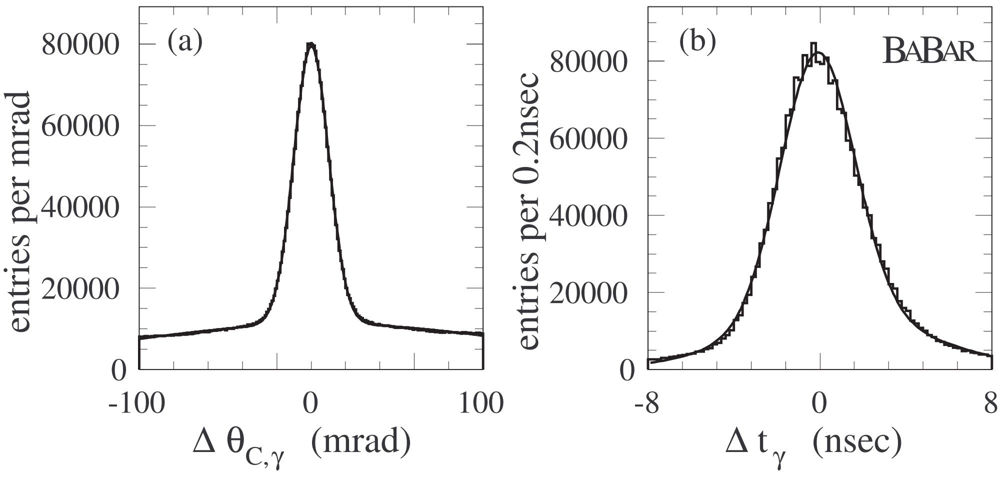

Figure 2.13: DIRC Performance

(a) The resolution of the reconstructed Čerenkov angle for single photons $\Delta\theta_{C,\gamma}$ and (b) the difference between measured and expected arrival time, for single muons in $\mu^+\mu^-$ events.

Charged particles exiting the barrel region of the Drift Chamber cross an array of 144 quartz bars: particles above Čerenkov threshold radiate photons that are internally reflected in the bars and guided to an array of 10752 photomultiplier tubes (PMT), arranged on the surface of a half torus outside the return yoke of *BABAR*. A water tank optically couples the quartz bars to the photomultiplier array. By knowing the particle direction from the tracking system, and the location of the photomultiplier tube that observes a Čerenkov photon, the photon angle with respect to the track direction (Čerenkov angle) can be deduced.

The angular resolution for a single photon is about 10.2 mr (see Figure 2.13(a)) and, with an average of 30 photons per track, the "per track" Čerenkov RMS resolution is about 2.8 mr. This corresponds to an approximate separation of three standard deviations between charged K's and π's at 3 GeV/c.

The DIRC is intrinsically a three-dimensional imaging device. This occurs by recording the time of the PMT signal (measured to a precision of 1.7 ns see Figure 2.13(b)), that is related to the photon propagation angle with respect to the bar axis. As the track position and angles are known from the tracking system, two angles can be determined. This over-constraint on the angles is particularly useful in dealing with ambiguities and high background rates.

2.5 The Electromagnetic Calorimeter

The electromagnetic calorimeter (EMC) is designed to measure electromagnetic showers with excellent efficiency, and energy and angular resolution, over the energy range from 20 MeV to 9 GeV. This capability allows the detection of photons from π^0 and η decays as well as from electromagnetic and radiative processes. By identifying electrons, the EMC contributes to the flavor tagging of neutral B mesons via semi-leptonic decays, to the reconstruction of vector mesons like J/ψ, and to the study of semi-leptonic and rare decays of B and D mesons, and τ leptons.

The upper bound of the energy range is set by the need to measure QED processes, like $e^+e^- \to e^+e^-(\gamma)$ and $e^+e^- \to \gamma\gamma$, for calibration and luminosity determination. The lower bound is set by the need for highly efficient reconstruction of B-meson decays containing multiple π^0s and η^0s. On average, generic B decays contain 5.5 photons with about half of the photon energies below 200 MeV. This causes the π^0 and B reconstruction efficiency to fall off very quickly as the minimum detectable photon energy increases. Because of this sensitivity, it is extremely important to keep the amount of material in front of the EMC to the lowest possible level. In addition many of the B decays used to study CP violation contain at least one π^0 and have characteristically small branching fractions. Thus, high efficiency for low energy photons is required.

The most stringent requirements on energy resolution, namely of order 1–2%, are dictated by measurement of extremely rare decays of B mesons containing π^0s (*e.g.* $B^0 \to \pi^0\pi^0$). Below energies of 2 GeV, the π^0 mass resolution is dominated by the energy resolution. At higher energies, the angular resolution becomes dominant, and therefore it is required to be of the order of a few mrad.

The calorimeter is also used for the separation of hadrons from electrons and, in conjunction with the IFR, for the reconstruction of neutral hadrons and the muon identification.

2.5.1 Overall Layout

The Electromagnetic Calorimeter is composed of a finely segmented array of 6580 CsI crystals doped with thallium at about 1000 ppm. Each crystal is a truncated trapezoidal pyramid and ranges from 16 to 17.5 radiation lengths in thickness. The crystals are arranged quasi-projectively in a barrel structure of 48 polar (θ) rows by 120 crystals in azimuth (ϕ), with an inner radius of 90 cm. The forward end is closed by a separable endcap capable of holding nine additional rows[2].

The EMC has full coverage in azimuth and extends in polar angle from 15.8° to 141.8° corresponding to a solid-angle coverage of 90% in the c.m. system (see Figure 2.14).

Though in CsI the intrinsic efficiency for the detection of photons is close to 100% down to a few MeV, the minimum measurable energy in colliding beam data is expected to be about 20 MeV, a limit that is largely determined by beam- and event-related background and the amount of material in front of the calorimeter.

Crystals are read out with two independent 2 cm^2 large area PIN photodiodes glued to their rear faces. The analog signals are preamplified by chips mounted directly on the blocks, and then carried to an ADC board at the exterior of the detector. A short shaping time of 400 ns is used in the preamplifiers to reduce the probability of overlap with low energy photons (<5 MeV) from beam background.

Upon receipt of the L1 *Accept* signal, which starts the event readout, data sampled within a time window of $\pm 1\,\mu$s are selected for the feature ex-

[2]At present, eight are filled with crystals and the innermost with shielding absorber

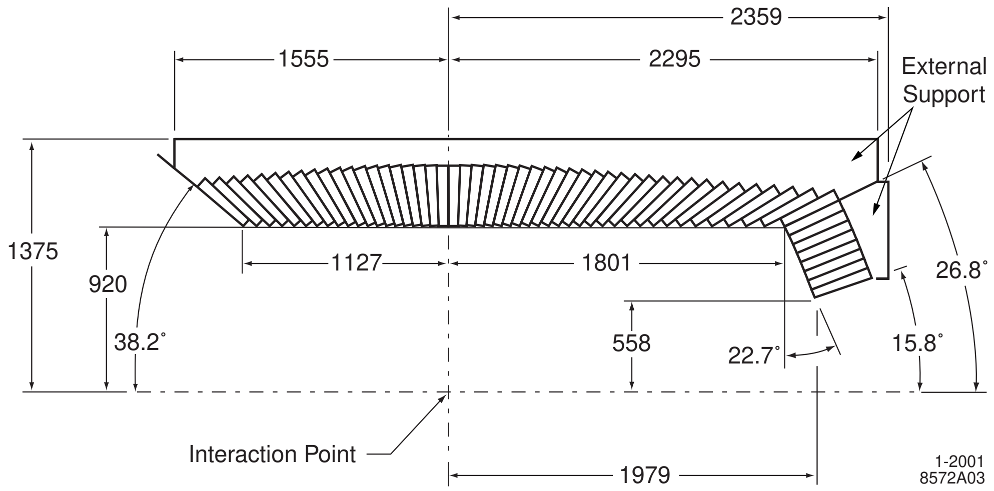

Figure 2.14: The EMC

The Electromagnetic Calorimeter: cross-sectional view. The detector is axially symmetric around the z-axis. All dimensions are given in mm.

traction. Up to now, the calorimeter feature extraction algorithm performs a parabolic fit to the peak of the signal waveform to derive its energy and time. In the future, it is planned to employ a digital filter prior to the signal fit to further reduce noise. The electronic noise accounts for about 10%, while the remaining signals originate from beam-generated background. A typical hadronic event contributes signals in 150 crystals.

Electronic Calibration: To measure pedestal offsets, determine the overall gain, and remove non-linearities, the Front End Electronics are calibrated by precision charge injection into the preamplifier input.

Energy Calibration: It proceeds in two steps.

First, the measured pulse height in each crystal has to be translated to the actual energy deposited. Individual cristals light yield is generally non-uniform and varies significantly with time under the impact of beam-generated radiation. The light yield must therefore be calibrated at different energies, corresponding to different average shower penetration. Two energies at opposite ends of the dynamic range are logarithmic interpolated: a 6.13 MeV radioactive photon source (a neutron activated fluorocarbon fluid) provides an absolute calibration at low energy, while at higher energies (3–9 GeV) the relation between polar angle and energy of $e^{\pm}$ from Bhabha events is exploited.

Second, the energy deposited in a shower spreading over several adjacent crystals has to be related to the energy of the incident photon or electron by correcting for energy loss, mostly due to leakage at the front and the rear, and absorption in the material between and in front of the crystals, as well as shower energy not associated with the cluster. The correction is performed as a function of cluster energy and polar angle. At low energy ($\mathrm{E} < 0.8\,\mathrm{GeV}$), it is derived from π^0 decays: the algorithm constrains the two-photon mass to the nominal π^0 mass and iteratively finds the coefficients of the correction function, tipically of order $6 \pm 1\%$. At higher energy ($0.8\,\mathrm{GeV} < \mathrm{E} < 9\,\mathrm{GeV}$) the correction is estimated from single-photon Monte Carlo simulations. A second technique using radiative Bhabha events is being developed.

2.5.2 Clusters Reconstruction Algorithms

A typical electromagnetic shower spreads over many adjacent crystals, forming a *cluster* of energy deposits. Pattern recognition algorithms have been developed to efficiently identify these clusters and to differentiate single clusters with one energy maximum from merged clusters with more than one local energy maximum, referred to as a *bump*.

Clusters are required to contain at least one seed crystal with an energy above 10 MeV. Surrounding crystals are considered as part of the cluster if their energy exceeds a threshold of 1 MeV, or if they are contiguous neighbors (including corners) of a crystal with at least 3 MeV. Clusters are divided into as many bumps as there are local maxima. An iterative algorithm is used to determine the energy of the bump, giving a weight to each crystal depending on its distance from the centroid of the bump, until the centroid position is stable to within a tolerance of 1 mm. The position of a bump is calculated using a center-of-gravity method with logarithmic, rather than linear weights, emphasizing lower-energy crystals.

Furthermore, the algorithms have to determine whether a bump is generated by a charged or a neutral particle. A bump is associated with a charged particle by projecting a track to the inner face of the calorimeter, assuring the consistency of the distance between the track impact point and the bump centroid with the momentum and the angle of the track. Otherwise, it is assumed to originate from a neutral particle.

On average, 15.8 clusters are detected per hadronic event, of which 10.2 are not associated with charged particle tracks. At current operating conditions, beam-induced background contributes on average 1.4 neutral clusters with energies above 20 MeV. This number is significantly smaller than the average number of crystals with energies above 10 MeV.

2.5.3 Energy and Angular Resolutions

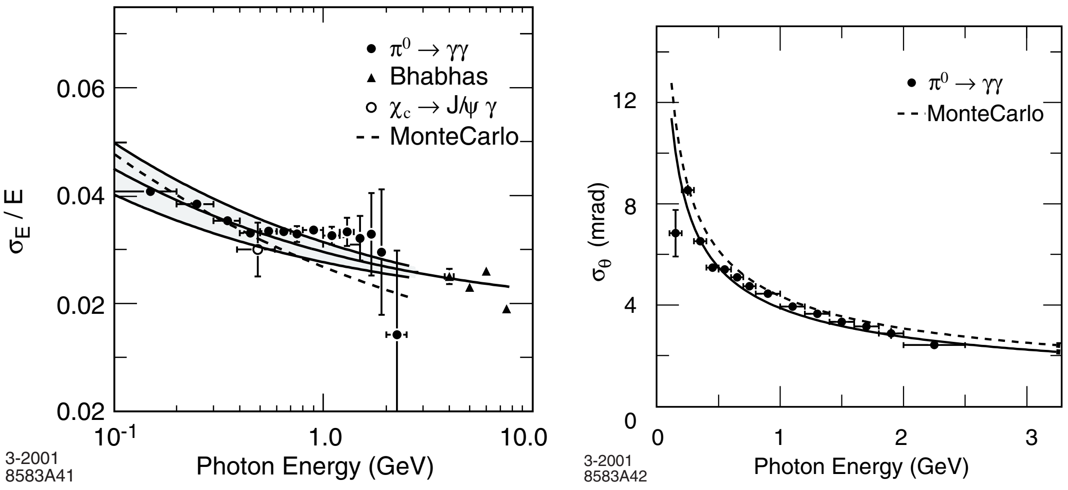

Figure 2.15: EMC Resolution

Left: The Energy Resolution measured for electrons and and photons as function of energy. Right: The angular resolution for photons from π^0 decays.

At low energy, the energy resolution of the EMC is measured directly with the radioactive source while at higher energies the energy resolution is extracted from a variety of processes. Below 2 GeV, the mass resolution of π^0 and η mesons decaying into two photons of approximately equal energy is used. The decay $\chi_{c1} \rightarrow J/\psi\,\gamma$ provides a measurement at an average energy of about 500 MeV, and measurements at high energy are derived from Bhabha scattering. A fit to the energy dependence results in

$$\frac{\sigma_E}{E} = \frac{(2.32 \pm 0.30)\%}{\sqrt[4]{E(\,\mathrm{GeV})}} \oplus (1.85 \pm 0.12)\%. \tag{2.2}$$

where the constant term arises from non-uniformity in light collection, from leakage or absorption in the material between and in front of the crystals, and from uncertainties in the calibrations. Its large amount is believed to result from a yet uncorrected coherent effect from cross talk in the Front End Electronics. The result of the fit is shown in Fig. 2.15. The values of the fit parameters are higher than the somewhat optimistic earlier estimates, but

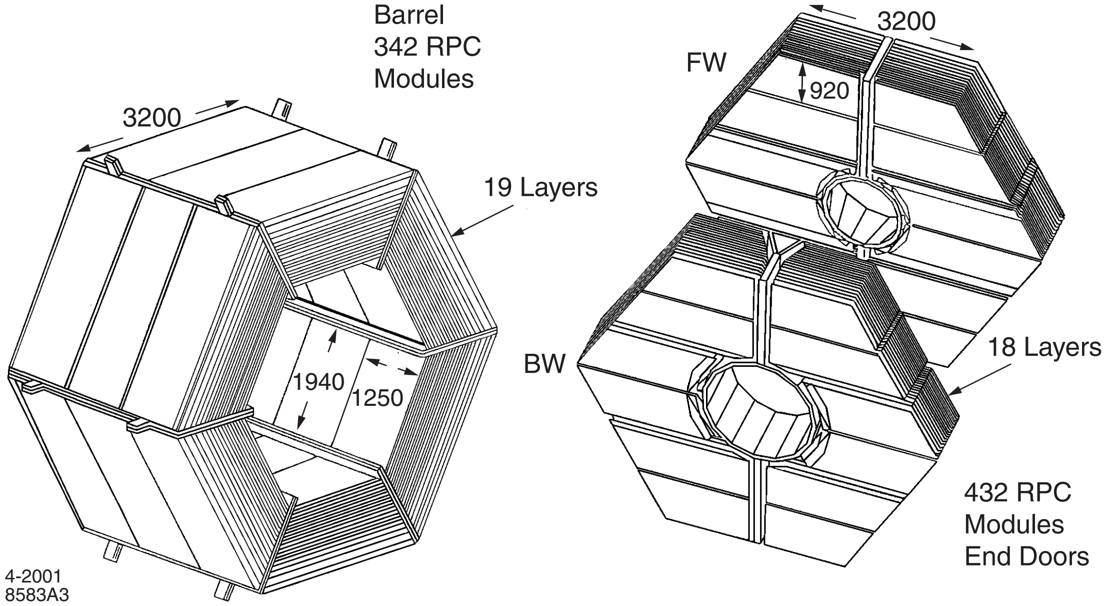

Figure 2.16: Overview of the IFR: Barrel sectors and forward (FW) and backward (BW) end doors; the shape of the RPC modules and their dimensions are indicated.

they agree with detailed Monte Carlo simulations which include the contributions from electronic noise and beam background, as well as the impact of the material and the energy thresholds.

The measurement of the angular resolution is based on the analysis of π^0 and η decays to two photons of approximately equal energy. The result is presented in Figure 2.15. The resolution varies between about 12 mr at low energies and 3 mr at high energies. A fit to the empirical parameterization of the energy dependence results in

$$\sigma_\theta = \sigma_\phi = \left(\frac{3.87 \pm 0.07}{\sqrt{E(\,\mathrm{GeV})}} \; + \; 0.00 \pm 0.04 \right) \; \mathrm{mr} \tag{2.3}$$

These fit values are slightly better than one would expect from detailed Monte Carlo simulations.

2.6 Detector for Muons and Neutral Hadrons

The detection of muons and neutral hadrons in *BABAR* is performed by the Instrumented Flux Return detector (IFR). For this purpose, the magnet flux return steel in the barrel and the two end doors are segmented into layers, increasing in thickness from 2 cm on the inside to 10 cm at the outside. Between these steel absorbers, single gap resistive plate chambers (RPCs) are inserted, which detect streamers from ionizing particles via external capacitive readout strips.

The IFR detectors cover a total active area of about 2000 m^2, with a total of 806 RPC modules. There are 19 layers of RPCs in the barrel sectors and 18 layers in the end doors, as illustrated in Figure 2.16. In addition, two layers of cylindrical RPCs are installed between the EMC and the magnet cryostat to detect particles exiting the EMC. The total thickness of steel at normal incidence is 65 cm in the barrel region, 60 cm in the endcaps.

The planar RPCs consist of two bakelite sheets, 2-mm thick and separated by a gap of 2mm. The bakelite has a bulk resistivity of $\approx 10^{11} - 10^{12}\,\Omega\cdot m$ and is painted on the outside with graphite with a high surface resistivity. These two graphite surfaces are connected to high voltage, a $\approx 8KV$. The interior sides of the bakelite facing the gap are painted with linseed oil, which spatially limits the sparks. The gas used is a non-flammable mixture containing approximately 56.7% Argon, 38.8% Freon 134a and 4.5% isobutane. A cross section of the active detector, with the schematics of the HV connection is shown in fig. 2.17. The RPCs modules operate in limited streamer mode and the signals are read out on both sides of the gap by external electrodes made of aluminum strips.

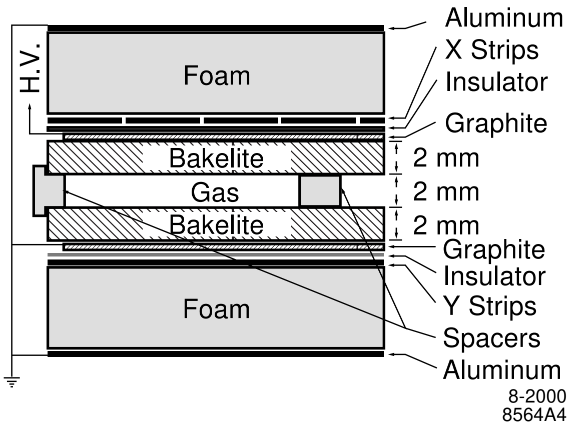

Figure 2.17: Cross Section of the Planar RPC

A particle, crossing the active layers of the detector, leaves a number of "hits", causing signals to be detected from one or more strips per plane. The single hits are then collected and associated in "clusters", each in principle

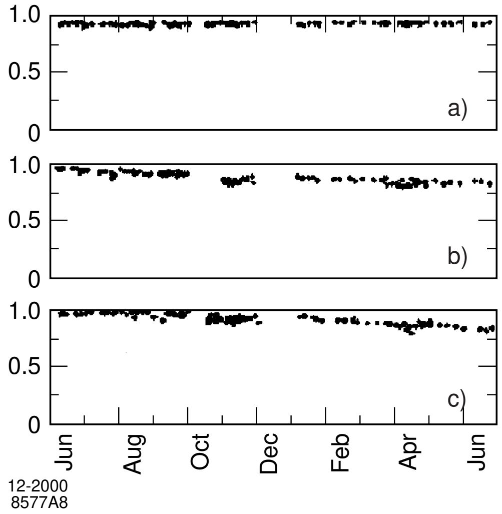

Figure 2.18: Efficiency history for 12 months starting in June 1999 for RPC modules showing different performance: a) highly efficient and stable; b) continuous slo w decrease in efficiency; c) more recent, faster decrease in efficiency.

associated with a single particle. Two different algorithms are used to reconstruct clusters in the Instrumented Flux Return. The first, used when a reconstructed track from the Drift Chamber is available, collects and groups hits around the extrapolation of the track into the IFR; the other, that runs after that, scans through all the hits that could not be associated to a track and tries to form "neutral" (i.e. not associated with a charged track) clusters. Muon-pion discrimination is based on the number of traversed interaction lenghts in the entire detector and on the distribution of RPC strips in each active layer, since one expects the average number of strips per layer to be larger for pions producing an hadronic interaction than for muons. With all these variables and additional others exploiting clusters distribution shapes, some selection criteria are applied to select muons.

Clusters that are not associated with a charged track are identified as neutral hadrons. Monte Carlo simulations predict that about 64% of K_L^0's above a momentum of 1 GeV/c produces a cluster in the cylindrical RPC, or a cluster with hits in two or more planar RPC layers. The combination of multiple clusters takes into account the large fluctuations in the hadronic showers. The direction of the neutral hadron is determined from the event vertex and the centroid of the neutral cluster, while no information on the energy of the cluster can be obtained. Since a significant fraction of the hadrons interact before reaching the IFR, information from the EMC are also used. The K_L^0 detection efficiency increases roughly linearly with momentum;

it varies between 20% and 40% in the momentum range from 1 GeV/c to 4 GeV/c (EMC and IFR combined).

2.6.1 Performance Overview

During data taking, the efficiency of the RPC chambers are monitored by both analysis of collision data and weekly dedicated cosmic ray runs. It should be noted that a small fraction of the RPC's is presently disconnected because of high-voltage instabilities, accounting for approximately half of the chambers with zero efficiency. The average efficiency of non-dead chambers during the 2000 run was ∼78% in the barrel, and ∼87% in the forward endcap, significantly lower than those measured in June 1999, that averaged ∼92%. The decline of the performance has been slowed down by the installation of water cooling, and the efficiency of a few resistive plate chambers have been improved by increasing the gas flow. After the cooling was installed and the RPCs were reconnected, some of them continued to deteriorate while others remained stable, some of them ($> 30\%$) at full efficiency (see Figure 2.18). Detailed studies revealed large regions of very low efficiency in these modules, but no clear pattern was identified. Studies are ongoing of the possible causes of this efficiency loss, but several possible causes have been excluded as the primary source of the problem, such as the change in the bakelite bulk resistivity, loosened spacers, gas flow, or composition.

Thanks to the large number of RPC layers, this problem has not yet impacted the overall performance severely, but present extrapolations, even after installation of water cooling on the steel, indicate a severe problem for the future operation.

2.7 Trigger and Data Acquisition

The high luminosity of PEP-II, and particularly the high frequency of the bunch crossing (238 MHz at the design luminosity, corresponding to a 4.2 ns spacing), posed new challenges to the Data Acquisition systems, since collisions are essentially continuous in terms of the response time of the electronics. Moreover, luminosity is also achieved with high beam currents, wich in turn generate high machine backgrounds, producing large occupancies in the detectors and imposing high bandwidth availability in the system to pass large events to the next processing level. Last, *BABAR* has more than 230000 signal channels from five different detectors (plus data from the trigger system), delivering signals with shaping times ranging from 1 ns to 3 μs.

Having to cope with such a high bunch crossing frequency, no way exists to select events before collecting them. A requirement of the electronics system, consequently, is to recognize, process and store data in a somehow parallel fashion. *BABAR* has adopted an innovative trigger/DAQ architecture [41] in which all the data transfers are pipelined; data acquisition system can buffer data from multiple bunch crossings while trigger components are processing the information.

The trigger basic requirement is to select events of interest (as $b\overline{b}$, $q\overline{q}$ and $\ell^+\ell^-$) and reject background in order to keep the total event rate under 120 Hz [3] . The total trigger efficiency is required to exceed 99% for all $B\overline{B}$ events and at least 95% for continuum events.

BABAR works with a two-level trigger system, consisting of a hardware Level-1 and a software Level-3. The L1 trigger decision is based on charged tracks in the DCH above a preset transverse momentum, showers in the EMC, and tracks detected in the IFR. The Level-1 trigger decision is issued within a latency of 11–12 μs after the corresponding beam crossing to initiate the Data Acquisition (DAQ) readout of the relevant time slice of the pipelined data for all detectors; the latency for hadronic events is confined to a smaller, $\pm150\,$ns range. The L3 receives the L1 output, performs a second stage rate reduction for the main physics sources, and identifies and flags the special categories of events needed for luminosity determination, diagnostic, and calibration purposes. At design luminosity, the L3 filter acceptance for physics is ∼90 Hz, while ∼30 Hz contains the other special event categories.

Both the L1 and L3 trigger systems have met their original design goals at a luminosity of $3\times10^{33}\,\mathrm{cm}^{-2}\mathrm{s}^{-1}$. The triggering efficiencies for $B\overline{B}$ events generally meet the 99% design goal for both L1 and L3. The current system also provides a solid foundation for an upgrade path to luminosities of $10^{34}\,\mathrm{cm}^{-2}\mathrm{s}^{-1}$ or more.

2.7.1 Level 1 Trigger

The Level-1 trigger system operates in a continuous sampling mode, processing input data and generating output trigger information at fixed time intervals. The basic trigger primitives generated by the DCT (Drift Chamber track trigger), EMT (calorimeter energy trigger) and IFT (IFR muon trigger) are collected by the GLT (Global Trigger system) to form 24 trigger lines for the fast control system. If a valid trigger remains, a *L1Accept* is issued to initiate event readout. The DCT and EMT event processing times are 4–5 μs, followed by another $\sim3\,\mu$s of processing in the GLT to issue a L1

[3]At design luminosity, beam-induced background rates are typically about 20 KHz

trigger.

The Level-1 trigger system is designed to be able to trigger independently from pure DCT and pure EMT triggers with high efficiency for most physics sources, in order to allow cross-calibration of efficiencies. In particular, the $B\overline{B}$ events are triggered at $> 99\%$ efficiency from either DCT or EMT and the combined efficiency is $> 99.9\%$.

The total Level-1 trigger rate for a typical run (700 mA in the HER, 1100 mA in the LER for a luminosity of 2.0 $\times 10^{33}\mathrm{cm}^{-2}\mathrm{s}^{-1}$) is $\sim$700 Hz, usually stable to within 10% and causing no significant deadtime. Bhabha events and other e^+e^- interactions amount to around 120 Hz, and cosmic ray interactions to 130 Hz, with the remaining triggers mainly originating from beam backgrounds.

2.7.2 Level 3 Trigger

The Level-3 trigger, the first component of the system to see complete events, is embedded in the Online Event Processing (OEP) framework running in parallel on a 32-nodes UNIX farm. It processes data from the Drift Chamber track trigger and from the Calorimeter, forming and subsequently filtering and selecting track and cluster objects using two independent algorithms. To increase time performance, both algorithms use lookup tables; the Drift Chamber trigger track segments and hit data are also used to determine the event t_0 to better than 5 ns.

The logging decision is based on generic track/cluster topologies rather than on the identification of individual physics processes: the track filter (efficiency for $B\overline{B}$ around 99%) requires either one track with $p_{\mathrm{t}}> 800\,\mathrm{MeV/c}$ coming from the interaction point, or two tracks with $p_{\mathrm{t}}> 250\,\mathrm{MeV/c}$ and slightly looser vertex cuts. The cluster filter (efficiency 94%) accepts events with a high multiplicity or with a large total energy in the Calorimeter and a high invariant (pseudo) mass.

In addition to the physics lines, L3 logs various other samples for calibration and monitoring purposes, such as radiative Bhabhas, cosmics, and random triggers. The luminosity is measured online by L3 using a track-based algorithm with a scale calibration precision of $< 5\%$. The typical logging rate is ~ 85 Hz, again well within the design specifications.

2.7.3 Data Acquisition Electronics

The *BABAR* data acquisition system employs a set of standard Readout Modules (ROMs) to communicate with the front-end electronics of the detector systems. A common communications protocol on 1Gbps optical fibre links

(G-Link) is used for readout by all the systems, with detector-specific extensions to the protocol for control.

Final event building is performed by sending these data fragments via 100–Mbps switched Ethernet to the nodes of the Online Event Processing (OEP) farm, which are commercial Unix workstations.

The OEP farm applies the Level 3 trigger algorithms and perform fast data quality monitoring functions. Events passing the Level 3 selection are then sent to a single server process which logs them to disk.

2.8 Computing Systems and Software

All colliding beam events are filtered and tagged; interesting events are completely reconstructed by a farm of about 150 commercial Unix processors. The system, called "Online Prompt Reconstruction" (OPR), is operating continuosly. While processing a run, a set of updated calibration constants (the so-called "rolling calibrations") is extracted from the data and used for subsequent reconstructions. A second, identical farm of workstations is used for periodical data reprocessing, when improved code or newer reconstruction constants become available.

All the recontructed events (from colliding beams data or Monte Carlo simulation) are dumped in an Objectivity database, physically stored in RAID disk arrays and StorageTek tape robots, controlled by the HPSS file system. The database is structured in four levels of detail:

Digi The raw, or "digi" database, includes all details about all hits in the detector for each event;

Reco The "reco" database contains all the reconstructed quantities (four-vectors) of each "candidate" (reconstructed track or neutral object) in each event;

Micro The "micro" database contains a limited number of information for each candidate; the values are discretozed and packed in order to save disk space. Most of the analysis is done with this data;

Tag The "tag" database contains global reconstructed event variables and boolean flags (the *tags*) useful to filter events before further processing.

Most of *BABAR* software, from Monte Carlo generators to reconstruction and data analysis code, is written in C++, using Object Oriented technology [42]. In particular any reconstructed object that passes the selection is referred as `candidate` and all the candidates of the same kind and event are stored in `List of candidates`.

To reduce the volume of data which form the input of the analysis, all the events passing preliminar selections have been recorded in the so called `Skims`, *i.e.* collections of small-sized pointers built in the Object-Oriented database, without duplicating the information kept on disk.

Monte Carlo Simulation

The Monte Carlo simulation of the detector is structurally divided in three parts; the software produces data that are written into the Objectivity database and can be processed with the same code as real data, without changes to the interface other than those needed to read Monte Carlo "truth" data.

The **Event Generators** provide the first step of the simulation; while several are available, the main one for $B\overline{B}$ is `EvtGen` [45]. The beam parameters (tilt angle, beam spot, etc.) are modeled on observed beam characteristics.

The **Detector Model** is based on the detector description and simulation tool `Geant321` [46]. Long-lived particles ("primaries") produced in the event generation stage are stepped through the detector and allowed to interact or decay. Secondaries resulting from those are tracked as well; however, only the `Geant321` kinematics of primaries and secondaries resulting from decays are recorded. The final output is a list of "GHits" (Monte Carlo track hits) in each detector.

The **Digitization Simulation**, or simulation of the detector response, is provided by a separate package, that uses the GHit information as input and produces digitized data in the same format as the real detector. To simulate backgrouds, real events from samples recorded with random triggers are overlayed (using the appropriate luminosity weighting factor) with Monte Carlo simulated events (`digimixing`).

Parameter	Design	Best Achieved	Typical in-run
	High Energy Ring		
Energy	9.0 GeV	9.0 GeV	9.0 GeV
Number of Bunches	1658	1658	553-829
Total Beam Current	0.75A (1.0A)	0.92A	0.940A
Beam Lifetime	4hrs @ 1A	11hrs @ 0.9A	9hrs @ 0.70A
	Low Energy Ring		
Energy	3.1 GeV	3.1 GeV	3.1 GeV
Number of Bunches	1658	1658	553-829
Total Beam Current	2.15A	1.72A	1.63A
Beam Lifetime	4hrs @ 2A	3.3hrs @ 1.4A	3hrs @ 1.1A
	PEP-II Luminosity		
Peak Luminosity ($cm^{-2}s^{-1}$)	3×10^{33}	4.5×10^{33}	4.0×10^{33}
Specific Luminosity ($cm^{-2}s^{-1}$/bunch)	3.1×10^{30}	2.9×10^{30}	2.4×10^{30}
IP Hor. Spot Size Σ_X	220 μm	190 μm	
IP Ver. Spot Size Σ_Y	6.7 μm	6.0 μm	
Top-off Time	3min	2min	3min
Fill Time	6min	8min	10min
Integrated Luminosity:			
pb^{-1}/day	135	278	
fb^{-1}/month		2.7	
Total Int. Luminosity	62.9fb^{-1}	(thru 12/20/2001)	

Table 2.2: PEP-II Numbers

PEP-II Design and Performance Results, adapted from [34].

	Physical Dimensions Acceptance	Performance
SVT	5 Layers $-0.87 < \cos\theta_{lab} < 0.96$	$\sigma_x = \sigma_{xy} = 50\,\mu\text{m}/p\ \oplus 15\,\mu\text{m}$ $\sigma_\phi = \sigma_\theta = 1.6$ mrad$/p$ (at 90°)
DCH	$R_{\text{Inner}} = 23.6\,\text{cm}$ $R_{\text{Outer}} = 80.9\,\text{cm}$ $L \simeq 277.0\,\text{cm}$ 40 Layers $-0.92 < \cos\theta_{lab} < 0.96$	$\sigma_{p_T}/p_T = 0.21\% + 0.14\% p_{\text{t}}$ Single point res. $\sim 140\,\mu\text{m}$ Track resolution $\sim 125\,\mu\text{m}$
DRC	$R_{\text{Inner}} = 81.0\,\text{cm}$ $R_{\text{Outer}} = 89.0\,\text{cm}$ Bar $L = 490\,\text{cm}$ $-0.84 < \cos\theta_{lab} < 0.90$	$K^\pm/\pi^\pm$ separation 3σ 2.0 GeV/c Čerenkov angle res. $\sigma_{\theta_C} \sim 2.8\,\text{mr}$
EMC	$R_{\text{Inner}} = 90.0\,\text{cm}$ $R_{\text{Outer}} = 136.0\,\text{cm}$ $-0.78 < \cos\theta_{lab} < 0.96$	$\sigma_E/E = (1\%/E)^{1/4} \oplus 1.2\%$ $\sigma_\theta \simeq 3\text{mrad}$
IFR	$L = 629.0\,\text{cm}$ 18-19 Planar + 4 Cyl. Layers $-0.90 < \cos\theta_{lab} < 0.96$	K_L^0 resolution $\sim 200\,\text{mr}$ FWHM Muon efficiency 77% $\pi^\pm$ fake rate 2.5%

Table 2.3: The *BABAR* subdetectors: characteristics and performance.

Chapter 3

Reconstruction of the B Decay Chain

The search of neutral B decays into two-body final states containing a charmonium resonance and a kaon is mainly motivated by the possibility they give to observe CP-violating effects. Just after the golden-channel $B^0 \to J/\psi\, K^0_S$, the $B^0 \to \psi(2\mathrm{S}) K^0_S$ process provides the second larger sample of data available for the measurement of the $\sin 2\beta$ parameter, which is cleanly related to the CP asymmetry magnitude.

The first *BABAR* results on CP violation have included a sample of events from the $B^0 \to \psi(2\mathrm{S}) K^0_S$ decay, in which the $\psi(2\mathrm{S})$ meson has been reconstructed in the $J/\psi\, \pi^+\pi^-$ decay (with the J/ψ decaying in turn to $\ell^+\ell^-$), which is the largest exclusive mode, and in its dileptonic decay ($\psi(2\mathrm{S}) \to \ell^+\ell^-$) which on the other hand has a higher reconstruction efficiency due to its clear signature. Furthermore the neutral kaon was observed only in its short-lived component decaying into two charged pions, $K^0_S \to \pi^+\pi^-$. As listed in table 3.1, *BABAR* also provided measurements of the branching fraction for the neutral B and the charged B decays into a state containing a $\psi(2\mathrm{S})$ and a kaon meson, which are $B^0 \to \psi(2\mathrm{S}) K^0$ and $B^\pm \to \psi(2\mathrm{S}) K^\pm$ respectively. Isospin symmetry requires that the ratio of charged to neutral partial width be unity for this decays.

The present work describes the attempt to identify an independent sample of events $B^0 \to \psi(2\mathrm{S}) K^0_S$ using the $\psi(2\mathrm{S}) \to J/\psi\, \pi^0\pi^0$ decay process in the available *BABAR* data sample (44.7 fb^{-1}). This decay has a considerable branching ratio (18.2%) but the disadvantage of the low reconstruction efficiency due to the low energy spectrum ($< 0.8\,\mathrm{GeV}$) of the two neutral pions. The sample, whenever checks on the selection are performed and the flavor tagging by the rest of the event are applied, will be studied for CP asymmetry purpose. The measure of the branching ratio of the decay $B^0 \to \psi(2\mathrm{S}) K^0_S$

Decay	$\mathcal{B}(10^{-4})$
$B^0 \to \psi(2S)K^0$	$6.8 \pm 1.0 \pm 1.1$
$B^\pm \to \psi(2S)K^\pm$	$6.3 \pm 0.5 \pm 0.8$

Table 3.1: $B \to \psi(2S)K$ decay channels and their branching fractions, as recently measured by *BABAR* [84]. The neutral decay has been studied using K^0_S in the final state only. These measurements do not include events with the $\psi(2S)$ meson reconstructed in its $J/\psi\,\pi^0\pi^0$ decay.

is used as a cross check on the event selection procedure.

The high purity required by the sin2β measurement and the exclusive channel in which the neutral kaon is reconstructed (only $K^0_S{\to}\pi^+\pi^-$) also affect the statistical significance of the sample. Thus the reconstruction of the charged B decay $B^\pm \to \psi(2S)K^\pm$ is used as a higher statistics control sample in order to validate the analysis. The expected yields from the two B meson decays in the data sample are indeed $\approx 40\%$ different.

While the kinematic characteristics of the $\psi(2S){\to}\pi^0\pi^0$ decay are largely described in the next Chapter, here I'd like to present the procedure that has been followed to select all the particles participating in the B meson decay process.

3.1 Reconstruction Outline

The selection is actually a full reconstruction of the B meson decay starting from the information on stable particles given by the various *BABAR* subdetectors. B mesons from the $\Upsilon(4S)$ decay have some characteristics which allow to distinguish them from events coming from both the non-resonant continuum and from random combinations of candidate daughters. In order to enhance the purity of the $B\overline{B}$ sample, some global information are used, such as the quality of the reconstructed primary vertex and the shape of the total event. It will be described in Section 3.2.

The main challenge of the decays discussed here is the π^0 detection at low energy, that is largely described in Sec. 3.3. B, $\psi(2S)$, J/ψ and K^0_S mesons are referred as `composite` candidates since identified by their decay processes: Composite mesons are reconstructed by combining sets of track and/or neutral clusters whose mass is fixed at that of the particle type they are assigned to. This is true either for the B mesons and for the intermediate states of its decay chain. The particle identification criteria used in *BABAR* and their performances as well as the selection criteria of the charmonium

Mode	$\mathcal{B}(\%)$
$\psi(2S)\rightarrow J/\psi\,\pi^0\pi^0$	18.2±2.3
$J/\psi \rightarrow e^+e^-, \mu^+\mu^-$	5.93±0.10, 5.88±0.10
$K^0 \rightarrow K^0_s$	0.5
$K^0_s \rightarrow \pi^+\pi^-$	68.61±0.28

Table 3.2: Decay modes of daughter mesons which will be reconstructed, and their branching fractions [3].

and the light strange meson are also discussed in the next sections.

The steps of the reconstruction of a candidate $B\rightarrow(\psi(2S)\rightarrow J/\psi\,\pi^0\pi^0)$ + K event proceed as follows:

- the J/ψ mesons are identified through their decay products, e^+e^- and $\mu^+\mu^-$, and π^0 decays into two photons are identified within the electromagnetic calorimeter;
- with a vertexing procedure the J/ψ mesons and a pair of π^0s are selected in order to share the same decay vertex, thus leading to the $\psi(2S)$ meson reconstruction;
- any identified kaon in the event that comes from the same vertex complete the full B meson decay.
- finally some cuts are imposed to definitively clean the sample and optimize the selection.

The selection uses variables as the invariant masses of the composite mesons and of the $\pi^0\pi^0$ dipion system. In order to improve the resolution on the kinematic quantities, a kinematic fit with the mass of the composite constrained to the official PDG value is imposed. Simultaneously, a topological fit allows to reconstruct the decay vertex of the composite particles.

3.2 $B\overline{B}$ Event Selection

As previously described, besides the $e^+e^-\rightarrow\Upsilon(4S)\rightarrow B\overline{B}$ events, other events are in minor quantities produced by the e^+e^- collisions on-peak, such as continumm events from light and charmed quark and generic $B\overline{B}$ events.

To provide good separation between jet-like continuum events and more spherical $B\overline{B}$ events we use the second Fox-Wolfram moment [56]. Fox-Wolfram moments are event shape observables used in e^+e^- collisions defined

Variable	Value
Number of charged tracks	≥ 3
L3DchOut = True or L3EmcOut = True	
R2All	≤ 0.5
E_{Tot}	$\geq 4.5\,\mathrm{GeV}$
(R_{xy}, d_z)	(0.5 ,6) cm

Table 3.3: Summary of the skim event selection criteria

by

$$H_l = \sum_{i,j} \frac{|p_i|\,|p_j|}{E_{\mathrm{Vis}}^2} P_l\left(\cos\theta_{ij}\right) \tag{3.1}$$

where i and j run over all pairs in a given set of reconstructed particles in the event; E_{Vis} is the total "visible" energy in the event, and $P_l\left(x\right)$ is the l-th Legendre polynomial. If the particle masses are negligible, $H_0 = 1$, while H_1 is always equal to zero; the moments are normalised as

$$R_l \equiv \frac{H_l}{H_0}. \tag{3.2}$$

In two-jet events, for example, $R_l \sim 1$ for even values of l, and $R_l \sim 0$ for odd values. R_l can be calculated using only charged tracks or tracks and neutrals together; the latter is used here and in the following.

The $B\overline{B}$ purity of the sample is enhanced by requiring the events to pass the selection criteria summarized in Table 3.3. All tracks in the fiducial region ($0.410 < \theta < 2.54\,\mathrm{rad}$) and all neutral clusters with energy greater than 30 MeV in the calorimeter fiducial region ($0.410 < \theta < 2.409\,\mathrm{rad}$) are considered:

- The event must satisfy either the L3 DCH or L3 EMC trigger.
- There must be at least three tracks that satisfy the standard selection requirements in the fiducial region: this rejects low multiplicity final states (Bhabha, radiative Bhabha, $\gamma\gamma$ interaction events) and beam-gas interaction events. A primary vertex is formed on an event-by-event basis from a vertex fit with all charged tracks in the fiducial volume. Tracks with a large χ^2 contribution to the vertex fit are removed until an overall χ^2 probability greater than 1% is obtained or only two tracks remain.

- The primary vertex which is constructed from these tracks must be within 0.5 cm of the beam spot in x-y and within 6 cm in z. The beam spot has an RMS of about 120 μm in x, 5.9 μm in y, and 0.9 cm in z. The point of closest approach of a high-momentum track to the beam spot is measured with a resolution of 23 μm in x and y, and 29 μm in z, as determined with dimuon events.

- The total energy in the fiducial volume for charged tracks and neutral clusters is required to be greater than 4.5 GeV.

- R_2 (the normalized Fox-Worfram moment of the event), calculated with both charged tracks and neutrals in the acceptance region, must be less than 0.5 in hadronic decay modes.

These requirements are $95.4 \pm 1.4\%$ efficient for $B\overline{B}$ events, as estimated from a Monte Carlo simulation. All events used in this analysis are required to pass this selection.

3.3 Neutral Particles Reconstruction

The details of the neutral particles reconstruction in the calorimeter are influenced by the energy range in question; noise, split-offs and combinatorial are the major issues at the lower end of the energy spectrum, while the proximity of the two photons in the calorimeter is the major issue at the higher end.

The typical energy of neutral pions coming from the $\psi(2S) \to J/\psi \pi^0 \pi^0$ decay is lower than 0.8 GeV, with the most probable value peaking around 0.3 GeV. Thus the results of this analysis depend on the precise knowledge of both the calorimeter performances and the π^0 reconstruction performances at these energies.

Neutral particles reconstruction starts from neutral clusters in the calorimeter, defined as clusters of energy not associated to charged tracks. The cluster reconstruction methods are been presented in Sec. 2.5.2. Some variables describing the shower shape can be used to distinguish between electromagnetic and hadronic ones.

Electromagnetic clusters can comprise both one and two local energy maxima (*bumps*). Photons are identified among the electromagnetic neutral clusters with a single bump. On the contrary high energy neutral pion can be characterized by both the energy distributions, in which cases are referred as *merged* π^0. *Composite* π^0 are those reconstructed using a pair of identified photon in the calorimeter. In the following we describe the mechanisms and the performances of such reconstruction criteria for photons and neutral pions.

3.3.1 Photon Candidates Selection

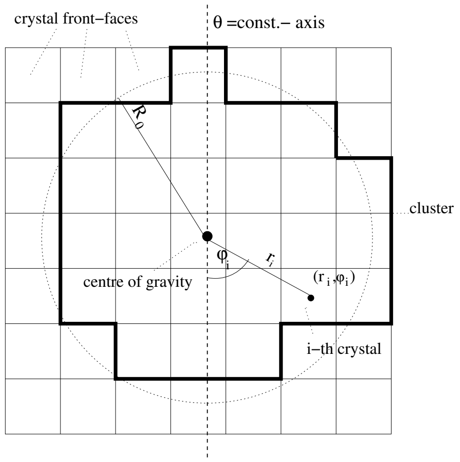

Figure 3.1: Definition of the variables r_i,ϕ_i e R_0 used to calculate the shower shape variables.

Among the neutral clusters in the calorimeter, we can distinguish between those generated by electromagnetic and hadronic interactions, *i.e.* between photons and neutral hadrons like K_L^0s and neutrons.

Electromagnetic and hadronic showers have different signatures, resulting in different longitudinal and lateral energy distributions. It's useful to introduce a local (cylindrical) coordinate system in which the position of each crystal of the cluster in the (r, ϕ) plane is referred to that of the energy center of gravity, as described in Fig. 3.1, while the z axis is along the line going from the interaction point to the center of the cluster. The *BABAR* electromagnetic calorimeter does not allow the measurement of the longitudinal distribution of the shower along the direction of its development, but its finely segmentation in the transversal plane permits the reconstruction of the lateral distribution with an accurate precision. Two lateral shower shapes are presently used:

- Lateral energy distribution LAT, first introduced at Argus [47]:

$$\mathrm{LAT} = \frac{\sum_{i=3}^{n} E_i r_i^2}{\sum_{i=3}^{n} E_i r_i^2 + E_1 r_0^2 + E_2 r_0^2}, \qquad E_1 \geq E_2 \geq \ldots \geq E_n$$

  where the sum extends over all crystals in a shower, but the 2 most energetic, $r_0 = 5\,\mathrm{cm}$, the average distance between two crystal front-faces, and r_i is the distance between crystal i and the shower center (calculated as the center of gravity with linear energy-weighting of every crystal).

Electromagnetic showers in the EMC have most of their energy deposited in one or two crystals, hence LAT is smaller for electromagnetic showers than for hadronic showers. Thus this variable is used to distinguish both photons and electrons.

- Furthermore, hadronic showers in the EMC tend to be more irregular than electromagnetic showers. This is exploited in the expansion of the lateral shower shape in terms of Zernike moments (first introduced at ZEUS [48]), corresponding to :

$$A_{nm} = \sum_{r_i \leq R_0}^{N_{cell}} \frac{E_i}{E} \cdot f_{nm}(\frac{r_i}{R_0}) \cdot e^{-im\phi_i}, \qquad R_0 = 15\,\mathrm{cm}$$

with

$$f_{nm}(\rho_i \equiv \frac{r_i}{R_0}) = \sum_{s=0}^{(n-m)/2} \frac{(-1)^s (n-s)! \rho_i^{n-2s}}{s!((n+m)/2-s)!((n-m)/2-s)!},$$

with $n, m \geq 0$ integers, $n - m$ even and $m \leq n$ (see Fig. 3.1). The angles ϕ_i describe the orientation of the cluster in a plane orthogonal to this axis. Hence these functions provide an expansion independent of the orientation of the local coordinate system

Only one of these moments, the Zernike-moment $|A_{42}|$, showed up to be very useful in electron identification and is currently used in *BABAR*.

To summarize, electromagnetic showers have LAT peaked at about 0.25 and A_{42} close to zero, while showers from hadrons have a broader distribution in LAT, and extend to larger values of A_{42}.

Electromagnetic clusters in the calorimeter in the *fiducial* polar angle range $0.41 < \theta_{lab} < 2.409$ rad that are not associated with charged tracks, have an energy greater than 30 MeV, and a shower shape consistent with a photon interaction ($LAT < 0.8$) are taken as photons.

3.3.2 π^0 Reconstruction

Two different π^0 topologies are reconstructed starting from neutral bumps in the calorimeter: *composite* from two separated bumps and *merged*, either from two bumps coming from the same cluster or from one-bump cluster.

Bumps are either whole clusters (continuous regions of deposited energy) if one local maximum is found, or fractions of clusters in the presence of two or more local maxima where a splitting alghoritm distributes the energy measurements with distance-based weight to all local maxima. For distances between the two photons below 25 cm it is likely that both end up in the same cluster, while if they are separated by at least one crystal in most cases a second local maximum will be found and thus two bumps will be created.

Any pair of photons with a total energy above 200 MeV is considered as a composite π^0. Neutral pion momentum is calculated imposing the PDG mass value hypotesis (135. MeV), while its direction is estimated as it comes from the *BABAR* origine. Different selections are possible for the composite π^0, more or less loose depending on the selected π^0 mass window and the vertex fit procedure. Given the current performance of the detector a mass region of (100–160) MeV corresponding to $(-4\sigma; +3\sigma)$ is imposed.

Merged π^0s can be separate from photons using the cluster second moment defined as

$$S(\theta, \phi) = \sum_{i}^{Ncell} \frac{E_i}{E} \cdot (\varDelta\phi_i^2 + \varDelta\theta_i^2) \tag{3.3}$$

where $\varDelta\theta_i$ and $\varDelta\phi_i$ are angular distances of the crystall i from the center of the cluster, in the *BABAR* global coordinates. This is actually the estimation of the RMS spread of the cluster. From this, a powerful variable to distinguish between photons and high energy π^0s which appear in a single bump is the invariant mass of the overlapping photons [49] defined as:

$$m = E \cdot \sqrt{|S - S_\gamma|}$$

where E and S are the energy and the second moment of the reconstructed merged π^0 candidate. The constant $S_\gamma = 0.0009945$ is the average second moment of a single photon cluster, derived from simulation. In multi-hadron events the single bump π^0s are 25% of the total composite π^0s that can be reconstructed. They also give a slightly better mass resolution (by 0.3–0.5 MeV) and their mass distribution contains less combinatorial under the π^0 peak.

Due to the low energy spectrum of the neutral π^0 involved in the $\psi(2S) \to J/\psi\ \pi^0\ \pi^0$ decay, the merged π^0 are not relevant in this analysis: henceforth only composite π^0s from pairs of separated photons will be considered.

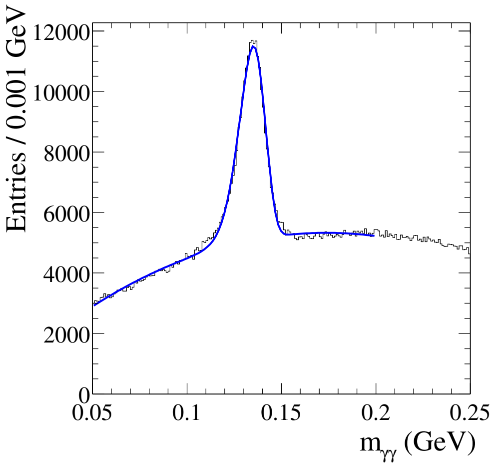

Figure 3.2: Invariant mass of two photons in $B\overline{B}$ events from data. The energies of the photons and the π^0 are required to exceed 30 MeV and 300 MeV, respectively. The solid line is a fit to the data [40].

3.3.3 π^0 Mass and Width

The energy resolution in the electromagnetic calorimeter suffers from some shower leakage effects, due to the energy depositions beyond the end of the crystal and in the inactive material in front of and between the crystals.

The amount of leakage at the end varies with the shower depth and therefore with the energy itself, whereas the material in front of the calorimeter is a function of the polar angle, but this effect is of minor significance.

Due to energy leakage and shower shape fluctuations, the photon energy resolution and all masses of particles reconstructed from photons have a characteristic asymmetric shape with a tail towards lower values. This shape is clearly visible in both data and simulation. To account for this asymmetry the mass peak is fitted to a logarithmic normal distribution, known in *BABAR* as the “Novosibirsk” function [50].

$$f(E) = A \cdot \exp\left[-\frac{1}{2}\left(\frac{ln(1+\tau\cdot(E-\nu)\cdot\frac{sinh(\tau\sqrt{ln4})}{\sigma\,\tau\,\sqrt{ln4}})}{\tau}\right)^2 + \tau^2\right] \tag{3.4}$$

Figure 3.2 shows the two-photon invariant mass in $B\overline{B}$ events from data. The reconstructed π^0 mass is measured to be 135.1 MeV/c^2 and is stable to better than 1% over the full photon energy range. The fitted width is

6.9 MeV/c^2 while in low-occupancy events and for isolated photons from hadronic events is slightly smaller, 6.5 MeV/c^2 , for π^0 energies below 1 GeV.

Combinatorial background

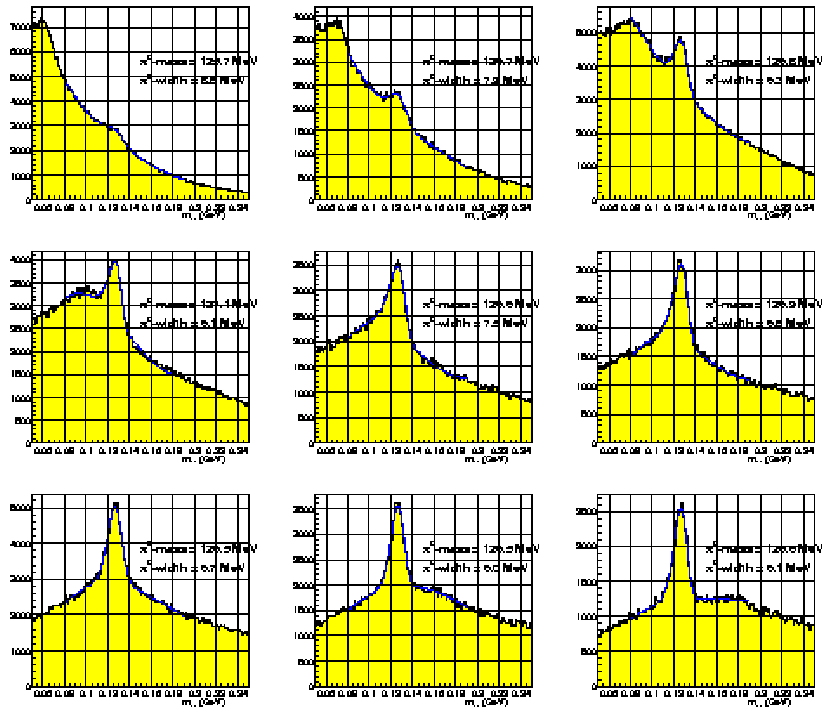

Figure 3.3: The reconstructed $\gamma\gamma$ mass for different energy bins. At least one of the two photons is required to fall into the specified energy range. The interval boundaries from top left to down right are (in MeV): 30, 40, 50, 75, 100, 125 150, 200, 250 [52].

The combinatorial background shape depends on the energy range of photons and π^0s, the machine background level and noise in the Calorimeter. Figure 3.3 shows the two-photon mass spectra for 9 different energy intervals. The combinatorial background is dominant for lower energy intervals, making the extraction of the π^0 signal very difficult especially for the first energy interval. It's further interesting to note the change in the shape of the background distribution. Starting out as a steeply falling distribution for small energies, it changes into a peaked distribution from medium energies and turns into an almost flat one at high energies.

3.3.4 Systematics from Neutrals

The performances of the neutral pion selection have been checked on dedicated π^0 samples. Comparisons between data and Monte Carlo events, either inclusive and exclusive involving τ, D and D* decays have shown that in general the simulation gives a good description of the neutral efficiency and resolution. In particular a study has been performed on $\tau^+\tau^-$ "1-to-1" decays, where the tag τ decays into $e^-\overline{\nu}_e\nu_\tau$ and the other decays to a hadron plus one or two π^0s. The energy spectrum for π^0s in hadronic τ decays extends to $\sim 8\,\mathrm{GeV}$ and allows validation of the Monte Carlo simulation across almost the entire range of energies observed at *BABAR*.

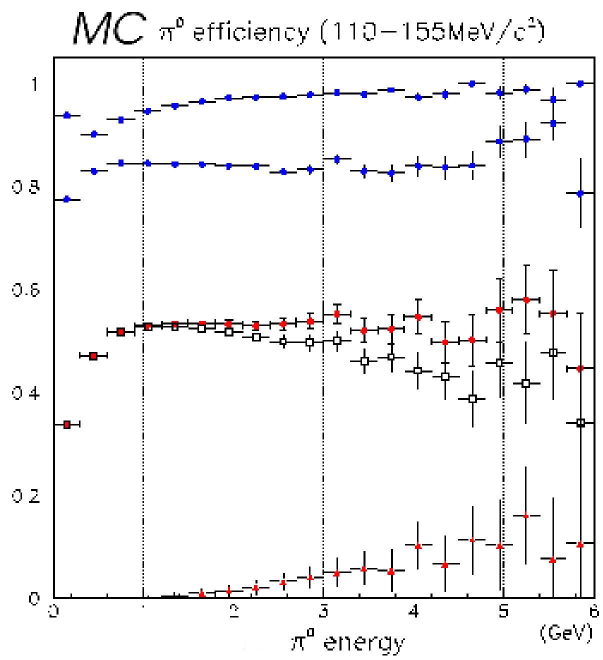

Figure 3.4: π^0 efficiency from Monte Carlo. From the top curve to the lower: 1) loss due to the 30 MeVphoton energy cut; 2) geometrical acceptance of the EMC; 3) (filled red circle) total reconstruction efficiency; 4) (open black square) contribution from composite π^0 s; 5) (red triangle) contribution from the merged π^0.

The estimation of the efficiency of the π^0 reconstruction has been performed counting the events inside the peak of the π^0 mass spectrum modelled with a Novosibirsk function of Eq.3.4 plus a 3rd order polynomial. Systematics from the fit, such as correlation between the background and peak partition, cancel to first order as long as the peak and background shapes are equal.

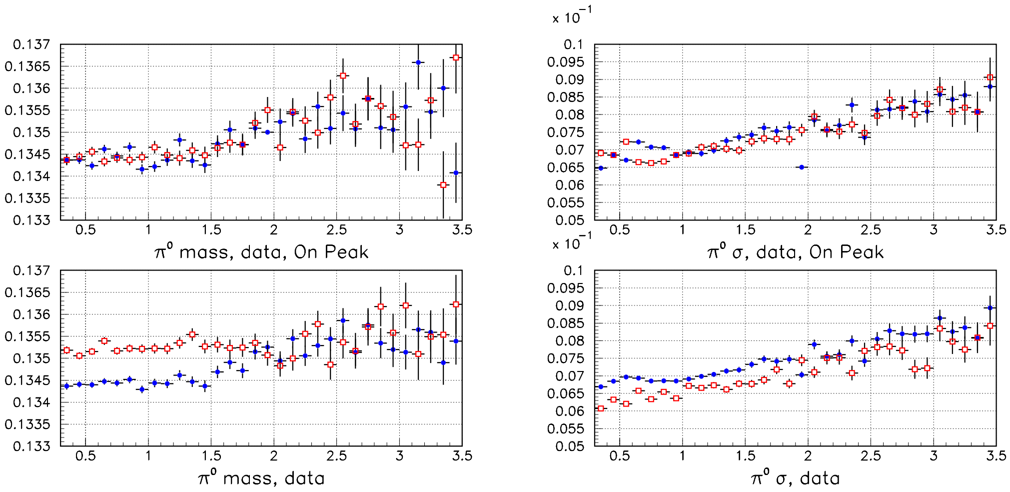

Figure 3.5: Inclusive π^0 mass (left) and width (right). Top plots are the comparison between on-peak (blue filled circles) and off-peak (red open squares) data comparisons. Lower plots show data (blue filled circles) and simulated (red open squares) generic events. The data sample corresponds to $\sim 105\ pb^{-1}$ [40].

The studies on neutral identification and reconstruction report [40]:

reconstruction efficiency: π^0 inclusive yields from Monte Carlo and from on/off resonance data show π^0 recontruction efficiency agreement within 5%, corresponding to 2.5% per neutral bump. To correct for this effect the single photon efficiency is adjusted by randomly removing 2.5% of photons in the Monte Carlo, accounting for statistical fluctuations.

identification efficiency: The fitted π^0 mass peak values and widths obtained from the inclusive study are shown in Figure 3.5 as a function of the π^0 energy for data and the simulated samples. The top plots show the on-peak and off-peak results, which are identical within statistical fluctuations. The lower plots show the data–Monte Carlo comparison: whereas above 2 GeV data and Monte Carlo agree for the mass and width, below 2 GeV a discrepancy is clearly visible. The π^0 mass peak is 0.4% lower and the width is 7% larger in Run1 data than in Monte Carlo. So when extracting the Monte Carlo π^0 efficiency correction an energy smearing of 1.5% and a 0.75% energy shift are introduced on the remaining π^0s. Only the bigger error among them is accounted for.

These values were estimated from π^0s over an energy range (0. ; 3.5) GeV and designed to take into account the worst discrepancies, while the 1.5%

smearing has been used in π^0 efficiency studies using τ [51], where has been shown to remove all the discrepancies. Further studies on single photon Monte Carlo sample have demonstrated that the addition of machine background (through "digimixing") has a small degrading effect on the mass resolution, while the event multiplicity doesn't affect at all, as seen comparing inclusive $q\overline{q}$ events to two prong $\tau^+\tau^-$ events.

One plausible reason for the higher Monte Carlo π^0 efficiency is that there is more material in the real detector than in the simulation. This would lead to a higher γ conversion in data compared to Monte Carlo and thus to a smaller probability of photons reaching the EMC. This is confirmed by other observations (higher Bremsstrahlung rates for electrons from J/ψ [77] and bhabha events in luminosity studies) that tend to demonstrate that the detector model has some missing material in the beam pipe and the support tube. This defect in the detector model should be overcome with a better description of the materials in the center of the detector which has been recently implemented within `Geant4`. The simulated event sample used in this analysis do not include this upgrade, thus the corrections ar applied and the corresponding error is included in the systematics.

3.4 Particle identification

Identification of electrons, muons and kaons is an essential ingredient of both B reconstruction and flavor tagging. Particle species can be distinguished by mixing information from different measurements:

- the specific energy loss ($\mathrm{d}E/\mathrm{d}x$) in the SVT and in the DCH along the particle trajectory,
- the number of Čerenkov photons and the Čerenkov angle in the DIRC,
- the electromagnetic shower energy in the CsI calorimeter,
- the particle penetration length in the IFR.

Selection criteria are based on these quantities, on likelihood ratios derived from them, or on neural network algorithms combining different detector likelihoods. Tracks with no particle information are assumed to be pions. Typically looser selection criteria are applied for B reconstruction in comparison to B-flavor tagging. Efficiencies and particle misidentification probabilities are determined from data control samples.

3.4.1 Electron Identification

Electrons are separated from charged hadrons primarily on the basis of the shower energy in the calorimeter and the track momentum, since the most discriminating power is their ratio E/p, which for electrons its expected to be close to unit, while hadrons can either not interact in the calorimeter, like muons, or leave only a part of their energy, with a resulting lower average value of E/p. It's crucial that the (transverse) momentum of the track is well measured in order to ensure a good match between the track and the energy deposit in the EMC, and a well-determinated E/p value. Therefore electron tracks need to be `GoodTrackLoose`. The energy deposition of a minimum ionizing particle in the EMC amounts to roughly 200 MeV and this limits the power of E/p for very low momenta. So other information are needed.

Two shower shape variables, LAT and A_{42} as defined in Sec. 3.3.1, can be used to exploit the differences of lateral shower development for electrons and hadrons. The difference in the longitudinal energy distribution it's examined by the track-bump separation variable, defined as $\Delta\phi = q \cdot (\phi_{EMC} - \phi_{Cl})$ where q is the sign of the charge of the particle, and ϕ_{EMC} and ϕ_{Cl} are, respectively, the azimuth of the intersection of the track with the EMC and that of the cluster associated to the track. Electrons shower shortly after entering the EMC, while interacting hadrons usually shower later and thus show a larger $\Delta\phi$ value.

In addition, the dE/dx energy loss in the DCH and the DIRC Čerenkov angle can be used to ensure the consistence with an electron hypotesis. The dE/dx distribution for electrons, in arbitrary units, peaks at ~ 650 with a width of $\sigma \sim 50$.

The cut-based electron selectors provide five different levels of efficiency and purity, which definitions are shown in Table 3.4.

Table 3.4: Definition of the various electron selector criteria.

Electron Selectors						
Category	dE/dx	E/p	LAT	A_{42}	$\Delta\phi$	Drc
`noCal`	[540, 860]					
`veryLoose`	[500,1000]	[0.50,5.0]	[-10.,10.]	[-10.,10.]	no	no
`Loose`	[500,1000]	[0.65,5.0]	[-10.,10.]	[-10.,10.]	no	no
`Tight`	[500,1000]	[0.75,1.3]	[0.,0.6]	[-10.,10.]	no	no
`veryTight`	[540,860]	[0.89,1.2]	[0.,0.6]	[-10.,0.11]	yes	yes

Shower shapes and E/p are complementary since hadronic showers depositing a larger amount of energy (and hence with larger E/p) tend to have larger values for the shower shape variables (due to the irregularities of the hadronic shower).

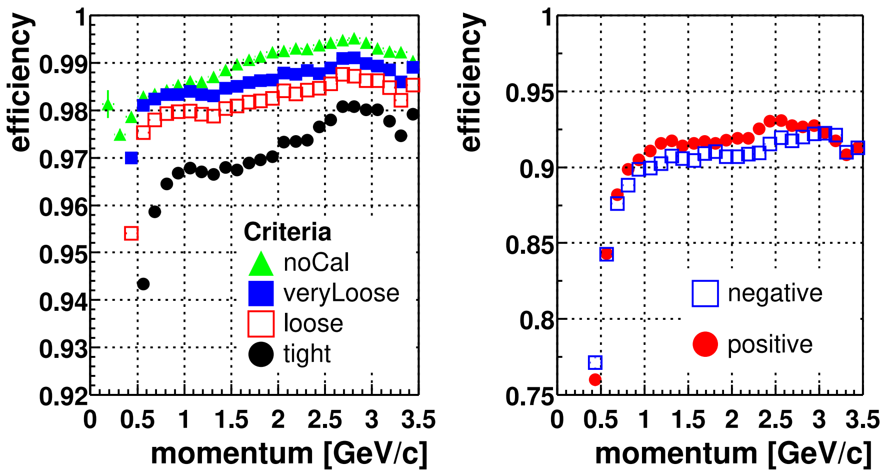

Figure 3.6: The electron efficiency of the four looser selectors (left) and the tighter (right) as a function of momentum. Electrons are selected from the conversion sample, $\gamma\gamma \rightarrow\ eeee$ [54].

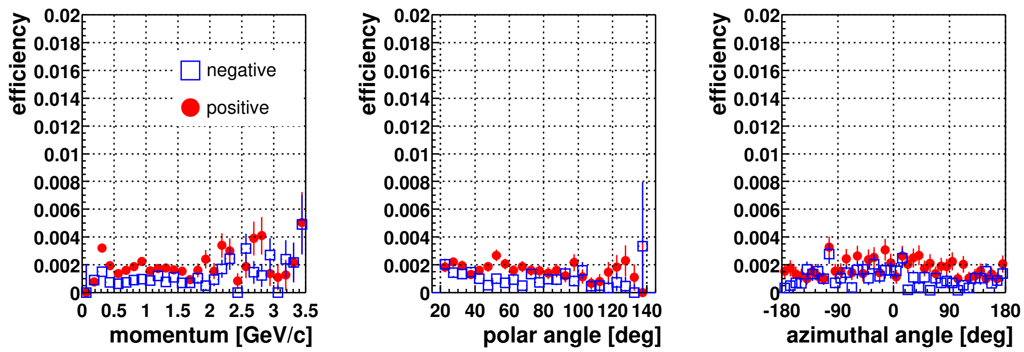

Figure 3.7: Pion misidentification probabilities of the `veryTight` electron selector as a function of momentum, polar angle and azimuthal angle. Pions are selected from K_s^0 and $\tau \rightarrow\ 3h^{\pm}$ control samples [54].

Fig.3.6 and Fig.3.7 show the performances of some of these selectors. While the `veryLoose` and `Loose` ones have efficiencies $\epsilon > 97\%$ with high level of misidentification for momenta greater than 0.5 GeV, the `Tight` selector provides a high efficiency of $\epsilon > 96\%$ for $p > 0.7\,\text{GeV}$ with a pion misidentication rate of roughly $1 - 2\%$. The efficiency is determined with control samples [54]. The `noCal` category is used only in regions outside of the EMC acceptance: they are candidates that are not matched to an EMC cluster, but their $\mathrm{d}E/\mathrm{d}x$ satisfies the tighter electron requirement.

3.4.2 Muon identification

Although muon identification relies almost entirely on the IFR, other detectors can provide additional information. Charged tracks reconstructed in the SVT and DCH, which meet the criteria for a minimum ionizing particles in the EMC, are extrapolated to the IFR taking into account the non-uniform magnetic field, multiple scattering and the average energy loss. All clusters detected within a predefined distance from the extrapolated track are associated with it.

Table 3.5: Criteria used for selecting available categories of muon candidates.

Muon Selectors							
Category	n_λ	Δn_λ	$\overline{n}_{hits}$	$\sigma_{n_{hits}}$	χ^2_{trk}/n_{lay}	χ^2_{fit}/n_{lay}	E_{EMC} [GeV]
`veryLoose`	> 2.0	< 2.5	< 10	< 6	–	–	< 0.5
`Loose`	> 2.0	< 2.0	< 10	< 6	< 7	< 4	< 0.5
`Tight`	> 2.2	< 1.0	< 8	< 4	< 5	< 3	$[0.05, 0.4]$
`veryTight`	> 2.2	< 0.8	< 8	< 4	< 5	< 3	$[0.05, 0.4]$

Muons below $\sim 1.3\,\text{GeV/c}$ stop in the IFR (but it depends on their angle θ), while the penetrating ones typically leave a thin track, with very few hits per layer. On the opposite, pions and other hadrons (of which only $0.2 \div 1.7\%$, depending on the polar angle and momentum, fail to be absorbed in the iron) can generate a hadronic shower with non-negligible transversal development, leaving thus more than one hit per layer.

A number of variables are defined for each IFR cluster associated with a charged track to discriminate muons from charged hadrons. Muon candidates are primarily identified by the measured number of hadronic interaction lengths traversed in the IFR iron n_λ, and the difference between n_λ and the predicted penetration depth for a muon of the same momentum and angle, Δn_λ. Contamination from hadronic showers is rejected by a combination of the average number and the variance of hits per RPC layer ($\overline{n}_{hits}$ and $\sigma_{n_{hits}}$, respectively), the χ^2 for the geometric match between the track extrapolation into the IFR and the RPC hits (χ^2_{trk}), and the χ^2 of a polynomial fit to the RPC hits (χ^2_{fit}). In addition, for those muons within the acceptance of the EMC, the calorimeter cluster energy E is required to be consistent with a minimum ionizing particle.

Four different categories of muon candidates (`veryLoose`, `Loose`, `Tight` and `veryTight`) are selected with the criteria listed in Table 3.5.

In the forward region, which suffers from some machine background, additional requirements on the fraction of RPC layers with hits are made.

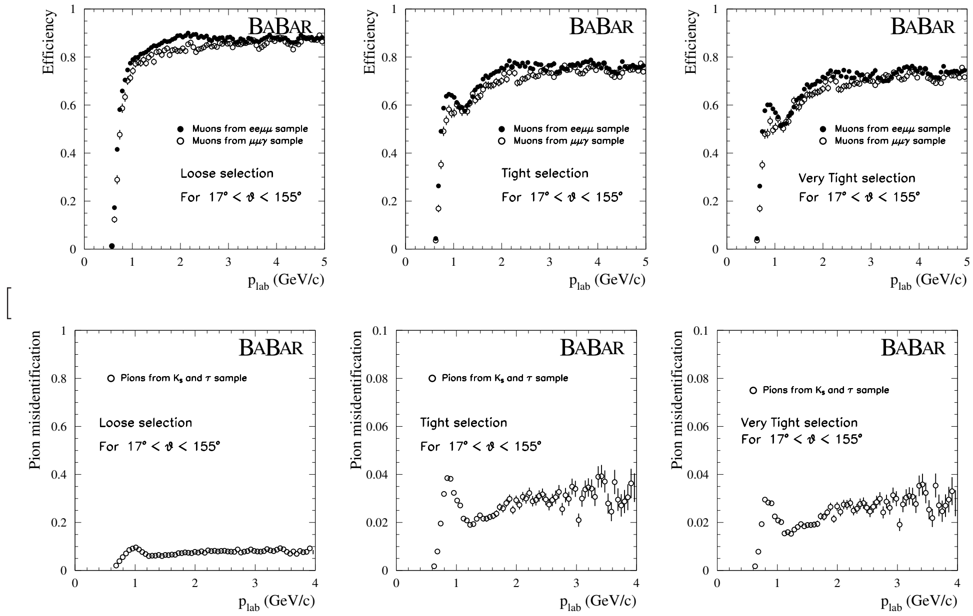

Figure 3.8: Muon Efficiency (top) and Pion Misidentification Probability (bottom) for `Loose`, `Tight` and `veryTight` selection as a function of the particle momentum in the laboratory frame, in the angular region covered by the IFR. Efficiencies [55] are shown for two control samples: $e^+e^- \rightarrow \mu^+\mu^-\gamma$ and $e^+e^- \rightarrow e^+e^-\mu^+\mu^-$. Pions are extracted from K^0_S and and $\tau \rightarrow\ 3h^{\pm}$ control samples.

The performance of muon selection has been tested from collision data on samples of unbiased muons from $\mu^+\mu^- ee$ and $\mu^+\mu^-\gamma$ final states, and pions from three-prong τ decays and $K_S \rightarrow \pi^+\pi^-$ decays. As illustrated in Figure 3.8, where the performances of some selectors are shown, a muon detection efficiency close to 90% has been achieved with the looser criterion, in the momentum range of $1.5 < p < 3.0\,\mathrm{GeV/c}$ with a fake rate for pions of about

6–8% [1]. The hadron misidentification can be reduced by a factor of about two by tighter selection criteria which lower the muon detection efficiency to about 80%.

3.4.3 Charged Kaon identification

Kaons are distinguished from pions and protons on the basis of specific energy loss measurements $\mathrm{d}E/\mathrm{d}x$ in SVT and DCH and the number of Čerenkov photons and the Čerenkov angle in the DIRC. The signature of kaons in the different detectors is complicated by the fact that kaons with different electric charge decay and interact with the material of the detector differently. Towards higher momenta, the $\mathrm{d}E/\mathrm{d}x$ separation power fastly reduces, due to relativistic effects on the particle mass, thus kaon identification efficiency and pion misidentification show a fast degradation. Efficiency also depends of the π ans K composition of the sample, that for generic B decays is strongly momentum dependent. In particular, due to the decreasing kaon composition at higher momenta, tighter cuts must be applied.

A likelihood test assignes each track a particle identity through the comparison between three likelihood functions with an assigned particle hypotesis: $\mathcal{L}_\pi$, $\mathcal{L}_K$ and $\mathcal{L}_p$. Kaon candidates are rejected if the likelihood ratios satisfy $\mathcal{L}_K/\mathcal{L}_\pi < r_\pi$ and $\mathcal{L}_k/\mathcal{L}_p < r_p$, where r_π and r_p are numerical values, fixed *a priori* in each momentum region.

Each likelihood function uses a combination of individual likelihoods from SVT, DCH and DIRC in different momenta ranges. The difference between the measured truncated mean $\mathrm{d}E/\mathrm{d}x$ and the expected mean for the pion, kaon and proton hypothesis is used to compute likelihoods for the drift chamber and the SVT. In the DIRC, a likelihood is obtained for each particle hypothesis from the product of two components: the expected number of Čerenkov photons, with a Poisson distribution, and the difference between the measured average Čerenkov angle to the expected angle for a given mass hypothesis, assuming a Gaussian distribution.

Five kaon selectors have been created: `NotApion`, `veryLoose`, `Loose`, `Tight` and `veryTight`. They mostly differ in the momentum ranges in which the likelihood functions of each subdetector are used and in the likelihood cut values and conditions for K/π and K/p separations. Their performances are studied [53] on different control samples: pions from $K^0_S \to \pi^+\pi^-$ and pions and kaons from $D^* \to D^0\pi_{soft}, D^0 \to K\pi$.

In the reconstruction of B decays, many decay mode do not require particle identification. In this analysis a very loose (`NotApion`) selection

[1]Decays in flight contribute about 2% to the pion misidentification probability

is imposed to reduce background. This kaon consistency requirement has a nearly constant kaon-identification efficiency of about 97% and a pion-misidentification probability of at most 20%.

For B-flavor tagging the likelihood variables from SVT, DCH and DIRC are combined as inputs to a neural network whose output is a single discriminating variable for kaon selection. The average efficiency of the selection is about 85% for a pion-misidentification probability of about 2.5%. The efficiency and pion misidentification level plots for the kaon selectors used for tagging in *BABAR* are shown in Fig 3.9.

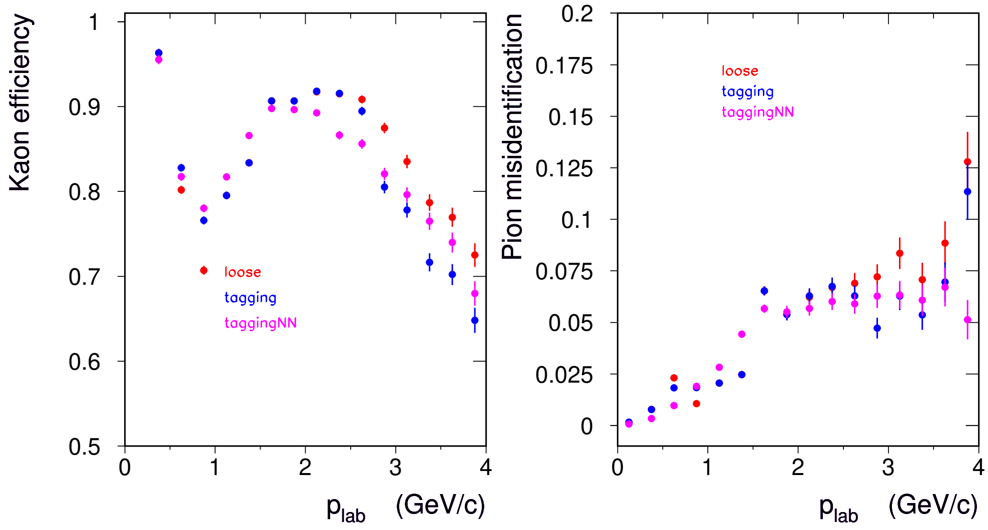

Figure 3.9: Kaon efficiencies and pion misidentification vs momentum for the criteria used for tagging in *BABAR*.

3.5 Reconstruction of Composite Particles

The whole process $B \rightarrow \psi(2S)$K that we want to study involves many decays: $\psi(2S)$ decaying to J/ψ and two π^0s, the J/ψ decaying into two leptons, both electrons and muons, and, in the case of the neutral B mode, K_S^0 decaying into two charged pions. Each of these decays is identified by imposing a common vertex to all the particles involved and requiring that the invariant mass of the reconstructed daughters to be consistent with the mass of the mother. Then the decay tree is built and the B vertex found.

3.5.1 Vertexing procedures

The procedures to perform the vertexing exploit the kinematic properties of the decay in order to reach better mass and position resolutions and larger signal-to-background ratios, as well as a better resolution when measuring the time difference between decaying B mesons in the $\Upsilon(4S) \rightarrow B\overline{B}$ decay. The clear signature of the J/ψ decay into leptons, above all, helps in reconstructing the entire decay tree. In the case of $B^0 \rightarrow \psi(2S)K^0_S$, the position measurement of the B^0 can be improved using the constraint that the line-of-flight of the reconstructed K^0_S contains the J/ψ vertex. The energy resolution of the B^0 can also be improved by applying a mass constraint to the J/ψ and K^0_S daughters. As far as the $\psi(2S)$ decay is concerned, in the $\psi(2S)$ rest frame J/ψ is almost at rest, given the small difference in mass, hence in the laboratory frame the two charmonium states share the same vertex. Then in the fitting procedure the two decay vertexes are forced to coincide and the momentum direction of the $\psi(2S)$ is alligned to that of the J/ψ. The same procedure for the $B \rightarrow \psi(2S)$K decay improves the B vertex resolution. Similarly, the momentum resolution of neutral pions can be improved using the decay vertex of the J/ψ as their decay vertex and by applying a mass constraint on the invariant mass of the two photons (the π^0 energy resolution improves from 3% to 2.5% after a mass constrained fit).

Given the similar tracking resolutions of the *BABAR* detector in the transverse plane and longitudinal direction, calculations are in all cases performed in three dimensions. Non-linearities in the fits require the use of an iterative procedure. To semplify the implementation of the constraints and also to treat composites, neutrals and tracks in the same way, the candidates are parameterized, instead of helices, in the so-called *X-P representation* which gives the position and momenta of the candidate at distance of closest approach for tracks and at decay point for composites.

3.5.2 Selection of the J/ψ mesons

For each event, a search is made for candidate J/ψ decaying into either e^+e^- or $\mu^+\mu^-$. The two selection mechanisms are very similar. A set of tracks is selected with appropriate track quality criteria, and particle identification requirements (described below) are imposed on them. Each pair of selected tracks is combined by vertex fitting if their invariant mass (calculated by simple 4-vector sum) lies in the range $2.5\,\text{GeV} < M_{\ell^+\ell^-} < 3.5\,\text{GeV}$. If the fitting algorithm does not converge, the candidate is created with the 4-momenta sum. Then, the invariant mass is required to lie in the range $3.02\,\text{GeV} < M_{e^+e^-} < 3.14\,\text{GeV}$ for electrons and $3.05\,\text{GeV} < M_{\mu^+\mu^-} < 3.14\,\text{GeV}$ for muons.

For e^+e^-, the mass window is chosen slightly asymmetric to accept candidates subject to Bremsstrahlung energy loss. To enchance the efficiency of the selection we applied a Bremsstrahlung recovery procedure to each pair of tracks that pass the electron `Loose` selection criteria.

Bremsstrahlung Recovery

Final state radiation following $J/\psi \rightarrow e^+e^-$ decays (internal bremsstrahlung), as well as radiation of bremsstrahlung photons from $e^{\pm}$ in the detector material produce a long radiative tail in the e^+e^- mass distributions. This reduces the efficiency of the event selection for this decay mode, when we impose a cut on the invariant mass to suppress background. The detection of the radiative photons and the measurement of their energy is used to correct the momentum of the tracks determined by the tracking alone. Both in data and Monte Carlo, almost 23 % of all $J/\psi \rightarrow e^+e^-$ events are found to have a Bremsstrahlung photon associated. The net effect of adding these photons to the e^+e^-tracks in the J/ψ reconstruction can be seen in Fig.3.10.

3.5.3 Reconstruction of the $\psi(2S)$ mesons

The $\psi(2S) \rightarrow J/\psi \pi^0\pi^0$ candidates are reconstructed combining J/ψ and a pair of π^0 candidates, both constrained to their PDG mass value. All $\psi(2S)$ candidates which have a recontructed $\psi(2S)$ within 3.3 and 4.0 GeV are retained as $\psi(2S)$ candidates. No cut is applied on the vertex fit probability. In addition, candidates are required to have a $\pi^0\pi^0$ invariant mass between 0.4 and 0.6 GeV, as will be motivated in Sec. 4.1.1.

3.5.4 K_S^0 Reconstruction and Selection

In this analysis K_S^0 candidates are reconstructed in the $\pi^+\pi^-$ mode, using all pairs of opposite charged tracks and assigning them the π mass. To further reject background the most discriminating variable has turned out to be the flight length (in three dimensions) of the candidates with respect to the J/ψ vertex and its significance, obtained dividing it by its error. The error is evaluated taking into account the errors from the vertexing procedure and from the beam spot position. The number of observed K_S^0 and their mass value, computed at the vertex of the two tracks, are evaluated from a fit to the $\pi^+\pi^-$ invariant mass distribution, using a double gaussian with a linear background.

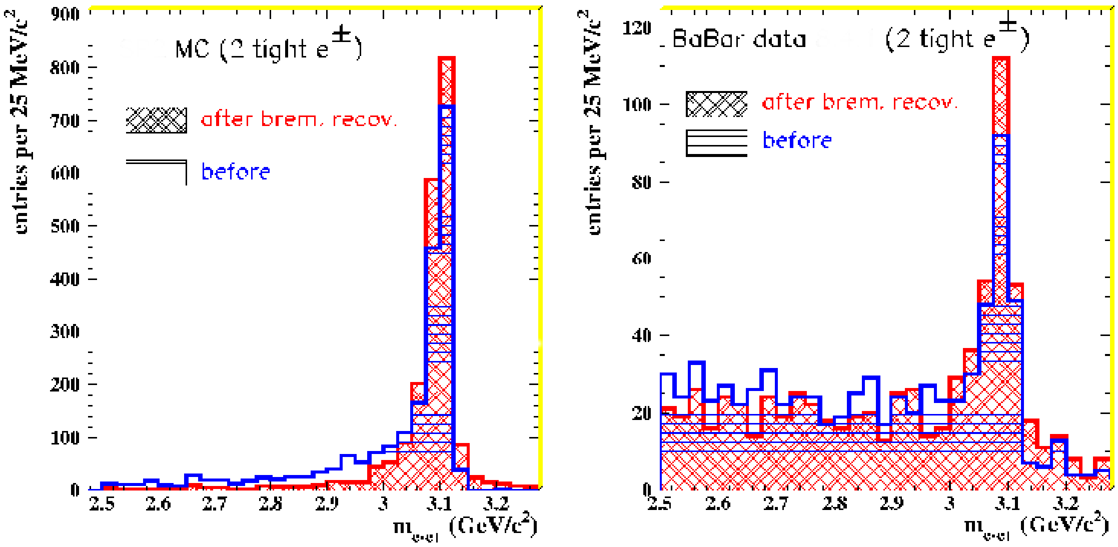

Figure 3.10: Left : e^+e^- mass distribution for $B^0 \to J/\psi K^0_S$, $B^+ \to J/\psi K^+$, $B^0 \to J/\psi K^{*0}$and $B^+ \to J/\psi K^{*+}$ exclusive modes in Monte Carlo, before and after applying the bremsstrahlung recovery algorithm. Right : same for an early year 2000 data sample. The distributions are given for the 2 tight $e^{\pm}$ hypothesis.

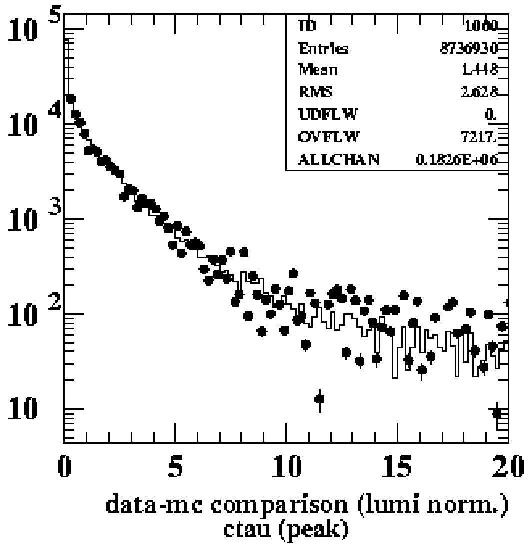

Figure 3.11: K_S^0 reconstructed flight length: the K_S^0 flight length in $b\bar{b}$ events in data (points) is obtained from a sideband and off-resonance subtraction and compared with the K_S^0 flight length in $b\bar{b}$ Monte Carlo events (line). The comparison is done with both a luminosity normalization and an area normalization.

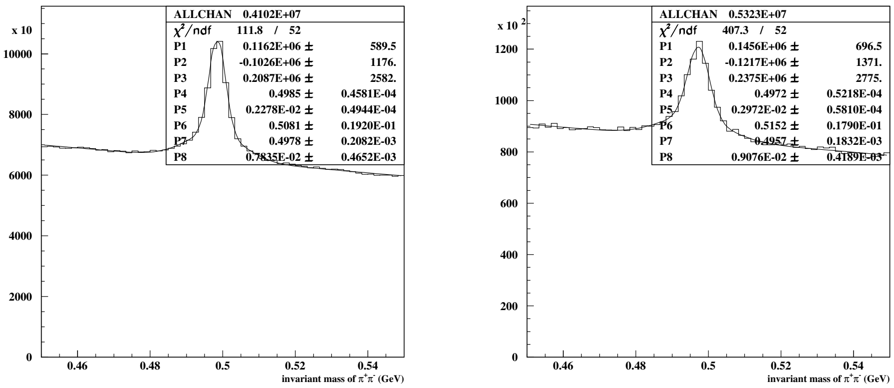

Figure 3.12: K_S^0 reconstruction efficiency in $b\bar{b}$ events: $\pi^+\pi^-$ invariant mass in $b\bar{b}$ events in Monte Carlo (left) and in data (right).

The properties of the reconstructed $K_S^0 \to \pi^+\pi^-$ have been studied in detail and are reported in [83] and the stability of resolution, mean mass and yields is monitored during the whole online prompt reconstruction process. The reconstruction efficiency measured on a sample of simulated $B^0 \to J/\psi\, K_S^0$ events is around 68% (79% within the geometrical tracking acceptance), while a lower value is found on data hadronic events (54%). The inefficiency is mainly due to missing tracks at low momentum and at the edge of the acceptance. Hence the overall efficiency is strongly momentum dependent, worsening at low K^0_S momenta. The resolution on the K^0_S mass is evaluated using a single gaussian and linear background fit. Comparisons between generic Monte Carlo and on resonance data show a 0.2% shift in data for the mass value and a bit worst resolution. This difference has been taken into account into the systematic studies. The distributions of the flight length and mass for $K^0_S \rightarrow \pi^+\pi^-$candidates in data are shown in Fig. 3.11 and 3.12 respectively.

3.6 Selection of the B mesons

After reconstructing the $\psi(2S)$ mesons and the light meson candidates (charged kaons or K^0_S), an attempt is made to reconstruct the B mesons, using all combinations of candidates. Both the charmonium and light meson candidates are constrained to their PDG masses in the B vertex fit procedure.

3.6.1 B variables

Two almost independent kinematic variables are used to isolate B meson candidates, following the study of other experiments (CLEO, ARGUS [58]). One is ΔE, the difference between the reconstructed energy of the B candidate and the beam energy in the $\Upsilon(4S)$ center-of-mass frame:

$$\Delta E = E^*_B - E^*_{beam} \tag{3.5}$$

The other is the beam energy substituted mass m_{ES}defined as:

$$m_{ES} = \sqrt{\left(\frac{\frac{1}{2}s + \mathbf{p}_B \cdot \mathbf{p}_i}{E_i}\right)^2 - p^2_B} \tag{3.6}$$

with E_i and $\mathbf{p}_i$ the total energy and the three momentum of the initial state in the laboratory frame, and $\mathbf{p}_B$ the three momentum of the B candidate in the same frame. The m_{ES} variable depends on the B momentum in the laboratory frame, and not on its energy, thus is completely independent of the mass which is assigned to the final state particles. The small variations of E^*_{beam} over the duration of the run are taken into account when calculating m_{ES}: the beam parameters are recordered every 20 minutes.

For signal events ΔE will be zero within the experimental uncertainties, while m_{ES} is close to the B meson mass, 5.279 GeV/c^2. The signal region is a rectangular area in the (m_{ES},ΔE) plane, whose dimensions are based on the separately observed resolutions of m_{ES} and ΔE distributions.

Chapter 4

Study of the $\psi(2S) \rightarrow J/\psi\,\pi^0\pi^0$ decay

$\psi(2S)$ decays such as $\psi(2S)\rightarrow\ell^+\ell^-$ and $\psi(2S)\rightarrow J/\psi\,\pi^+\pi^-$ have been already studied in *BABAR*, providing a considerable sample of $B^0\rightarrow\psi(2S)K^0_S$ events for the first important results on CP violation. The $\psi(2S)\rightarrow J/\psi\,\pi^0\pi^0$ decay studied in this analysis is expected to give an independent contribution to the $B^0\rightarrow\psi(2S)K^0_S$ sample, limited by the low efficiency of the neutral reconstruction.

The purpose of this chapter is to give an overview on the $\psi(2S)\rightarrow J/\psi\,\pi^0\pi^0$ decay, with respect to the kinematic properties of the signal events. To do so, the first section introduces the theoretical studies developed in the last 30 years to understand the spectra from the $\psi(2S)\rightarrow J/\psi\,\pi\pi$ decays (with both charged and neutral pions) observed by a large number of experiments aimed at the study of three body decays of different heavy quarkonium resonances. Namely the shape of the invariant mass of the dipion system spectrum gives us the chance not only to identify the decay events, despite the low reconstruction efficiency, but also to enhance the purity of the selected sample. The final states containing a $\pi^+\pi^-$ pair and those containing a $\pi^0\pi^0$ pair have similar kinematics, but they require analysis procedures that are very different and largely independent; they rely mostly on different components of the detector and are subject to different systematic errors and biases.

Three exclusive $B\overline{B}$ Monte Carlo samples have been generated following the simultaneous results from many charmonium dedicated experiments. Besides the $B^0\overline{B}^0$ and the B^+B^- samples, the third one is specifically generated to allow the study of a single B^0 decay with less combinatorial background. This is realized constraining one of the B^0 mesons from the $\Upsilon(4S)$ decay to decay through the undetectable process $B^0\rightarrow\nu\overline{\nu}$.

Combinatorial background to the $\psi(2S)\rightarrow J/\psi\,\pi^0\pi^0$ decay arises from random combinations of leptons and π^0 s, which can be either real or from machine background. The reconstruction mechanism of the decay has been already described in the previous chapter, where we also noted how the neutral pion identification at low energies has a quite low purity, due to the large combinatorics. This is the central topic of the chapter, since mass and energy distributions are affected by this fake background component, that generally appears as a broad distributions below the signal peak. Here a point must be stressed, which is that these components are also visible after the reconstruction of simulated signal events, as will be shown by the exclusive signal Monte Carlo samples. By the other hand, the clear signature of the J/ψ decaying into two leptons and the known spectrum of the invariant mass of the two recoil π^0s are the most powerful tools we can use to enhance the purity of the sample. Other background sources are different ψ(2S) inclusive decays, continuum and generic $B\overline{B}$ events, so that studying all the background Monte Carlo samples is also useful for the same purpose.

4.1 Decay Overview

$J/\psi\ \pi^+\pi^-$ and $J/\psi\ \pi^0\pi^0$ are the two largest decay modes of the ψ(2S) meson, with branching ratios (31.0$\pm$2.8)% and (18.2$\pm$2.3)% [3]. Since there are two pions in the final state the two charmonium mesons have the same G-Parity, which is preserved in the process. To describe these decays the following conventions are used:

$\vec{\boldsymbol{l}}$ – $\pi\pi$ angular momentum

$\vec{\boldsymbol{L}}$ – J/ψ - $\pi\pi$ angular momentum

$\vec{\boldsymbol{s}}$ – spin of the J/ψ

$\vec{\boldsymbol{s}}\,'$ – spin of the ψ(2S)

Defining $\vec{S} = \vec{s} + \vec{l}$ the spin of the channel, then $\vec{s}\,' = \vec{S} + \vec{L} = \vec{s} + \vec{l} + \vec{L}$.

The quantum numbers of the ψ(2S) and J/ψ are $J^P = 1^-$ and $I^{GC} = 0^{--}$, while the $\pi\pi$ system has $I^{GC} = 0^{++}$, which requires for C-conservation its angular momentum to be even, $l = 0, 2$. Moreover parity conservation in the decay requires $(L + l)$ to be even. The relative prevalence of $J/\psi\ \pi^+\pi^-$ with respect to $J/\psi\ \pi^0\pi^0$ decay suggests the $\pi^+\pi^-$ system is an isospin singlet, I = 0. Isospin conservation, after taking phase space differences into account, precisely relates the branching fractions of the $\pi^+\pi^-$ and $\pi^0\pi^0$ modes in these transitions.

Characteristic of these decays are:

Table 4.1: Characteristics of the two resonances J/ψ and $\psi(2S)$ as reported in PDG [3].

$c\bar{c}$ Meson	Mass (MeV)	Width Γ_{Tot} (keV)
$\psi(2S)$	3685.96 ± 0.09	277 ± 31
J/ψ	3096.87 ± 0.04	87 ± 5

- As shown in table 4.1 the difference in mass between the J/ψ and $\psi(2S)$ mesons is (589.07 ± 0.13) MeV [3], so a very small residual energy is available for the pions. The spectrum range is $4m_\pi^2 \leq M_{\pi\pi}^2 < (M_{\psi(2S)} - M_{J/\psi})^2$, *i.e.* $0.08 \leq M_{\pi\pi}^2 \leq 0.35\,\mathrm{GeV}^2$.
- With this small energy stock, no strong resonance at tree level is present in the final states for both charged and neutral pions cases. As far as $\pi - \pi$ resonance is concerned, effective theory can exclude any possible state: gauge invariance ensures the spin-0 contribution to vanish, isospin (for charged pions) and boson symmetry (for neutrals) forbid the spin-1 resonance, while $n \geq 2$ are not fenomenologically allowed. Furthermore $\psi(2S)$ and J/ψ are very narrow resonances and their interactions with the pions can be neglected.

Therefore most part of the amplitude is expected to be the contribution from contact interactions. This validates the low energy expansion in the treatment of the chiral symmetry in the whole physical momentum region.

4.1.1 The Hadronic Matrix Element

These decays, transitions between bound $c\bar{c}$ states, have been extensively studied in the last 30 years, as a laboratory for studying heavy quark-antiquark dynamics at short distance.

Early investigation of the $J/\psi\pi^+\pi^-$ decay by Mark I [61] found that the $\pi^+\pi^-$ mass distribution was strongly peaked towards higher mass values, in contrast to what was expected from phase space. Further, angular distributions strongly favoured S-wave production of J/ψ $\pi\pi$, as well as an S-wave decay of the dipion system.

The challenge of describing the mass spectrum attracted considerable theoretical interest, and many approaches were applied:

- using chiral symmetry arguments and partially conserved axial currents (PCAC), Brown and Cahn [62] derived a matrix element, contain-

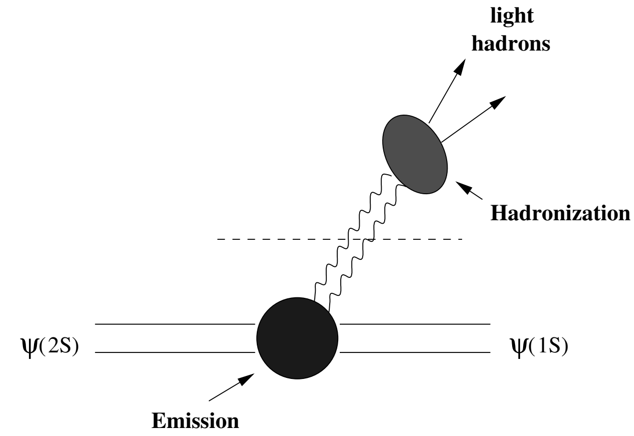

Figure 4.1: Diagram of $J/\psi\ \pi\pi$ decay process, showing it as a two step process with the emission of two gluons followed by hadronization to pion pairs.

ing three terms with different momentum dependence. Two of these terms produce strong angular correlation in the decay, so imposing the isotropic S-wave behaviour in the decay, only one of these terms survives, the one that gives a peak at high invariant mass. Moreover Cahn [63] calculated all the angular distributions in terms of partial wave amplitudes, as will be described in Sec. 4.1.2.

- We can think these transitions to occur in a two steps process by the emission of two gluons followed by hadronization to pion pairs, as indicated in Fig. 4.1. Because of the small mass difference involved, the gluons are soft and cannot be handled by perturbative QCD. However, Gottfried [64] suggested that the gluon emission can be described by a **multipole expansion**, with the gluon fields expanded in a multipole series as in the electromagnetic transitions. With this model [65] one of the terms that Brown and Cahn assumed to be zero should have a small but non-zero value.

- Later on, pion hadronization matrix element was studied [66] [67] using **current algebra** [1], PCAC and gauge invariance. An amplitude was calculated, derived from "first principles" and it's important to stress the fact that predicted a small amount of D-wave in the dipion system.

- As far as decays of heavy quarkonia are concerned there has been a lot of

[1] this algebra relates the decay amplitude to the matrix element of axial currents which have their pion poles removed

theoretical progress recently with an **effective theory** approach. For decays of heavy excited S-wave spin-1 quarkonium into a lower S-wave spin-1 state, such as $\psi(2S)\to J/\psi\ \pi\pi$, the chiral symmetry arguments help to construct the effective Lagrangian on which a derivative $1/m_Q$ expansion can be performed starting from the infinite mass limit for the heavy quarkonium [68]. This model predicts a highly suppressed contribution of D-wave transition in the scale of the heavy quark mass in processes with two pions in the final state.

All models are based on chiral symmetry which relates the properties of the $\psi(2S)$ - J/ψ system to the structure of the axial current matrix elements. Chiral symmetry modifies the phase-space decay spectrum, since it adds an additional term to the matrix element, which is proportional to $(m^2_{\pi\pi}-2m^2_{\pi})^2$. So it predicts the spectrum to peak at high mass, as it does also in $\Upsilon(2S)\to\Upsilon(1S)\pi\pi$ found in CLEO II [70]. However, $\Upsilon(3S)\to\pi^+\pi^-\Upsilon(1S)$ has a peak at low mass, as well as a peak at high mass, that disagrees with these predictions. See Ref. [70] for a list of theory papers that attempt to deal with this problem.

Thought strongly suppressed, the D-wave transition is predicted, mostly near the lower endpoint of the dipion mass spectrum. Using a partial wave analysis in an effective theory, a method is presented in [69] to experimentally measure these beyond-leading-order effects, providing significant information to the dynamics.

Up to now, the biggest $\psi(2S)$ sample was produced by the Bejiing Electron Spectrum (BES) on BEPC [71], that has accumulated 3.8×10^6 $\psi(2S)$ events. These events make it possible to see the $\pi^+\pi^-$ D-wave in the $J/\psi\ \pi^+\pi^-$ decay mode. Moreover since the processes are flavor disconnected, the strong interactions are suppressed, and there is the chance [72] to see CP-violating effects beyond (or even within) the Standard Model in these decays, through the measure of the CP-violating terms in the decay amplitudes.

The most recent results on $\psi(2S)\to J/\psi\pi^0\pi^0$ have been published by the Fermilab E835 Collaboration [73], that provides new branching ratio measurement and a $M_{\pi\pi}$ spectrum that is reported in Fig. 4.2. Its shape confirms the observation by the other experiments and is consistent with the hypothesis of S-wave decay to J/ψ and a $J^P=0^+$ $\pi\pi$ system.

4.1.2 A Partial Wave Analysis

Cahn [63] provided a useful decomposition of the amplitudes of these decays in terms of partial waves, using the very general formalism of a $V'\to VP\overline{P}$

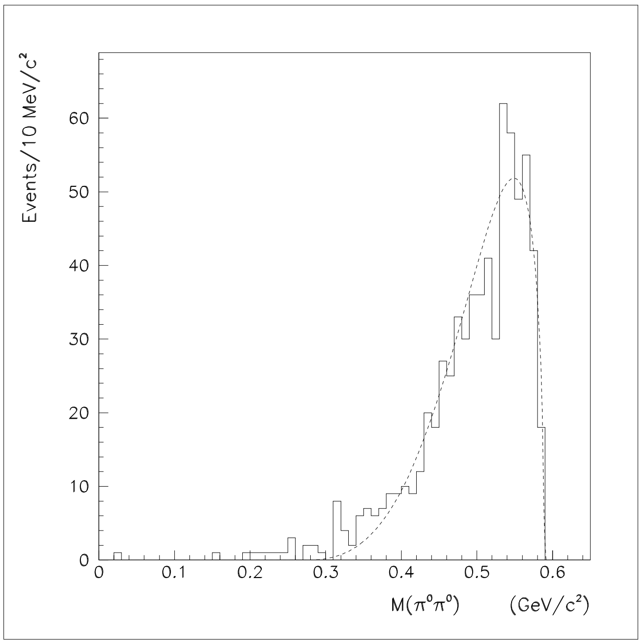

Figure 4.2: The $\pi\pi$ invariant mass for the $J/\psi\,\pi^0\pi^0$decay. The dashed curve is calculated assuming S-wave decay and a $J^P = 0^+$ $\pi\pi$ system [73].

decay. The process is considered to take place via sequential two-body decays: $\psi(2S)\rightarrow J/\psi\,X$, $J/\psi\rightarrow\ell^+\ell^-$and $X\rightarrow\pi\pi$, so describing each decay in its rest frame. This expansion is truncated after a few terms, substantially reducing the difficulty of the analysis, and the leptonic decay of the J/ψ can make angular information available, since the QED vertex requires two opposite leptonic helicities. As a result of the partial wave analysis, the distributions coming from single particles depend only on the magnitude of the partial wave amplitudes M_{lLS} which are functions of $M_{\pi\pi}$. On the contrary, joint distributions depend on the relative phase of the amplitudes. Thus amplitudes such as $d\Gamma/d\Omega_{J/\psi}$ and $d\Gamma/d\Omega_{\pi}$, where Ω' s are measured in the rest frames of J/ψ and π respectively, depend only on $|M_{001}|$, $|M_{021}|$ and $|M_{201}|$. The $d\Gamma/dM_{\pi\pi}$ spectrum is also correlated to these amplitudes, and its shape suggests that M_{001} is the most significant component.

The most meaningful results about this angular components come from BES that analysed 3.8×10^6 $\psi(2S)$ events. They are summarised in Tab. 4.2 as resulting from simultaneous fits to three 1-D angular distributions. Results from 2-D likelihood fits show that $|M_{201}|/|M_{001}|$, which measures the relative amount of D-wave of the dipion system, varies between 0.12 and 0.18 and is at least two sigmas from zero. On the other hand, $|M_{021}|/|M_{001}|$, which measures the relative amount of D-wave of the J/ψ X system, varies between

Table 4.2: Results from BES [71] of simultaneous χ^2 fits to the three 1-D distributions of $\cos\theta_l$, $\cos\theta_X$, and $\cos\theta_\pi$. The phase shifts used are $\delta_0^0 = 45°$ and $\delta_2^0 = 0°$.

BES Results	
$\lvert M_{001}\rvert$	$41.6 \pm 0.4 \pm 0.9$
$\lvert M_{201}\rvert$	$7.5 \pm 1.4 \pm 1.9$
$\lvert M_{021}\rvert$	$-0.56 \pm 0.60 \pm 0.64$
$\lvert M_{201}\rvert/\lvert M_{001}\rvert$	$0.18 \pm 0.03 \pm 0.05$
$\lvert M_{021}\rvert/\lvert M_{001}\rvert$	$-0.013 \pm 0.014 \pm 0.015$
χ^2/DOF	89/111

-0.04 and 0.06 and is, in all cases, consistent with zero.

4.2 Monte Carlo Samples

In order to estimate signal efficiencies for any given set of event selection criteria, three signal Monte Carlo samples containing 20,000 events each have been generated, as described in Sec. 4.2.1. In addiction some simulated background samples have been used in this analysis. This Monte Carlo simulation production is completely GEANT3-based [76].

The generic Monte Carlo samples include $B\overline{B}$ events, with an approximately equal number of $B^0\overline{B}^0$ and B^+B^- events; continuum $c\overline{c}$ events and continuum uds events; inclusive $\psi(2S)$ and J/ψ events. These samples are used extensively to perform data/simulation comparisons. For this purpose, the Monte Carlo samples need to be scaled to the data luminosity. The scaling factors F_{sc} are calculated in the following way. If N_{sam} is the number of Monte Carlo events in a given sample (*e.g.*, the number of generic $B\overline{B}$ events), then:

$$F_{sc} = \frac{\sigma_{sam}\,\mathcal{L}}{N_{sam}} = \frac{\mathcal{L}}{\mathcal{L}_{sam}}, \tag{4.1}$$

where $\mathcal{L}$ is the integrated data luminosity, while $\mathcal{L}_{sam}$ is the equivalent luminosity for the process in question and σ_{sam} is the cross-section. The number of events in each generic Monte Carlo sample, as well as the cross-sections used in Eqn. 4.1 and the equivalent luminosities are listed in Table 4.3.

MC Sample	# Evts	# Evts/ fb	$\mathcal{L}_{sam}(\mathrm{fb}^{-1})$
	`Signal`		
$B^{\pm} \to \psi(2S)K^{\pm}$, $\psi(2S) \to J/\psi\,\pi^0\pi^0$	20,000	13.07	1530
$B^0 \to \psi(2S)K^0_s$, $\psi(2S) \to J/\psi\,\pi^0\pi^0$	20,000	4.6	4210
	`Backgrounds`		
Inclusive J/ψ [a]	489,000	2727	179.3
Inclusive $\psi(2S)$	98,000	306	320.3
generic B^+B^-	4,657,402	0.525×10^6	8.47
generic $B^0\overline{B}^0$	3,943,361	0.525×10^6	7.17
Continuum uds	18,191,830	2.09×10^6	8.7
Continuum $c\overline{c}$	12,096,226	1.3×10^6	9.3

[a]This sample includes some SP4 simulation production.

Table 4.3: The number of total produced events in the Monte Carlo samples, with corresponding events/ fb and equivalent luminosities, for the signal and background (inclusive J/ψ and $\psi(2S)$, generic $B\overline{B}$ and continuum $udsc$), used for data/Monte Carlo comparison.

The same information are shown for the two signal Monte Carlo samples. One can obtain a good reproduction of the expected background by exclusively summing all the rescaled background samples and collecting the `cocktail-background` sample used in this analysis.

4.2.1 The Exclusive Signal Monte Carlo Samples

Due to the results from BES and using the branching fractions from PDG 2000, a decay model was constructed (VPIPI model [45]) and used in the Monte Carlo generation within the *BABAR* experiment to study the $\psi(2S) \to J/\psi\,\pi\pi$ decay. This is based to some approximations

1. The amplitude for the mass of the $\pi\pi$ system is empirically given by:

$$\frac{d\sigma}{dm_{\pi\pi}} \propto (\text{phase space}) \times (m^2_{\pi\pi} - 4m^2_{\pi})^2$$

2. $\vec{L} = 0$. The orbital angular momentum between the dipion system and the J/ψ is equal to zero (S-wave approximation). The X and the J/ψ are uniformly distributed in $\cos\theta_{J/\psi}$ in the ψ(2S) rest-frame.

3. $\vec{l} = 0$. The orbital angular momentum between the two π's in the $\pi\pi$ system is zero. The pions are uniformly distributed in $\cos\theta_\pi$, where θ_π is the angle between the J/ψ direction and the π in the X rest frame.

Two signal Monte Carlo samples have been generated, one for charged and one for neutral B's . In both of them, one B meson must decay to ψ(2S) K ($K^\pm$ for $B^\pm$ and K^0_S for B^0) following the required decay chain, while the other B decay follows the B meson decay modes without any assumption. They are generated in such a way that all the J/ψ mesons decay in an equal fraction into e^+e^- and $\mu^+\mu^-$.

Both samples contain 20,000 signal events and include the machine background as recorded by data (digi-mixing)

During the analysis, the association between Monte Carlo generated and reconstructed events has been considered not completely reliable for the reconstructed neutral candidates, and was not used. Thus in the analysis we cannot make any distinction between the well-reconstructed signal events and the fake candidates combinations. This latter is quite a big component, since π^0 mass at this energy is almost flat and thus there is a non-zero probability to substitute the real π^0 (from the decay $\psi(2S)\to J/\psi\pi^0\pi^0$) with a π^0 either from the decay of the other B meson, the not reconstructed one, or by machine background. These fake candidates are clearly visible in many variables distributions, like the B meson energy or the ψ(2S) mass spectra, generally appearing as a broad background below the signal peak. This fake combinatorial part of the signal, which will be call the **internal combinatorics background**, can be studied on simulated events. For this pourpose, a third Monte Carlo sample is generated, in which the not-reconstructed B is forced to decay to $\nu\overline{\nu}$, thus leaving no trace in the detector. This is worthwhile in order to bypass the combinatorics coming from the total event multiplicity and thus to eliminate noise coming from the misreconstructed Bs. This $B^0\overline{B}^0$ Monte Carlo sample is henceforth referrred to as the '`pure`' sample.

These three Monte Carlo samples have been studied to understand the signal shape and to identify variables to discriminate against the background. The analysis is exclusive, *i.e.* requires the total reconstruction of the $B\to$($\psi(2S) \to J/\psi\ \pi^0\ \pi^0$) K events. The two exclusive samples $B^0\to\psi(2S)K^0_S$ and $B^\pm\to\psi(2S)K^\pm$are described without distinction in the following, since they are characterized by the same kinematics, although the same procedures have been applied and the same results have been checked on both. Thus, unless specified, we will speak only about the signal $B \to \psi(2S)K$ sample and the pure $B \to \psi(2S)K$ sample.

4.3 Signal Definition

In this Section we carefully examine the predicted kinematic properties of the decay, as they are observed from Monte Carlo.

Studies on the Monte Carlo generated events report that only 70% of the π^0 s have both photons inside the EMC acceptance region, while 81% have both photons over the EMC energy threshold (30 MeV) and pass the total energy cut ($E_{\gamma\gamma} > 200\,\mathrm{MeV}$) used to select π^0 candidates. Combining these two limits, at least 55% of all the neutral pions are expected to be lost.

The energy substituted mass m_{ES} and ΔE have been introduced in Sec. 3.6 as useful variables to select B meson candidates. Their distributions are shown in Fig. 4.3 for the $B^{\pm} \to \psi(2S)K^{\pm}$ decay events from Monte Carlo: first the ΔE spectrum is presented, for events within $5.27 \le m_{ES} \le 5.29\,\mathrm{GeV}$ while in the second plot the m_{ES} distribution is visible for events within $--0.04 \le m_{ES} \le 0.03\,\mathrm{GeV}$. These ranges, which define the signal region, have been set studying the different signal and background distributions and applying on them an optimization method that will be discussed later (see Sec. 5.4). The scatter plot in the $(m_{ES}, \Delta E)$ plane, also presented in Fig. 4.3, shows the events clustering within this signal region.

We need to model the m_{ES} distribution in the most likely way in order to reduce the systematic error on the signal extraction, which, as already outlined, is performed through a fit on the m_{ES} spectrum. Using the Monte Carlo samples described above, the best parameterizations for the distributions of both the variables have been found, which are:

m_{ES} signal distribution is modeled by a Crystal Ball line-shape distribution [59], centerd at the nominal B mass value:

$$C(m\,; m_0, \sigma, \alpha, n) = \frac{1}{N} \cdot \begin{cases} \exp\left(-(m-m_0)^2/(2\sigma^2)\right) & , \; m > m_0 - \alpha\sigma \\ \dfrac{(n/\alpha)^n \, \exp(-\alpha^2/2)}{((m_0-m)/\sigma + n/\alpha - \alpha)^n} & , \; m \le m_0 - \alpha\sigma \end{cases}$$

where m_0 and σ are the Gaussian mean and resolution, α determines the crossover point from the Gaussian distribution to the power law tail distribution, in units of the peak width σ, and n is the exponent.

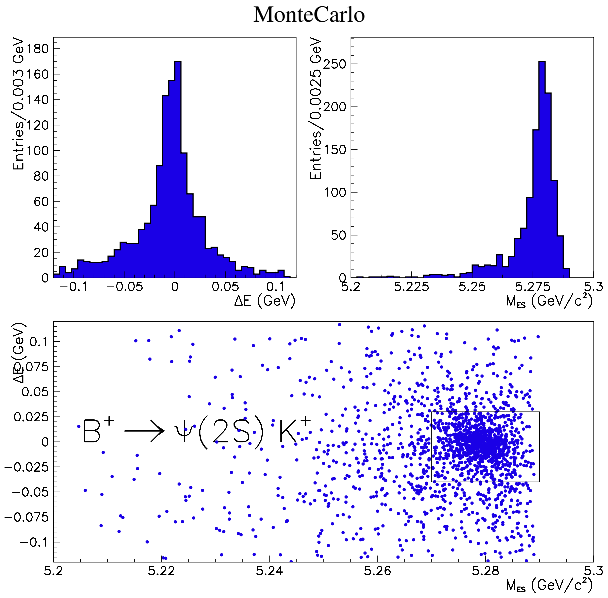

Figure 4.3: In the upper plots, distributions of m_{ES} and ΔE for all $B^{\pm}$ simulated events passing raw selection criteria. The lower scatter plot in the (m_{ES}, ΔE) plane shows the accumulation of events in the signal region, represented with a box. The ranges of the signal region are set with an optimization method, that will be described in Sec. 5.4.

Note that the parameter n is not necessarily integer, and lower values generate a longer tail. Typical values for α are 0.6–1.1, with $\alpha > 0$ because the tail is below the peak. The fit is performed on events surviving the chosen ΔE window cut and the resolution is typically 3 MeV/c^2.

ΔE distribution is parameterized with a narrow Crystall Ball distribution plus a wide gaussian. The width of the narrow component provides the ΔE resolution. The ΔE resolution is dominated by the π^0 energy resolution and the spread in the beam center-of-mass energy. The former component is the main subject of the next section, the latter is measured using $J/\psi\, K^+$ events, in which it is the dominant term and is found to be 4.2 MeV.

As already mentioned, one signal event can be mis-reconstructed because of a fake combination of the signal daughter particles. This combinatorial component generated by signal events is clearly visible in some signal distributions and are largely described in the following sections.

4.3.1 Selection of Unique B Candidates

With the B reconstruction tecnique described in Chapter 3, the final sample of events surviving the selection is a collection of B meson candidates.

On average, each event is characterized by about 5 reconstructed B meson candidates, but not all of them are kept in the subsequent analysis. After the selection about 10% of events still has more than one B candidate. After applying the selection criteria among all the surviving candidates, about 10% of events still has more than one B candidate. A unique B candidate per event is required by the sin2β measurement, and therefore this strategy is applied also in the branching ratio measurement. Note that the unique candidate is chosen among all the withstanding candidates after all the cuts are applied.

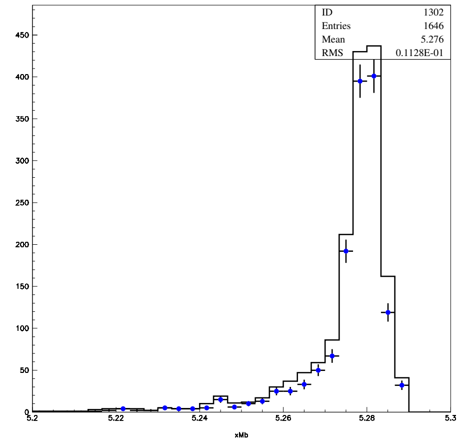

Figure 4.4: Best candidate selection

m_{ES} distributions for events passing the selection in the signal Monte Carlo neutral B sample: histogram is for all the B candidates, dots are for the best candidate (minimum ΔE) in the event only.

The unique B candidate is chosen in the following way: if more than two candidates are found in the signal region, the one with the smallest absolute ΔE value is chosen. The best candidate selection effect is visible in Fig. 4.4.

Other approaches were tried, such as selections based on χ^2 variables based on the reconstructed masses, but resulted in a further reduction of the efficiency. When combinatoric background is a great component, as in this analysis, using the π^0s mass in a chi-squared variable is useless, since the π^0 mass distribution is almost flat and there is a non zero probability to pick up some background. Adding the ψ(2S) mass in the chi-square is a too small

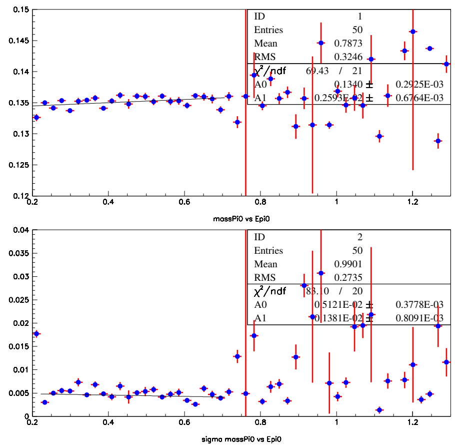

Figure 4.5: The π^0 mass central value (upper plot) and resolution (lower plot) as a function of the pion energy, extracted from Monte Carlo by fitting the π^0 mass distributions with a Crystal Ball plus a linear background. Energies are measured in GeV and masses in GeV/c^2.

constraint, since using this criterion a 20% efficiency reduction was obeved with respect to the minimum ΔE approach, without a visible decrease of the m_{ES} tail.

Concerning the study of the best variable to use, the π^0 mass resolution at different energies has been studied, in order to see whether we could improve the χ^2 variable significance adding an energy dependent error. The results from this study are shown in Fig. 4.5 in which a 5 MeV resolution on the π^0 mass is visible, in the energy range of interest.

4.4 Internal Combinatorial Background

While the J/ψ resonance has a very clear signal (as in Fig. 4.6), the reconstruction of two neutral pions can create fake candidates due to random combinations of photons. This combinatorial contribution may have different sources and different selection criteria are applied to reduce the wrong combinations and enhance the purity of the sample:

- a selection based on the π^0 mass spectrum ($m_{\pi^0} \leq 144\,\text{MeV/c}^2$), and
- a selection based on the $M_{\pi\pi}$ mass spectrum ($0.45 < M_{\pi\pi} < 0.59\,\text{MeV/c}^2$).

Typical photon energy is very close to the EMC reconstruction threshold (30 MeV), so that one photon can escape detection and be mimicked by

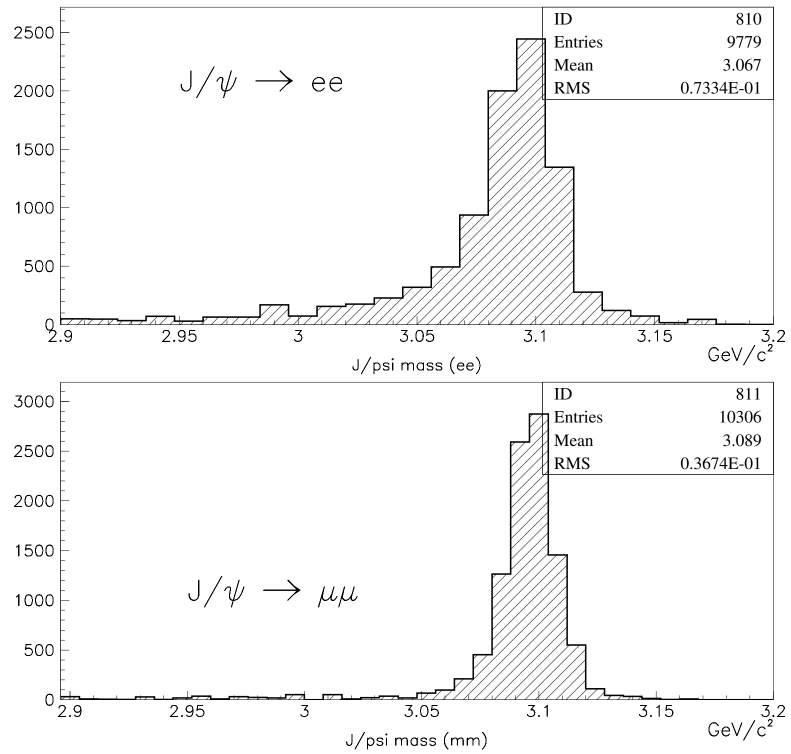

Figure 4.6: J/ψ mass distributions reconstructed in the two modes $J/\psi \to e^+e^-$ and $J/\psi \to \mu^+\mu^-$ as extractected from the Monte Carlo sample.

spurious energy in the detector (like photons from machine background or from the other B decays). Events in this class show a $\gamma\gamma$ invariant mass

$$M_{\gamma\gamma} = \sqrt{2 \cdot E_1 \cdot E_2 \cdot (1 - \cos\theta_{\gamma\gamma})} \tag{4.2}$$

greater than the expected one, because of the additional energy contribution from the fake photons. This effect is visible mostly when the π^0 decay is very asymmetric, *i.e.* the two photons have very different energy in the laboratory frame. Due to the little available energy, the most asymmetric decays are not reconstructed.

Because of the boost, the larger open angles between the two photons correspond in the laboratory to a bigger energy difference. If we define the π^0 helicity angle θ^* as the photon decay angle in the π^0 rest frame with respect to the π^0 lab momentum and look at the $|\cos\theta^*|$ distribution, like in figure 4.7(right), we see that the events having $|\cos\theta^*|$ close to 1 are missing because they are not reconstructed. We can also observe that the combinatorics tend to accumulated in the right end side of the reconstructed interval.

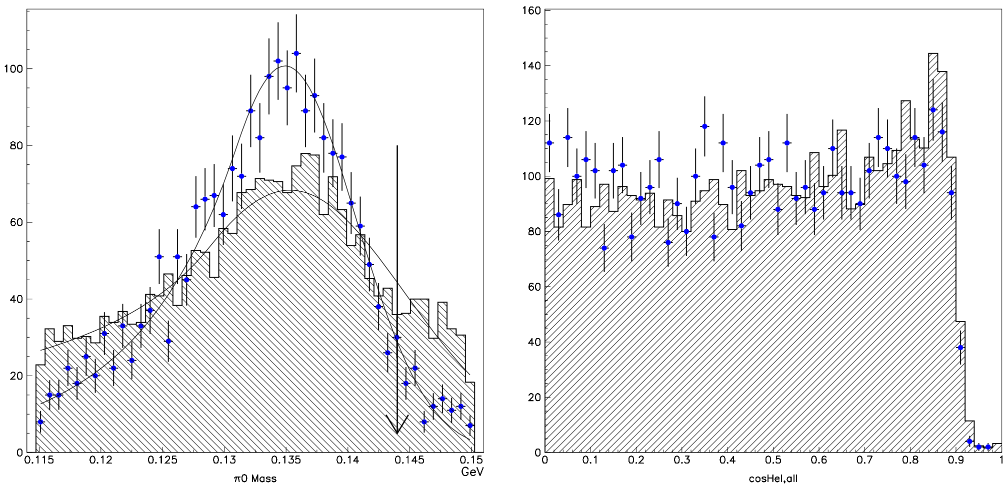

Figure 4.7: Distributions from Monte Carlo samples. Left: Mass distribution of neutral pions, as obtained after the kinematic fit at the J/ψ vertex. Results from the signal B sample (hatched histogram) and the B pure sample (dots) are shown, with superimposed Crystal Ball function fits. Also the cut applied to the selection is shown. Right: π^0 s helicity distribution. Results from two samples are shown: neutral B (solid-plain) and neutral pure B (dots).

Fig. 4.7(left) shows, from simulated events, the two photon invariant mass of each pairing combination passing the π^0 selection criteria, with the constraint of the J/ψ vertex as their origine. The same distribution is shown for both the signal and the pure Monte Carlo samples. Any difference between these two, clearly visible at the higher invariant mass limit, is a combinatorial contribution, which is not present when the reconstructed neutral pions are those from the pure sample, *i.e.* when the other B meson coming from the $\Upsilon(4S) \rightarrow B\overline{B}$ decay cannot be detected at all. To minimize the number of misreconstructed pions, a tighter cut on m_{π^0} is applied, refusing candidates with $m_{\pi^0} \geq 144\,\mathrm{MeV/c^2}$.

In Figure 4.8, where the $M_{\pi\pi}$ spectrum is shown for both the signal and the pure samples, the energy leakage in the calorimeter is visible in the low energy tail of the spectrum. The comparison between the signal and the pure samples gives us again more information. The badly reconstructed events appearing outside the kinematic allowed $M_{\pi\pi}$ region are due to small

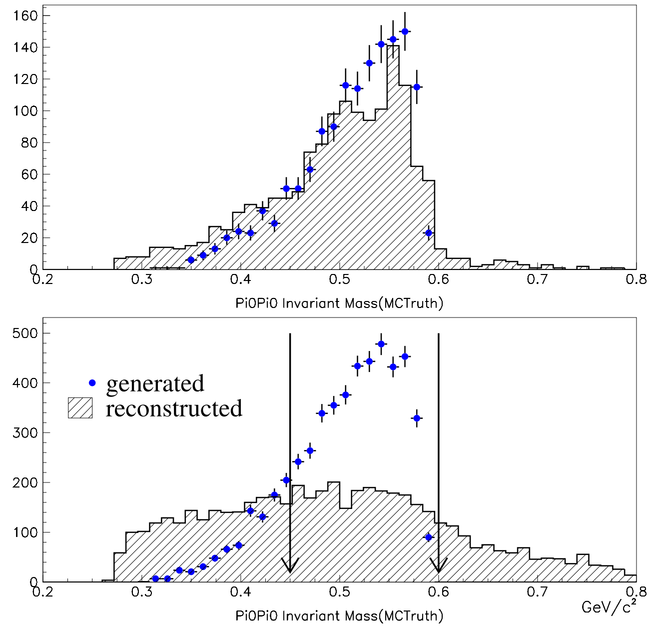

Figure 4.8: The dipion invariant mass $M_{\pi\pi}$ for reconstructed events (dashed histogram) and their correspondently generated ones (dots), for the two samples: the pure B sample (top) and the signal B sample (bottom). Also the selected cut window is shown.

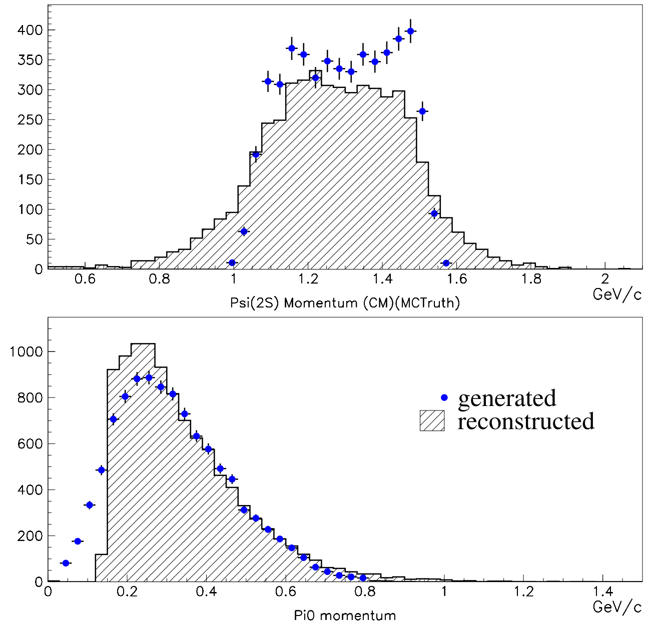

Figure 4.9: Momentum distributions in the laboratory frame from the Monte Carlo signal sample: for ψ(2S) mesons (upper plot) and for neutral pions (lower plot), both the generated (dots) and reconstructed (dashed area) events are shown.

probability of photons overlap and wrong combinations, for two different reasons. First, the four photons from the $\psi(2S) \rightarrow J/\psi\,\pi^0\pi^0$ decay have very comparable energy because of the low total available energy ($\sim 600\,\mathrm{MeV}$) and can be easly combined in the wrong way. Second, photons from background, both from beam background and from the rest of the event, are boosted forward and thus tend to overlap to the photons from the decay. Hence on average the reconstructed angle between the two pions decreases because of background. This affects the reconstructed dipion invariant mass

$$M_{\pi\pi} = \sqrt{m_{1\pi^0}^2 + m_{2\pi^0}^2 + 2 \cdot E_1 \cdot E_2 \cdot (1 - \beta_1\beta_2 \cdot \cos\theta_{\pi\pi})} \tag{4.3}$$

where $\beta_i = p_i/E_i$ and $\theta_{\pi\pi}$ is the angle between the two pions. Then, as $M_{\pi\pi}$ approaches its lower kinematic limit, an increasing overlap probability between photons from different pions is experienced. Since events with the smallest angular separation between the four photons are in the low part of the spectrum, here the big part of the background combinatorics is present. A tight cut is imposed to the dipion invariant mass in order to eliminate this component from the signal, considering only events in the $M_{\pi\pi}$ range (0.45 ; 0.59) $\mathrm{MeV/c^2}$.

Other kinematic variables have been studied, like the $\psi(2S)$ and the π^0s momenta calculated in their rest frames respectively, but are left off the selection requirements. Their distribution are shown in Fig. 4.9.

The momentum spectrum of the neutral pions peaks close to its minimum detectable value, at $\approx 250\,\mathrm{MeV}$, and then additional cuts on this variable could lead to eccessive efficiency reduction. As expected at this low energy, no contamination from hadronic showers is present and all π^0 s are resolved, that is to say that the two costituent photons form two distinct bumps.

The background rejection is achieved in such a way as to avoid using observables either with a high degree of mutual correlation, or potentially leading to implicit cuts on B meson kinematic quantities. Hence even if the kinematics of the $B \rightarrow \psi(2S)K$ decay constraints the $\psi(2S)$ momentum p^* calculated in the B rest frame to a limited range, it is strongly correlated with ΔE and $m_{ES}$and a p^* cut modifies the expected shape of the background without increasing the signal over background ratio. So in this analysis no p^* cut is applied in order not to include any bias.

4.4.1 Residual Combinatorics Description

The combinatorial component can be only partially removed by the *ad-hoc* selections on the invariant masses we have chosen. As visible in Fig. 4.10,

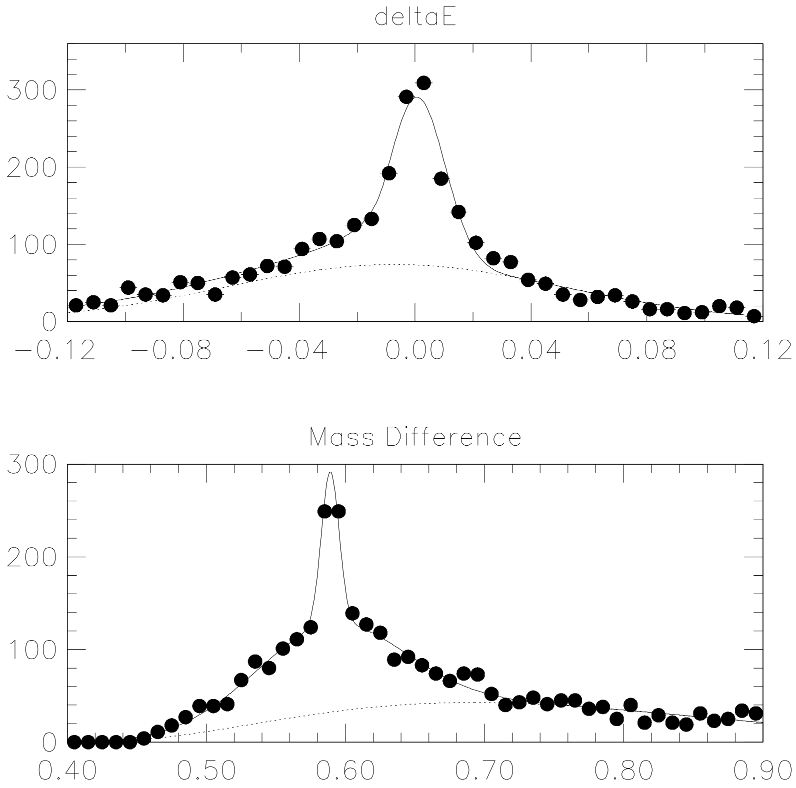

Figure 4.10: Distributions of ΔE (top plot) and of $(M_{\psi(2S)} - M_{J/\psi})$ (bottom plot) of Monte Carlo events, passing the selection described above, with fit functions superimposed.

the signal Monte Carlo events surviving the selection show two clear components in both the ΔE distribution and the invariant mass difference $\Delta M = M_{\psi(2S)} - M_{J/\psi}$ [2]. The narrow peak is due to well reconstructed B mesons, while the broader component is originated by combinatorics. Unfortunately they mostly peak in the same region. It's also to be noticed that the combinatoric components in the two variables are not corresponding to the same events. Because of this uncorrelation, one can select the events studying the two variables separately, addressing the requirement of either bigger efficiency or best signal over backgroun ratio. Here the main characteristics of the signal Monte Carlo events, primarly due to the residual combinatorial fake candidates, are analized and the ΔE and ΔM distributions described.

[2]This variable is usually considered in order to minimize the impact of the J/ψ candidate mass resolution, particularly bad in the $J/\psi \to e^+e^-$ channel because of bremsstrahlung. In this analysis, the J/ψ mass is constrained to its PDG value, so this contribution is subtracted *a priori*.

The selection criteria involving these variables will be described later, in Sec. 5.4.2.

Mass Resolution

The best Probability Distribution Function (PDF) parameterization for the ΔM distribution is a double gaussian plus a threshold function with the form:

$$D(m\,; m_0, c_1, c_2, a) = (m - m_0)^a \cdot \exp^{\left[c_1(m-m_0)+c_2(m-m_0)^2\right]} \cdot \theta(m > m_0) \quad (4.4)$$

which well describes the background distribution for a mass (or mass difference) spectrum near a threshold. This description is used in Fig. 4.10. The parameter m_0 is the kinematic threshold, and is equal to the minimum allowed dipion invariant mass, in this case $0.45\,\mathrm{GeV/c^2}$. Gaussian central values are fixed at the expected mass difference value ($589\,\mathrm{MeV/c^2}$) while the fitted value for the two sigmas are $\sigma_1 = 6.2{\pm}1.0\,\mathrm{MeV/c^2}$ and $\sigma_2 = 53.8{\pm}1.8\,\mathrm{MeV/c^2}$.

Energy Resolution

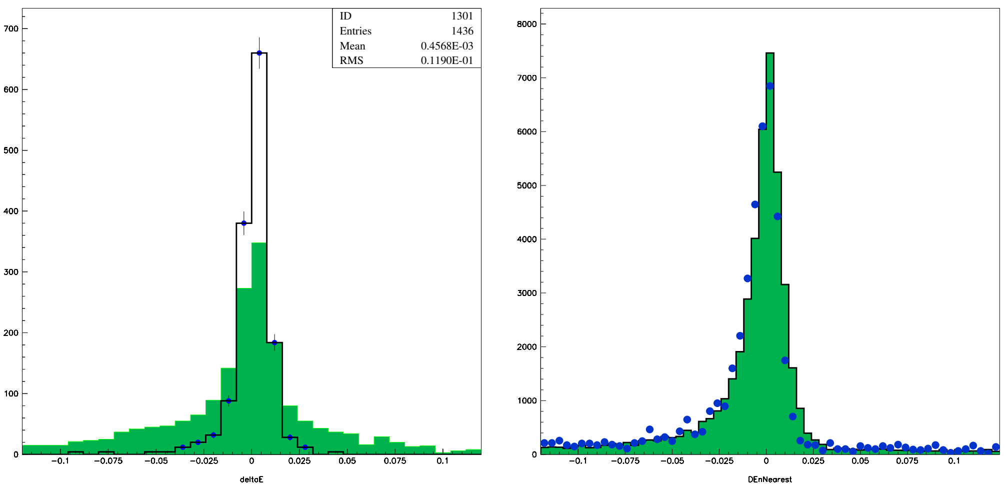

Figure 4.11: Left: ΔE distributions for the pure B sample (solid-empty) and the signal sample (solid-plain). Right: $E_{rec} - E_{gen}$ for all the generated photons associated with a reconstructed one as explained in the text: note the small shift between the pure sample (dots) and the signal sample (solid-plain).

Looking at Monte Carlo events, the ΔE distribution can be well described by a Crystall Ball function plus a gaussian, as already stated. The

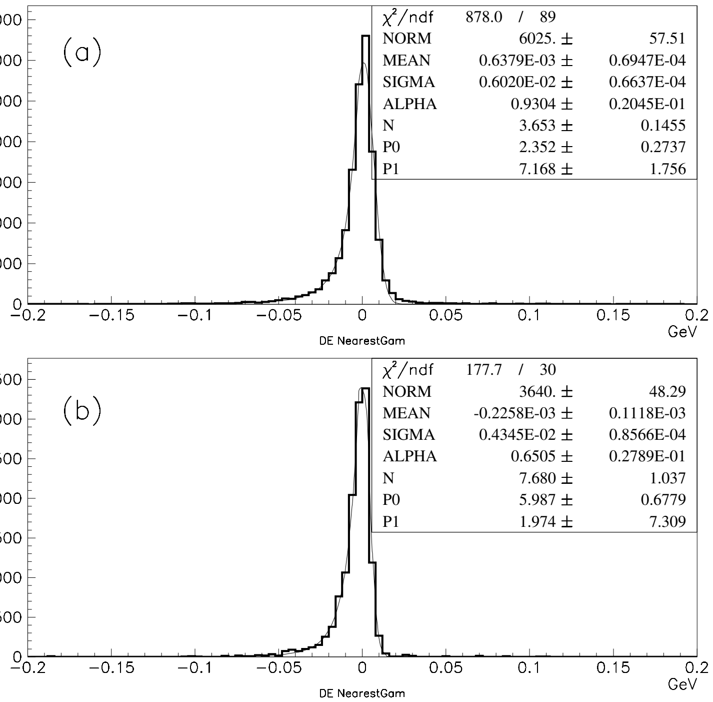

Figure 4.12: $E_{rec} - E_{gen}$ for all the generated photons associated with a reconstructed one as explained in the text, with a Crystal Ball fit superimposed, for a) the generic signal B sample and b) the pure sample.

expected energy resolution on B mesons, determined by fitting the ΔE spectrum from simulation, is highly correlated with the energy resolution of the reconstructed daughters, and the π^0 s above all. To understand how the double component in the ΔE spectrum arises, as visible in Fig. 4.11(left), one can have a look at the reconstructed and the generated energies of the π^0's in the laboratory frame, and make a comparison between the two cases: the signal B meson sample and pure B meson sample, defined in the previous sections. Combinatorial background is responsible for the wider component in the ΔE spectrum of the reconstructed B's. This contribution is clearly expected to increase the resolution, but also a small energy shift is visible when comparing the two samples, as described in the following.

A very simple association between the generated and the reconstructed photons was used. For each generated photon of energy E_{gen}, a reconstructed one with energy E_{rec} is associated if it lays at the minimum angular distance from the former one, within a cone of 50 mr . The $E_{rec} - E_{gen}$ distributions, shown in Figure 4.11(right), peaks at zero and shows a left tail from the π^0

leakage, as expected. When fitting the two Monte Carlo samples $E_{rec} - E_{gen}$ distributions to a Crystal Ball function, as in Fig. 4.12, two types of information can be extracted. Firstly, when passing from the pure sample to the signal one, a small increase in the width, *i.e.* in the energy resolution, is visible, confirming that the multeplicity of the event is the main source of resolution loss. Secondly, the peak value is slightly shifted towards higher values proving that with the additional combinatorics from the other not-reconstructed B some changes in the reconstructed photons energy occur, such as superposition of clusters or picking up some remaining soft background gammas. As a consequence, a change in the reconstructed B's energy moves these events from the ΔE peak region to the tails.

This study was performed in order to understand the abundantly populated wide tails arising in the ΔE spectrum from signal Monte Carlo events. I made use of a rough association between generated and reconstructed events in order to identify the source of these faking component, which was found to be the change in the reconstructed photon energy due to additional spurious clusters in the calorimeter.

4.5 Angular Distributions

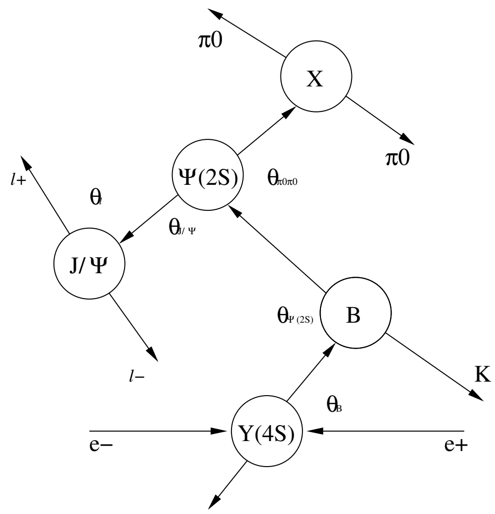

Figure 4.13: Helicity angles for the decay Υ(4S)$\rightarrow B\overline{B}\rightarrow\psi$(2S)+K (with ψ(2S)$\rightarrow J/\psi\,\pi^0\pi^0$ and $J/\psi\rightarrow e^+e^-$or $\mu^+\mu^-$).

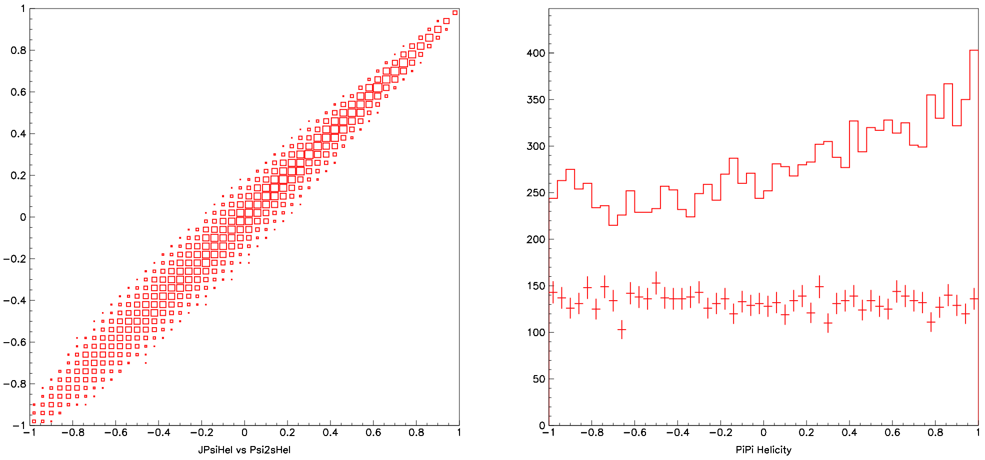

Figure 4.14: Left: Correlation between $\psi(2S)$ and J/ψ helicity from the generated signal Monte Carlo events. Righ: Angle between the kaon and the π^0s in the $\psi(2S)$ rest frame. It's flat for generated events (point) because $\vec{L} = \vec{l} = 0$, while reconstructed events have a slight aboundance at $\cos\theta_{\pi^0\pi^0} = 1$.

Angular distributions are also used within the selection. The relevant angles involved in the decay are shown in Figure 4.13. They are constraints for the signal events, and therefore they are clearly useful tools for rejecting background from generic events. Even less powerfully, they are also used to reject misreconstructed B mesons from signal events. Angular distributions for signal and generic background events as extracted from Monte Carlo sample are shown in Fig. 4.15.

4.5.1 $\psi(2S)$ Meson Helicity

As discussed in the previous sections, we can have information of the $\psi(2S)$ polarization from the angles of the leptons coming from the J/ψ decay. Indeed the small value of M_{021}/M_{001} and M_{201}/M_{001} confirms that the J/ψ and the $\pi^0\pi^0$ pair create an almost pure (0.04%) $L = 0$ system, while the two π^0s have a 83% $l = 0$ component. Thus, using the terminology described at the beginning of the Chapter, since $\vec{s}' = \vec{s} + \vec{l} + \vec{L}$ the $\psi(2S)$ and J/ψ mesons have the same helicity ($|S_{\psi(2S)} = S_{J/\psi} = 1, 0\rangle$) at 90% level, or, in other words, the J/ψ and $\psi(2S)$ rest frames are almost coincident. This is obviously true in our Monte Carlo sample, where $\vec{l} = \vec{L} = 0$. In Fig. 4.14 the kaon-lepton angle is shown, as calculated both in the J/ψ and in the $\psi(2S)$ rest frame for the generated events.

Let's now describe the expected $\psi(2S)$ polarization. The $B \to \psi(2S)K$ decay is a $S \to VS$ decay. In order to preserve the total angular momentum $\vec{J} = \vec{L'} + \vec{s'} = 0$ in the B rest frame $\psi(2S)$ has a transverse polarization. If we translate to the $\psi(2S)$ rest-frame, this is equivalent to say that $s'_z = 0$ if z is the direction of the B meson (or equally of the kaon) in this frame.

Considering the decay $J/\psi \to \ell^+\ell^-$, the system has $\vec{J} = \vec{L}_l + \vec{S}_l = 1$ and $P = -1$ in the J/ψ rest frame. The final state can only have even values of L_l, because of parity conservation (the opposite intrinsic parity of the two leptons are added), so $L_l = 0, 2$ are both good values for the angular momentum of the two leptons system. We can set the lepton direction as the z axis, so that the dilepton state can be: $|J_l = 1, \pm 1\rangle$ or $|J_l = 1, 0\rangle$ and the the J/ψ state $|S_{J/\psi} = 1, 0\rangle$ can be written as:

$$-\frac{1}{\sqrt{2}} \sin\theta_l \, |J_l = 1, +1\rangle + \cos\theta_l \, |J_l = 1, +0\rangle + \frac{1}{\sqrt{2}} \sin\theta_l \, |J_l = 1, -1\rangle$$

QED vertex only allows leptons with opposite helicity, so the $|J_l = 1, 0\rangle$ is forbidden. This results to $dN/\cos\theta_l$ distribution proportional to $\sin^2\theta_l$ where θ_l is the angle between the J/ψ direction and that of the (positive) charged lepton in the J/ψ rest-frame. Due to the previous statements, this $\sin^2\theta_l$ dependence must be also visible if the same angle is calculated in the $\psi(2S)$ rest-frame. Then the distribution of the $\theta_{\psi(2S)}$ angle is shown in Fig.4.15 where signal and background components from Monte Carlo are shown. This variable will be used to select the sample, following the prescription described in Section 5.4.1.

4.5.2 B Meson Helicity

In the electromagnetic process $e^+e^- \to \Upsilon(4S)$ the two light leptons can only have opposite helicity, so the vector meson $\Upsilon(4S)$ is produced with a longitudinal polarization, $J_z = \pm 1$. In the $e^+e^- \to \Upsilon(4S) \to B\overline{B}$ process, this is inherited by the $B\overline{B}$ system so that the pseudo-scalar B meson can be both $|1, \pm 1\rangle$ states and its decay angle θ_B can be distributed as:

$$\frac{dN}{d\cos\theta_B} \propto \left|Y_1^1(\theta_B, \phi_B)\right|^2 + \left|Y_1^{-1}(\theta_B, \phi_B)\right|^2 \propto \sin^2\theta_B \tag{4.5}$$

On the contrary fake B candidates coming from continuum background don't show this behaviour, and the dstribution is roughly flat: strictly speaking, the quark jets follow the $1 + \cos^2\theta$ distribution, but this angular dependence is not reflected in the randomly formed B candidates. Thus this variable can be used to extract the $B\overline{B}$ events cutting the continuum light quarks component.

4.5.3 More Angular Distributions

More angular distributions can be observed from both generated and reconstructed events to test the reconstruction alghoritm and possible contribution from combinatorics. For example, if $\vec{L} = 0$ and $\vec{l} = 0$, then the distribution of the angle between the kaon and the π^0s in the $\psi(2S)$ rest frame, must be flat: in Fig. 4.14(right) this distribution is shown for reconstructed events and their corresponding generated ones. The former are more abundant in the $\cos\theta_{\pi^0\pi^0} = 1$ region where random π^0s are present because of the boost. The same happens for the π^0 helicity as described in section 4.4.

4.6 The Event Shape Variables

Typically channels of interest in *BABAR* have very small branching ratios, so many tools have been developed for generic background suppression. They are built in order to select $e^+e^- \to \Upsilon(4S) \to B\overline{B}$ events which have a characteristic shape. Therefore they are referred as event shape variables. In spite of this, they are also good discriminant variables against the signal internal background, since B mesons of this category are not well reconstructed so as they might not satisfy the event shape constraints.

Many events shape variables exist (most of them highly correlated), that can be used to distinguish $e^+e^- \to \Upsilon(4S) \to B\overline{B} \to \psi(2S)$K decays from the events not forming the $\Upsilon(4S)$ and involving primarily light quarks (u, d, s) and *charm* quark pairs. Their production rates are reported in Table 2.1. Because of the small B momentum in the centre-of-mass frame, the $B\overline{B}$ events are isotropically distributed whereas the continuum background is typically jet-like, with a strongly preferred direction characterizing the whole event and the B candidate itself. In $c\overline{c}$ event the jet structure is less pronounced, so these tools are less powerful in subtracting them.

All the variables used in this analysis in order to increase the purity of the sample are summarized in Tab. 4.4. One of them is the Fox-Wolfram moment R_2 already introduced in Section 3.2. A second powerful shape variable has been analyzed in this analysis, the *Thrust angle*. The thrust [74] is the axis along which the sum of the transverse momenta of a group of particles is minimised. In other words, it's the versor $\hat{T}$ along which the event maximally alignes, maximizing the variable:

$$T = \frac{\sum_i \left|\hat{T} \cdot \vec{p}_i\right|}{\sum_i |\vec{p}_i|} \tag{4.6}$$

Variable	Definition
$\cos\theta_B$	cosine of the angle between the B candidate and the z axis in CM frame
$\cos\theta_{\mathrm{Thrust}}$	cosine of the angle between the signal thrust axis and the z axis in CM frame
R_2	normalized 2nd order Fox-Wolfram moment
$\cos\theta_{\psi(2\mathrm{S})}$	cosine of the angle between the kaon candidate and the positive charged lepton in the $\psi(2\mathrm{S})$ rest-frame

Table 4.4: Continuum suppression variable definitions.

where $\vec{p}_i$ are calculated in the center of mass frame. It varies from 0.5 for isotropic events to 1 for extremely directional ones. The Thrust angle is defined as the angle between the thrust of the reconstructed B (of all the particles used to make it) and the thrust of the rest of the event. The $B\overline{B}$ events isotropy leads to a uniform thrust angle distribution while the continuum jet-like background tends to have a thrust angle peaked at π radiants in the center-of-mass frame.

In figure 4.15 one can see the signal and background distribution of all the shape variables and the angular distributions studied in this analysis. The second Fox-Wolfram moment R2 and the Thrust angle are highly correlated, as it's shown in Fig. 4.16 for both signal and background events. Background is mostly concentrated in a small region $\cos\theta_{Thrust} > 0.9$ and $R2 > 0.25$. Also from the signal an excess of events is present in that region, probably due to fake combinatorics. They are also correlated to the angular distributions because they both reject the same continuum component. Figure 4.17 shows the $\cos\theta^*_B$ correlations with $\psi(2\mathrm{S})$ helicity and the Thrust angle for both signal and background.

When all these variable are studied on signal Monte Carlo, they also appeared as useful tools to remove the internal combinatoric background. This latter is mostly concentrated at high value of R2 and $\cos\theta_{Thrust}$ like the events from continuum. We also noted that the surviving internal combinatorics originate the wide gaussian component in the ΔM spectrum, under the signal peak. Then, counting the events under the ΔM broad gaussian, we can measure its contribution with different cuts on R2, θ^*_B and θ_{Thrust} variables. The combination of cuts that reduces the combinatorial component is choosen. The integration of the fit shape over the allowed window gives the results shown in Table 4.5 for some reasonable cuts. The values are referred to the ratio of the area of the narrow gaussian peaking component

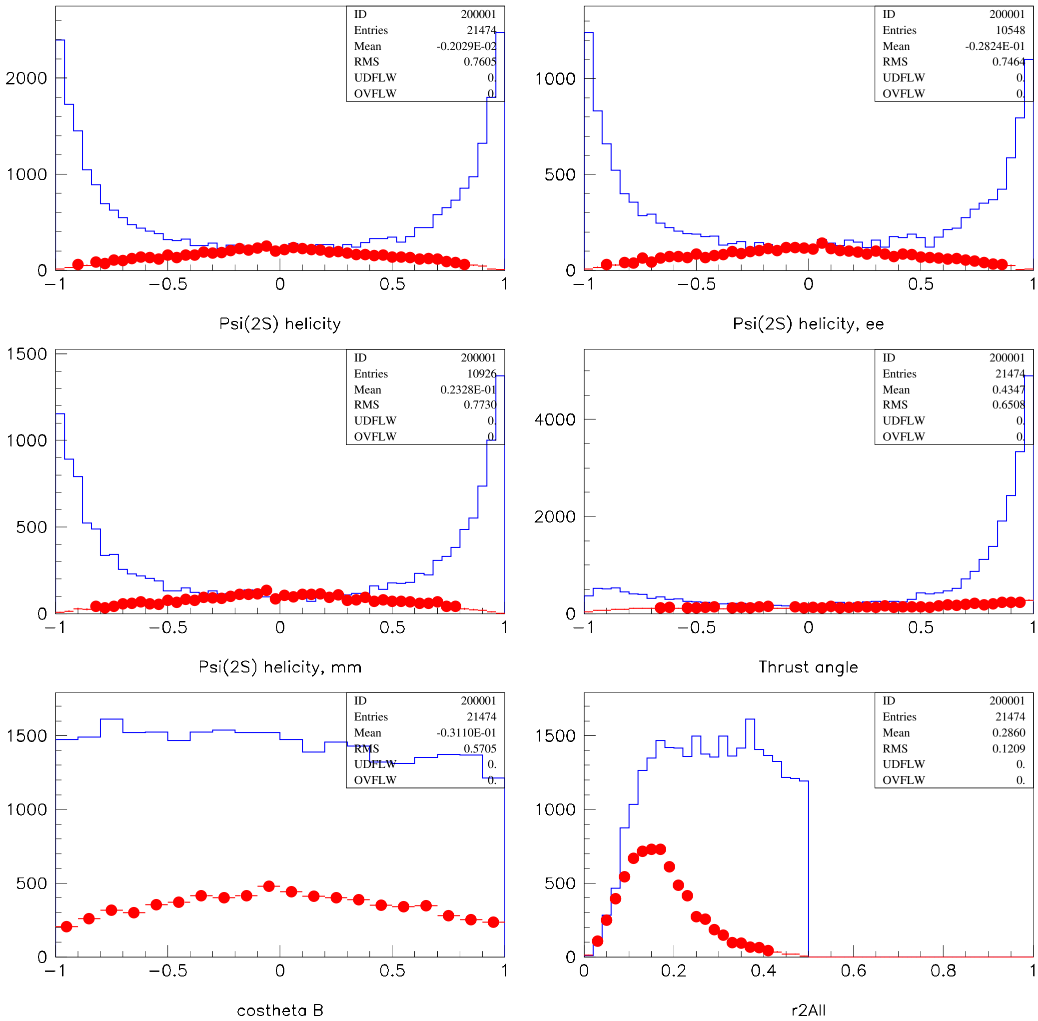

Figure 4.15: Some variables used to separate signal (red dots) from continuum+generic$B\overline{B}$ background (blue line). From the top left: ψ(2S) helicity, ψ(2S) helicity for $J/\psi \rightarrow e^+e^-$, ψ(2S) helicity for $J/\psi \rightarrow \mu^+\mu^-$, Thrust angle, B meson helicity, R2 (second F-W moment). All distribution are normalized to the same integrated luminosity.

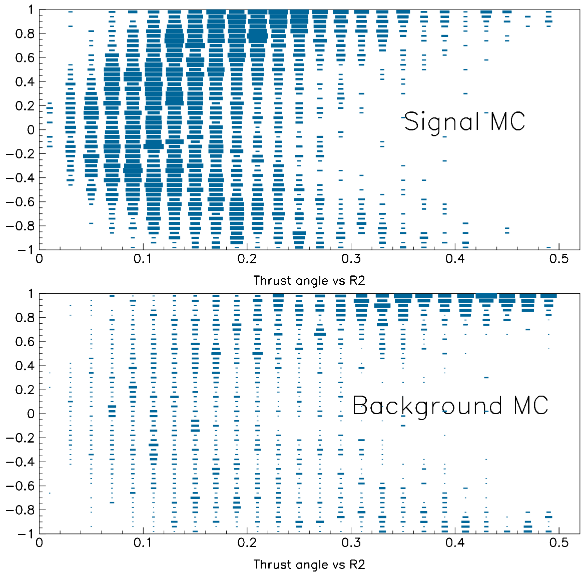

Figure 4.16: Correlation between R2 and Thrust angle in signal and background Monte Carlo samples.

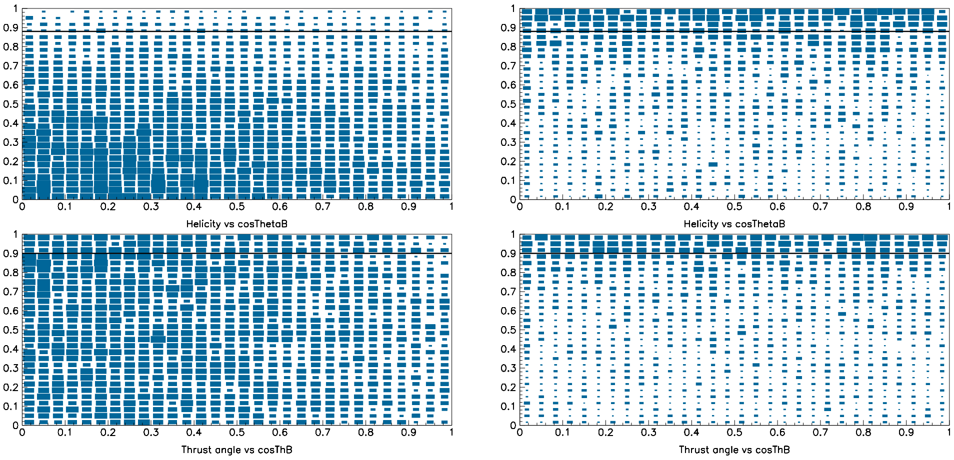

Figure 4.17: $\cos\theta^*_B$ correlations with $\psi(2S)$ helicity and Thrust angle in signal (left plots) and background (right plots) Monte Carlo samples.

to the wider one in the signal mass spectrum (see Fig. 4.10).

	R2< 0.5	R2< 0.25	$\cos\theta^*_B < 0.95$	$\cos\theta^*_B < 0.9$
$\cos\theta_T < 1.$	0.54	0.55	0.55	0.55
$\cos\theta_T < 0.9$	0.66	0.61	0.58	0.58
$\cos\theta_T < 0.8$	0.60	0.55	0.59	0.59

Table 4.5: Relative peaking component in the ΔM spectrum with different cuts on Thrust angle, $\cos\theta^*_B$ and R2. Cut on $\cos\theta^*_B$ has no effect on the combinatorial rejection, while R2 cut affects the peak component.

The results are:

- the $\cos\theta^*_B$ has no effect on the background rejection;
- the cut on R2 worsens the purity of the sample;
- the single cut on the Thrust angle $\cos\theta_T < 0.9$ gives the highest purity on the signal, and is applied.

The selection $\cos\theta_T < 0.9$ is choosen in order to reduce the internal combinatoric on the signal Monte Carlo. This cut is also optimal to reduce the continuum that mostly peaks in this region.

Chapter 5

Measurement of Branching Ratios

While the aim of this work is to confirm the possibility to increase the sample of events $B^0 \to \psi(2S) K^0_S$ for the $\sin 2\beta$ measurement using the selection of the $\psi(2S)$ meson through its decay $\psi(2S) \to J/\psi\, \pi^0 \pi^0$, the measurement of the Branching Ratios for the $B^0 \to \psi(2S) K^0_S$ and $B^{\pm} \to \psi(2S) K^{\pm}$ decays, described in this chapter, is meant to be a consistency check of the event selection procedure. The general criterion adopted in the analysis arises from a compromise between a good sensitivity to the measure and a high purity of the sample. Thus in order to obtain the suitable purity for the $\sin 2\beta$ measurement, the efficiency of the $\psi(2S) \to J/\psi\, \pi^0 \pi^0$ selection turns out to be quite low.

The Branching Ratio measurement also requires the knowledge of the number of $B\overline{B}$ events from which the $B \to \psi(2S)$K signal is selected, and the efficiency of the selection, which is evaluated from Monte Carlo. These measurements are described in this chapter, along with that of the signal yield and the study of the expected background composition of the sample, also important for the CP asymmetry extrapolation.

5.1 Analysis Outline

Since the $B^0 \to \psi(2S) K^0_S$ signal, selected with the $\psi(2S) \to J/\psi\, \pi^0 \pi^0$ mode, is expected to be small, the tecnique of the "blind analysis" is a good method to avoid biases in the event selection. As a matter of fact, optimizing the event selection criteria by looking at the signal region in data, may bring to enhancing a statistical fluctuation, while in this approach the signal region in data is kept hidden until all of the selection criteria have been finalized and fixed.

All the selection criteria are tuned on simulated data, while in order to verify that they adequately reproduce the real data, I compare the efficiencies of various selection criteria and the shapes of kinematic distributions in both simulated data and the ΔE sidebands data, a sub-sample excluded from the final measurement. As far as the Monte Carlo studies and the tuning of the cut selection are concerned, the charged channel has been used and then firstly unblinded. Then the same selections are applied to the neutral one, that is expected to have a lower statistics. Thus in the following, all the results shown on Monte Carlo are referred to $B^{\pm} \to \psi(2S) K^{\pm}$ events, unless esplicitely declared.

The analysis can be outlined as follows:

- optimize the analysis cuts by maximizing the sensitivity $\frac{N_S}{\sqrt{N_S+N_B}}$, where N_S and N_B are the number of selected signal and background events respectively. When the sensitivity to a particular cut exhibits a broad plateau, the cut value is chosen so as to optimize the signal purity;

- predict the expected signal and background rates in the signal box and measure the signal efficiency from Monte Carlo data samples;

- verify the consistency of background estimates derived separately from on-resonance data sidebands and generic Monte Carlo events;

- unblind the $B^{\pm}$ channel applying the defined cuts to full on-resonance data set. If the observed signal yield is in good agreement with the predictions, then apply the same selection to the B^0 sample and measure the corresponding signal yields;

- count the $B\overline{B}$ events in the available data sample and perform the branching ratio measurements;

- apply the correction to the measured yields accounting for the data/Monte Carlo differences in evaluating the branching ratios of each decay mode.

5.2 Data samples

The data sets used in this analysis were recorded with the *BABAR* detector in the period October 1999-October 2001. The total integrated luminosity of the on-peak data set is equivalent to 44.7 fb^{-1} collected at the $\Upsilon(4S)$ resonance.

The data are divided into two subsamples, also summarized in Table 5.1:

1. 'Run1' data set, including data collected in 1999-2000, about $20.3\,\mathrm{fb}^{-1}$. These data are divided into two blocks according to the drift chamber high voltage, which was raised from 1900 V to 1960 V approximately in the middle of the run. Table 5.1 lists the integrated luminosities per block.

2. 'Run2' data set, including data recordered in 2001, about $24.4\,\mathrm{fb}^{-1}$. This is the available subsample of the 2001 *BABAR* data.

Data set	$\mathcal{L}dt$ (fb^{-1})	
Run1		20.3
Block 1 (DCH HV=1900 V)	11.1	
Block 2 (DCH HV=1960 V)	9.2	
Run2		24.4
Total		44.7

Table 5.1: The structure of the 1999-2001 available on-peak data sample. Roughly half of the Run1 data was taken with the high voltage (HV) of the drift chamber set at 1900 V, and the other half, with the voltage raised to 1960 V. Run2 sample includes data recordered until October 2001.

The two data set differ primarily in the quality of the SVT alignment and more modestly on DCH track-finding efficiency. Since up to the time in which this analysis was performed, the systematic studies on the Run2 data set have not been completed, all the systematic errors on the Branching Ratio measurements are referred to the quality of Run1 data only.

A fraction of the data, referred as *off-peak* data, was taken slightly below the peak of the $\Upsilon(4S)$ resonance, providing a sample of continuum data ($e^+e^- \to q\overline{q}$, where $q = u, d, s$ or c).

Only good runs, as flagged by the *BABAR* data quality processing, are in the analysis. The main criteria for the goodness of run are the status and performance of all subdetectors, as well as the total luminosity of the run.

5.2.1 B counting

Measurements of Branching Ratios require a precise knowledge of the number of $B\overline{B}$ events in the data sample that is used for the Branching Ratio analysis. Instead of measuring the integrated luminosity and the total $B\overline{B}$ cross section at the $\Upsilon(4S)$ peak, we can count directly $\Upsilon(4S)$ decays. To this aim the hadronic event selection criteria are applied to both on-resonance and off-resonance data sets, with the assumption that the increase in the ratio of hadronic events to muon pairs between on and off resonance running is due to $\Upsilon(4S)$ production. The number of $\Upsilon(4S)$ mesons satisfying the criteria is therefore given by:

$$N_{\Upsilon} = N_{\mathrm{MH}} - N_{\mu\mu} \cdot R_{\mathrm{off}} \cdot \kappa, \tag{5.1}$$

where

$\boldsymbol{N_{\mathrm{MH}}}$ is the number of hadronic events satisfying the selection criteria in the on-resonance sample;

$\boldsymbol{N_{\mu\mu}}$ is the number of muon pairs selected in the on-resonance sample;

$\boldsymbol{R_{\mathrm{off}}}$ is $N^{\mathrm{off}}_{\mathrm{MH}}/N^{\mathrm{off}}_{\mu\mu}$, the ratio of hadronic events to muon pairs in the appropriate off-resonance sample;

$\boldsymbol{\kappa}$ is a factor, close to 1, that takes into account the dependence of cross-section on the center of mass energy and also possible variations of efficiencies.

The hadronic selection is described in Sec. 3.2 and is based on requirements of Table 3.3 that enhance $B\overline{B}$ events relatively to non-$\Upsilon(4S)$ hadronic decays.

In a data set the total number of *produced* $\Upsilon(4S)$ is:

$$N^0_{\Upsilon} = N_{\Upsilon}/\epsilon_{B\overline{B}}, \tag{5.2}$$

where $\epsilon_{B\overline{B}}$ is the efficiency for $B\overline{B}$ events to satisfy the selection criteria. $\epsilon_{B\overline{B}}$ is evaluated with Monte Carlo simulation after a careful validation confirming that the variable shapes used in the hadronic selection are well reproduced.

Assuming the $B\overline{B}$ production saturates $\Upsilon(4S)$ decays and $\mathcal{B}(\Upsilon(4S) \to B^0\overline{B}^0)$ is equal to $\mathcal{B}(\Upsilon(4S) \to B^+B^-)$, N^0_{Υ} is the number of $B\overline{B}$ pairs, $N_{B\overline{B}}$, in the data set. In Run1+Run2 data I measured

$$N_{B\overline{B}} \;=\; (50.5 \pm 1.2)\, 10^6$$

The error is dominated by systematic uncertainty on $\epsilon_{B\overline{B}}$, mainly due to the uncertainty on the number of the good-quality tracks.

5.3 Signal and Background Definition

The whole analysis is performed in a limited area of the (m_{ES}, ΔE) plane, referred as the *grand sidebands* and defined as $|\Delta E| < 120\,\mathrm{MeV}$ and $5.2 < m_{ES} < 5.3\,\mathrm{GeV}$. All the one dimensional plots in m_{ES} use 40 bins, 2.5 MeV wide between 5.2 and 5.3 GeV.

The *signal region*, also referred as the **signal box**, is a rectangular area defined in the (m_{ES}, ΔE) plane, with $5.270 < m_{ES} < 5.290\,\mathrm{GeV/c^2}$, because of the $\approx 3\,\mathrm{MeV}$ resolution due to the beams spread, and $-40 < \Delta E < 30\,\mathrm{MeV}$. The choice of the ΔE signal window is the result of an optimization of the signal over background ratio, which will be described in Section 5.4.2. N_S and N_B are the expected signal and background events in this signal region.

They are extracted by a fit to the m_{ES} distributions of B candidates, modelling the distribution with a Crystal Ball function for the signal (see Sec. 4.3) and an ARGUS background shape [60] for the combinatorial background, which has the functional form

$$\frac{dN}{dm_{ES}} = N \cdot m_{ES} \cdot \sqrt{1 - x^2} \cdot \exp\left(-\xi \cdot (1 - x^2)\right) \tag{5.3}$$

where $x = m_{ES}/m_{\max}$ and the parameter ξ, determined from the fit, defines the shape of the function. This is an empirical distribution to model the expected distribution of beam-constrained mass values for background which is uniformly distributed in phase space. Note that $m_{\max}$ represents the kinematic upper limit for the constrained mass and is usually held fixed at half of the center of mass energy (nominally 5.29 GeV for $e^+e^- \to \Upsilon(4S)$) in a fit.

Two types of background in the sample of selected B meson candidates are distinguished. First, the combinatorial background arising from combining random leptons, pions and kaons from continuum or generic $B\overline{B}$ events: it usually does not peak in the signal region and its m_{ES} spectrum has an Argus PDF. A second class of background arises from $B \to \psi(2S)+$ X and $B \to J/\psi+$ X on resonance events, which have the same signal appearance, *i.e.* a m_{ES} peak in the signal region. They are tipically events in which the charmed resonance (J/ψ or $\psi(2S)$) decays into leptons, which are correctly reconstructed, while two soft neutral pions from the tagging B decay supersede the π^0 candidates of the $\psi(2S) \to J/\psi \pi^0 \pi^0$ decay. The initial state kinematics (E^*_B and p^*_B) is then similar to that expected from signal and therefore events usually accumulate in the signal region, showing a peak near the nominal B mass. When measuring the branching ratios, this background component must be subtracted from the signal yield, which is extracted by a fit on the m_{ES} spectrum as will be described. Moreover the peaking background is considered as a specific class of background source in the construction of the full likelihood function used for the sin2β measurement, since these events have a particular time-dependent structure.

A dedicated region in the (m_{ES},ΔE) plane is defined in order to study the background behaviour on data: the *sidebands*. They are two bands corresponding to $|\Delta E| > 0.05\,\mathrm{GeV}$, which are far enough from the signal region so to consider events in this region as essentially 100% background. The data-sidebands is the only subsample of data that have been studied before fixing the analysis procedure, especially useful to validate the Monte Carlo background samples.

5.4 Signal Selection Strategy

Since this study is aimed at the selection of a sample of $B^0 \to \psi(2\mathrm{S})K^0_S$ events to be used for the measure of the CP-violation parameter sin2β, the event selection criteria must be optimized to the best sin2β significance. Thus the selection strategy is based on a compromise between good background rejection and high efficiency. For this purpose, if N_S and N_B are the number of signal and background events in the signal region, one can choose to maximize one of the following two variables:

$\frac{N_S}{N_B}$ In this way, one prefers to enhance the signal compared to background, and therefore to maximize the purity of the sample, without taking into account the efficiency of the selection. A larger background rejection can minimize the systematic error on the Branching Fraction measurement;

$\frac{N_S}{\sqrt{N_S+N_B}}$ In this way, one grants a privilege to an efficient selection and tends to minimize the statistical error on the branching ratio measurement. Note that maximazing this variable enhances the significance of the observed signal with respect to the observed background, since it's the probability that the excess number of observed events is a statistical fluctuation of the background. Explicitly if $N_Y = N_S + N_B$ is the total selected yield and $\sigma^2_{N_B}/N_B << 1$:

$$\epsilon_S = \frac{BR}{\sigma_{BR}} = \frac{N_S}{N_{B\overline{B}}} \cdot \frac{1}{\sigma_{(N_Y - N_B)}} \sim \frac{1}{N_{B\overline{B}}} \cdot \frac{N_S}{\sigma_{N_Y}} = \frac{1}{N_{B\overline{B}}} \cdot \frac{N_S}{\sqrt{N_S + N_B}}$$

This factor also enters the expression for the precision one may expect from the sin2β measurement, that can be estimated as [78] :

$$\sigma_{\sin 2\beta} = \frac{\sigma_0}{\sqrt{\epsilon_{\text{tag}}\,(1-2w)^2}} \frac{\sqrt{1+\frac{N_B}{N_S}}}{\sqrt{N_S}\left(1+\frac{A_B}{A_S}\frac{N_B}{N_S}\right)} \tag{5.4}$$

where A_S and A_B are the asymmetry of the signal and background events. σ_0 represents the error for a single event and depends on the value of sin2β, on $\Delta M/\Gamma$ and on the vertex resolution σ_z; its value has been tabulated in [79]. ϵ_{tag} is the tagging efficiency and w is the B flavour misidentification probability. By temporarily neglecting the background asymmetry, one gets

$$\sigma_{\sin 2\beta} \propto \frac{\sqrt{N_S + N_B}}{N_S} \tag{5.5}$$

In this analysis a trade off is reached between the two criteria for any selection variable. The large part of the variables has been optimized using the second criterion, *i.e.* maximizing $\frac{N_S}{\sqrt{N_S+N_B}}$, while for the others I mean to estabilish a good compromise between the two. Thus two different optimization procedures are set, which will be accurately described in the next subsections:

- An optimization to the maximun $\frac{N_S}{\sqrt{N_S+N_B}}$ value, which will be described in Sec. 5.4.1. This method is referred as the *iterative optimization method* since it's applied with an iterative procedure which takes into account any possible correlation between the variables. This is applied for selections based on the particle identification selectors (PID) and the J/ψ and K^0_S identification. The optimization method is iterative because of possible correlations between the variables. This method fails when the signal and the background distributions have similar shapes.

- An alternative method is used for ΔM and ΔE variables, as described in Sec. 5.4.2. These two variables show a clean component from the internal combinatorial background in their signal Monte Carlo distributions, as described in Sec. 4.4. In this case the analysis grants a privilege to the background rejection, so both N_S/N_B and $\frac{N_S}{\sqrt{N_S+N_B}}$ are considered.

5.4.1 Iterative Optimization Method

This first method aims at maximizing the $\frac{N_S}{\sqrt{N_S+N_B}}$ value in the selection.

N_S estimation is performed on Monte Carlo signal events in the ΔE signal region $|\Delta E| < 35\,\mathrm{MeV}$, which is fixed in the whole procedure as the ΔE signal range [1]. On the other hand N_B is estimated from data samples in the sideband regions. No cut on m_{ES} is applied on both to increase the available samples.

The procedure has been applied to variables such as J/ψ mass and helicity, as well as K_S^0 mass and decay length. Since these variables are weakly correlated a simple multivariate method is applied. It consists in iterating the linear analysis [2] of single variables, changing the global set of cuts at any step of the iteration. Thus within each step one variable at a time is optimized while all the other cuts of the analysis are fixed. After repeating the procedure for each variable and having determined all their cut values, the same is repeated with the new set of cuts until a convergence is found.

The single variable optimization proceeds as follows:

1. For each variable to be optimized, the shape of the signal distribution is obtained from a fit to the Monte Carlo spectrum. This is a single Gaussian in the case of the $J/\psi \rightarrow \mu^+\mu^-$ mass spectrum, a Crystal Ball for $J/\psi \rightarrow e^+e^-$, a double Gaussian in the case of the K_S^0 mass spectrum. J/ψ helicity is modeled by a second order polynomial and the K_S^0 decay length by an exponential. For the $J/\psi \rightarrow e^+e^-$ mass spectrum the upper cut is taken as that from $\mu^+\mu^-$ case, and the lower one is optimized. The parameters of the mass distributions are listed in Table 5.2 while the results from the fits, for both signal and background are shown in figures 5.1 to 5.5.

2. The shapes of the background distributions are obtained from the on-peak data sidebands and fitted with the appropriate functions (see Figures 5.1 to 5.5).

3. In order to count the selected events N_S and N_B, both signal and background functions obtained from the above fitting procedures are numerical integrated within different intervals, all centered at the expected value of the variable (for example the nominal mass of the mesons in the case of mass distributions). Each interval corresponds to a possible cut for which the $\frac{N_S}{\sqrt{N_S+N_B}}$ value needs to be evaluated. The number of signal and background events corresponding to that cut window are only proportional to the integration results, and need to be rescaled.

[1] The optimization of the ΔE signal region is described in the next section. Its value is not far from the value chosen in this procedure.

[2] Within a linear method each variable is studied indipendently from the others, unlike a multivariate analysis in which all the correlated variables are studied together.

Variable	PDF parameterization	
$J/\psi\to\mu^+\mu^-$Mass	Gauss	$\sigma = 13.1 \oplus 7.79$ MeV $mass = 3.097$ GeV
$J/\psi\to e^+e^-$Mass	Crystal Ball	$\sigma = 14.5 \oplus 7.79$ MeV $mass = 3.095$ GeV $tail = 0.89 \pm 0.01$ MeV
$K^0_S\to\pi^+\pi^-$ Mass	Double Gauss	$\sigma_1 = 1.88$ MeV $mass_1 = 499.$ MeV $\sigma_2 = 5.1$ MeV $mass_2 = 498.$ MeV

Table 5.2: Parameters obtained from the fits of the signal Monte Carlo distributions. The 7.79 MeV factor added to the J/ψ mass widths accounts for the difference in mass resolution between data and Monte Carlo (see text).

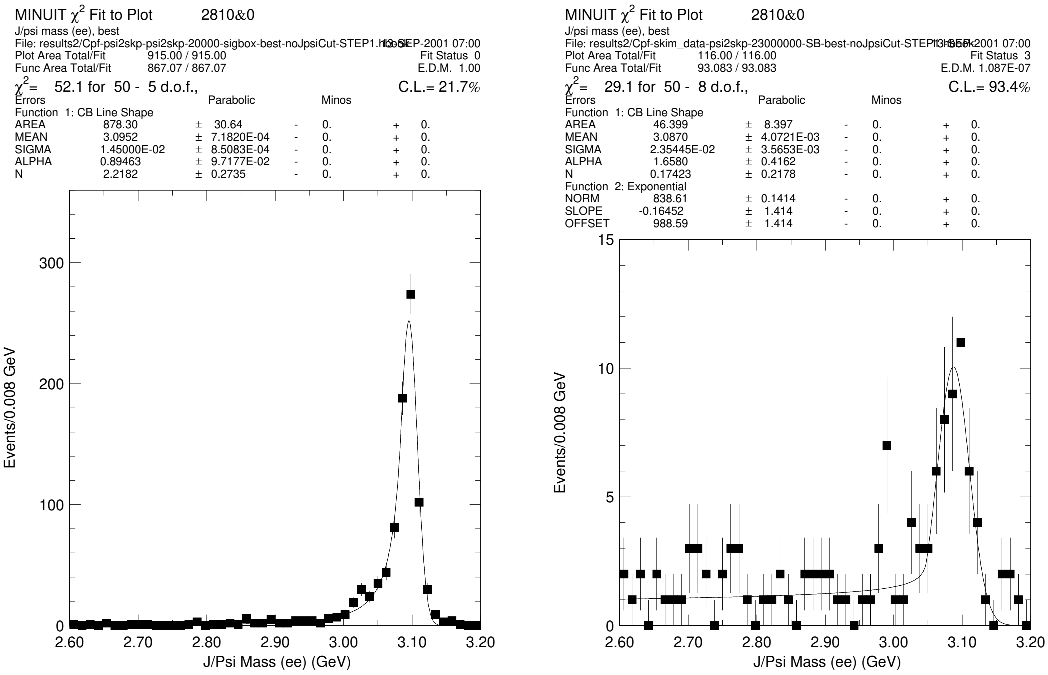

Figure 5.1: Fit of the J/ψ mass distributions with $J/\psi\to e^+e^-$ events: signal Monte Carlo (left) and data-sidebands (right).

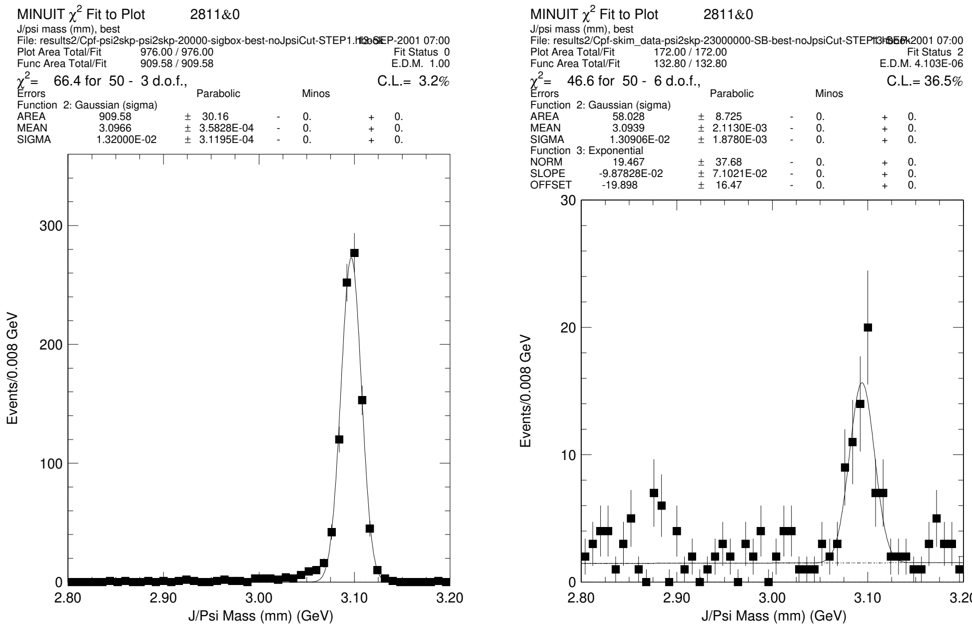

Figure 5.2: Fit of the J/ψ mass distributions with $J/\psi \to \mu^+\mu^-$ events: signal Monte Carlo (left) and data-sidebands (right).

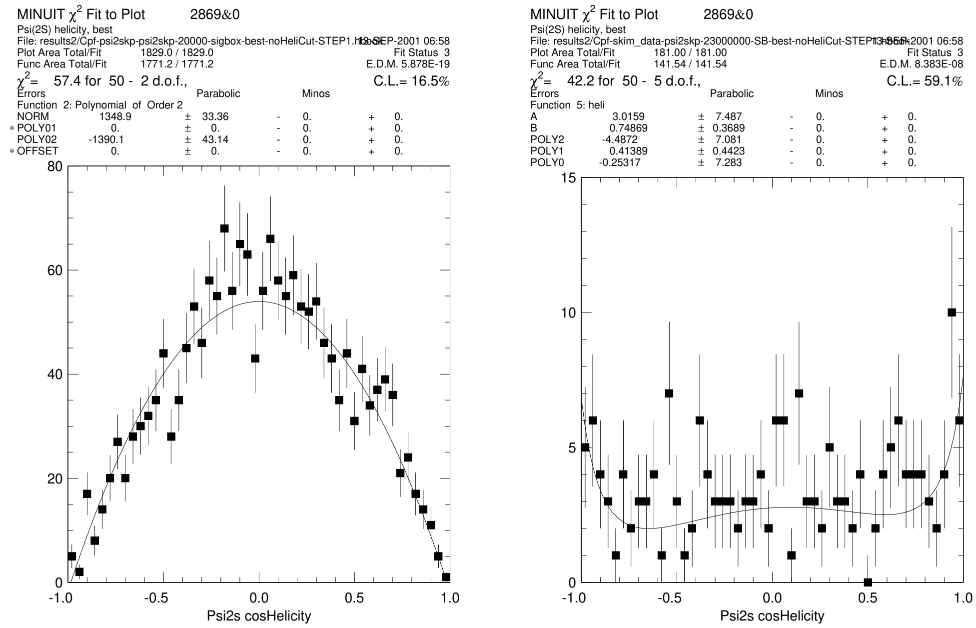

Figure 5.3: Fits of the J/ψ helicity distribution with $J/\psi \to \ell^+\ell^-$ events: signal Monte Carlo (left) and data-sidebands (right).

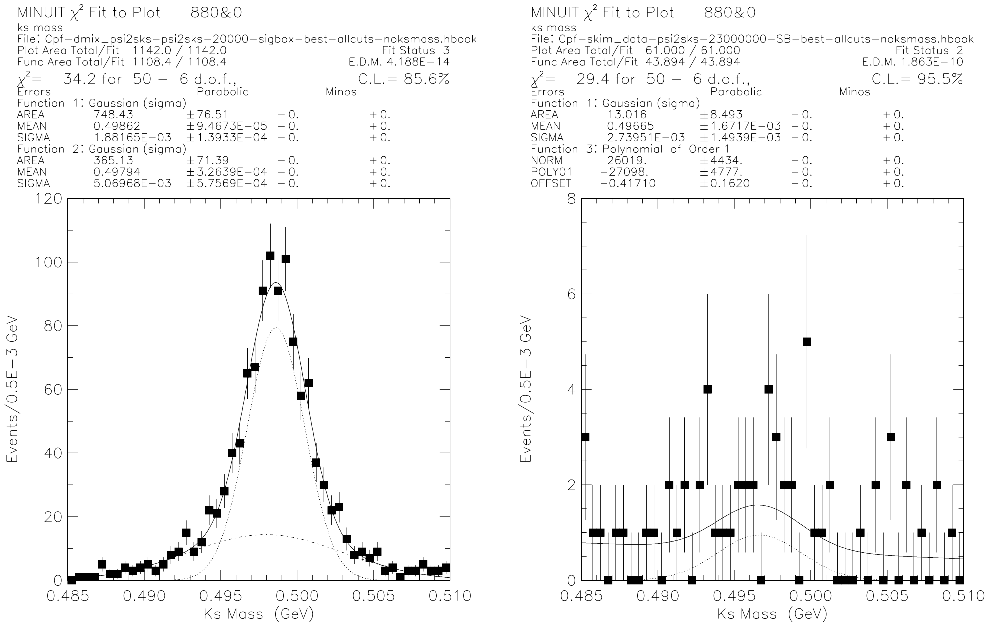

Figure 5.4: Fits of the K_S^0 mass distribution with $K_S^0 \to \pi^+\pi^-$ events: signal Monte Carlo (left) and data-sidebands (right).

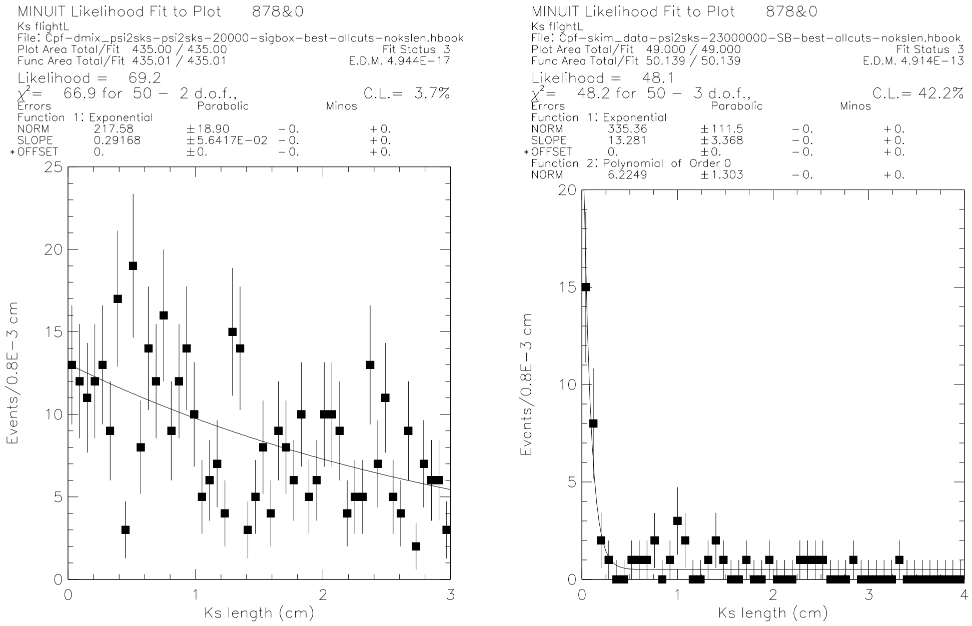

Figure 5.5: Fits of the K_S^0 decay length distribution with $K_S^0 \to \pi^+\pi^-$ events: signal Monte Carlo (left) and data-sidebands (right).

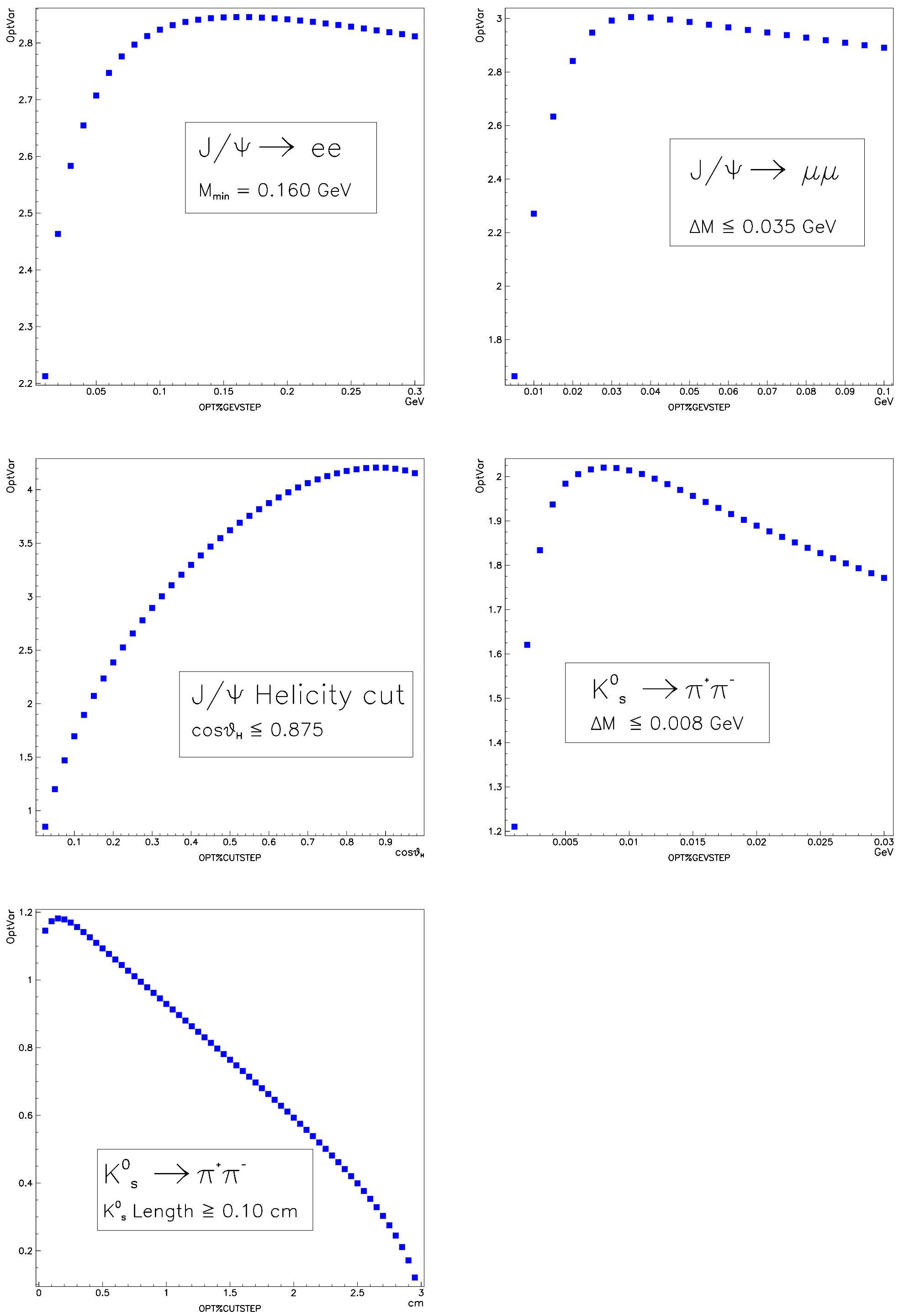

Figure 5.6: Optimization plots for J/ψ mass (e^+e^- and $\mu^+\mu^-$), J/ψ helicity, K^0_S mass and helicity. The optimized variable $\frac{N_S}{\sqrt{N_S+N_B}}$ is plotted as a function of the cut value. The one corresponding to the maximum $\frac{N_S}{\sqrt{N_S+N_B}}$ value is chosen as the selection value. All the results from the optimization are listed in table 5.3.

4. N_S is computed rescaling the integral result by the efficiency for the selection (calculated as the fraction of events in the m_{ES} signal region) and normalising it to the same luminosity as the data sample, using the factors listed in Tab. 4.3.

5. In the same way, the number of background events N_B is taken as the integral between the chosen limits of the data-sidebands distribution and scaling down the number of events in the sidebands into the signal region.

6. The quantity $\frac{N_S}{\sqrt{N_S+N_B}}$ is then calculated in each cut window and the maximum is chosen as the "optimal" value and fixed as the starting point in the next step of the iteration. Typical plots showing $\frac{N_S}{\sqrt{N_S+N_B}}$ as a function of the cut value are those in Fig. 5.6.

Since correlation is feeble among the chosen variables, only few steps are required to reach the convergence of the method.

In order to account for different mass resolutions of the J/ψ meson between data and Monte Carlo, a smearing factor is added within the fitting procedures. Hence the width of the J/ψ mass distribution is taken as the sum in quadrature between the fit result and a smearing component $\sigma = 7.79\,\mathrm{MeV}$ measured from inclusive data samples [77].

This optimization method assumes that the background is flat in ΔE and that the signal m_{ES} distribution shape is independent on the cut window. The former assumption has been checked on Monte Carlo background samples, while the latter has been studied for one variable only, the J/ψ mass, by directly measuring N_S and N_B with modified cut windows. Similar values were obtained in both cases. Convergence to absolute maxima is confirmed by repeating the complete procedure using different cut values as the starting point, and no difference is found.

The PID criteria have been optimized with a similar method, adjusted for discrete, and not continuous, variables. By comparing the results from all the possible combinations of selectors (`veryLoose`, `Loose`, `Tight` and `veryTight` for electrons, muons and kaons) the one maximazing $\frac{N_S}{\sqrt{N_S+N_B}}$ is found. The procedure is applied twice, before and after the other cuts optimization, in order to account for possible correlations, but in both cases results are equal.

The cut windows chosen for the selection with this procedure are all listed in Table 5.3.

5.4.2 ΔE and ψ(2S) Mass Optimization Procedure

For selections involving the ψ(2S) mass and the ΔE variable, an alternative approach is taken. For these variables, the internal combinatorial component in the Monte Carlo signal distribution is quite clear and abundant, as was largely described in Section 4.4.1. Figures 5.7(left) and 5.8(left) show respectively the ψ(2S) mass and the ΔE distributions, with their fit results, as obtained from signal simulated events. In each plot, events outside the narrowest peakare those originated from internal combinatorics. Apart from the small narrow peak, distributions obtained from signal and from background Monte Carlo samples are quite similar, as visible from the same Figures 5.7 and 5.8. As a consequence, the iterative procedure previously described in Sec. 5.4.1, when it's applied to the ΔE and ΔM variables, brings to very loose selections: $\sim 130\,\mathrm{MeV/c^2}$ for the ΔM window and $\sim 100\,\mathrm{MeV}$ for ΔE. This looseness is not acceptable since the ΔE cut is important to reject peaking background arising from $B \to \psi$(2S)X events, which is expected to be the largest background contribute. A compromise must be therefore reached: since for these variables $\frac{N_S}{\sqrt{N_S+N_B}}$ has a flat dependence on cut criteria, the highest N_S/N_B values is chosen within those close to the maximum $\frac{N_S}{\sqrt{N_S+N_B}}$ value. Moreover the two variables are optimized simultaneously, thus leading to the best combination of (ΔE, ΔM) cuts. The ΔE selection window must account for the asymmetry of the corresponding distribution, so both the low and the high limits are subject to the optimization procedure separately. The cut values are varied in steps between reasonable limits and the number of Monte Carlo signal and background events passing the selection are computed at each step, using respectively the Monte Carlo signal and the data sidebands samples as before, and applying the appropriate normalizations. The results are graphically shown in Fig. 5.9 and summarized in Table 5.3.

5.5 Summary of Event Selection and Efficiency

The results from both the optimization methods, together with the criteria described in Chapter 4, define the final selection of the analysis and are summarized in Table 5.3. In Fig. 5.10 the m_{ES} and ΔE distributions for $B^{\pm} \to \psi(2S)K^{\pm}$ and $B^0 \to \psi(2S)K^0_S$ Monte Carlo samples are shown, after all the selection criteria are applied. The expected resolutions in m_{ES} and ΔE resulting from the fits are summarized in Table 5.4. Throughout the analysis, two quantities have been defined:

- efficiency: $\epsilon = \frac{N_S+N_B}{N_{B\overline{B}}}$,

  the fraction of generated B mesons that passes the selection;

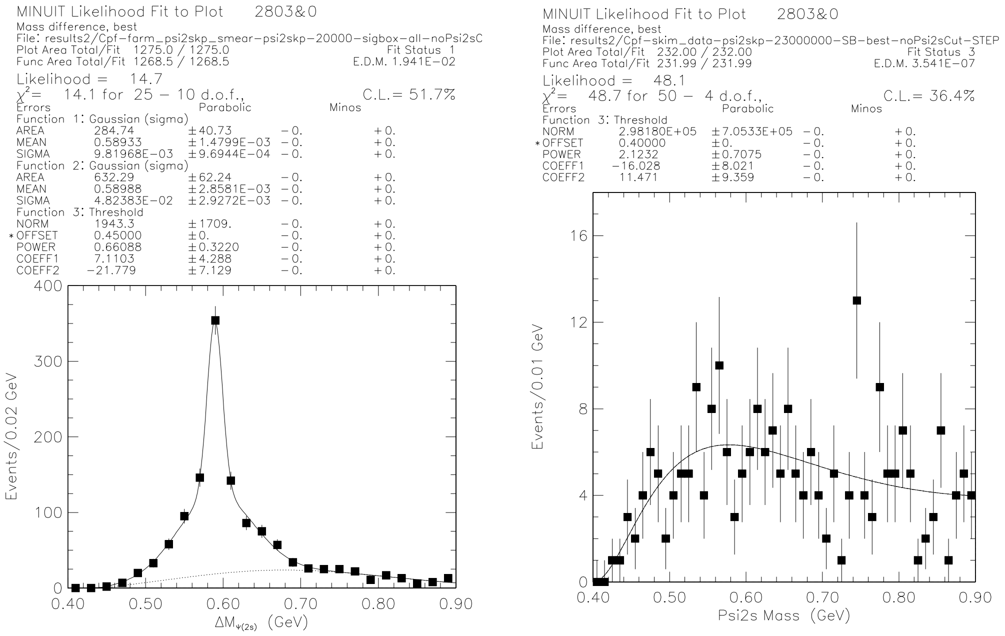

Figure 5.7: Fits of the $\psi(2S)$ mass distribution with $\psi(2S)\to J/\psi\pi^0\pi^0$ events selected: signal Monte Carlo (left) and data-sidebands (right). The dashed line on the left plot shows the threshold function contribution.

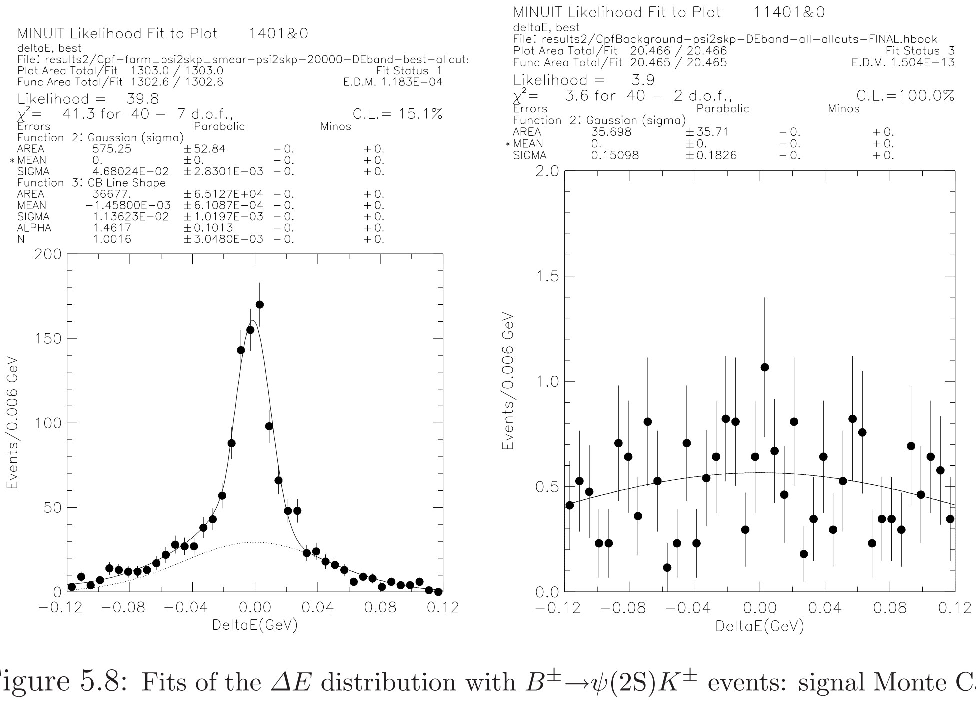

Figure 5.8: Fits of the ΔE distribution with $B^{\pm}\to\psi(2S)K^{\pm}$ events: signal Monte Carlo (left) and cocktail-background Monte Carlo (right). ΔE background shape is approximately flat within the analized range.

Table 5.3: Summary of the event selection criteria.

$J/\psi \rightarrow e^+e^-$ Selection	
Electron selection[a]	`Tight` for both legs
	$0.41 < \theta < 2.409$ rad
Vertex constrained mass	$2.937\,\mathrm{GeV} < M_{e^+e^-} < 3.132\,\mathrm{GeV}$
$J/\psi \rightarrow \mu^+\mu^-$ Selection	
Muon selection[b]	`Loose` for one leg, `veryLoose` for the other
	$0.3 < \theta < 2.7$ rad
Vertex constrained mass	$3.097\,\mathrm{GeV} < M_{\mu^+\mu^-} < 3.132\,\mathrm{GeV}$
Kaon Selection	
Kaon selection[c]	`NotAPion`
	$0.35 < \theta < 2.5$ rad
$K^0_S \rightarrow \pi^+\pi^-$ Selection	
Vertex constrained mass	$0.489\,\mathrm{GeV} < M_{K^0_S} < 0.507\,\mathrm{GeV}$
Decay lenght	$\mathrm{d}_l > 0.1$ cm
Neutral Pions Selection	
π^0 Vertex constrained Mass	$115.\,\mathrm{MeV} < M_{\pi^0} < 144.\,\mathrm{MeV}$
Dipion Invariant Mass	$0.450\,\mathrm{GeV} < M_{\pi^0\pi^0} < 0.600\,\mathrm{GeV}$
$\psi(2S) \rightarrow J/\psi\,\pi^0\pi^0$ Selection	
Vertex constrained mass	$3.626\,\mathrm{GeV} < M_{\psi(2S)} < 3.746\,\mathrm{GeV}$
Helicity angle	$\lvert\cos\theta_{\psi(2S)}\rvert \leq 0.875$
Global Event Selection	
Event shape	$\lvert\cos\theta_{Thrust}\rvert \leq 0.9$
B meson Selection	
Signal Box	$-0.040 < \Delta E < 0.030$ GeV
	$5.27 < m_{ES} < 5.29$

[a]See sec. 3.4.1 for details on the variables used.
[b]See sec. 3.4.2 for details on the variables used.
[c]See sec. 3.4.3 for details on the variables used.

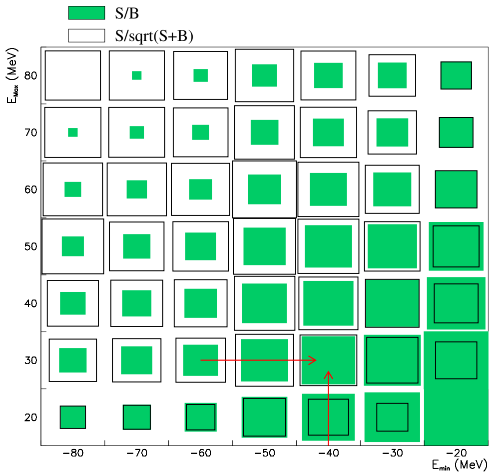

Figure 5.9: $\frac{N_S}{N_B}$ and $\frac{N_S}{\sqrt{N_S+N_B}}$ values as functions of ΔE window cuts (ΔE_{min} and ΔE_{max}), with a fixed ΔM value set. The combination ΔE_{min}=-40 MeV and ΔE_{max}=30 MeV is chosen.

Table 5.4: Results of fitting for Monte Carlo m_{ES} and ΔE distributions, for events passing the final selection requirements.

Fit Parameters		$B^{\pm}\to\psi(2S)K^{\pm}$	$B^0\to\psi(2S)K^0_S$
m_{ES}	μ	5.2794 ± 0.0002	5.2798 ± 0.0002
	σ	$(3.7 \pm 0.2)10^{-3}$	$(3.5 \pm 0.2)10^{-3}$
	α	0.9 ± 0.1	0.9 ± 0.1
	N	2.7 ± 0.4	2.5 ± 0.4
ΔE	σ	$(1.13 \pm 0.1)10^{-2}$	$(0.80 \pm 0.06)10^{-2}$

- purity: $\eta = \frac{N_S}{N_S+N_B}$,
  the fraction of signal events selected. The signal/background distinction is featured by a m_{ES} fit.

The efficiency of the selection is a fundamental ingredient of the Branching Ratio measurement, whereas the purity of the sample is a fundamental parameter in the sin2β extraction. Monte Carlo efficiencies for each cut are displayed in Table 5.5 for both the decay samples. The $\psi(2S)\to\pi^+\pi^-$ veto is applied, which will be described in the next section.

The difference in reconstruction efficiency between real and simulated events is taken into account during the analysis by using scaling factors, as will be described in Section 5.10. These corrections to Monte Carlo efficiency are not included here, but are included in the systematics of the Branching

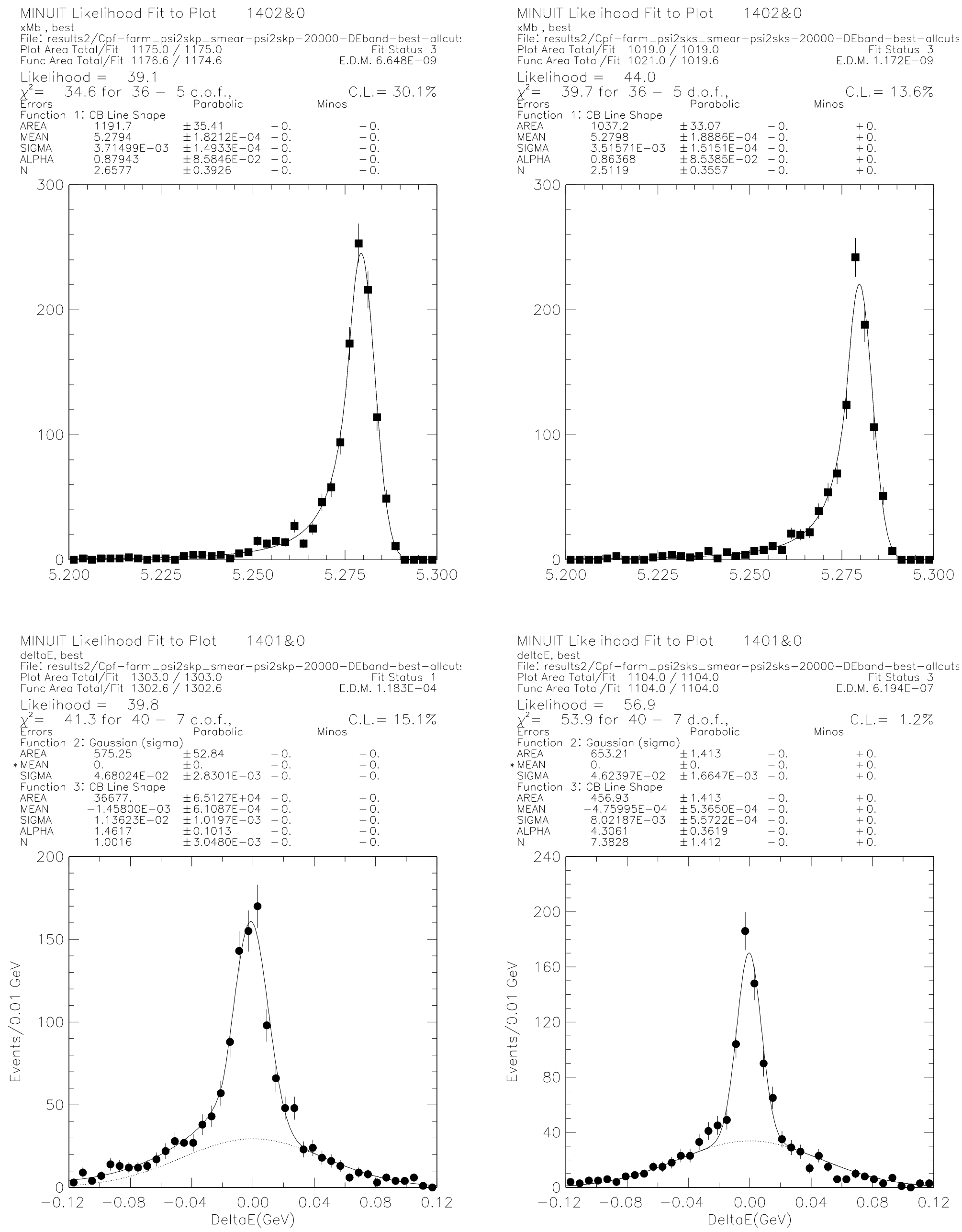

Figure 5.10: m_{ES} and ΔE distributions for $B^{\pm}\to\psi(2S)K^{\pm}$ (left) and $B^0\to\psi(2S)K^0_S$ Monte Carlo samples after the selection described, with fit functions superimposed.

Ratio measurement.

MC cut efficiency	$\boldsymbol{B^{\pm}\to\psi(2S)K^{\pm}}$	$\boldsymbol{B^{0}\to\psi(2S)K^{0}_{s}}$
Preselection	0.487	0.347
$J/\psi\,\pi^+\pi^-$ Veto	0.973	0.964
Lepton selection	0.794	0.848
Kaon selection	0.951	0.893
Tracks Acceptance	0.875	0.955
J/ψ Mass	0.905	0.912
Photons Acceptance	0.775	0.778
π^0 Mass	0.888	0.898
$M_{\pi^0\pi^0}$	0.825	0.839
ψ(2S) Mass	0.685	0.712
ψ(2S) Helicity	0.972	0.977
$\cos\theta_{Thrust}$	0.905	0.895
Signal box	0.512	0.536
Total $\boldsymbol{\epsilon}$	4.97 ± 0.16%	4.31 ± 0.15%

Table 5.5: Summary of the event selection efficiencies for $B^{\pm}\to\psi(2S)K^{\pm}$ and $B^{0}\to\psi(2S)K^{0}_{s}$ modes. Selections are applied one after another, with the efficiency defined as the fraction of events passing the previous set of criteria plus a new requirement.

5.6 Background Characterization

The larger background component, as for each B meson decay into charmonium final state, comes from the J/ψ and ψ(2S) inclusive decays, in which the experimentally clear J/ψ signal is accompained by a random combination of neutral pions coming from the rest of the event. These decays are kinematically so similar to the signal as their events usually accumulate in the (ΔE,m_{ES}) signal region, therefore giving the major contribution to a peaking component in the background. The peaking background cannot be distinguished from signal and its contribution, evaluated from Monte Carloevents, must therefore be subtracted from the selected yield of events. The number of these background events must be limitated as much as possible within the selection, because of the large systematics brought by their subtraction to the branching fraction measurement.

In the following a useful tool for peaking background rejection is presented. This is a veto to the $\psi(2S)\rightarrow J/\psi\,\pi^+\pi^-$ decay events, which are identified as a source of this background component.

The background composition is evaluated from Monte Carlo events passing the final requirements of the selection, including the veto, and the expected number of peaking and non-peaking background in the data sample is estimated.

5.6.1 $\psi(2S)\rightarrow J/\psi\,\pi^+\pi^-$ Charged Veto

The peaking component from generic $\psi(2S)$ decays represents about 13% of the expected signal peak. This contribution is shown in Fig. 5.11(left), where the m_{ES} shape from inclusive $\psi(2S)$ Monte Carlo events is parameterized with an Argus background shape plus a Crystal Ball function. The Crystal Ball parameters are fixed at the values obtained from the signal Monte Carlo fit (Table 5.4), the Argus shape is the same as that from the cocktail-background Monte Carlo fit (which will be presented in Table 5.10), while the relative areas are free to vary. Note that the mass peak is slightly shifted at low values with respect to the signal.

A significant source for the inclusive $\psi(2S)$ background can be identified as coming from $\psi(2S)\rightarrow J/\psi\,\pi^+\pi^-$ decay events. In this decay the available energy for the dipion system is the same as that for the signal events, and it's therefore likely to select events having the two oppositely charged tracks replaced by two random π^0s from the rest of the event. Such events must be rejected without high loss of efficiency, since they are not expected to be the most significant background class.

The criterion to reject the $\psi(2S)\rightarrow J/\psi\,\pi^+\pi^-$ events is chosen in a way that it enhances the signal over background ratio S/B, preserving the highest efficiency. The number of events in the signal region from the $\psi(2S)$ inclusive sample is used to estimate B while S is calculated from the signal Monte Carlo sample.

First the $\psi(2S)\rightarrow J/\psi\,\pi^+\pi^-$ decay events are identified and then are rejected applying a veto to this german charged channel. A selector for this process is provided within the *BABAR* recontruction code, for decays in which the charged or neutral Bs are fully reconstructed. More details on the $\psi(2S)\rightarrow J/\psi\,\pi^+\pi^-$ decay reconstruction can be found in reference [77]. The performance of the selector on the $\psi(2S)$X Monte Carlo sample is shown in the upper plot of Figure 5.13, where the ΔM and m_{ES} value for candidates reconstructed in the $J/\psi\,\pi^+\pi^-$ mode are plotted together. Also the selection

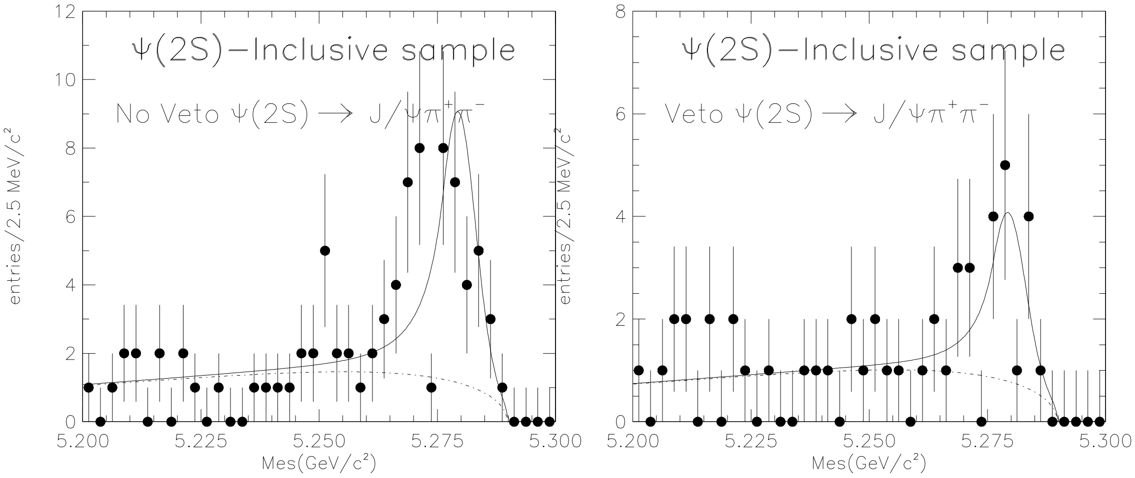

Figure 5.11: Inclusive ψ(2S) signal in the $J/\psi\,\pi^0\pi^0$ mode before and after applying the veto of $J/\psi\,\pi^+\pi^-$ events, using the Monte Carlo $B \rightarrow \psi$(2S)X sample. The corresponding integrated luminosity is 320.3 fb^{-1}.

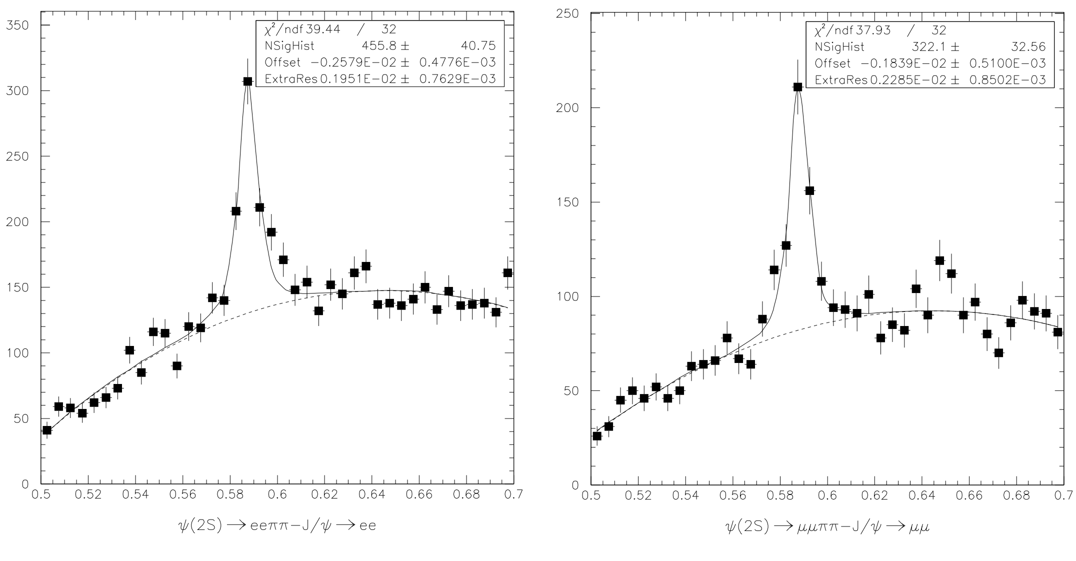

Figure 5.12: Inclusive ψ(2S) signal in the $J/\psi \rightarrow e^+e^- + \pi^+\pi^-$ (left) and $J/\psi \rightarrow \mu^+\mu^- + \pi^+\pi^-$ (right) modes, using the Run1 data sample [84].

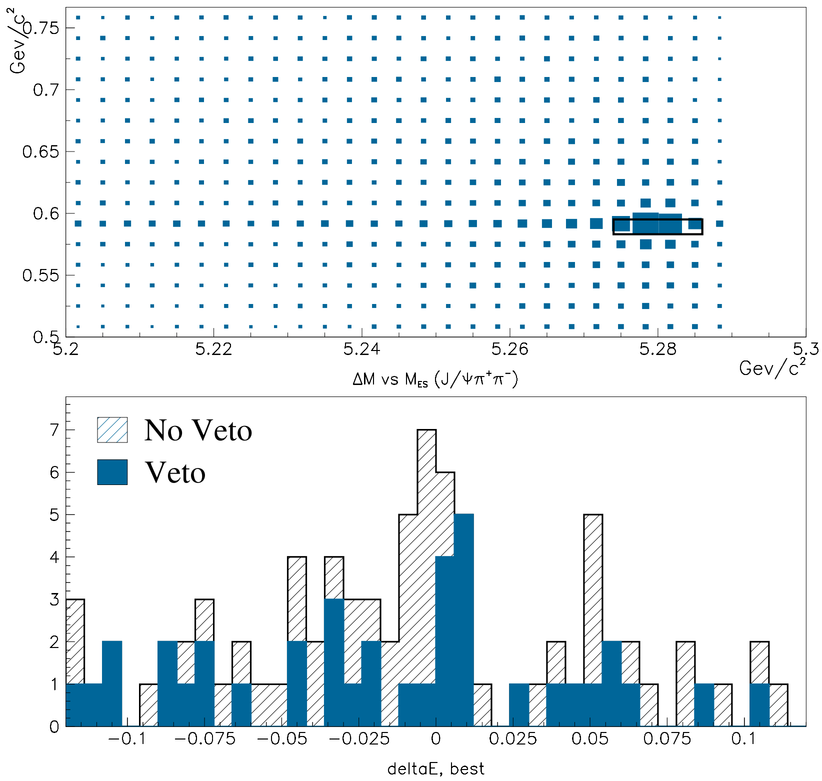

Figure 5.13: Upper plot: ΔM vs m_{ES} for events reconstructed as $\psi(2S) \to J/\psi \pi^+\pi^-$ in the $\psi(2S)$ inclusive decays. The box shows the selection applied. Lower plot: Veto effect on the ΔE distribution in the inclusive $\psi(2S)$ sample, the peaking component at $\Delta E = 0$ is visibly reduced.

values for the two variables are shown as a box in the (ΔM,m_{ES}) plane.

Let's now see how this "charged veto" works. When it's applied on the sample, the event is ignored if at least one $B \to \psi(2S)$K candidate is found, with the $\psi(2S)$ reconstructed in the charged channel $J/\psi \pi^+\pi^-$ meeting both the following conditions:

- its energy substituded mass m_{ES} lies within 2σ ($\sigma = 3\,\mathrm{MeV/c}$) from the nominal B mass;
- the $\psi(2S)$ invariant mass lies within 2σ from the nominal PDG value; $\sigma = 7 \pm 1\,\mathrm{MeV/c}$ value is measured from the inclusive $\psi(2S)$ signal in Run1 data sample, as shown in Fig. 5.12.

The overall effect on $\psi(2S) \to J/\psi \pi^0\pi^0$ signal is a 3% efficiency reduction, as can be seen from Table 5.5 while the S/B ratio duplicates its value after

	# Evt Peaking	# Evt Argus	P/A Ratio
No Veto Applied	3.9 ± 0.8	1.0 ± 0.8	3.8 ± 0.8
Veto Applied	1.6 ± 0.4	0.8 ± 0.6	2.3 ± 1.5

Table 5.6: Peaking (P) and Argus (A) components of the ψ(2S) inclusive background expected in the data sample, from the selection of the $B^{\pm}\to\psi(2S)K^{\pm}$ decay. The number of events in the m_{ES} peak and in the Argus background derive from a likelihood fit of the m_{ES} distribution. The explicit $J/\psi\,\pi^+\pi^-$ mode veto operates as halving the peaking part of the selected background events.

applying the veto. Moreover the peaking background component in the m_{ES} region has been measured after the veto and only a residual 50% of the peak remains when the veto is applied. A summary of the expected contribution of this background in the data sample, obtained after the explicit $J/\psi\,\pi^+\pi^-$ mode veto, is in Table 5.6.

5.6.2 Background estimation

The background total size and its composition expected in each exclusive decay mode has been determined independently in different regions of ΔE by studying the m_{ES} spectrum both on data and Monte Carlo. The definition of such regions shown in Figure 5.14 are in the (m_{ES},ΔE) plane:

signal box m_{ES}=[5.27;5.29] GeV and ΔE=[-0.040;0.030] GeV;

A+B m_{ES}=[5.2;5.3] GeV and ΔE=[-0.040;0.030] GeV is the signal ΔE band;

C+D m_{ES}=[5.2;5.3] GeV and $|\Delta E|$ >0.05 GeV are the sidebands;

B+D+E m_{ES}<5.26 GeV

B m_{ES}<5.26 GeV and ΔE=[-0.040;0.030] GeV is the signal ΔE band outside the signal box;

D m_{ES}<5.26 GeV and $|\Delta E|$ >0.05 GeV are the sidebands outside the signal box;

First of all one has to describe the composition of the background. One can measure the relative contributions from different backgrounds by counting the selected events in the signal box from any background Monte Carlo sample. The two-dimensional plots (m_{ES}, ΔE) for each of them (iclusive J/ψ and ψ(2S), generic $B\overline{B}$, $c\overline{c}$ and uds) and for any signal selection, $B^0\to\psi(2S)K^0_S$ and $B^{\pm}\to\psi(2S)K^{\pm}$, are shown in Figure 5.15, while the number of the selected background events in the signal box are in Table 5.7. The

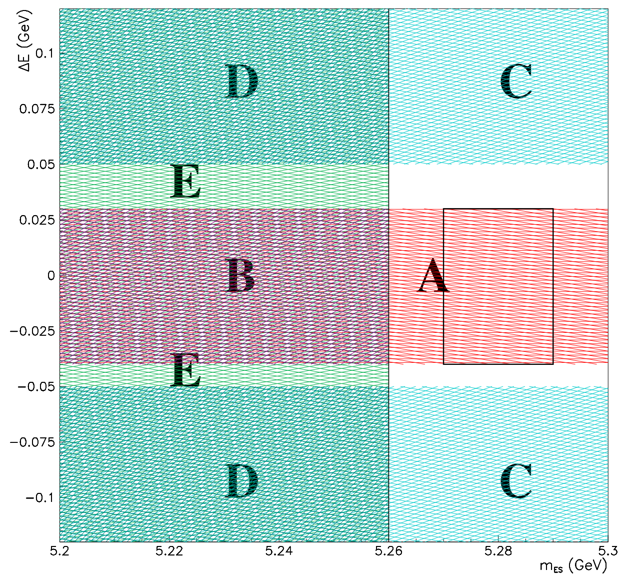

Figure 5.14: Definition of the signal region (black box) and the different sidebands used in the text.

Monte Carlo study predicts $15. \pm 1.8$ background events in the data sample for the $B^{\pm}\to\psi(2S)K^{\pm}$ mode and $4. \pm 1.$ for the $B^{0}\to\psi(2S)K^{0}_{S}$ mode. Only events from different J/ψ and $\psi(2S)$ decays contribute to the total background, while no events from continuum and generic $B\overline{B}$ are expected.

The background coming from the $B\to\psi(2S)$+X and $B\to J/\psi$+X decays has two components, one Argus shaped and one peaking in the signal region, which is described by a Crystal Ball centered at the B mass value. Part of this background accumulates in the signal region and we have indicated these events as peaking background. To estimate this contribution we can parameterize the m_{ES} background spectrum with an Argus function plus a Crystal Ball, and measure their relative contributions in the signal region from the Monte Carlo samples.

The Crystal Ball parameters are fixed at the signal Monte Carlo values (Table 5.4) and the Argus shape ξ to the background Monte Carlo value (Table 5.9) in the signal sidebands (B). The Crystal Ball integration results give the peaking component contribution shown in Table 5.7, which are then rescaled to Run1+Run2 luminosity to extrapolate the expected value in the data sample.

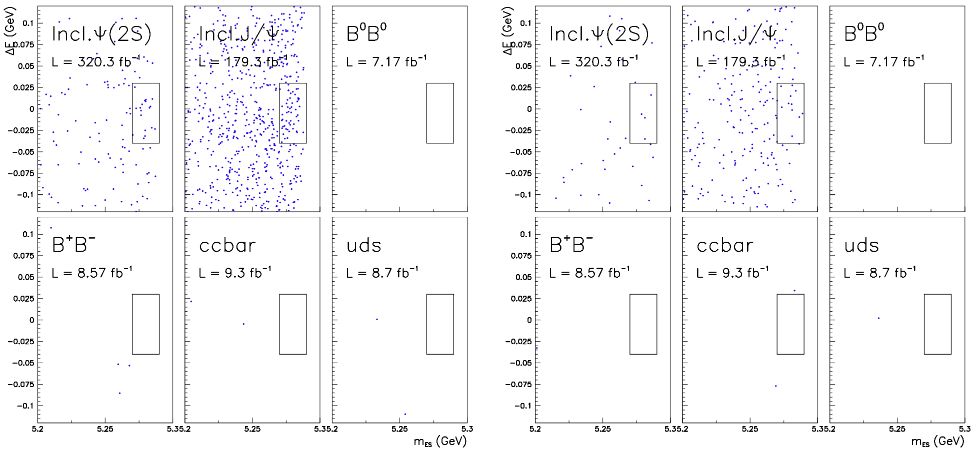

Figure 5.15: ΔE *vs* m_{ES} for the different backgrounds for $B^{\pm}$ (left) and B^0 (right) channels, as predicted by the generic Monte Carlo. All cuts have been applied except for the signal box requirement, indicated in the plots. The effective luminosities of each MC sample is also shown.

	Incl.-J/ψ $\mathcal{L}$=179.3 fb^{-1}	Incl.-ψ(2S) $\mathcal{L}$=320.3 fb^{-1}	Run1+Run2 $\mathcal{L}$=44.7 fb^{-1}
$\boldsymbol{B^{\pm}\rightarrow\psi(2S)K^{\pm}}$			
Total	52	19	15. $\pm$ 1.8
Peaking	8.6 $\pm$ 3.9	12.0 $\pm$ 4.2	3.7 $\pm$ 0.8
$\boldsymbol{B^{0}\rightarrow\psi(2S)K^{0}_{s}}$			
Total	15	5	4.3 $\pm$ 1.
Peaking	5.0 $\pm$ 3.6	4.5 $\pm$ 2.2	1.8 $\pm$ 0.6

Table 5.7: Background Composition

Number of selected events in the Monte Carlo background inclusive samples by the $B^{\pm}\rightarrow\psi(2S)K^{\pm}$ and $B^0\rightarrow\psi(2S)K^0_S$ selection. Peaking components are the results from the m_{ES} fitting procedure. These numbers can be scaled to the available luminosity of the data sample: last column shows the projected values for Run1+Run2 luminosity.

5.7 Monte Carlo Predictions

Here we want to summarize the predictions from the Monte Carlo study on both signal and background events and validate them through the comparison with a data subsample, the data-sidebands.

A summary of signal efficiencies, purities and other quantities from Monte Carlo are shown in Table 5.8 for both $B^{\pm}\to\psi(2S)K^{\pm}$ and $B^0\to\psi(2S)K^0_S$ decays. Efficiency is less than 5% for both the B modes, while the selection ensures a purity as high as 70%. The neutral mode appears as the more pure, with a slightly lower efficiency, as expected because of the additional requirements brought by the K^0_S reconstruction. If we project the number of selected signal Monte Carlo events to the available data luminosity, we expect (27.2 ± 0.9) events for $B^{\pm}\to\psi(2S)K^{\pm}$ and (8.8 ± 0.3) events for $B^0\to\psi(2S)K^0_S$ decays.

MC Projections	$\boldsymbol{B^{\pm}\to\psi(2S)K^{\pm}}$	$\boldsymbol{B^0\to\psi(2S)K^0_S}$
efficiency ϵ	4.9 ± 1.6	4.2 ± 1.5
N_S/N_B	1.7	2.4
$N_S/\sqrt{N_S+N_B}$	2.88	1.71
purity η	0.6 ± 0.1	0.7 ± 0.2
Exp. yield Run1+Run2	27.2 ± 0.9	8.8 ± 0.3

Table 5.8: Characteristic values of the two decay modes as extracted from Monte Carlo. Also expected yields in Run1+Run2 luminosity are shown.

5.7.1 Sidebands Comparison

Some kinematic variables and mass spectra have been checked on data before unblinding the signal region, in order to make the Monte Carlo results completely reliable. In Figure 5.16 some of them show the great agreement one can obtain between the data and the cocktail-background Monte Carlo, for events in the sidebands when normalizing them to the same luminosity and the same ΔE area.

The m_{ES} distributions for events in the sidebands are separately shown in Figures 5.17 and 5.18 for both data and Monte Carlo samples and for both the B modes. Since background events are uniformely distributed in ΔE, as previously shown in Fig. 5.8, one can estimate the number of expected background events in the signal region from that in the sidebands: one first integrate the sidebands Argus shape across the m_{ES} signal region and then rescale the result by the ratio of the areas of two ΔE regions (=0.7). The results obtained from Data and Monte Carlo are shown in Table 5.9.

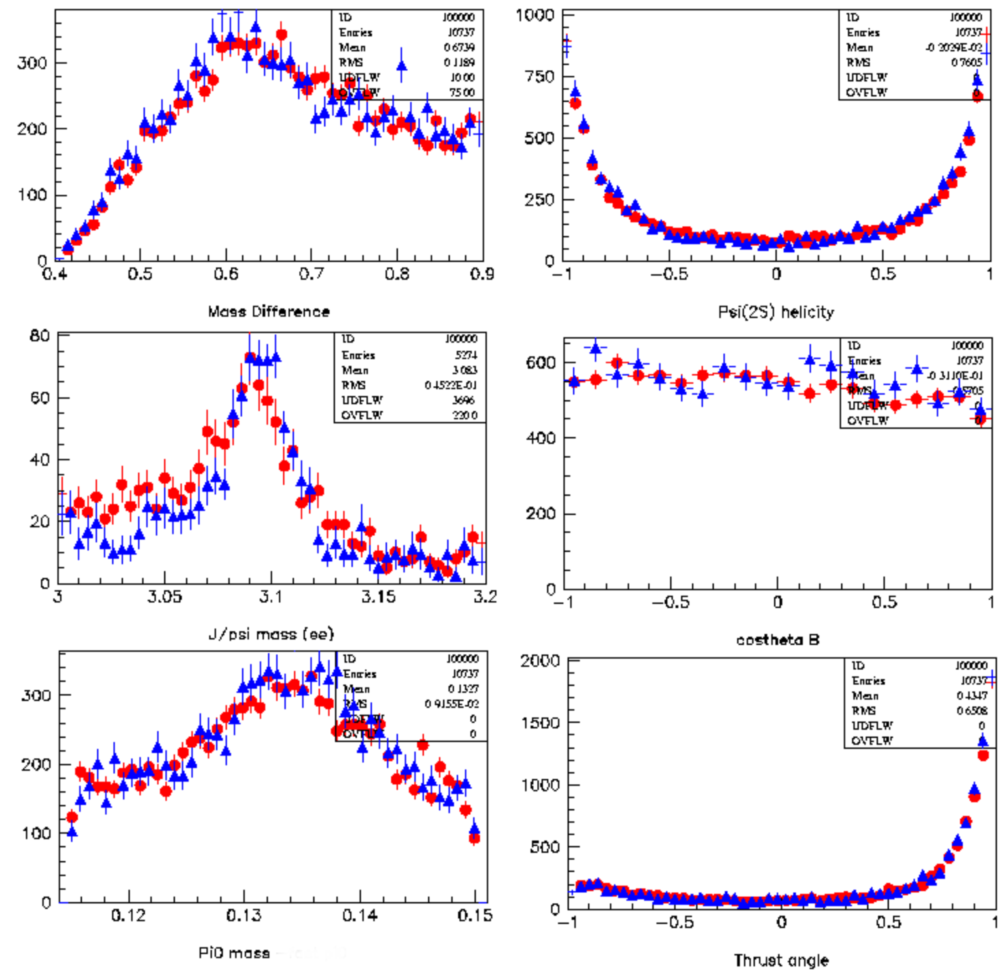

Figure 5.16: Some kinematic variables and mass spectrum for events in the sidebands, from data (red dots) and Monte Carlo background (blue triangles). From the top: left): $\psi(2S)$ mass difference, $J/\psi \rightarrow e^+e^-$ invariant mass and π^0 mass spectrum; right): $\psi(2S)$ helicity, Thrust angle and B helicity. All distributions are normalized to the same integrated luminosity. Monte Carlo well describes the data.

Sample	#Evt SideBands	# ProjEvt Signal region
$B^{\pm}\to\psi(2S)K^{\pm}$		
Data on-peak	25.7 ± 5.1	18.0 ± 3.5
Monte Carlo	21.6 ± 4.6	15.1 ± 3.3
$B^0\to\psi(2S)K^0_s$		
Data on-peak	5.5 ± 2.3	3.9 ± 1.6
Monte Carlo	7.6 ± 2.8	5.3 ± 1.9

Table 5.9: Background study for $B^{\pm}\to\psi(2S)K^{\pm}$ and $B^0\to\psi(2S)K^0_S$ in the ΔE sidebands region. The number of expected events in the side bands region and of the projected events into the signal region are shown.

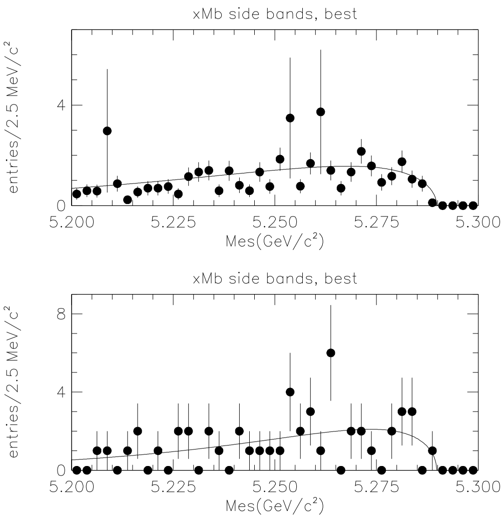

Figure 5.17: $B^{\pm}\to\psi(2S)K^{\pm}$ mode: background determination via Argus fit to the ΔE sidebands for Monte Carlo (upper plot) and data (lower plot) samples. The Argus shape parameters obtained by the fit are shown in Table 5.10.

5.8 Validation of the Fitting Procedure

This section describes the way in which the fitting procedure applied to the data sample in order to extract the signal yield has been chosen. Then a validation is presented, performed on both data and Monte Carlo samples and on different subsamples of events, corresponding to different regions of the (m_{ES}, ΔE) plane.

The fit procedure applied on background using an Argus function and

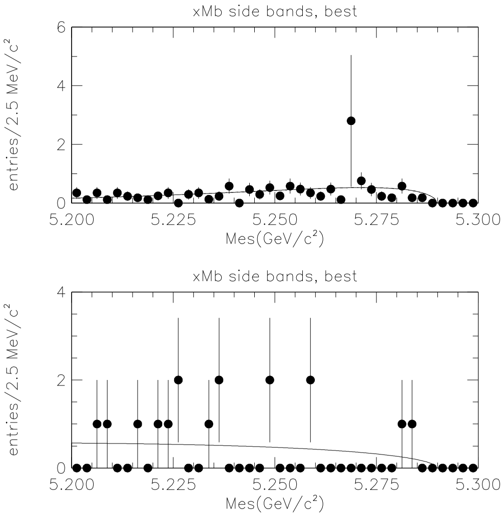

Figure 5.18: $B^0 \to \psi(2S) K^0_S$ mode: background determination via Argus fit to the ΔE sidebands for Monte Carlo (upper plot) and data (lower plot) samples. The Argus shape parameters obtained by the fit are shown in Table 5.10.

the signal fit with a Crystal Ball function have been tested separately. In the first case we want to ensure that the Argus shape given by the Monte Carlo well describes the data, in the second the stability of the Crystal Ball fit is tested with very low statistics signal samples.

5.8.1 Argus Shape Stability

Different sideband regions are used to test the stability of the Argus fit and the results are presented in Table 5.10 for both Run1 data and Monte Carlo, using $B^{\pm} \to \psi(2S) K^{\pm}$ selected events. We expect the background shape in the (m_{ES}, ΔE) region called 'B' in Fig. 5.14 to give the best description of the Argus shape in the signal region.

For the background Monte Carlo sample the regions B and C+D(sidebands) have been studied in order to estimate how the Argus shape changes when going from ΔE sidebands to ΔE signal band, for events outside the signal box. Events in these two regions have largely different kinematic properties because they receive different relative contributions from continuum and from inclusive $\psi(2S)/J/\psi$ events. The resulting Argus shape parameters ξ vary therefore from one region to the other, but their values are equal within the errors.

For on-peak data the fitting background shape has been checked in all the regions outside the signal box: B, C+D (sidebands) and B+D+E. Due to the low statistics of the sample, the comparison with the expected values from Monte Carlo sample has a small significance, but the Argus shapes in the B region, that is the part of background we better want to model, are in good agreement.

The background shape from Monte Carlo in the B region is taken as the best parameterization of what we expect in the signal region: $\xi = (-38.0 \pm 18.9)$ for the $B^{\pm}\to\psi(2S)K^{\pm}$ mode and $\xi = (-14.4 \pm 30.1)$ for the $B^0\to\psi(2S)K^0_S$ mode. In the extraction of the signal yield, the ξ value will be fixed at these values. The systematics coming from our choice of modelling and fitting the Argus background will be accounted for in the final systematic error.

Sample	Region	ΔE	m_{ES}	ξ
$\boldsymbol{B^{\pm}\to\psi(2S)K^{\pm}}$				
Monte Carlo	B	[-0.040;0.030]	<5.26	$-38.0\pm$ 18.9
	C+D	[-0.05;0.05]	[5.2;5.3]	$-60.6\pm$ 19.5
Run1 Data on-peak	B	[-0.040;0.030]	<5.26	$-47.9\pm$ 36.1
	C+D	[-0.05;0.05]	[5.2;5.3]	$-107.2\pm$ 21.
	B+D+E	[-0.120;0.120]	<5.26	$-86.2\pm$ 20.5

Table 5.10: Fit stability study on the $B^{\pm}\to\psi(2S)K^{\pm}$ sample: Argus shape parameters ξ obtained as the results of numerical fitting of the m_{ES} distribution within different (m_{ES}, ΔE) regions, defined in figure 5.14 .

5.8.2 Crystal Ball Stability

As far as the signal is concerned, the Crystal Ball model well describes the expected m_{ES} spectrum, as already discussed. The expected values for the parameters of the function have been already presented in Table 5.4 as extracted from the signal Monte Carlo samples. The stability of different Crystal Ball procedures have then been tested on Monte Carlo samples corresponding to the same luminosity as expected from the available data sample: the fit is repeated on 20 samples with a corresponding $\sim$44.7 fb^{-1} integrated luminosity. The mean and σ values have been fixed at the values found from the entire samples (20,000 events), while the n and α Crystal Ball parameters have been estimated. The complete convergence of the fit largely depends on these last two parameters which describe the low mass tail in the m_{ES} spectrum and make sure that the function is continuous in the crossover point to the gaussain peak. The 20 fits have been repeated fixing α and n at a time since, as visible in Fig. 5.19, leaving both the parameters free is not always expected to converge on a limitated sample of data. To ensure convergence

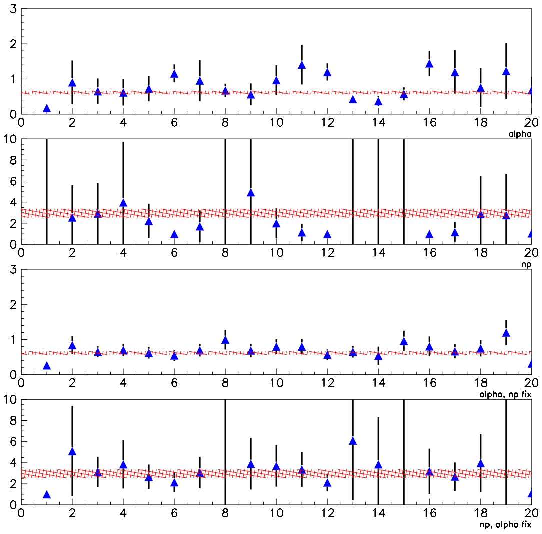

Figure 5.19: Crystall Ball fit stability check: α and n parameters are measured in different 44.7 fb^{-1} luminosity samples, with σ and mean values fixed (first two plots) and with all other parameters fixed (lower two plots). The red stripes are the values, with their errors, that are extracted from the entire Monte Carlo sample and then are used in the data fits.

in the fit procedure applied on data sample, all the Crystal Ball parameters are fixed at the values extracted from the high statistic Monte Carlo samples.

5.9 Data Fit and Yields

The preliminary Monte Carlo studies predict a small yield for both the neutral and the charged B meson decays that we are analyzing. During the analysis, the results from the search on data of the charged B mode $B^{\pm}\to\psi(2S)K^{\pm}$ were firstly unblinded, because of to the higher statistics expected on the 44.7 fb^{-1} data sample. Then I checked the validity of the selection procedure through the comparison with the number of Monte Carlo predicted events inside the signal box and the data yield.

The yield of candidate events in the data is determined using the following procedure:

- The number of events $N_{\rm cand}$ in the signal box in the (ΔE,m_{ES}) plane is counted. Figure 5.20 shows the ΔE and m_{ES} spectra for $B^{\pm}\to\psi(2S)K^{\pm}$ and $B^0\to\psi(2S)K^0_S$ decay modes on data.
- The distribution of m_{ES} for candidates in the grand sidebands which lie within the ΔE signal band (A+B) is fitted with a Crystal Ball

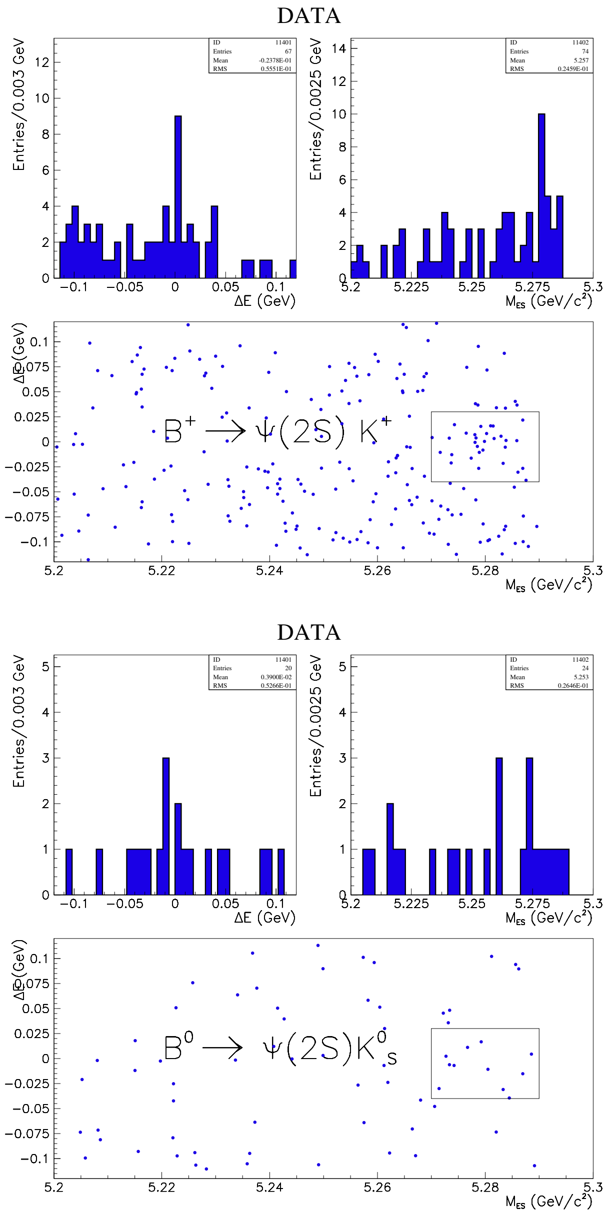

Figure 5.20: ΔE, m_{ES} distributions and ΔE vs m_{ES} plot in the $B^{\pm}\rightarrow\psi(2S)K^{\pm}$ (upper plot) and $B^0\rightarrow\psi(2S)K_S^0$ (lower plot) decay modes on data.

Sample	N_{cand}	N_{peak}	$\eta_{\mathrm{peak}} = \frac{N_{\mathrm{peak}}}{N_{\mathrm{cand}}}$	$\frac{N_{\mathrm{peak}}}{N_B}$
$\boldsymbol{B^{\pm}\rightarrow\psi(2S)K^{\pm}}$				
Data	32	21.5 ± 5.5	0.67 ± 0.08	2.04 ± 0.65
$\boldsymbol{B^{0}\rightarrow\psi(2S)K^{0}_{s}}$				
Data	10	7.9 ± 3.2	0.79 ± 0.13	3.76 ± 1.50

Table 5.11: Yields of N_{cand} and $N_{\mathrm{peak}} = N_{\mathrm{cand}} - N_B$ from the fit on m_{ES} in data: also purity and signal over background ratios are shown.

signal and an Argus function background parameterisation, as shown in Figure 5.21. In the fit the shape parameter of the Argus function and all the Crystal Ball parameters are fixed at the Monte Carlo predictions. The Argus function is subsequently integrated across the m_{ES} signal range limit to determine the background (N_B) and the signal peak (N_{peak}).

- The size of the feed across background from other $\psi(2S)$ and J/ψ decay channels which peaks under the signal in m_{ES} (N_{PB}) is determined from inclusive J/ψ and $\psi(2S)$ Monte Carlo samples.

The signal yield is defined as

$$N_S = N_{\mathrm{cand}} - N_B - N_{PB}. \tag{5.6}$$

Table 5.11 lists the results from the m_{ES} fit in term of the peaking and argus components: the yields determined for each of the decay channels, the purity of the selections and the signal over background ratio as extrapolated from the data samples.

The distributions of the $\psi(2S)$ mass difference ΔM and of the ΔE from real data are shown in Figures 5.22, with the Monte Carlo predictions superimposed.

5.10 Systematics on Decay Fraction Measurements

The Monte Carlo simulation does not adequately represent the data and some corrections are needed: they are summarized here with the corrisponding errors. Many of these corrections are referred to the Run1 data set, since no Run2 data corrections are available up to now. In order to extend the branching ratio measurements to both data sets, the same correction factors and systematical errors are taken as from Run1 data.

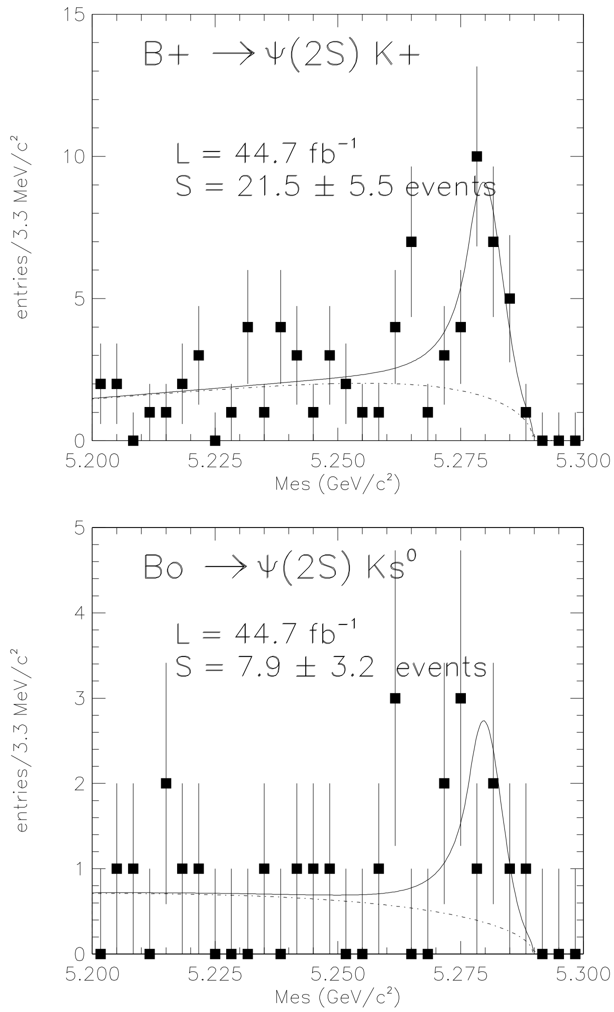

Figure 5.21: Signal yields and m_{ES} fit on Data for $B^{\pm}\to\psi(2S)K^{\pm}$ and $B^0\to\psi(2S)K^0_s$ modes.

Momentum resolution

The momentum resolution is worse in data than in Monte Carlo, likely because the amount of material in the simulation is underestimated, and also for an incorrect determination of the SVT/DCH alignment. Moreover uncertainties in the magnetic field, in SVT alignment and detector geometry can lead to difference in momentum scale. Both effects lead to a different ΔE resolution in data and Monte Carlo. To account for it, the signal efficiency is corrected by introducing an artificial bias on the transverse momentum p_t and increasing the p_t resolution in the full simulation. The $J/\psi\,(\mu\mu)K^+$ sample was used to determine the size of the smearing and the shifting of the momentum scale required in the Monte Carlo such that it matches the ΔE

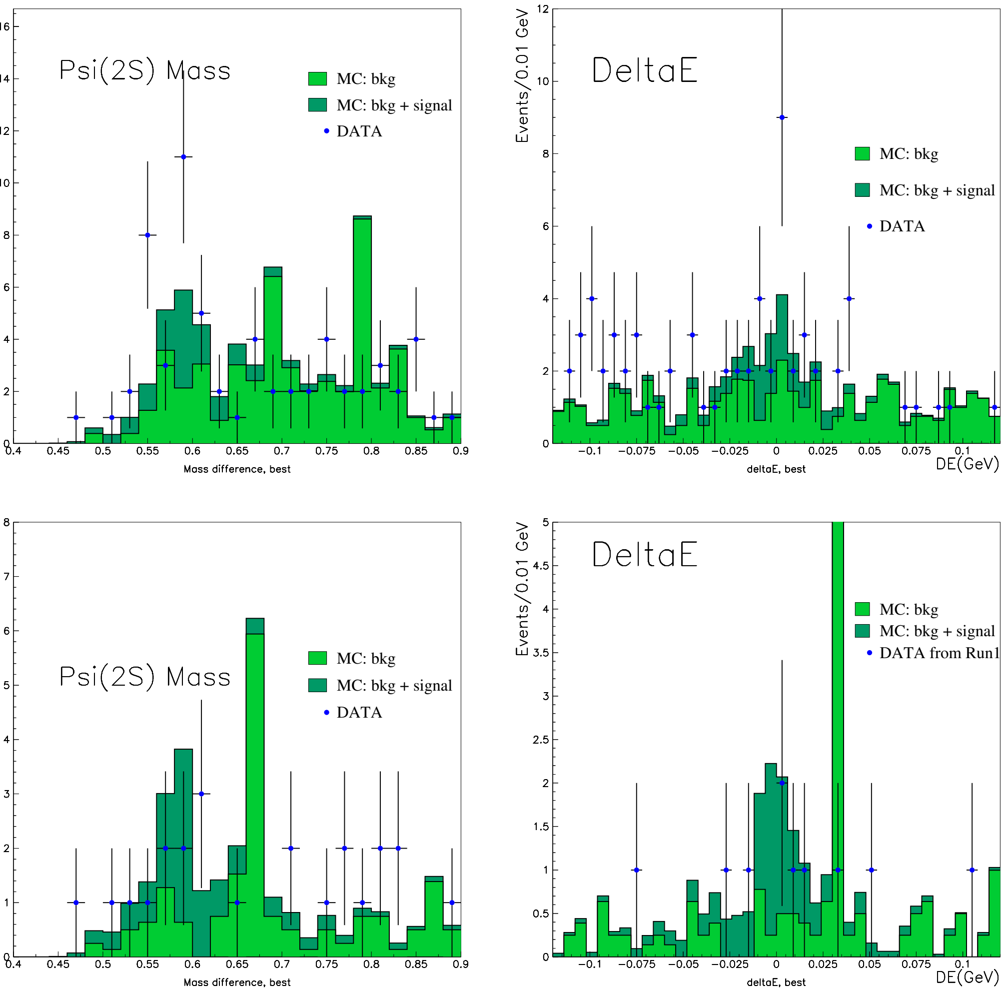

Figure 5.22: Data - Monte Carlo Comparisons. Upper plots: $\psi(2S)$ ΔM and ΔE distributions for $B^{\pm}\rightarrow\psi(2S)K^{\pm}$ events. Lower plots: $\psi(2S)$ ΔM and ΔE distributions for $B^0\rightarrow\psi(2S)K^0_S$ events. Due to the low statistics, the mass and energy resolutions from the data samples cannot be evaluated.

resolution and reproduces the J/ψ mass and width observed in data. Two sets of value for the smaearing scaling factor were found for the two Run1 data blocks (1900 Volt: 1.32 $\pm$ 0.13 ; 1960 Volt: 1.13 $\pm$ 0.13) [77]. The size of the shift was found to be 2.3% and 2.0% for $\psi(2S)K^{\pm}$ and $\psi(2S)K^0_S$ respectively. The corresponding systematic error on the branching ratio measurement has been determined by varying the smearing parameters within the their errors.

Track finding efficiency

One of the largest systematics error in the branching ratios measurements arises from the DCH uncertainties in tracking efficiency. Having *BABAR* two devices (DCH and SVT) that give independent tracks reconstruction, efficiency of each device can be computed using the other as a trigger. In practice measuring SVT efficiency turns out to be more complicated and less useful for the following reason:

- all long-lived particles (such as K^0_S) may decay outside the SVT volume, so SVT calibration for these particles would be less known.
- in the reconstruction sequence SVT tracks are found as an extension inward from the DCH, with a consistency test. So its efficiency is correlated to the DCH one.
- `GoodTracksLoose` selection contains the minimum DCH hit requirements on a track (12 at least). Infact the only other requirements are that the tracks point back to the beamspot within a area much larger than the DCH resolution, which is uninfluent.

Efficiency tables have been computed in order to weigh the Monte Carlo tracks according to differences between Run1 data and Monte Carlo, as a function of p_t, θ, ϕ and event multeplicity. The method used for creating these tables is described in [38] and uses all events passing the $B\overline{B}$ event selection. Two sets of tables have been created for the two Run 1 data blocks of Table 5.1. The associated systematic error is 1.2% for each `GoodtracksLoose` used, to be added linearly.

Photon efficiency

The incorrect description of the EMC efficiency and resolution for neutral particles described in Section 3.3.4 must also be included. Comparisons between data and Monte Carlo report small differences in the neutral reconstruction and identification efficiency due to an incorrect description of the detector model in the `Geant3` simulation. To determine the systematic error from these effects the Monte Carlo is subjected to a technique which smears the photon energies, shifts the π^0 peak and randomly kills photon clusters according to the evaluated uncertainties. The change in the selection efficiency is included in the systematic error.

PID selectors inefficiency

The performances of the different PID selectors are not necessarily well modelled in MonteCarlo, but the difference is checked from data control samples and summarized into PID efficiency and mis-identification tables. A PID killing procedure is done at the reconstruction level, weigthing each track identified by Monte Carlo truth with the corrisponding PID selector probability as a function of its θ, ϕ, charge and momentum.

- **Electrons and Muons**
  For all lepton ID criteria, efficiencies calculated from the standard particle identification tables are compared to the efficiencies measured by fitting the inclusive J/ψ yields in *BABAR* Run1 data. The differences are used to calculate the correction factors and their systematics errors [80], found as 1.6% for electrons and 1.1% for muons for both the branching ratios measurements.

- **Kaons**
  An estimate of the systematic error associated with the Kaon efficiency calculation is taken [81] from varying the background subtraction procedure in the D^* based kaon control sample. Its value is 1.36% to be added linearly, given by summing the contributions from the counting method (0.8%) and the Monte Carlo truth difference (1.1%). Moreover a 0.4% error must be added quadratically, due to the statistics from the control sample in the background subtraction, and a 0.8% from the statistics included in the tables. Hence the systematics should be 1.6% for one kaon selection and the same is taken in the $B^{\pm}\to\psi(2S)K^{\pm}$ branching ratio measurement since no correction is found from the killing tables.

K^0_S efficiency

The uncertainty in the K^0_S efficiency has three components: one associated with the selection of the sample of K^0_S used to determine the efficiency correction, one from the statistical error on the efficiency correction and one from the difference in tracking efficiency for charged tracks from K^0_S decays in data and Monte Carlo. The first of these components is determined by comparing the efficiency corrections obtained from two different selections of an inclusive K^0_S sample. The third component is determined to be 1% per track. The component of the error associated with the tracking efficiency is combined linearly with the other systematic from tracking efficiency detailed above. The other components of the systematic for the K^0_S efficiency are added in quadrature, with the final 1.2% error on the branching ratio mesurement.

Background parametrization

A source of systematics is the uncertainty in the shape of the Argus function which is used to model the background. The systematic error from this purely statistic effect is however included in the systematic constribution from the choice of fitting procedure. In the fit, the parameters of the Argus function and of the Crystal Ball function are constrained to those obtained from fits to the corresponding Monte Carlo samples. To account for it, additional fits are performed where the ξ parameter of the Argus function and the α and n parameters of the Crystal Ball function are released, either one at a time or all together. The largest difference on the branching ratio value is taken as the systematic error.

Moreover the uncertainty in the size of the peaking component of the background must be taken into account. It's mainly the statistical error on the Monte Carlo samples used to extract this component.

Cut selection efficiency

The last component in the systematic errors is due to differences in the distributions of the cut variables between data and Monte Carlo. For each variable used to define the signal sample, the cut range values are varied by small steps, which are defined in table 5.12, from the chosen value and the branching fraction calculation repeated. Since no difference is found in the branching ratio values within the statistical error, as one can see in Fig. 5.23, the larger variation divided by $\sqrt{12}$ is taken as the systematic error.

Then the branching ratio measurement is repeated with and without the selection of a unique candidate (using the minimum $|\Delta E|$ value) in order to estimate the error on the efficiency calculation brought by this method, which is 1.8%.

Moreover we can consider other effects as sources of systematic errors: a 1.6% systematic error on the number of the produced $B\overline{B}$ events, the uncertaintly on the branching fractions of the secondary decays (from PDG 2000) and the uncertaintly on the efficiency calculation arising from the limitated Monte Carlo statistics.

The errors described above are all summarized in Table 5.13; they are combined quadratically to provide the total value of the relative systematic

Table 5.12: Cut Variations for systematic error determination

Cut	Step Variation
$\pi^0\pi^0$ Inv. Mass	± 2 MeV
ψ(2S) Mass	± 10 MeV
π^0 Mass	± 3 MeV
Helicity	± 0.025
Thrust Angle	± 0.05
$K^0_S(\pi^+\pi^-)$ Mass	$\pm 1\sigma$
K^0_S flight length	Remove cut
ΔE range	± 10 MeV

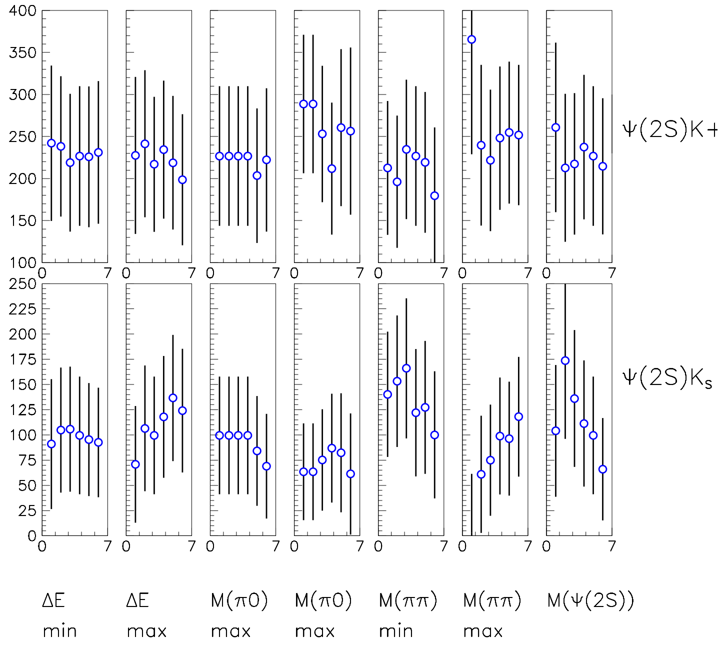

Figure 5.23: Branching ratio cut variations for the two B modes for the more relevant selection variables. Units are arbitrary.

error on the Branching Ratio. The low statistics of the neutral B decay events sample also affects the systematic uncertainty on its branching fraction.

Mode	Parameters									
	PBr	PID	σ_p	ϵ_{Trk}	ϵ_γ	Bkg	MC	$N_{B\overline{B}}$	Cuts	Tot
$\psi(2S)K^\pm$	12.7	2.5	1.2	3.6	9.1	8.6	1.6	1.6	10.1	21.1
$\psi(2S)K^0_S$	12.7	2.5	2.2	4.8	8.4	29.8	1.5	1.6	26.2	43.0

Table 5.13: Summary of the % systematic errors used in the branching fraction measurements. They include: Product of Branching Fractions (PBr), Particle Identification (PID), Track Momentum resolution (σ_p), Tracking Efficiency (ϵ_{Trk}), Neutral Efficiency (ϵ_γ), Backgrounds Parameterizations (Bkg), Monte Carlo Statistics (MC), B Counting and cut selection. The total (Tot) is given in the last column.

5.11 Summary of Branching Ratio Measurements

We determine branching fractions for $B^\pm \to \psi(2S)K^\pm$ and $B \to \psi(2S)K^0_S$ decays using the individual efficiencies reported in Section 5.5. Branching fractions are calculated as

$$\mathcal{B} = \frac{N_S}{\epsilon \times N_{B\overline{B}} \times \Pi_i f_i}, \tag{5.7}$$

where N_S comes from the m_{ES} fit described in Section 5.9, $N_{B\overline{B}} = (50.5 \pm 1.2) \times 10^6$ is the total number of $B\overline{B}$ pairs in our dataset, ϵ is the total efficiency and f_i are the associated branching fraction (as quoted from PDG 2000 and listed in Table 3.2) of all the secondary decays considered. Implicit in Eq. 5.7 is the assumption of equal branching fractions for $\Upsilon(4S) \to B^0\overline{B}^0$ and $\Upsilon(4S) \to B^+B^-$. The statistical error on the branching ratio measurement is determined as

$$\sigma_{\mathcal{B}} = \frac{\sqrt{N_{\text{cand}}}}{\epsilon \times N_{B\overline{B}} \times \Pi_i f_i} \tag{5.8}$$

the simply statistical fluctuation with respect to the total of the selected events, and doesn't reflect the statistical contribution of the background subtraction, which is included in the systematic errors.

Finally the results on the branching ratio measurements are summarized in Tab. 5.14. The values are 1 σ consistent with those obtained using other samples of *BABAR* data listed in Table 3.1 (the table provides the $B^0 \to \psi(2S)K^0$ branching ratio, which is two times the $B^0 \to \psi(2S)K^0_S$ I've measured).

Sample	Obs. Yield	Background Argus	Background Peaking	Eff. (%)	$\mathcal{B}\pm\sigma(\text{stat})\pm\sigma(\text{syst})$ $/10^{-4}$
$\boldsymbol{B^{\pm}\to\psi(2S)K^{\pm}}$	32	10.5	3.7	4.9 ± 1.6	3.3 ± 1.1 ± 0.8
$\boldsymbol{B^{0}\to\psi(2S)K_s^{0}}$	10	2.1	1.8	4.2 ± 1.5	3.9 ± 2.1 ± 1.7

Table 5.14: Summary of branching fraction results
Shown are the sample yields N_{cand}, the background composition numbers, the Monte Carlo efficiency ϵ and the measured branching fractions $\mathcal{B}$. For $\mathcal{B}$ the first error is statistical and the second is systematic.

Chapter 6

Measurement of $\sin 2\beta$ in Exclusive Charmonium Channels

The aim of the analysis presented so far is to collect a pure and independent sample of events produced by the $B^0 \to \psi(2S) K^0_S$ decay process. 10 signal events have been selected in the available data sample, with a corresponding 70% purity and the result from the branching ratio measurement confirms the validity of the selection. Each of the events passing the selection will provide information on the *CP* asymmetry through the analysis of the time evolution of the decay.

This Chapter describes the main steps leading to time dependent CP asymmetry measurements, referring to the analysis that brought to the first *BABAR* results and that will be mainly repeated using the next increased sample of data. The description is focalized on the results obtained from the $B^0 \to \psi(2S) K^0_S$ sample, where the events selected with the analysis presented in this thesis are not included. As a first step to extract CP asymmetry, each event of the selected sample is tagged by the flavor of the other B meson coming from the $\Upsilon(4S)$ decay. Tagging efficiency in *BABAR* is around 70%, thus about one third of the events do not survive. All events with the same *CP* eigenvalue (± 1) in the final state are grouped together, and the algorithm to extract the $\sin 2\beta$ value is then applied to the whole sample.

The primary ingredients of the experimantal measurement, namely the tagging efficiency and dilutions and the Δt resolution function, play an important role, as well as the purity of the sample and the residual background contamination.

The procedure described below has been followed by the *BABAR* $\sin 2\beta$ Working Group, in order to achieve the latest $\sin 2\beta$ measurement on the

$29.7\,\mathrm{fb}^{-1}$ *BABAR* data sample (recoredered up to June 2001). This measure has been presented during the International Europhysics Conference on High Energy Physics (HEP 2001), Budapest [85] and published in [86]. At this time the detailed results are going to be published by Phys.Rev.D [87], so that one can refer to this reference for further details. This measure claimed the observation of *CP* violating asymmetry in the B meson system, since the value $\sin 2\beta = 0.59 \pm 0.14\,(\mathrm{stat}) \pm 0.05\,(\mathrm{syst})$ demonstrates at the 4.1σ level that *CP* violation exists in this system. Concurrently no direct *CP* violation is expected, since $|\lambda| = 0.93 \pm 0.09$ (stat) $\pm\, 0.03$ (syst) is consistent with the expectation of $|\lambda| = 1$. These results are also consistent with the previous results released by the *BABAR* Collaboration [88]. Next measurement with an enlarged statistics will be provided for the next 2002 Winter Conferences.

The theoretical approach for the CP asymmetry measurement in a B Factory has been already described in Chapter 1. The analysis consists of different parts which are in order: choosing the optimal B meson samples, determining the flavor through the tagging procedures, then measuring the distance Δt between the two B decays and performing a Log Likelihood study to extract the $\sin 2\beta$ value. The last part of this section is dedicated to a discussion of the results in the CKM framework, throughout a comparison with some indirect measurements within the Standard Model.

6.1 B Meson Samples

The measurement of the time-dependent *CP* asymmetry in a B-Factory needs more than one B meson sample: the *CP* eigenstates B_{CP} and the flavor eigenstates B_{flav}, both need to be tagged by the flavor of other B (B_{tag}) coming from the $\Upsilon(4S)$ decay. Before any tagging requirements the following sample have been used in the latest $\sin 2\beta$ measurement:

$\boldsymbol{B_{CP}}$ sample contains the final states $B^0 \to J/\psi\, K^0_S$, $\psi(2S)K^0_S$, $\chi_{c1}K^0_S$, $J/\psi\, K^{*0}$ ($K^{*0} \to K^0_S\pi^0$) and $J/\psi\, K^0_L$.

$\boldsymbol{B_{\mathrm{flav}}}$ sample contains two samples of hadronic final states: $b{\to}c\overline{u}d$ open charm decays, such as $B^0 \to D^{(*)-}\pi^+$, $D^{(*)-}\rho^+$, $D^{(*)-}a_1^+$, and charmonium decays $b{\to}(c\overline{c})s$, like $J/\psi\, K^{*0}(K^+\pi^-)$; in addition the semileptonic decay mode $B^0 \to D^{*-}\ell^+\nu$ is considered.

$\boldsymbol{B^{\pm}}$ In some cases, control samples of charged B decays are studied, where the hadronic final states $B^+ \to \overline{D}^{(*)0}\pi^+$, $J/\psi\, K^{(*)+}$, $\psi(2S)K^+$ and $\chi_{c1}K^+$ are used.

All final state particles, with the exception of the neutrino in the semileptonic decay, are reconstructed following the same prescriptions and reconstruction algorithms used for the Branching Fractions measurements [89] and that are similar to those described in Chapters 3 used for this analysis. A summary of the various reconstructed B_{CP} samples and purities extracted from fits to the m_{ES} distribution is provided in Table 6.1.

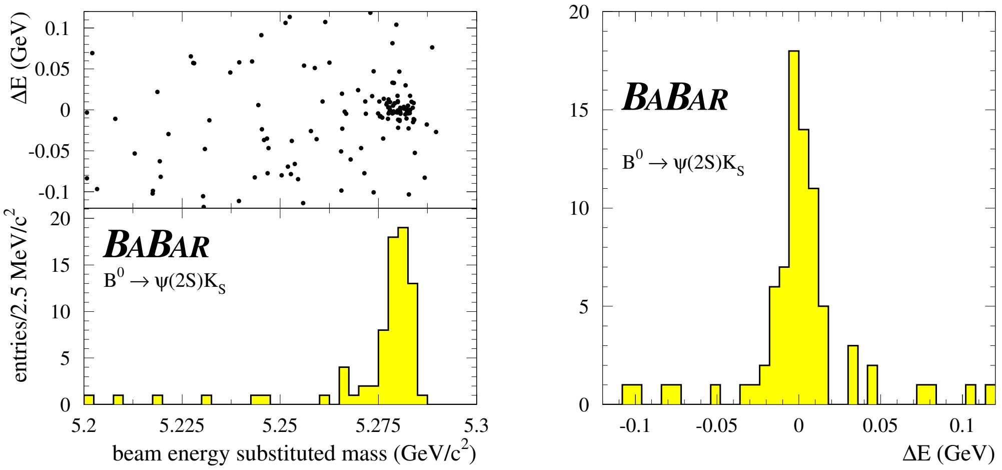

Figure 6.1: m_{ES} and ΔE distributions for the selected CP-eigenstate $B^0 \to \psi(2S)K^0_S$ candidates, with $\psi(2S)$ mesons reconstructed in the $J/\psi\pi^+\pi^-$ and $\ell^+\ell^-$ decays.

The final state $\psi(2S)K^0_S$ includes 86 ± 17 $\psi(2S)$ mesons reconstructed in $\ell^+\ell^-$ and $J/\psi\pi^+\pi^-$ decays only, with a 96% purity. Figure 6.1 shows the m_{ES} and ΔE distribution of the CP-sample with the two-dimensional signal plot. The m_{ES} distribution is fitted with a Gaussian distribution for the signal and an Argus background form. The complete sample of all the hadronic B_{CP} modes are shown in Fig. 6.2.

6.2 B Tagging

The time-dependent CP asymmetry is measured whenever two quantities are estabilshed: the time difference $\Delta t = t_{CP} - t_{\rm tag}$ between the decay of the CP mode B meson B_{CP} and the recoiling meson $B_{\rm tag}$; and the flavor of the b-quark in this tagging B.

The b-quark flavor is derived from the correlation between the sign of the charge of the quark and signed characteristics of the decay products.

The most simple example of such correlation are decays with a lepton in the final state. There are two possibilities:

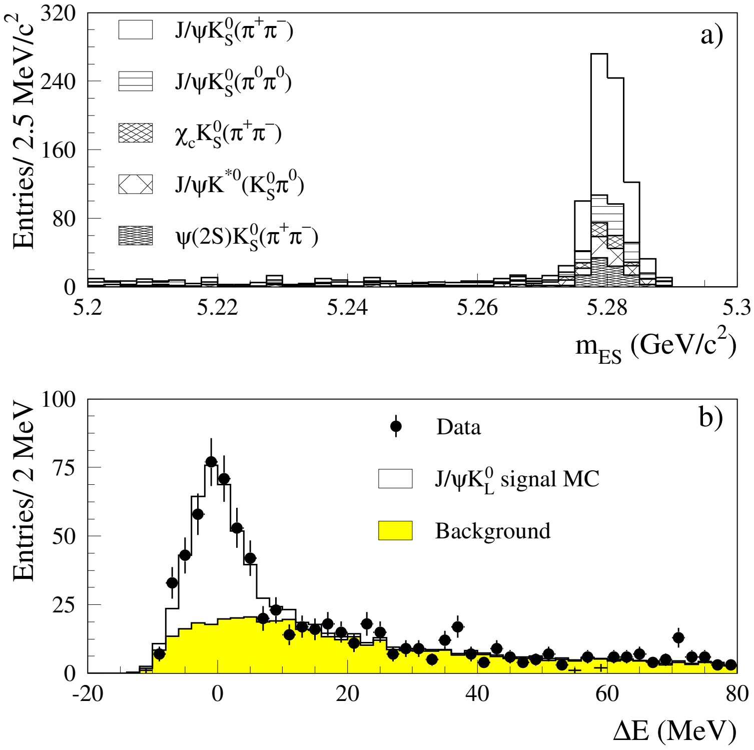

Figure 6.2: The complete sample of B mesons decaying into CP-eigenstates used for the $\sin 2\beta$ measurement: $CP = -1$ in the upper plot, $CP = +1$ in the lower plot.

Table 6.1: Event yields for the different B_{CP} samples used to measure $\sin 2\beta$ before any tagging or tagging vertex requirements. The yields, purity, and signal size for B decays to hadronic final states are obtained from a fit to the m_{ES} distribution. The results for $J/\psi K^0_L$ are obtained from a fit to the ΔE distribution for events with $\Delta E < 10\,\mathrm{MeV}$.

Final state	Signal	Purity (%)
$J/\psi K^0_S$ ($K^0_S \to \pi^+\pi^-$)	461 ± 22	99
$J/\psi K^0_S$ ($K^0_S \to \pi^0\pi^0$)	113 ± 12	93
$\psi(2S) K^0_S$	86 ± 17	96
$\chi_{c1} K^0_S$	44 ± 8	98
$J/\psi K^{*0}$ ($K^{*0} \to K^0_S \pi^0$)	64 ± 10	74
$J/\psi K^0_L$	257 ± 24	60
Total	1025 ± 41	83

1. *direct-sign* decays: semileptonic decays of the B or cascade decays in which the lepton has the same sign of the b quark,

2. *reverse-sign* decays, cascade decays with the lepton of opposite sign.

Whereas it is not possible to distinguish between the two types of cascade decays, leptons from the semileptonic decays ($b \to c$) are in general harder (in the $\Upsilon(4S)$ reference frame) than those from cascade decays [1].

The flavor tagging uses an hybrid algorithm, which classifies events with clearly identified tagged final state through a cut-based selection, while uses the output of a neural network algorithm to tag the remaining events. The main motivation of using a hybrid algorithm is that about 55% of the events cannot be tagged in a cut-based way, nor much performance can be gained with a probability based algorithm for these events, while on the other hand with a cut-based approach systematics are easier to assess.

Four different tagging categories have been used: the first two use rely upon the presence of a prompt lepton or one or several charged kaons, the next two make use of a neural network algorithm to exploit a variety of inputs. These categories are hierarchical and mutually exclusive. The `Lepton` and `Kaon` tagging categories use the correlation between the flavor of the decaying b quark and the charge of a primary lepton from a semileptonic decay (both

[1] This due both to the kinematic difference between B mesons decays and charmed meson secondary decays and to the opposite helicity of c quarks with respect to the b quarks.

electrons and muons with the appropriate selection cuts) or the charge of a kaon from the chain $b \to c \to s$. All the tracks passing a track-quality selection are used to tag leptons and kaons, while very tight requirements for leptons and looser for kaons are preferred for an optimal tagging performance.

Hence if there is a selected high momentum lepton ($p^* > 1.0\,\mathrm{GeV/c}$ for electrons and $p^* > 1.1\,\mathrm{GeV/c}$ for muons), the event is assigned to the `Lepton` category unless the sum of the charges of any kaons present has the opposite sign. Next, events are assigned to the `Kaon` category if the sum of the kaon charge is non-zero, but roughly 15% of these events have wrong-sign charge due to B decays into two charmed mesons.

All remaining events, approximately 55% of the total including those with inconsistent lepton and kaon charge (0.5% of all events in simulation) and those with two oppositely-charged kaons (4.6% of all events in simulation), are passed to the neural-network-based categories. These use other, less effective, features wich include: soft pions from D^* decays, high-momentum primary leptons that are not selected by the electron or muon identification algorithms, lower-momentum primary leptons, and charged kaons that are not selected by the kaon identification algorithm. Combining all these sources with a multivariate method, the final neural network produces an output, x_{NT}, mapped onto the interval $[-1, 1]$:

- The assigned flavor tag is B^0 if x_{NT} is negative, and $\overline{B}^0$ otherwise.
- Events with $|x_{NT}| > 0.5$ are assigned to the `NT1` tagging category
- Events with $0.2 < |x_{NT}| < 0.5$ are assigned to the `NT2` tagging category
- Events with $|x_{NT}| < 0.2$, approximately 30% of the total, have very little tagging power and are rejected.

The distribution of x_{NT} for all events not assigned to the `Lepton` or `Kaon` category is shown in Fig. 6.3a.

The tagging algorithm performs the most efficienct discrimination between these classes.

As a measurement of the discriminating power of each tagging category, the effective tagging efficiency is defined, $Q_i = \epsilon_i\,(1 - 2w_i)^2$, where ϵ_i is the fraction of events associated to the tagging category i and w_i is the mistag fraction, the probability of incorrectly assigning the tag to an event in this category. As already mentioned $\mathcal{D} = (1 - 2w)$ is the dilution factor that reproduces the tagging separation. The statistical errors in the measurements of the asymmetry for events tagged in a given category i are inversely proportional to $\sqrt{\sum_i Q_i}$. Thus, as far as CP violation is concerned, maximizing

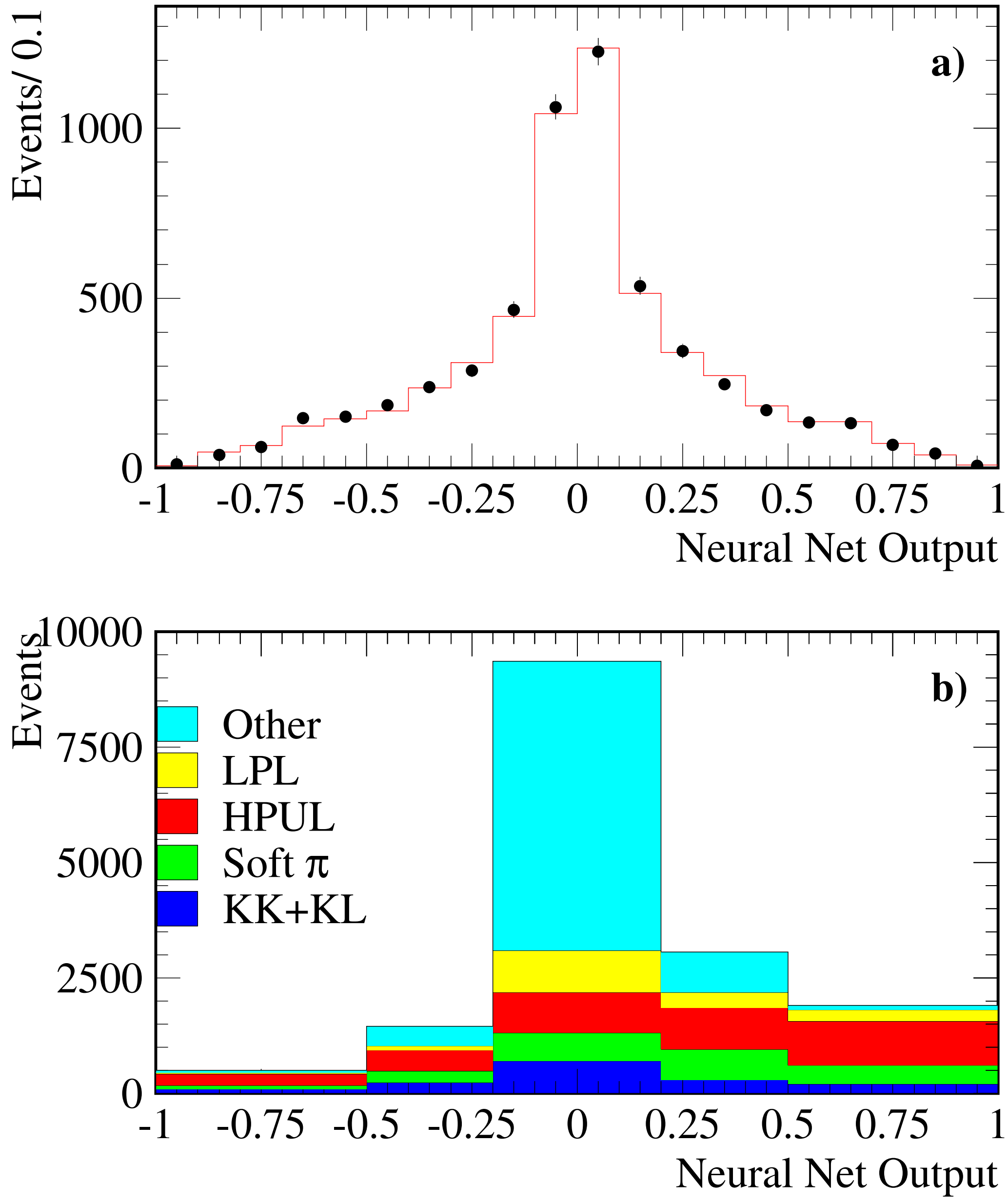

Figure 6.3: a) Output of the final neural network for events that are not assigned to the `Lepton` or `Kaon` category, where the points are from the B_{flav} data after a background subtraction and the histogram is simulation; b) Neural network output from B^0 simulation, again for events not in the `Lepton` or `Kaon` category, where the breakdown in events is, from bottom to top: events with two kaons or a kaon and lepton (KK+KL), events with a soft pion, events with a high momentum unidentified lepton (HMUL), events with a lower momentum lepton (LPL), and all remaining events. The outermost bins correspond to the category `NT1`, the next to `NT2`. The center bin contains events for which no tag is assigned.

the absolute separation:

$$S^2 = \sum_{\text{category}} \epsilon_i \left(1 - 2w_i\right)^2 \tag{6.1}$$

plays a crucial role in order to maximize the sensitivity of the measurement. While the tagging algorithm was optimized and the neural networks were trained with Monte Carlo simulations only, the mistag fractions w_i are measured directly on data, using the B_{flav} sample. Thus discrepancies between performance in Monte Carlo and data do not contribute to the systematic uncertainty of the *CP* violation measurements. The probabilities of mistagging a B^0 or $\overline{B}^0$ meson are expected to be very nearly, but not exactly equal. The response of the detector to positive pions and kaons differs from its response to negative pions and kaons due to differences in total and charge-exchange cross sections. To account for any possible mistag difference, separate mistag probabilities w are introduced for B^0 and $\overline{w}$ for $\overline{B}^0$.

Simulation studies indicate that roughly 37% of the effective tagging efficiency in this sample is due to events with unidentified primary leptons, 28% is due to events with a soft pion, a further 11% from events with a lower momentum primary lepton, and the remainder from a mixture of the various inputs. This classification is shown for the `NT1` and `NT2` categories in Fig. 6.3b for a simulation of B^0 decays.

6.3 Measurement of Δt

The difference between the B decay time, $\Delta t = t_{CP} - t_{\text{tag}}$, is determined from the measured separation Δz between the vertex of the reconstructed B meson (B_{rec}) and the vertex of the flavor-tagging B meson (B_{tag}) along the z axis. This distance must be reconstructed from the products of the decay chain, since it's not observable for the absence of charged stable particles emerging from the $\Upsilon(4S)$ decay point [2].

To retain high efficiency, the fully reconstructed B_{CP} is kinematically vertexed using all the particles of the decay chain identified as charged tracks, while the B_{tag} vertex is reconstructed with an inclusive approach, using the remaining charged tracks in the event (see Fig. 6.4). A number of requirements are made in order to ensure a well-determined vertex separation [87]. The efficiency in data and Monte Carlo simulation is about 97% for all reconstructed B modes, and from simulation no dependence on the true value of

[2] This is different from Z^0 peak or hadronic collider experiments, where the production point can be reconstructed from fragmentation particles.

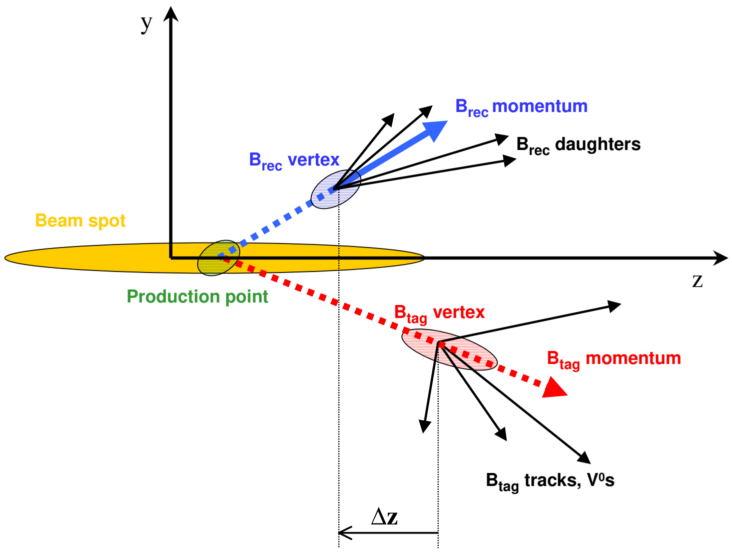

Figure 6.4: Schematic view of the geometry in the yz plane for a $\Upsilon(4S) \to B\overline{B}$ decay. For fully reconstructed decay modes, the line of flight of the $B_{\rm tag}$ can be estimated from the (reverse) momentum vector and the vertex position of $B_{\rm CP}$, and from the beam spot position in the xy plane and the $\Upsilon(4S)$ average boost. Note that the scale in the y direction is substantially magnified compared to that in the z direction.

Δt is found. By far the dominant limitation on the accuracy with which Δt is determined from the measured decay length difference Δz is the experimental resolution on the Δz measurement.

Event-per-event the reconstructed Δz and an estimate $\sigma_{\Delta z}$ of its uncertainty is calculated. A time-dependent analysis must estimate Δt as:

$$\Delta t = t_{CP} - t_{\rm tag} = M_B \left[\frac{z_{CP}}{p_{z,CP}} - \frac{z_{\rm tag}}{p_{z,{\rm tag}}} \right] \tag{6.2}$$

where t_{CP} and $t_{\rm tag}$ are defined in different frames. The standard approach in *BABAR* consists in assuming that both B's have the same average boost, $p_{z,CP} = p_{z,{\rm tag}} \approx \langle p_z \rangle$, and take it to be the same as for the $\Upsilon(4S)$ frame. This is equivalent to neglect the momentum of the B mesons in the $\Upsilon(4S)$ decay frame ($\langle p_B^{cms} \rangle = \sqrt{E_{e^+}E_{e^-} - M_B^2} \approx 340$ MeV/c). With these assumptions,

$$\Delta t = \Delta z / \gamma\, \beta_z\, c \tag{6.3}$$

where γ is the boost factor of the $\Upsilon(4S)$ in the laboratory frame and β_z its velocity projected on the z axis. At PEP-II $\beta_z\gamma$ is about 0.56, as calculated directly from the beams energy. Using β_z instead of β we account for the rotation in the (x, z) plane of the beam axis with respect to the z axis (tilt angle about 20 mrad), reducing the full boost by about 1.2 MeV/c(0.02%). As a result, there is a small boost along the x axis (about 188 MeV/c) which generates azimuthal dependencies. This has, however, no direct effect when estimating Δz. Compared with the experimental resolution on Δz, the effects on Δt produced by this approximation are small. They can eventually corrected using the reconstructed B momentum. The impact on the Δt measurement of the spread in the two beam energies, which results in a distribution of $\Upsilon(4S)$ momenta with a Gaussian width of about 6 MeV/c, is negligible.

6.3.1 Δt Resolution Function

The decay time distribution must take into account the not perfect accuracy in measuring the proper time difference Δt. Therefore the Δt reconstruction is modelled with a resolution function $\mathcal{R}(\delta_{\mathrm{t}} = \Delta t - \Delta t_{\mathrm{true}}; \hat{a})$ with resolution parameters $\hat{a}$:

$$\mathcal{F}(\Delta t) = \mathcal{R}(\delta_{\mathrm{t}}; \hat{\alpha}) \otimes \mathcal{F}(\Delta t_{\mathrm{true}}) \tag{6.4}$$

This function is represented by the sum of three gaussians, the `core`, the `tail` and the `outlier` components, with different widths and means. The widths of this residual distribution is higly correlated to the vertex fit error estimate, $\sigma_{\Delta t}$, which is derived event-by-event, in order to include any variation with all the tag-side topologies considered throughout the sample. In any case, significant information is contained in $\sigma_{\Delta t}$, proved to be correlated with the weight the long lived charm mesons have in the tagging vertex reconstruction. Therefore it's taken as a good estimation of the relative uncertainty on the Δz measure and put as one of the additional parameters $\hat{a}$ in the resolution function. The fitting functions are moreover allowed to have no zero mean to allow for residual charm decay products included in the B_{tag} vertex. This bias can be different in each tagging category, since Monte Carlo shows that lepton tag is less biased.

Since the B_{tag} vertex precision dominates the Δt resolution, no significant difference between the Δt resolution functions for the flavor-eigenstates sample and the CP-eigenstates sample is expected. Hence, identical resolution functions are used for all modes, after including the event-by-event errors as described above. The resolution function parameters are indeed extracted from the higher statistic B_{flav} sample.

Many control samples, such as D^* and continuum events, have been studied to validate these assumptions on both data and Monte Carlo and the measure of the transverse beam spot position is used to estimate the vertex resolution and bias. One of the most significant systematic effect is due to the internal SVT misalignments.

The fit on the $B_{\rm flav}$ sample from data gives the following results for $\mathcal{R}(\delta_{\rm t};\hat{\alpha})$:

1. `core` Gaussian: It contains approximately 65% of the total area and its width, rescaled by the $\sigma_{\Delta t}$ fitting error, is 110 μm (or 0.7 ps).

2. `tail` Gaussian: its width, rescaled by the $\sigma_{\Delta t}$ fitting error in the fit, is approximately 300 μm or 1.8 ps and the bias is $\delta_2 \sim -0.4$

3. `outlier` Gaussian has a fixed width of 8 ps and no offset. It account for the fewer than 1% of events with incorrectly reconstructed vertices.

The combined rms error is 1.1 ps. Separate resolution functions have been used for the data collected in year 1999 and 2000 and those collected in year 2001 due to the significant improvement in silicon vertex detector (SVT) alignment in the later period.

6.4 $\sin 2\beta$ Extraction

The value of $\sin 2\beta$ is extracted from the tagged B_{CP} sample with an unbinned maximum likelihood technique, based on $\ln \mathcal{L}_{CP}$ of Eq. 1.41. This likelihood function is made from the decay time distribution, containing the $\sin 2\beta$ parameter, the resolution function and the dilution factors for each tagging cathegory. As already mentioned, the dilutions $\mathcal{D}_i$ and Δz resolution parameters $\hat{a}_i$, also needed for the measurement, can be best determined with the much larger mixing sample, since they also appear in $\mathcal{L}_{mix}$ of Eq. 1.40. In order to properly incorporate the correlations between these parameters and $\sin 2\beta$, the fit is performed by simultaneously maximizing the sum:

$$\ln \mathcal{L}_{CP} + \ln \mathcal{L}_{\rm mix} \tag{6.5}$$

for the combined tagged $B_{\rm flav}$ and B_{CP} samples. The values of B^0 lifetime and $\Delta m_{\rm d}$ are kept fixed in extracting $\sin 2\beta$.

6.4.1 Background Parameterization

The B_{CP} sample is a collection of B mesons reconstructed in final states with a charmonium resonanace and a kaon, accompanied by a quite small background component, which can originate from either continuum or from inclusive charmonium decays, $B \to J/\psi\,\mathrm{X}$ and $B \to \psi(2\mathrm{S})\mathrm{X}$.

Since the decay time distribution of B mesons varies depending on the CP and flavor properties of the decay, the background contamination of the sample can modify the probability distributions. Hence Eqns. 1.35 and 1.37 must be extended to include a term for each significant background source. Rather than attempting to determine the various physics contributions, an empirical description is used in the likelihood fit.

As seen in the analysis described in this work, the background for the $B^0 \to \psi(2\mathrm{S})K^0_S$ channel is mostly combinatoric from inclusive charmonium decays. It's not expected to have a significant lifetime component and have, to a very good approximation, the same flavor tagging and Δt resolution properties as the signal. This may not be true for $q\overline{q}$ continuum events, hence the two types of background must be differently accounted for. Moreover the background parameterizations are allowed to differ for each tagging category i, thus for each source and tagging category we can define the fraction of background events $f_{i,b}$ and the corresponding Δt PDFs $\mathcal{B}_{\pm,i,b}$ normalized such that:

$$\int_{-\infty}^{\infty} d\Delta t(\mathcal{B}_{+,i,\beta} + \mathcal{B}_{-,i,\beta}) = 1. \tag{6.6}$$

The $\mathcal{B}_{\pm,i,b}$ provide an empirical description of the Δt distributions of the background events in the sample so that the terms $\sum_{b=\mathrm{bkgd}} f_{i,b}\mathcal{B}_{\pm,i,b}$ can be added to the likelihood functions for both flavor and CP samples. Each $\mathcal{B}_{\pm,i,b}$ contains its own effective dilution factor $\mathcal{D}_i$ and a common resolution function $\mathcal{R}(\Delta t; \hat{b}_1)$, but differ in the formulation among prompt, non-prompt and peaking components.

The likelihood fit includes as free parameters the fraction of each time component, as well as apparent lifetimes, resolutions, mixing frequencies and dilutions that best describe the events with high weights for being background.

Signal and background events can be separated by their m_{ES} value, since the signal is parameterized by a gaussian (or Crystal Ball) function $\mathcal{S}(m_{ES})$, centered at the M_B value, while for background an Argus shape $\mathcal{A}(m_{ES})$ is used. Moreover the $B \to J/\psi\,\mathrm{X}$ events give a peaking background in m_{ES} and δ_{peak} is the fraction of signal gaussian events due to this background measured from Monte Carlo. The event-by-event signal and background probabilities

$f_{i,b}$ are calculated by a likelihood fit to the m_{ES} distribution

$$\begin{aligned} f_{i,\mathrm{sig}}(m_{ES}) &= \frac{\mathcal{S}(m_{ES})}{\mathcal{S}(m_{ES}) + \mathcal{A}(m_{ES})}(1-\delta_{\mathrm{peak}}) \\ f_{i,\mathrm{peak}}(m_{ES}) &= \frac{\mathcal{S}(m_{ES})}{\mathcal{S}(m_{ES}) + \mathcal{A}(m_{ES})}\delta_{\mathrm{peak}} \\ \sum_{b=\mathrm{bkgd}} f_{i,b}(m_{ES}) &= \frac{\mathcal{A}(m_{ES})}{\mathcal{S}(m_{ES}) + \mathcal{A}(m_{ES})} \end{aligned} \tag{6.7}$$

For example, in the $B^0 \to \psi(2S) K^0_S$ sample collected using the $\psi(2S) \to J/\psi\,\pi^0\pi^0$ decay, I extrapolated, using the m_{ES} fitting procedure on data and Monte Carlo samples (described in the previous chapter) and without applying any flavor tagging selection:

$$\begin{aligned} \mathcal{S}(m_{ES}) + \mathcal{A}(m_{ES}) &= 10, \\ \mathcal{A}(m_{ES}) &= 2.1 \\ \delta_{\mathrm{peak}} &= 0.23 \end{aligned} \tag{6.8}$$

Thus each selected event is a signal event at 61% level, a peaking background event at 18% level and a random background for the remaining 21% of the cases. This estimation must be taken into account when the likelihood fit will be performed using these events.

6.4.2 Global Likelihood Fit

The unbinned likelihood fit for sin2β has a total of 45 free parameters:

1 sin2β value;

16 $\hat{a}_i$ parameters to describe the resolution function for the signal (8 for Run1 and 8 for Run2 data samples);

8 parameters to describe the measured average dilutions $\langle\mathcal{D}_i\rangle$ and dilution differences $\Delta\mathcal{D}_i$ in each tagging category;

6 parameters to describe a common resolution function for all non-peaking backgrounds, different between Run1 and Run2 data samples;

13 parameters to describe the B_{flav} background composition. Some assumptions were made to reduce this number, such as removing the mixing background contribution and assign a corresponding systematic uncertainty. The size and parameters of the peaking background are determined from Monte Carlo simulation;

1 parameter, the fraction of prompt relative to non-prompt background, to describe the CP background composition. It's assumed to be the same for each tagging category. The effective dilutions of the non-prompt and peaking contribution are set to zero, corresponding to no CP-asymmetry in the background. The fraction of peaking background is $\delta^{CP}_{\rm peak} = (1 \pm 1)\%$ of the signal contribution, independent of tagging category. This contribution is assumed to have lifetime parameters in common with the signal.

The determination of the mistag fractions and signal Δt resolution function comes from the high-statistics $B_{\rm flav}$ sample, while background parameters are governed by events with $m_{ES} < 5.27\,{\rm GeV/c^2}$ (except $J/\psi\, K^0_L$).

A blind analysis technique was adopted for the extraction of sin2β in order to eliminate possible experimenter's bias. The method used hides not only the central value for these parameters from the unbinned maximum likelihood fit, but also the visual CP asymmetry in the Δt distribution, while the error on the asymmetry is not hidden. The amplitude of the asymmetry $a_{CP}(\Delta t)$ from the fit was hidden by randomly flipping its sign flip and adding an arbitrary offset. With these techniques, systematic studies can therefore be performed while keeping the numerical value of sin2β hidden.

6.4.3 $\Delta m_{\rm d}$ and Mistag Rates Measurement

When including the dilutions in the mixing asymmetry Eqn. 1.38, $(1 - 2w)$ is simply the coefficient of the cosine term, thus it represents the maximum of the asymmetry oscillation amplitude, calculated at the zero starting time Δt=0. On the contrary $\Delta m_{\rm d}$ is the frequency of the oscillation and its value doesn't influence the mistag rate. Using the tagged $B_{\rm flav}$ sample alone, the value of $\Delta m_{\rm d}$, as well as the dilution factors $\mathcal{D}_i$, the Δt resolution parameters $\hat{a}_i$, and the background Δt parameterization, are obtained with an unbinned maximum likelihood fit, where the log-likelihood $\ln \mathcal{L}_{\rm mix}$ is maximized while keeping the B^0 lifetime fixed. The final sample consists of 12310 fully-reconstructed and tagged B^0 candidates, of which 7399 are in the signal region $m_{ES} > 5.27\,{\rm GeV/c^2}$.

The Δt distributions of the signal ($m_{ES} > 5.27\,{\rm GeV/c^2}$) and background ($m_{ES} < 5.27\,{\rm GeV/c^2}$) candidates, overlaid with the projection of the likelihood fit, are shown in Fig. 6.5. The clear time-dependent mixing asymmetry has been already shown in Fig. 1.7.

The tagging efficiency, the mistag rates and the tagging separation calculated from them for the individual tagging categories in data are listed in Table 6.2. Summing over all tagging categories, a combined effective tagging

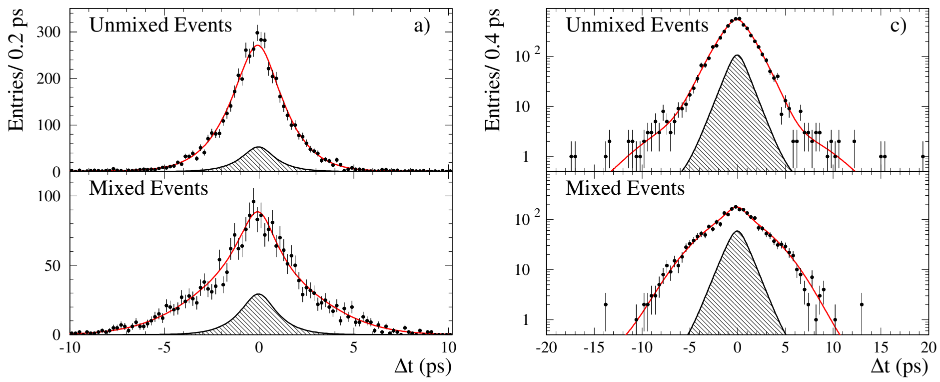

Figure 6.5: Distributions of Δt for unmixed (upper panel) and mixed (lower panel) events in the hadronic B sample in the signal region with a linear (left plot) and logarithmic scale (right plot). The data points are overlaid with the result from the global unbinned likelihood fit. The Δt distributions obtained from the likelihood fit to the full sample are overlaid, along with the simultaneously determined background distribution.

Category	$\epsilon(\%)$	$w(\%)$	$\Delta w(\%)$	Q (%)
Lepton	10.9 ± 0.3	8.9 ± 1.3	0.9 ± 2.2	7.4 ± 0.5
Kaon	35.8 ± 0.5	17.6 ± 1.0	-1.9 ± 1.5	15.0 ± 0.9
NT1	7.8 ± 0.3	22.0 ± 2.1	5.6 ± 3.2	2.5 ± 0.4
NT2	13.8 ± 0.3	35.1 ± 1.9	-5.9 ± 2.7	1.2 ± 0.3
Total	68.4 ± 0.7			26.1 ± 1.2

Table 6.2: Tagging performance for combined Run 1 and Run 2 B_{flav}+B_{CP} samples as published in [86].

efficiency $Q \approx 26\%$ is found. The value of Δm_{d} obtained after applying some corrections is

$$\Delta m_{\text{d}} = 0.516 \pm 0.016 \pm 0.010 \text{ ps}^{-1},$$

where the first error is statistical and the second systematic. The fitted value for Δm_{d} is consistent with the values obtained from various subsamples of the full data set, including individual B decay channels, separate tagging categories, the state of the reconstructed B_{rec} or tagging B_{tag}, and different time periods.

6.4.4 $\sin 2\beta$ Results

The value of $\sin 2\beta$ is extracted with an unbinned maximum likelihood fit to the flavor-eigenstate B_{flav} and B_{CP} samples as described in Section 1.6.3. The Δt resolution parameters $\hat{a}_i$ and the background fractions and time distribution parameters are measured from the CP sample, while the dilution factors $\mathcal{D}_i$ and the vertex parameters are predomintly determined from the more abundant B_{flav} sample. Using the combined $\eta_{CP} = -1$, $\eta_{CP} = +1$, and $J/\psi\, K^{*0}$ *CP* samples the following result was determined:

$$\sin 2\beta = 0.59 \pm 0.14\,(\text{stat}) \pm 0.05\,(\text{syst}) \tag{6.10}$$

The values determined from the varius subsamples alone are 92% consitent with this value.

This result estabilishes *CP* violation in the B^0 system with a 4.1σ significance, computed from the sum in quadrature of the statistical and systematic errors. The probability of obtaining this value, or an highter one, in the absence of *CP* violation is less than 3×10^{-5}. The results obtained with the full B_{CP} samples for Run 1 and Run 2 are consistent at the 1.8 sigma level. In Figure 6.6 one can see the distribution of events as a function of Δt for B^0 and $\overline{B}^0$ tags for the full *CP* sample and for the high purity $\eta_{CP} = -1$ sample alone. Overlaid on the data are the projections of the signal and background Δt distributions obtained from the fit, where the latter is normalized to the projected background level.

The value of $\sin 2\beta$ obtained in bins of Δt by fixing all other parameters to the values obtained with the full *CP* sample are all consistent, demonstrating that the oscillation as a function of Δt has the expected behavior. The observed asymmetry $a(\Delta t)$ is shown in Fig. 6.7 for both the $\eta_{CP} = -1$ and $\eta_{CP} = +1$ samples, along with the projections from the fit results.

The total tagging efficiency is $(68.4 \pm 0.7)\%$ (statistical error only), where the lepton categories have the lowest mistag fractions, but also low efficiency. Finally the mistag fractions are very similar to the mistag fraction that are obtained from the B_{flav} sample alone.

Systematic Uncertainties

The source of systematic error are various and can usefully be grouped into signal description (including detector reconstruction effects), background description, fixed external parameters and statistical limitations of Monte Carlo validation tests for the fitting procedure. The latter is obtained repeating the fit with all parameters fixed to their determined values except $\sin 2\beta$ and corresponds to the a contribution of ± 0.02 to the error on $\sin 2\beta$.

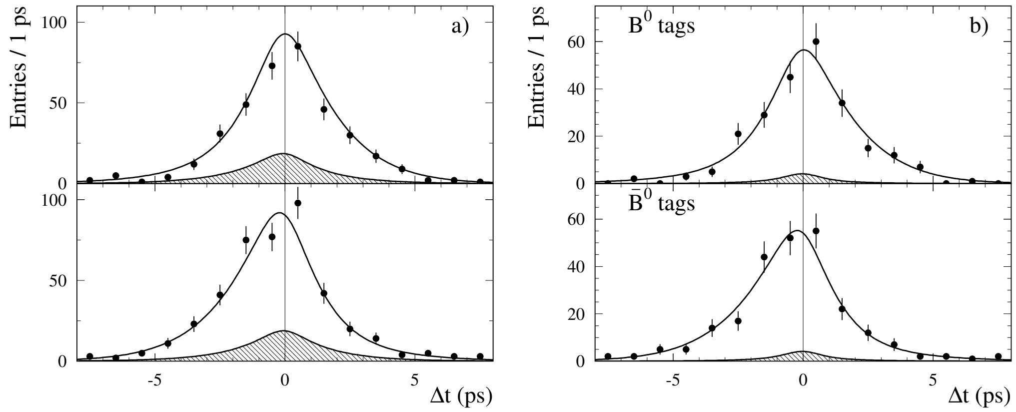

Figure 6.6: a) Distribution of Δt for tagged events in the full *CP* sample. The upper plot show the B^0-tagged events, while the $\overline{B}^0$-tagged are shown in the lower plot. The result from the global unbinned likelihood fit, projected on the basis of the individual signal and background probabilities, and event-by-event Δt resolutions, is overlaid. The probability-weighted Δt spectra of the background candidates obtained from the fit are indicated by the shaded areas. The corresponding distributions for the $\eta_{CP} = -1$ sample are shown in b), where the fitted global value sin2β= 0.59 is imposed.

The dominant sources of systematic error are the assumed parameterization of the Δt resolution function (0.03), due in part to residual uncertainties in the SVT alignment, possible differences in the mistag fractions between the $B_{\rm CP}$ and $B_{\rm flav}$ samples (0.03) and uncertainties in the level, the composition and the *CP* asymmetry of the background (0.02). The systematic errors from uncertainties in Δm_{B^0} and τ_{B^0} and from the parameterization of the background in the selected $B_{\rm flav}$ sample are found to be negligible. An increase of $0.02\,\hbar\,{\rm ps}^{-1}$ in the assumed value for Δm_{B^0} decreases sin2β by 0.015.

6.4.5 Validation Analyses

The large sample of reconstructed events allows a number of consistency checks, including separation of the data by decay mode, data taking period, tagging category and $B_{\rm tag}$ flavor. All the results from different tagging categories and subsamples of data are graphically plotted in Figures 6.8.

Validation studies of the analysis technique have been performed both on data and Monte Carlo samples. For example using fast parameterized Monte Carlo samples, 1000 experiments were generated with the same statistics as the data sample and a full fit was performed, in order to exclude any bias on the sin2β value and error. On the contrary, using large Monte Carlo

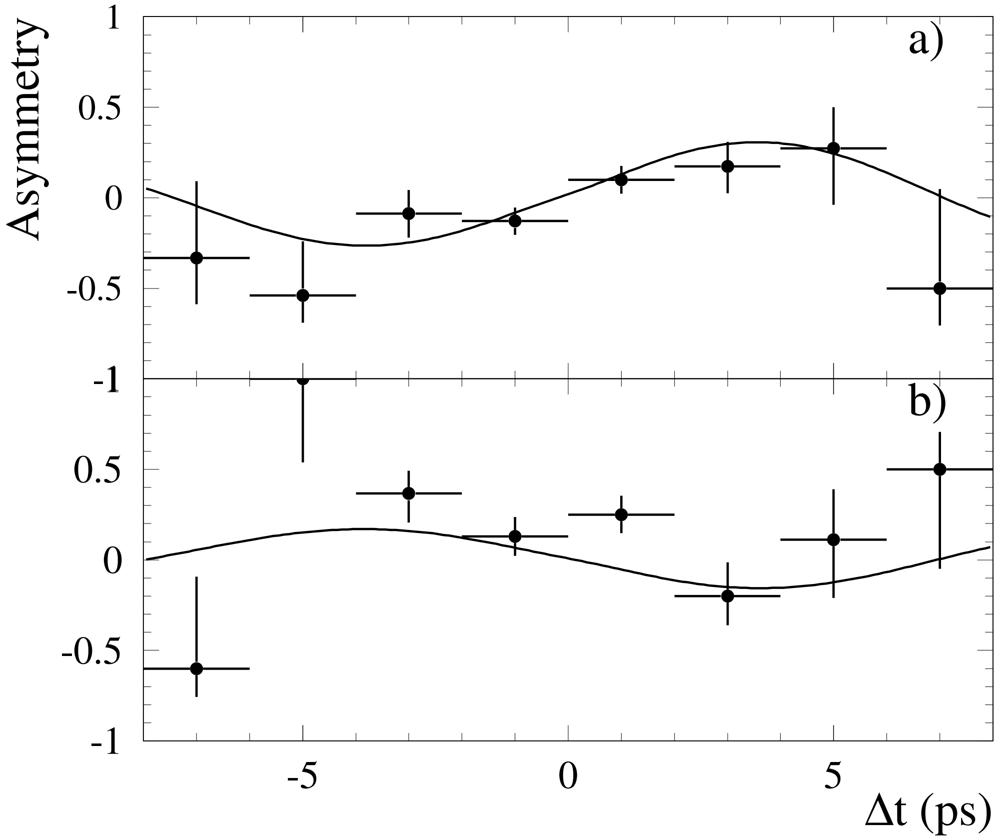

Figure 6.7: Raw asymmetry in the number of B^0 and $\overline{B}^0$ tags in the signal region, $(N_{B^0} - N_{\overline{B}^0})/(N_{B^0} + N_{\overline{B}^0})$, with asymmetric binomial errors, as a function of Δt for a) $\eta_{CP} = -1$ and b) $J/\psi K^0_L$ samples. The data points are overlaid with the separate fit results for the two samples.

samples with fixed values of $\sin 2\beta$, the resolution function parameters and the dilution factors are extracted from the $B_{\rm flav}$ events. Moreover no bias has been found on the result and its error, due to the effect of the background, mostly the J/ψX peaking one.

Other cross checks come from the values of the other parameters involved in the fit. These parameters, such as $\Delta m_{\rm d}$ and τ_{B^0}, are fixed in the global fit with the $B_{\rm flav}$ and B_{CP} samples, but can be allowed to float. The results are consistent with those obtained in their corresponding analysis, on $B_{\rm flav}$ and dilepton sample respectively [90, 86].

Furthermore some control samples in data, in which the asymmetry is expected to be zero, can be use. These are B^0 and B^+ meson decays to flavor-eigenstate mode with a $D^{(*)}$ or charmonium meson in the final state. Fixing

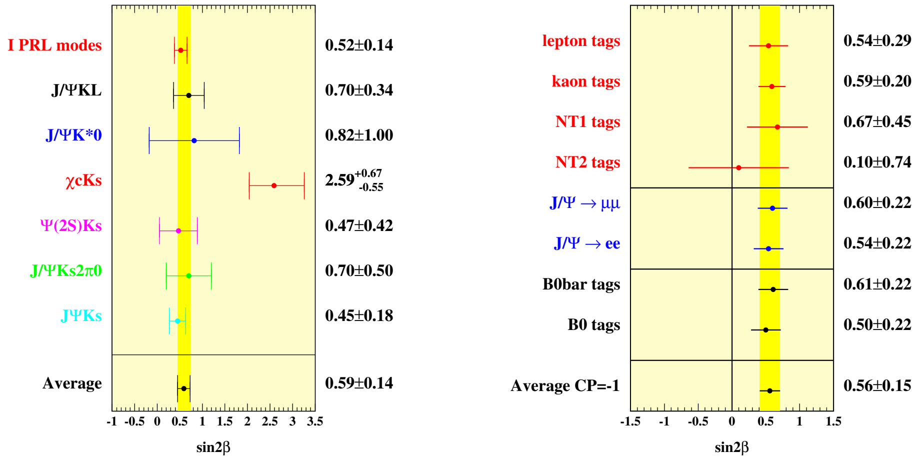

Figure 6.8: Graphical representation of sin2β measurement from different modes and tagging categories.

the Δt resolution function parameters and the dilutions, the CP asymmetry and the fraction of prompt background can be evaluated. With this study any bias coming from the tagging procedure can be excluded, and one can be sure of the adequacy of the assumption that the same resolution function can be used for both the B_{flav} and B_{CP} samples. With these non-CP decay modes no statistically significant asymmetry is found.

6.4.6 Comparison With Other sin2β Measurements

Soon after the *BABAR* results, the Belle Collaboration also announced the observation of the CP violation in the $B^0 \to J/\psi K^0_S$ and $B^0 \to \psi(2S)K^0_S$ channels, reporting the value sin2$\beta$$= 0.99 \pm 0.14 \pm 0.06$ at the 2001 Lepton-Photon Conference **??**. *BABAR* result is consistent at 1.9 sigma level with this measurement and to the previous ones.

Three pioneering measurements of sin2β had been published so far: the CDF Collaboration [92] with a sample of about 400 $B^0 \to J/\psi K^0_S$ candidates from $p\overline{p}$ annihilations at $\sqrt{s} = 1.8$ TeV at the Fermilab Tevatron; the OPAL Collaboration [93] and the ALEPH Collaboration [94], with respectively 24 and 23 $B^0 \to J/\psi K^0_S$ candidates from e^+e^- collisions at the Z^0 peak at the CERN LEP. The results are reported in Fig. 6.9, together with the current world average value, not reported in the PDG yet:

$$\text{World Average:}\ \sin 2\beta = 0.79 \pm 0.11$$

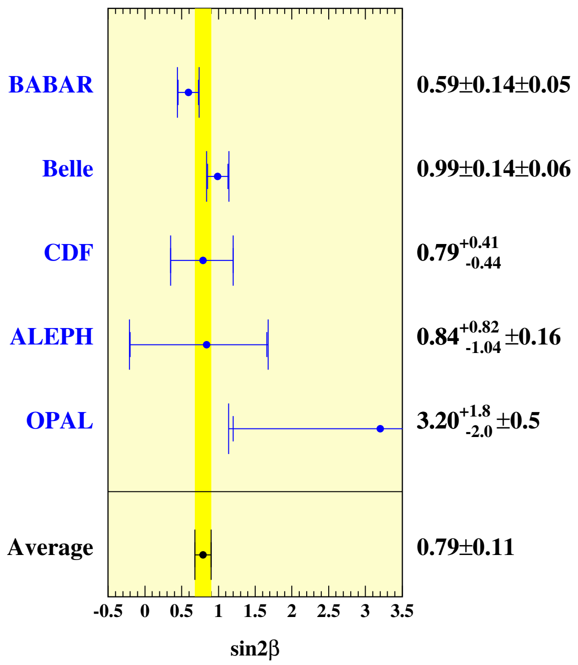

Figure 6.9: sin2β direct measurements world data and current averages.

6.5 Unitarity Triangle Predictions

The measured values of sin2β and $|\lambda|$ can be now interpreted in the context of the Standar Model, with different approaches: one can either simply achieve the best determination of the CKM parameters, or set a confidence level for the agreement between data and the Standard Model predictions, or else search for specific signatures for New Physics. In the Wolfenstein-Buras Standard Model parameterization, only the λ and A parameters are measurable from semileptonic decays of strange and beauty particles, respectively:

$$\lambda = |V_{us}| = 0.22, \qquad A = \frac{|V_{cb}|}{\lambda^2} = 0.826 \pm 0.041 \tag{6.11}$$

Some limits can be set on ρ and η using the available experimental data, namely B^0 and B_s mixing, kaon decay parameter ϵ_K and current measurement on $|V_{ub}|/|V_{cb}|$. These constraints depend, in addition, on other quantities obtained from measurements and/or theoretical calculations. Those can be translated into phenomenological ranges for the three angles α, β and γ.

6.5.1 The Phenomenological Constraints

The constraints on parameters $\overline{\rho}$ and $\overline{\eta}$ are represented as allowed regions in the $(\overline{\rho},\ \overline{\eta})$ plane, that are expected to overlap, as long as the Standard Model gives an overall description of the various experimental observations. At present, the four measurements that restrict the possible range of variations of the $\overline{\rho}$ and $\overline{\eta}$ parameters are the following:

- The relative rate of charmed and charmless b-hadron semileptonic decays allows to measure the ratio

$$\frac{|V_{ub}|}{|V_{cb}|} = \frac{\lambda}{1\ -\ \frac{\lambda^2}{2}}\sqrt{\overline{\rho}^2 + \overline{\eta}^2}\,. \tag{6.12}$$

  This is a circonference centered in (0,0) in the $(\overline{\rho},\ \overline{\eta})$ plane;

- The $B_d^0 - \overline{B}_d^0$ time oscillation period gives the relation on the mass difference, which represents a circonference centered in (1,0):

$$\Delta m_{\rm d}\ = F(x_t)\ A^2\lambda^6\ [(1-\overline{\rho})^2 + \overline{\eta}^2]\, \mathrm{m_{B_d}}\ \mathrm{f^2_{B_d}}\hat{\mathrm{B}}_{\mathrm{B_d}}\ , \tag{6.13}$$

  where $F(x_t)$ contains the perturbative QCD correction terms and $x_t = m_t^2/M_W^2$, with m_t the $\overline{MS}$ top mass, $m_t^{\overline{MS}}(m_t^{\overline{MS}})$. The remaining factor, $f_{B_d}^2\hat{B}_{B_d}$, encodes the information of non-perturbative QCD and, apart for $\overline{\rho}$ and $\overline{\eta}$, is the most uncertain parameter in this expression;

- The limit on the lower value for the time oscillation period of the $B_s^0 - \overline{B}_s^0$ system (not yet observed) is transformed into a limit on Δm_s that is compared with $\Delta m_{\rm d}$

$$\frac{\Delta m_{\rm d}}{\Delta m_s} = \frac{m_{B_d} f_{B_d}^2 \hat{B}_{B_d}}{m_{B_s} f_{B_s}^2 \hat{B}_{B_s}} \left(\frac{\lambda}{1-\frac{\lambda^2}{2}}\right)^2 \times [(1-\overline{\rho})^2 + \overline{\eta}^2]\,. \tag{6.14}$$

  The ratio $f_{B_s}\sqrt{\hat{B}_{B_s}}/f_{B_d}\sqrt{\hat{B}_{B_d}}$ is expected to be better determined from theory than the individual quantities entering into its expression;

- CP violation in the kaon system is expressed by ϵ_K which is represented as an hyperbola if we add the theoretical calculations of the box diagrams describing $K^0 - \overline{K^0}$ mixing, given that:

$$|\epsilon_K| = C_\varepsilon A^2\lambda^6\overline{\eta}\Big[-\eta_1 S(x_c) + \eta_2 S(x_t)\left(A^2\lambda^4\left(1-\overline{\rho}\right)\right) + \eta_3 S(x_c,x_t)\Big]\hat{B}_K \tag{6.15}$$

where

$$C_\varepsilon = \frac{G_F^2 \, f_K^2 \, m_K \, m_W^2}{6\sqrt{2}\pi^2 \Delta m_K} \,. \tag{6.16}$$

$S(x_i)$ and $S(x_i, x_j)$ are the appropriate Inami-Lim functions [95] of $x_q = m_q^2/m_W^2$, including the next-to-leading order QCD corrections [96, 97]. The most uncertain parameter is $\hat{B}_K$.

Constraints are obtained by comparing present measurements with theoretical expectations using the expressions given above and taking into account the different sources of uncertainties. In addition to $\overline{\rho}$ and $\overline{\eta}$, these expressions depend on other quantities measured experimentally. They are limited by the relatively large uncertainties in some of the theoretical quantities, mainly due to non-perturbative QCD effects. In particular, beside the theoretical uncertaintes in the QCD parameters entering in the predictions of $|\epsilon_K|$, Δm_{d} and Δm_s they suffer from theoretical and systematic uncertainties in the determination of $\frac{|V_{ub}|}{|V_{cb}|}$.

Since several years there has been intense activity to constrain the allowed region in the ($\overline{\rho}$, $\overline{\eta}$) plane for the best treatment of the experimental and theoretical inputs. All the methods infer regions in which the values of $\overline{\eta}$ and $\overline{\rho}$ are contained with a certain level of probability, *i.e.* confidence levels. The global uncertainty on $\overline{\eta}$ and $\overline{\rho}$ parameters are deduced combining together statistical and systematic errors from experiments, as well as theoretical uncertainties. They mainly differ in the treatment of these errors and also in the choice of the input values (see [98, 99] and [100]).

Here the current status of the CKM analisys as in Ref. [100] is presented, derived from a Bayesian statistical approach.

The region in the ($\overline{\rho}$, $\overline{\eta}$) plane selected is given in Figure 6.10 with the uncertainties bands for the quantities, described using Equations (6.12)–(6.15). Each band, corresponding to only one of the constraints, contains 68% and 95% of the events obtained by varying the input parameters. In the same figure, overlaid as diagonally hatched area, are the regions corresponding to one and two times the one-standard-deviation uncertainty on the new world average sin2β value, including the latest *BABAR* measurement. This comparison illustrates the consistency of the different constraints provided by the Standard Model.

As four constraints are used to determine the values of two parameters, it is possible to relax, in turn, one (or more) of them, still showing that the Standard Model picture of CP violation in the K system and of B decays and oscillations are consistent. In the near future, new measurements of the angle γ from two-body B decays and more accurate measurement of sin2β

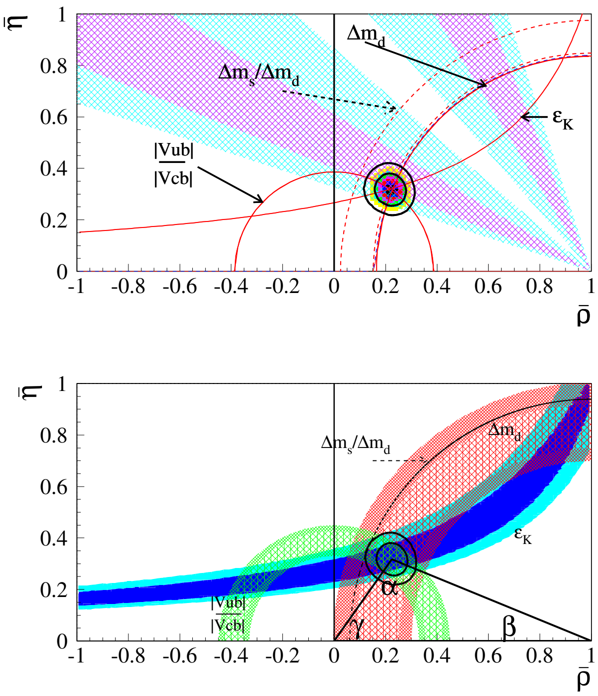

Figure 6.10: The allowed regions in $\overline{\rho} - \overline{\eta}$ space consistent with measurements of CP violation in K_L^0 decay (ϵ_K), V_{ub}/V_{cb} in semileptonic B decay and B_d^o mixing. Upper plot: The curves represent the case of ideal measurement, with infinite precision, obtained from the central values of each quantity. The two dotted curves correspond, from left to right respectively, to the 95% upper limit and to the value of the sensistivity obtained from the experimental study of B_S oscillations. The contours at 68%, 95%, 99% and 99.9% are shown, as defined by a fit from [100]. The linear bands are defined by the sin2β world average measurements. Lower plot: The bands represent the indetermination on the imposed limit, due to the errors in the measurements. The large width of the B_d mixing band is dominated by the uncertainty in $B_B f_B^2$.

from the B Factories, as well as the evidence of $B_s^0 - \overline{B}_s^0$ oscillations from LEP and SLD Collaborations and from Tevatron, could provide the evidence for new physics.

6.5.2 Prospects for sin2β

The method presented here allows a precise measurement of the $\overline{\rho}$ and $\overline{\eta}$ values:

$$\overline{\rho} = 0.218 \pm 0.038, \ \overline{\eta} = 0.316 \pm 0.040 \tag{6.17}$$

Fitted values for the angles of the unitarity triangle have been also obtained

$$\begin{aligned}
&\sin(2\,\beta) = 0.696 \pm 0.068 \\
&\sin(2\,\alpha) = -0.42 \pm 0.24 \\
&\gamma = (55.5 \pm 6.2)^\circ
\end{aligned} \tag{6.18}$$

The prediction of sin2β has to be compared with the world average value: $\sin(2\beta) = 0.79 \pm 0.10$. Althought the consistency with the predictions, these measurements leave open the possibility that the asymmetry is below the Standard Model predictions. Several versions of the Minimal Supersymmetric Standard Model and of models with two Higgs doublets allow an absolute lower bound on sin2β that is, with the present measurement of ΔM_{B_s}, sin2$\beta\geq$ 0.34[101]. To investigate the possibilities of new physics, a direct measurement of the Unitarity Triangle angle γ, usually regarded as being very difficult from an experimental point of view, may be stressed [102, 103]. Indeed very different ranges for γ are allowed for new physics, whethever in the B or in the K mesons mixing systems.

Conclusions

The aim of this work has been to ascertain the possibility to select a new sample of events for the *BABAR* measurement of the sin2β parameter, one of the angles of the unitarity triangle of the Cabibbo-Kobayashi-Maskawa matrix. For this purpose the main topic of this work is the search of the process $B^0 \to \psi(2S) K^0_S$ with the $\psi(2S)$ identified in the $J/\psi \pi^0 \pi^0$ final state. The neutral B meson decay to the final $\psi(2S) K^0_S$ CP-eigenstate directly relates the CP asymmetry with physical quantities that can be easly measured. On the other hand, the $\psi(2S) \to J/\psi \pi^0 \pi^0$ decay mode is the second most probable exclusive decay process and it has estensively studied in literature because of the particular observed shape of the $\pi^0 \pi^0$ invariant mass spectrum. This latter, among all the kinematic variables exploited for the selection, probes to be the most suitable to reach the high purity required by the sin2β measurement. An optimization procedure, tuned on Monte Carlo simulations, has been applied in order to find an adequate compromise between a reasonable efficiency and a good sensitivity for the measurement.

A non-trivial issue of the analysis has been the rejection of misreconstructed B mesons due to fake random combinations of reconstructed neutral pions. As described in the third Chapter, this is the main difficulty when identifing neutral pions at low energy.

The low energy spectrum of the neutral pions ($< 800\,\mathrm{MeV}$) from the $\psi(2S) \to J/\psi \pi^0 \pi^0$ decay also limits the reconstruction efficiency of this decay to be less than 5%. For this reason the charged B decay process $B^\pm \to \psi(2S) K^\pm$ has also been studied, since it's expected to reach a higher statistical significance due to the larger branching ratio (expected to be twice the neutral one) and to the more efficient selection (the neutral decay has the additional requirement of the $K^0_S \to \pi^+ \pi^-$ final state).

On the available *BABAR* data sample equivalent to $44.7\,\mathrm{fb}^{-1}$ integrated luminosity I found 32 events from the $B^\pm \to \psi(2S) K^\pm$ decay and 10 from the $B^0 \to \psi(2S) K^0_S$ decay. As a check on the consistency of the sample, I have presented the branching ratio measurements of the two B mesons decay modes:

$$\begin{aligned}
\mathcal{B}(B^\pm \to \psi(2S) K^\pm) &= (3.3 \pm 1.1(\mathrm{stat}) \pm 0.8(\mathrm{syst})) \times 10^{-4} \\
\mathcal{B}(B^0 \to \psi(2S) K^0_S) &= (3.9 \pm 2.1(\mathrm{stat}) \pm 1.7(\mathrm{syst})) \times 10^{-4}
\end{aligned}$$

which are one σ consistent with other *BABAR* measurements, which are currently the world's most precise ones. This sample of 10 $B^0 \to \psi(2S) K^0_S$ events, when added to the *BABAR* sample of CP-eigenstates from other $\psi(2S)$ final states ($\psi(2S) \to \ell^+ \ell^-$ and $\psi(2S) \to J/\psi \pi^+ \pi^-$), can then be used in the near future to extract the CP violating parameter sin2β.

Moreover the background contribution has been largely studied and the number of background events in the sample measured with a fit procedure on the B meson constrained mass. The relative amounts of background components coming from different sources (other $\psi(2S)$ decays or continuum $q\overline{q}$) have been found from Monte Carlo samples, as required by the sin2β measurement in order to estimate their relative contributions to the CP asymmetry.

Acknowledgements

I'm very grateful to my supervisor, Prof. Alberto Santroni, for giving me the chance to work within the *BABAR* collaboration. I also thanks Giancarlo Piredda for his final support. I'm indebted to Stefano Passaggio and Riccardo Faccini, this work would have not been possible without them. Special thanks to Enrico Robutti and Shahram Rahatlou for their invaluable advices. My gratitude also to the whole *charmonium working group* for their suggestions, and particular thanks to Christos Touramanis and Vincent Tisserand for their collaboration. I feel sincerely grateful to the whole *BABAR* Genova group for their warm welcome and their fruitful and amusing support. This work has made use of the help of many *BABAR* people, scattered all over the world. Many thanks to all of them and to those I met during these years. Particular thanks to the *BABAR* Rome group who has often given me hospitality during these years.

Bibliography

[1] J.H.Christenson, J.W.Cronin, V.L.Fitch, R.Turlay, *Phys. Rev. Lett.* [13], 138 (1964).

[2] G. Lüders, *Ann. Phys.* **2**:1 (1957)

[3] Particle Data Group (D. E. Groom *et al.*), *Review of Particle Physics*, *Eur. Phys. Jour. C* **15** (2000)

[4] E. Fermi, *Z. Phys.* **88**:161 (1934)

[5] C.S. Wu *et al.*, *Phys. Rev.* **105**:1413 (1957)

[6] R.L. Garwin , L. M. Lederman, M. Weinrich, *Phys. Rev.* **105**:1415 (1957)

[7] L.D. Landau, Zh. Eksp. Teor. Fiz. **32**:405 (1957); *Nucl. Phys.* **3**:127 (1957)

[8] V. L. Fitch, R. F. Roth, J. S. Russ, W. Vernon, *Phys. Rev. Lett.* **15**:73 (1965)

[9] M. Kobayashi, T. Maskawa, *Prog. Th. Phys.* **49**:652 (19 73)

[10] A. Carter, A.I.Sanda, *Phys. Rev. Lett.* 45,952 (1980); *Phys. Rev. D* 23,1567 (1981); I.I. Bigi, A.I. Sanda, *Nucl. Phys.* 193, 851 (1981).

[11] T. Lohse *et al.* DESY-PRC 94/02, (1984).

[12] *The CDF II Detector, Technical Design Report*, FERMILAB-Pub-96/390-E, November 1996. The D0 upgrade: *The Detector and its physics*, FERMILAB-Pub96/357-E, October 1996.

[13] BELLE Collaboration (A. Abashian et al.) *Measurement of the CP violation parameter* $\sin 2\phi$ *in $B^0(D)$ meson decays*, *Phys. Rev. Lett.* **86**, 2509-2514 (2001).

[14] *LHC-B Letter of Intent*, CERN/LHCC 95-5, LHCC/18, August 1995.

[15] G. C. Branco, L. Lavoura and J. P. Silva, *CP violation* (Clarendon Press, Oxford, 1999) and reference therein.

[16] A. D. Sakharov, ZhETF Pis. Red. **5**, 32 (1967); JETP Lett. **5**, 24 (1967).

[17] G. Bonvicini *et al.* (The CLEO Collaboration), *Phys. Rev. Lett.* **84**:5940 (2000)

[18] P. Huaet and E. Sather, *Phys. Rev.* **D51**:379, `hep- ph/9404302` (1995)

[19] C. Quigg, *The State of the Standard Model*, FERMILAB- Conf-00/-021-T, `hep-ph/0001145`

[20] S.L. Glashow, *Nucl. Phys.* **22**:579 (1961)

[21] S. Weinberg, *Phys. Rev. Lett.* **19**:1264 (1967)

[22] A. Salam, in N. Svartholm (Ed.), *Proceedings of the 8*$^{\text{th}}$ *Nobel Symposium*, Stockholm (1968)

[23] N. Cabibbo, *Phys. Rev. Lett.* **10** (1963) 531;

[24] L. Wolfenstein, *Phys. Rev. Lett.* **51**:1945 (1983)

[25] A.J. Buras, M.E. Lautenbacher and G. Ostermaier, *Phys. Rev.* **D50** (1994) 3433.

[26] I.I. Bigi, A.I. Sanda, *CP Violation*, Cambridge (2000)

[27] I.I. Bigi and A.I. Sanda, *Nucl. Phys.* **B193**:85 (1981)

[28] J.L. Rosner, Talk presented at the 2$^{\text{nd}}$ Tropic al Workshop in Particle Physics and Cosmology, Puerto Rico, EFI 2000-16, `hep-ph/0005258` (2000)

[29] The *BABAR* Collaboration, *Letter of Intent for the study of CP violation and Heavy Flavour Physics at PEP-II*, SLAC Report SLAC-443 (1994)

[30] The *BABAR* Collaboration, *Technical Design Report*, SLAC-REP-372 (1995)

[31] P. Oddone, in D. Stork, Editor, *Proceedings of the UCLA Workshop: Linear Collider* $B\overline{B}$ *Factory Conceptual Design* (1987)

[32] *PEP-II Conceptual Design Report*, SLAC Report SLA C-418 (1993)

[33] J. Seeman *et al.*, *Status Report on PEP-II Performance*, in *Proceedings of the VII European Particle Accelerator Conference* – EPAC 200 0, Vienna, Austria (June 2000)

[34] B.Aubert *et al.*, [*BABAR* Collaboration], SLAC-PUB-8569, [hep-ex/0105044], sub. to *Nucl. Instr. and Methods* .

[35] C. Bozzi *et al.*, *Nucl. Instr. and Methods* **A435**:25 (1999)

[36] A. Boucham *et al.*, *Nucl. Instr. and Methods* **A409**:615 (1998)

[37] P.Billoir, *Nucl.Instr.Methods* , A225 (1984) 225

[38] *Measurement of the GoodTrackLoose efficiency using SVT tracks*, *BABAR* Analysis Document # 157 (2001).

[39] J. Schwiening *et al.*, *Nucl. Instr. and Methods* **A409**:211 (1998)

[40] *Studies on* π^0*reconstruction: Status report*, *BABAR* Analysis Document # 20 (2001).

[41] N. Cavallo, *Nucl. Phys. B Proc. Suppl.* **78**:64 (1999)

[42] B. Jacobsen, *Nucl. Instr. and Methods* **A389**:1 (1997)

[43] T. S. Johnson, Talk presented at the International Conference on Computing in High-Energy Physics, Chicago, Illinois, SLAC-PUB-7963 (1998)

[44] E.D. Frank, B. Jacobsen, E. Sexton-Kennedy *et al.*, *Architecture of the BABAR Reconstruction Code*, *BABAR* Note # 379 (1997)

[45] A. Ryd *et al.*, http://www.slac.stanford.edu/BFROOT/www/Physics/Tools/generators/EvtGen/EvtGen.html

[46] CN/ASD, *GEANT: Detector description and simulation tool*, CERN (199 4)

[47] A. Drescher, *et al.*, Nucl. Instrum. Methods **A237**, 464 (1985).

[48] Ralph Sinkus and Thomas Voss, Nucl. Instrum. Methods **A391**, 360 (1997)

[49] Crystal Ball Collaboration (D. Antreasyan et al.), Z.Phys.C48:561-568 (1990).

[50] *Describing energy deposit in CsI crystals*, *BABAR* Note # 294 (1996).

[51] *Study of π^0Reconstruction Efficiency in Run1 data using $\tau^+\tau^-$1-on-1 decays*, *BABAR* Analysis Document # 196 (2001).

[52] *Calibration of the BABAR Electromagnetic Calorimeter with π^0 BABAR* Note # 528 (2000).

[53] *Kaon Selection at the BABAR Experiment*, *BABAR* Analysis Document # 116 (2001).

[54] *Cut-Based Electron Identification*, *BABAR* Analysis Document # 90 (2001).

[55] *Muon Identification in the BABAR Experiment*, *BABAR* Analysis Document # 60 (2001).

[56] G.C. Fox, S. Wolfram, *Nucl. Phys.* **B149**:413 (1979)

[57] *Studies on $K^0_S \rightarrow \pi^+\pi^-$reconstruction*, *BABAR* Analysis Document # 19 (2001).

[58] *Recomandation for Exclusive B Reconstruction*, *BABAR* Analysis Document # 19 (2001).

[59] *A User's Guide to RooFitTools Package...* , *BABAR* Analysis Document # 18, 2000.

[60] H. Albrecht, et al (ARGUS Collaboration), *Reconstruction of B Mesons*, *Phys. Lett.* **B 185**,218 (1987).

[61] G. Abrams, *Proceedings of the 1975 International Symposium on Lepton and Photon Interactions at High Energies*, Published by the Stanford Linear Accelerator Center, 36 (1975).

[62] L. S. Brown and R. N. Cahn, Phys. Rev. Lett. **35**, 1 (1975).

[63] R. N. Cahn, Phys. Rev. D **12**, 3559 (1975).

[64] K. Gottfried, Phys. Rev. Lett. **40**, 598 (1978).

[65] T. M. Yan, Phys. Rev. D**22**, 1652 (1980).

[66] M. B. Voloshin and V. Zakharov, *Phys. Rev. Lett.* **45**, 688 (1980).

[67] V. A. Novikov and M. A. Shifman, Z. Phys. C **8**, 43 (1981).

[68] T. Mannel and R. Urech, Z.Phys.C **73**, 541 (1997).

[69] T.Yan,*Phys. Rev.* D**22**, 1652 (1980).

[70] F. Butler *et al.* (CLEO Collaboration), Phys. Rev. D **49**, 40 (1994).

[71] BES Collaboration, *Phys. Rev. D* **62**, 032002 (2000).

[72] J. Zhu *et al.*, hep-ph/0001314

[73] M.Ambrogiani *et al.* (E835 Collaboration), *Phys. Rev. D* **62**, 032004 (2000)

[74] S.Brandt *et al.*, *Phys. Lett.* **12**, 57 (1964)

[75] *Measurement of the Number of Upsilon(4S) Mesons Produced in Run1 (B Counting)*, *BABAR* Analysis Document #134 (2001).

[76] GEANT Detector Description and Simulation Tool, Version 3.21, CERN Program Library W5103, CERN (unpublished) (1995).

[77] *Measurement of Inclusive Production of Charmonium States in B Meson Decays*, *BABAR* Analysis Document # 139 (2001).

[78] The *BABAR* Collaboration (P. F. Harrison and H. R. Quinn, Eds.), *The BABAR Physics Book*, SLAC-REP-504 (1998)

[79] F. Le Diberder, *Precision on CP Violation Measurements and Requirement on the Vertex Resolution*, *BABAR* Note # 34 (1990)

[80] *Lepton Identification Efficiencies and Systematic Errors*, *BABAR* Analysis Document # 126 (2001).

[81] See `http://www.slac.stanford.edu/BFROOT/www/Organization/CollabMtgs/2001/detJun2001/Wed1e/mancinelli.pdf`

[82] *The BABAR vertexing*, *BABAR* Analysis Document # 102 (2001).

[83] *Studies on* $K_S^0 \to \pi^+\pi^-$ *reconstruction: Status Report*, *BABAR* Analysis Document # 19 (2000).

[84] *Measurement of Branching Ratios of Charged and Neutral B Mesons into Exclusive Charmonium Final States*, *BABAR* Analysis Document # 113 (2001).

[85] See contributed to International Europhysics Conference on High Energy Physics (HEP 2001), Budapest, Hungary, 12-18 Jul 2001.

[86] *BABAR* Collaboration, B. Aubert *et al. Phys. Rev. Lett.* **87**, 091801 (2001);

[87] *Time-dependent CP-violating asymmetries and flavor oscillations in neutral B decays*, *BABAR* Analysis Document # 129 (2001). To be sub. to *Phys. Rev. D* **.**

[88] *BABAR* Collaboration, B. Aubert *et al.Phys. Rev. Lett.* **86**, 2515 (2001).

[89] *BABAR* Collaboration, B. Aubert *et al.*, *Measurement of branching fractions for exclusive B decays to charmonium final states*, *BABAR*-PUB-01/07, SLAC-PUB-8909, hep-ex/0107025, to appear in *Phys. Rev. D* .

[90] *BABAR* Collaboration, B. Aubert *et al.*, *Phys. Rev. Lett.* **87**, 201803 (2001).

[91] See Proceedings from Lepton-Photon Conference, Rome 2001.

[92] T. Affolder *et al.* (The CDF Collaboration), *Phys. Rev.* **D61**:720 05 `hep-ex/9909003` (1999)

[93] K. Ackerstaff *et al.* (The OPAL Collaboration), *Eur. Phys. Jour. C* **5** :397 (1998)

[94] R. Barate *et al.* (The ALEPH Collaboration), *Phys. Lett.* **B492**: 259 (2000)

[95] T. Inami and C.S. Lim, Prog. Theor. Phys. **65** (1981) 297; *ibid.* **65** (1981) 1772.

[96] A.J. Buras, M. Jamin and P.H. Weisz, *Nucl. Phys.* **B347** (1990) 491.

[97] S. Herrlich and U. Nierste, *Nucl. Phys.* **B419** (1994) 192;
G. Buchalla, A.J.Buras and M.E. Lautenbacher, *Rev. Mod. Phys.* **68**, (1996) 1125.

[98] A. Hocker, H. Lacker, S. Laplace and F. Le Diberder, Eur. Phys. J. C **21** (2001) 225 [arXiv:hep-ph/0104062].

[99] S. Stone, arXiv:hep-ph/0112008.

[100] M.Ciuchini *et al.* , *200 CKM-triangle analysis: A critical review with updated experimental inputs and theoretical parameters*, `hep-ph/0012308` .

[101] A. J. Buras, R. Buras, TUM-HEP-285/00, MPI-TH/2000-30, hep--ph/0008273

[102] J. P. Silva, L. Wolfenstein, hep-ph/0008004 (20 00)

[103] A.L. Kagan and M. Neubert, hep-ph/0007369 (2000)